

**Development of Microstructure-Informed Computational Models for the
Design of Cold-Sprayed Additively Manufactured Metal-Ceramic
Composite Materials**

by

Saman Sayahlatifi

A thesis submitted in partial fulfillment of the requirements for the degree of

Doctor of Philosophy

Department of Mechanical Engineering
University of Alberta

© Saman Sayahlatifi, 2024

Abstract

This thesis develops microstructure-based finite element (FE) models of cold-sprayed additively manufactured (CSAM) metal-ceramic composites – Al-Al₂O₃ in this research – to fill a gap in our understanding of the microscale failure progression in the material in correlation with its macroscale response across stress states and strain rates. Representative volume elements (RVEs) of the material are generated by Digimat based on the features of Al₂O₃ ceramic particles, including weight fraction, size distribution, and clustering in addition to porosity in the metal matrix that are achieved by the scanning electron microscopy (SEM) characterization. Stress state- and strain rate-dependent constitutive models are implemented via VUMAT subroutines in Abaqus/Explicit FE solver to capture the growth of failure mechanisms, namely debonding of interfaces, particle cracking, and matrix failure. The micromechanical models are validated by the experimental data both quantitatively (i.e., stress-strain curves) and qualitatively (i.e., the manifestation of failure mechanisms in fractography analysis). The validated micromechanical model is leveraged to quantify the growth history of failure mechanisms in association with the stress-strain response of the material under different stress states and strain rates, which is not readily within reach by the available experimental mechanics approaches. Such quantification framework is next employed to systematically track the interaction and propagation of failure mechanisms as a function of microstructural characteristics (i.e., particle weight fraction, particle size, and particle clustering), stress state (i.e., uniaxial compression, uniaxial tension, and pure shear), and strain rate (i.e., quasi-static and dynamic loading covering 10^{-3} to 10^{-2} s⁻¹ and 170 to 3200 s⁻¹,

respectively). This thesis is the first of its kind that provides a foundational understanding of the relationships between the microstructure, growth history of microscale failure mechanisms, and stress-strain response – as the general descriptor of the macro scale behavior – of CSAM metal-ceramic composites through establishing experimentally validated micromechanical FE models. As a comprehensive dataset generator covering the space of design across microstructures, stress states, and strain rates, the current computational framework will lay the foundation for the development of computationally efficient machine learning-based surrogate models of the microstructure-property-performance relationships of the material in addition to accelerating concurrent multiscale simulations for the design and optimization of CSAM metal-ceramic composites as structural materials and coatings with an application-specific fine-tuned mechanical performance.

Preface

Chapter 2 of this thesis has been published as **Saman Sayahlatifi**, Chenwei Shao, André McDonald, and James David Hogan, “[3D microstructure-based finite element simulation of cold-sprayed Al-Al₂O₃ composite coatings under quasi-static compression and indentation loading](#)”. Published in the *Journal of Thermal Spray Technology*, vol. 31, p. 102–118, 2022. As the first author, I was responsible for conceptualization, development of models and numerical methodologies, data analysis and visualization, and writing the original manuscript. Chenwei Shao was accountable for material fabrication, conducting experiments, and materials characterization. André McDonald was the supervisory author involved with concept formation, manuscript review & editing, and funding acquisition. James David Hogan was the supervisory author involved with concept formation, manuscript review & editing, and funding acquisition.

Chapter 3 of this thesis has been published as **Saman Sayahlatifi**, Zahra Zaiemyekheh, Chenwei Shao, André McDonald, and James David Hogan, “[Micromechanical damage analysis of Al-Al₂O₃ composites via cold-spray additive manufacturing](#)”. Published in the *International Journal of Mechanical Sciences*, vol. 259, p. 108–118, 2023. As the first author, I was responsible for conceptualization, development of models and numerical methodologies, data analysis and visualization, and writing the original manuscript. Zahra Zaiemyekheh was involved with numerical methodologies and validation. Chenwei Shao was accountable for material fabrication, conducting experiments, and materials characterization. André McDonald was the supervisory author involved with concept formation, manuscript review & editing, and funding

acquisition. James David Hogan was the supervisory author involved with concept formation, manuscript review & editing, and funding acquisition.

Chapter 4 of this thesis has been published as **Saman Sayahlatifi**, Zahra Zaiemyekheh, Chenwei Shao, André McDonald, and James David Hogan, “[Strain rate-dependent behavior of cold-sprayed additively manufactured Al-Al₂O₃ composites: Micromechanical modeling and experimentation](#)”. Published in *Composites Part B: Engineering*, vol. 280, p. 111–149, 2024. As the first author, I was responsible for conceptualization, development of models and numerical methodologies, data analysis and visualization, and writing the original manuscript. Zahra Zaiemyekheh was involved with numerical methodologies and validation. Chenwei Shao was accountable for material fabrication, conducting experiments, and materials characterization. André McDonald was the supervisory author involved with concept formation, manuscript review & editing, and funding acquisition. James David Hogan was the supervisory author involved with concept formation, manuscript review & editing, and funding acquisition.

Acknowledgements

I would like to express my deepest gratitude to my supervisors, Prof. [James David Hogan](#), and Prof. [André McDonald](#), for their unwavering support, guidance, and encouragement throughout my PhD journey. Your belief in my abilities has been a constant source of strength, and your mentorship has not only shaped my research but also profoundly influenced my personal growth. I am eternally grateful for everything you have done for me.

To the committee members of my final exam, Prof. [Leijun Li](#), Prof. [Mustafa Gül](#), Prof. [Tobin Filleter](#), and Dr. [David Gordon](#), your invaluable insights and constructive feedback have been pivotal in refining my work. I am grateful for putting your valuable time and effort in reviewing my work.

I extend my heartfelt appreciation to the Alberta Innovates Graduate Student Scholarship ([AI GSS](#)), the Natural Science and Engineering Research Council Canada (NSERC), the Alberta Graduate Excellence Scholarship ([AGES](#)), the [Sadler Graduate Scholarship in Mechanical Engineering](#), the [RR Gilpin Memorial Scholarship](#), and the [University of Alberta Doctoral Recruitment Scholarship](#), whose generous funding provided the foundation for my research, and I am sincerely grateful.

To my colleagues and friends at the Centre for Design of Advanced Materials ([CDAM](#)), thank you for sharing your knowledge with me through countless discussions over my time at the CDAM, your camaraderie, and collaboration. The friendships and memories we have built together have made this journey truly enjoyable. I also want to acknowledge Dr. [Maria Ophelia Jarligo](#) from the Advanced Heat Transfer and Surface Technologies ([AHTST](#)) Laboratory for her assistance and support.

Last but not least, to my beloved parents (Mostafa and Masoumeh) and wife (Zahra), your unwavering love, patience, and encouragement have been my rock. Your faith in me, has given me the strength to persevere. You have been my constant source of motivation, and for that, I am eternally thankful.

Table of Contents

1	Introduction	1
1.1	Motivation	1
1.2	Thesis Objectives	5
1.3	Research Contributions	7
1.4	Thesis Structure	8
2	3D microstructure-based finite element simulation of cold-sprayed Al-Al₂O₃ composite coatings under quasi-static compression and indentation loading	11
2.1	Abstract	11
2.2	Introduction	12
2.3	Experimental Procedures	15
2.3.1	Material and Specimen Preparation	15
2.3.2	Mechanical testing and characterization	15
2.4	Numerical Methodology	18
2.4.1	Geometry and model description	18
2.5	Material models	21
2.5.1	The GTN model for matrix failure	21
2.5.2	The JH2 model for particle cracking	23
2.5.3	The cohesive zone model for the interfacial debonding	25
2.6	Results	27
2.6.1	Quasi-static compression	27
2.7	Vickers micro-indentation	34
2.8	Discussion	36
2.9	Conclusion	39
2.10	Acknowledgment	39

3	Micromechanical damage analysis of Al-Al₂O₃ composites via cold-spray additive manufacturing	40
3.1	Abstract	40
3.2	Introduction	41
3.3	Methodology	45
3.3.1	Material fabrication and characterization	45
3.3.2	Micromechanical model and numerical procedures	48
3.3.3	Material constitutive models	51
3.4	Results and discussion	58
3.4.1	The effect of geometric parameters	59
3.4.2	Model validation and quantification of failure mechanisms	61
3.4.3	Load partitioning analysis	65
3.4.4	The effect of particle content	67
3.4.5	The effect of stress state	72
3.4.6	The effect of particle size	78
3.5	Conclusions	81
3.6	Acknowledgment	83
3.7	Supplementary materials	83
4	Strain rate-dependent behavior of cold-sprayed additively manufactured Al-Al₂O₃ composites: Micromechanical modeling and experimentation	86
4.1	Abstract	87
4.2	Introduction	87
4.3	Experimental methods	91
4.4	Micromechanical modeling	92
4.4.1	RVE reconstruction and numerical setups	92
4.4.2	Constitutive modeling of materials/interfaces	96
4.5	Results and discussion	98
4.5.1	Micromechanical model validation	98
4.5.2	Post-mortem SEM fractography	101
4.5.3	Strain rate-dependent evolution of failure mechanisms	105
4.5.4	Stress-bearing partitioning analysis	108
4.5.5	The role of particle clustering	110
4.5.6	The failure behavior of the material under elevated temperatures	113
4.6	Conclusions	119
4.7	Acknowledgment	120

4.8	Supplementary materials	120
4.8.1	Constitutive models	120
4.8.2	Supplementary figures	129
5	Conclusions & Future Work	134
5.1	Conclusions	134
5.2	Future work	137
5.3	Academic contributions	139
	Bibliography	142

List of Tables

2.1	GTN model constants used in this study. Here, the value of f_0 corresponds to the composites with 34wt.% of reinforcing particles. For Al-46 wt.% Al ₂ O ₃ composites, the initial porosity was determined to be 0.0023 on average, while all other constants remain the same as the 34 wt.% case.	23
2.2	The JH2 constants used for Al ₂ O ₃ reinforcing particles [57, 105] . . .	25
2.3	Summary of the matrix/particle interface properties.	27
3.1	The parameters of the material constitutive models used in this study. Note that the values without a reference were tuned to achieve the best match with the experimental data in this study.	55
3.2	The parameters used for the CZM of matrix/particle interfaces. Note that the parameter δ_m^f was tuned to achieve the best match with the experimental stress-strain responses in this study.	58
4.1	The constants of the enhanced Zhou et al. model [64] in the current work used in modeling of strain rate-dependent behavior of CSAM Al-Al ₂ O ₃ composites.	124
4.2	The JH2-V model constants used for Al ₂ O ₃ reinforcing particles accounting for the size of the particles in modeling of strain rate-dependent behavior of CSAM Al-Al ₂ O ₃ composites.	128
4.3	The particle size-dependent interfacial properties in modeling of strain rate-dependent behavior of CSAM Al-Al ₂ O ₃ composites.	129

List of Figures

1.1	Experimental evidence for the motivation of this thesis for developing stress state- and strain rate-dependent microstructure-based FE models for CSAM Al-Al ₂ O ₃ composites: (a) The experimentally captured stress-strain response of CSAM Al-35 wt.% Al ₂ O ₃ composites under quasi-static uniaxial tension [50] and compression [30]. (b) The experimentally captured stress-strain responses of CSAM Al-46 wt.% Al ₂ O ₃ composites under quasi-static and dynamic loading [51].	4
2.1	Preparation, test, and characterization of Al-Al ₂ O ₃ composite coatings: (a) A schematic illustration of the cold spray setup used for the fabrication of pure Al and MMC coating samples: The processing strategy for making the mixed powder includes gas atomization, sieving, and mixing using a rotated cylinder; (b) Typical compressive cuboidal specimen with dimensions 2.3 mm × 2.7 mm × 3.5 mm cut from the composite depositions via wire electrical discharge machining, which was loaded in the direction of the 3.5 mm dimension. The green contour shows the region of interest defined on the specimen surface in VIC-2D software for monitoring the strain fields. The top image shows an example of Al-Al ₂ O ₃ coating deposited on an Al substrate from which the cuboidal specimens were cut; (c) SEM characterization of the microstructure of Al-34 wt.% Al ₂ O ₃ composite coating showing the distribution and morphology of the reinforcing ceramic particles in the Al matrix; (d) SEM micrograph of Al-46 wt.% Al ₂ O ₃ composite coating. Note that the black arrows on the SEM micrographs show the deposition direction. The darker regions correspond to the Al phase and the lighter regions correspond to the alumina phase.	16

2.2	(a) Application of kinematic coupling between the boundary faces and the reference points (RP) in yellow color to apply compressive load and boundary conditions: All degrees of freedom were coupled to each other; (b) The boundary conditions applied on the RVE: The displacement control technique was applied to the RP in red color using a smooth amplitude to meet the quasi-static condition.	19
2.3	Finite element model of the micro-indentation Vickers test. The block and the indenter were discretized by 30,276 first order 8-node 3D elements with reduced integration (C3D8R) and 2104 quadrilateral 4-node 3D rigid elements (R3D4), respectively.	20
2.4	Numerical (Num) and experimental (Exp) stress-strain responses under quasi-static compression for different weight percentage of alumina in the Al matrix. The cuboidal samples were all tested in three different directions denoted by X, Y, and Z corresponding to the nozzle moving direction, the second in-plane direction perpendicular to the nozzle moving direction, and the deposition direction, respectively. The dashed curves correspond to the experimental responses for each coating and the solid curves represent the associated numerically predicted behavior.	28
2.5	The numerically predicted manifestation and evolution of the damage mechanisms in Al-34 wt.% Al ₂ O ₃ MMC at an axial strain of 4% and 10%: (a) The equivalent plastic strain (PEEQ), which reveals the evolution of plastic deformation in the thin ligaments between the ceramic particles; (b) The data shows the scatter of matrix/particle debonding failure criterion demonstrating the initiation of interfacial failure at the sharp corners of inclusions; (c) The distribution of the JH2 damage parameter shows the accumulation of damage and element removal in the concaves of particles either at the boundary surfaces or considerably close to each other; (d) SEM micrograph of the Al-34 wt.% Al ₂ O ₃ MMC subject to quasi-static compression showing the localized occurrence of damage mechanisms (e.g., matrix ductile failure, and matrix/particle decohesion) at a micro length scale, which does not lead to the coalescence of micro cracks and global failure of the composite at the macro scale.	30

2.6	The numerical qualitative results for the Al-46 wt.% Al ₂ O ₃ MMC shown at an axial strain of 4% and 10%: (a) The contour shows the distribution of void volume fraction in the Al matrix, which accumulates in the thin ligaments between the alumina particles forming ~ 45° shear cracks as the strain reaches 10%; (b) The spatial distribution of matrix/particle decohesion damage variable (CSDMG) which illustrates more severely debonding failure compared to the Al-34 wt.% Al ₂ O ₃ MMC (see Fig. 5(b)). This results in loss of stiffness and load sustaining capacity as shown in Fig. 4 (see the solid blue curve); (c) The data illustrates the evolution of particle cracking initiating from the sharp corners within the RVE as the axial strain increases from 4% to 10%.	32
2.7	SEM micrograph of the Al-46 wt.% Al ₂ O ₃ MMC subject to quasi-static compression showing the simultaneous occurrence of failure mechanisms, namely matrix ductile failure, matrix/particle interfacial failure, and particle cracking. The 3D numerical predictions of the failure mechanisms (see Fig. 2.6 for more details) have been correspondingly shown, which confirm the qualitative validity of the model. The damaged areas are shown in black. Note that this micrograph represents the cuboidal sample loaded in Y direction and has been observed through X (i.e., the nozzle moving direction) direction.	33
2.8	(a) Numerical prediction of the indented area for the MMC composites based on the homogenization approach. The numerically measured diagonal length, d, of the indented profile is substituted into the Eq. (2.25) to calculate the Vickers hardness; (b) The distribution of the residual von Mises stress in the homogenized block of Al-34 wt.% Al ₂ O ₃ composite after unloading.	35
2.9	Comparison of experimental and numerical Vickers hardness of the MMC coatings. The X, Y, Z on the horizontal axis represent the direction over which the Vickers indentation was carried out on the samples which correspond to the nozzle travel direction, the deposition direction, and the third perpendicular direction, respectively. Unlike the experimental results, there is no variation in the predicted hardness values due to the homogenization approach.	36

- 3.1 Schematic of the experimental methodology for fabricating and testing of CSAM Al-46 wt.% Al₂O₃ composites: (a) Aluminum and Al₂O₃ powders after sieving with a size distribution of 40 to 60 μm and 30 to 45 μm, respectively. (b) An SEM image of the CSAM Al-46 wt.% Al₂O₃ composite microstructure. (c) Al₂O₃ particle size distribution obtained by ImageJ software based on SEM images of the composite. The particle size distribution follows a log-normal curve with mean and standard deviation values of 2.04 μm and 0.54, respectively, that was used to generate the microstructure-informed RVEs by Digimat software. (d) The cuboidal specimen with dimensions of 2.3 mm × 2.7 mm × 3.5 mm cut by electrical discharge machining from the CSAM bulk Al-46 wt.% Al₂O₃ composite. The specimen was loaded under quasi-static uniaxial compression at a rate of 10⁻³ s⁻¹. Note that the speckle pattern on the sample surface was applied to capture the strain fields with DIC analysis. 46
- 3.2 The model description and numerical methodology: (a) The microstructure-informed RVE generated by Digimat for the CSAM Al-46 wt.% Al₂O₃ composite. Randomly oriented icosahedron-shaped (i.e., 20-faced polyhedron) Al₂O₃ particles were randomly distributed in the Al matrix with the size distribution represented in Fig. 3.1(c). Initial pores with an icosahedron morphology and with a volume fraction of 0.17% and a size of 1.5 μm were randomly dispersed in the matrix. (b) The mixed static-kinematic boundary condition [43] for applying the load on the RVE through displacement control with a smooth step amplitude. (c) The history of nominal axial strain applied to the model by displacement control and the balance of the internal (ALLIE) and the kinetic (ALLKE) energies which confirms the quasi-static condition (i.e., ALLKE/ALLIE ≤ 10%) [91]. (d) A summary of the mesh convergence study, including the element size, the number of elements, and the corresponding computational runtime. The element size of 0.75 μm was selected for further studies and this was chosen to balance the runtime and accuracy (see Fig. 3.3(b)). 49

3.3	The effect of the model and numerical variables on the predicted stress-strain response of CSAM Al-46 wt.% Al ₂ O ₃ composite under quasi-static uniaxial compression: (a) The effect of the RVE length size on the predicted response. An RVE size of 25 μm was selected for further studies. (b) The figure shows the mesh sensitivity analysis. As seen, the predicted curves converge for an element size less than 0.75 μm. The corresponding runtimes are represented in Fig. 3.2(d). (c) The effect of RVE randomness on the predicted stress-strain curve. Note that the spatial distribution of particles and voids only differs between the RVEs. (d) The predicted response for different loading directions compared to the experimental data.	60
3.4	The quantitative and qualitative validation of the micromechanical model with quasi-static uniaxial compression experimental data for CSAM Al-46 wt.% Al ₂ O ₃ composite: (a) The numerically predicted stress-strain curve compared to the experimental data represented by the gray area. The dashed curves show the quantified history of failure mechanisms based on Eqs. (3.31), (3.33) and (4.32). (b) The numerical lateral strain-axial strain curve compared to those of the experiments. (c) The qualitative history of failure mechanisms and the morphology of fractured areas in 3D at specified strains with the lettered point on Fig. 3.4(a). In the legends, SDV10 and SDV1 represent the accumulated damage in the particle and the equivalent plastic strain in the matrix, respectively. (d) The experimentally observed failure mechanisms across the length scales that are reflected in the numerical predictions (see Fig. 3.4(c)).	64
3.5	The micromechanical analysis of the strengthening mechanisms of the Al-46 wt.% Al ₂ O ₃ composite under quasi-static uniaxial compression: (a) The load partitioning analysis used to unravel the contribution of strengthening mechanisms. (b) The true stress versus composite true strain curves of the composite and its constituents to analyze the strain hardening rate behavior of the material.	66

3.6	The numerical study of the effect of particle content on the CSAM Al-Al ₂ O ₃ composites under quasi-static uniaxial compression: (a) The waterfall diagram shows the stress-strain curves with the history of failure mechanisms for the composite with different weight fraction of Al ₂ O ₃ particles ranging from 6% to 46% with an increment of 10%. (b-d) The evolution of failure mechanisms in the composite reinforced with different weight fractions of Al ₂ O ₃ particles.	69
3.7	The trajectory of the growth of normalized failure mechanisms of the composite reinforced with different weight fractions of particles. Note that the composite with 6 wt.% Al ₂ O ₃ was excluded due to no particle cracking. The mechanisms were normalized with respect to their maximum value. (b) Surface fitting on the normalized failure mechanism data across different particle weight fractions greater than or equal to 16% through a second-order polynomial function to analytically correlate the mechanisms. Note that the output of the equation needs to be set to zero for <i>DE*</i> and <i>PC*</i> less than 0.2 to achieve the highest accuracy.	70
3.8	The effect of the particle weight fraction on the mechanical properties of the CSAM Al-Al ₂ O ₃ composite: (a) The variation of the composite Young's modulus (YS) with the Al ₂ O ₃ wt.% that follows a linear relationship expressed by the dashed fitted line in blue. (b) The variation of the composite yield strength (YS) represented in blue with the Al ₂ O ₃ wt.% that follows an exponential relationship expressed by the dashed fitted curve in blue. The values used for the matrix yield strength depicted in gray were calibrated based on the experimental data [30, 144] to account for the work hardening and grain refinement effect induced in the matrix by high-velocity impacting Al ₂ O ₃ particles during the cold spray process.	71
3.9	The effect of the stress state, including uniaxial compression, uniaxial tension, and shear on the behavior of the CSAM Al-46 wt.% Al ₂ O ₃ composite under a quasi-static loading rate: (a) The comparison of the stress-state-dependent stress-strain response of the material. (b) The history of failure mechanisms under a shear stress state. (c) The history of failure mechanisms under uniaxial tension. The inset is provided to better show the evolution of the failure mechanisms. (d-f) Comparing the evolution of failure mechanisms in the composite under different stress states.	74

- 3.10 The micromechanical analysis of the stress-state-dependent ductile failure of the Al matrix of the CSAM Al-46 wt.% Al₂O₃ composite under a quasi-static loading rate: (a) The evolution of the volumetrically averaged void growth (f^*) and void distortion (D_s) mechanisms in the Al matrix when the composite is subjected to different stress states. (b) The history of volumetrically averaged equivalent plastic strain ($\bar{\epsilon}_M^p$) accumulation in the Al matrix when the composite is subjected to different stress states. The transparent stress-strain curves of the composite are added to provide a better understanding of the development of plastic deformation in the matrix. Note that all the parameters are volumetrically averaged in the whole domain of the RVE based on the equation $Q_{ave} = \sum_{k=1}^{N_{ip}} Q_k V_k / \sum_{k=1}^{N_{ip}} V_k$, where Q is the value of the intended parameter at each integration point, V_k is the volume of the integration point, and N_{ip} is the total number of integration points in the domain of the RVE. 77
- 3.11 The numerically predicted qualitative history of failure mechanisms of the Al-46 wt.% Al₂O₃ composite under tension and shear at quasi-static loading rate. In the last row, for both stress states, the fracture surface progression was visualized in 3D by the deleted elements of the composite constituents (i.e., the matrix in blue and the Al₂O₃ particles in gray). Note that SDV10 and SDV1 represent the accumulated damage in the particle and the equivalent plastic strain in the matrix, respectively. 78
- 3.12 The numerically predicted stress-state-dependent effect of average Al₂O₃ particle size on the behavior of the CSAM Al-46 wt.% Al₂O₃ composite under a quasi-static loading condition: (a-c) The stress-strain responses. (d-f) The quantified history of matrix/particle debonding mechanism. (g-i) The quantified history of particle cracking mechanism. (j-l) The quantified history of matrix ductile failure. 80

- 3.13 The predicted qualitative history of failure mechanisms in CSAM Al-Al₂O₃ composites with different weight fraction of Al₂O₃ particles under quasi-static uniaxial compression. The contours are provided at a global uniaxial strain of 10% (see Fig. 3.6(a)). The view-cut representations of the RVEs in the column of “Matrix Failure” show that the higher number of particles in the composite with 46 wt.% of particles leads to an earlier coalescence of plastic bands and the formation of fracture surface shown in blue on the right-hand side images, thereby a smaller elongation at failure when compared to the composites with a lower particle content (see Fig. 3.6(a)). The images numerically captured at the maximum strain show the 3D morphology of fractured areas of the composites via reactivating the deleted elements, where matrix fracture is shown by blue and fractured areas of particles are shown in black. As seen, the fracture surface of the composite under compression makes an angle of $\sim 45^\circ$ with respect to the loading direction. The debonded areas (flat surfaces) are numbered by 1 in green on the matrix fracture surface. 84
- 3.14 The visualization of failure mechanisms in CSAM Al-46 wt.% Al₂O₃ composites with different average Al₂O₃ particle sizes under different stress states. For different stress states, the pattern of initiation and propagation of debonding and particle cracking mechanisms show no difference when particle size changes. The fractured areas of the matrix and particles are shown in blue and black, respectively. Under tension, the fracture surface forms perpendicular to the loading direction, while it is parallel to the loading direction when shear dominates. Under compression, the fracture surface makes an angle of $\sim 45^\circ$ with respect to the loading direction. The hollow sections on the matrix fracture surface in blue represent the position of fractured particles located on the fracture surface. Additionally, the flat faces on the matrix fracture surface represent the debonded interface. 85

4.1	Microstructure-informed RVE generation of the CSAM Al-Al ₂ O ₃ composites: (a) SEM image of the CSAM Al-46 wt.% Al ₂ O ₃ composite before testing. (b) Characterization of the composite microstructure in terms of particle size distribution, particle contiguity, and porosity. (c) A random RVE realization with a length size of 80 microns of the CSAM Al-46 wt.% Al ₂ O ₃ composite for micromechanical FE simulations. Note that the white and yellow arrow refers to the particle-free areas and particle contiguity (clustering) in the material microstructure and the reconstructed RVE.	93
4.2	The micromechanical FE model setups: (a) Particle-size-dependent distribution of mechanical properties assigned to the hydrostatic tensile strength of the Al ₂ O ₃ particles and the matrix/particle interfacial strength. (b) Mixed-kinematic boundary condition applied on the meshed RVE model of the CSAM Al-46 wt.% Al ₂ O ₃ composite in Abaqus/Explicit. Here, the Al matrix in gray is half-cut to better show the spatial distribution of particles inside.	95
4.3	Validation of the micromechanical model:(a) Quantitative validation of the model in comparison with the experimental stress-strain responses of CSAM Al-46 wt.% Al ₂ O ₃ composites across quasi-static and dynamic loading rates. (b) Macro scale deformation pattern/failure and axial strain evolution ϵ_{yy} in the composite under quasi-static and dynamic loading conditions in correlation with those of the model at the microscale. Note that the numerical strain colormap is set to be the same as that of the DIC analysis for the sake of comparison.	100
4.4	Fractures surface morphology of the CSAM Al-46 wt.% Al ₂ O ₃ composite under quasi-static uniaxial compression: (a) SEM image of the full-scale fracture surface of the specimen, (b) Magnified views of the features observable on the full-scale fracture surface shown in boxes A and B.	102
4.5	Fractures surface morphology of the CSAM Al-46 wt.% Al ₂ O ₃ composite under dynamic uniaxial compression: (a) Low-magnification SEM image of the deformed specimen after testing, (b) Magnified views of the shear and axial cracks on side surface of the specimen shown in boxes A and B, respectively.	104

4.6	Evolution of the failure mechanisms predicted by the micromechanical model: (a) Quantified history of the initiation and growth of failure mechanisms of the CSAM Al-46 wt.% Al ₂ O ₃ composite across quasi-static and dynamic loading rates. (b) Strain rate-dependent time-resolved images of the qualitative evolution of the failure mechanisms.	106
4.7	Stress-bearing partitioning analysis via the micromechanical model:(a) Stress-bearing capacity partitioning of the CSAM Al-46 wt.% Al ₂ O ₃ composite across quasi-static and dynamic loading rates. (b) The percentage of increase ($\Delta\sigma$ (%)) in the stress-bearing capacity of Al matrix and Al ₂ O ₃ particles of the composite under dynamic strain rates with respect to the quasi-static strain rate of 10^{-2} s^{-1} . Note that σ_d and $\sigma_{\dot{\epsilon}=10^{-2}}$ denotes the matrix/particle stress under dynamic rates and the reference quasi-static rate, respectively.	109
4.8	The role of particle clustering in the mechanical behavior of the CSAM Al-46 wt.% Al ₂ O ₃ composite under quasi-static and dynamic compression analyzed by stress-bearing capacity partitioning and the quantified history of the evolution of the failure mechanisms.	111
4.9	(a) The effect of particle clustering on the stress distribution and particle cracking mechanism in the CSAM Al-46 wt.% Al ₂ O ₃ composite. (b) and (c) SEM images of the material after testing that confirm the numerical predictions of the features of cracking and debonding of clustered particles.	112
4.10	The effect of initial working temperature on the strain rate-dependent stress-strain response of the CSAM Al-46 wt.% Al ₂ O ₃ and the evolution of failure mechanisms predicted by the micromechanical model. . . .	115
4.11	(a) Volumetrically-averaged homogenized temperature increase (ΔT) profile of the CSAM composite, the volume fraction of the melted Al matrix, and the multiplicative contribution of the strain rate hardening and thermal softening mechanisms ($\sigma_{\dot{\epsilon}}[\dot{\epsilon}_M^p]\sigma_T[T]$) of the Al matrix of the composite across temperatures and strain rates predicted by the micromechanical model. (b) SEM images of the tested CSAM Al-46 wt.% Al ₂ O ₃ composite under the strain rate of 3200 s^{-1} at RT, showing evidence of partial matrix melting near the loading surfaces. (c) Qualitative evolution of temperature field in the Al matrix of the CSAM composite under quasi-static and dynamic loading at RT predicted by the micromechanical model.	118

- 4.12 Particle size distribution of the sieved pure Al (99.0%) and pure α - Al_2O_3 (99.5%) powder used for the fabrication of CSAM Al-46 wt.% Al_2O_3 composites in this study measured by an image-based automated particle size analyzer, resulting in a size of $\sim 53.3 \pm 4.9 \mu\text{m}$ and $\sim 38.7 \pm 3.9 \mu\text{m}$ for the sieved Al and Al_2O_3 powder, respectively. Note that both particle size distributions are fitted by a Gaussian function in the figure. 130
- 4.13 (a) The balance of the internal (ALLIE) and the kinetic (ALLKE) energies of the RVE model under quasi-static (i.e., $\dot{\epsilon} = 10^{-2} \text{ s}^{-1}$) and dynamic (i.e., $\dot{\epsilon} = 3200 \text{ s}^{-1}$) strain rates. Under quasi-static loading, the figure shows that the ratio of ALLKE/ALLIE holds less than 10% through the course of loading which confirms the quasi-static condition [91]. (b) A summary of the mesh convergence study that involves the element size, the number of elements, and the corresponding computational runtime under quasi-static and dynamic loading. (c) The strain rate-dependent stress-strain responses of the CSAM Al-46 wt.% Al_2O_3 composite captured with different element sizes shown in Fig. 4.13(b). With regard to the convergence pattern of stress-strain responses and the corresponding computational times represented in Fig. 4.13(b), an element size of $2 \mu\text{m}$ was selected for further studies in the current work. 131
- 4.14 The effect of RVE randomness on the predicted stress-strain response of the CSAM Al-46 wt.% Al_2O_3 composite under quasi-static and dynamic compression. As seen, the predicted stress-strain curves by different realizations, namely RVE 1, RVE 2, and RVE 3 slightly varies across strain rates which confirms the reliability of the developed micromechanical model of the material. Note that the results obtained by RVE 1 are only reported in the paper for brevity. 132
- 4.15 (a) The temperature-dependent yield strength profile of the Al matrix used as the input to the micromechanical model in this study that is reconstructed based on the corresponding data on Al alloys in the literature. (b) The temperature-dependent Young's modulus of the Al matrix used in the current study as a function of initial temperature, which is reproduced based on data for pure Al in the literature. . . . 133

Chapter 1

Introduction

1.1 Motivation

Thermal spraying refers to a group of manufacturing processes used for coating surfaces, where materials are deposited onto various structures in a molten or semi-molten state and form a coating upon resolidification [1]. As a subcategory of thermal spray processes, cold spray (CS) technology has been increasingly used for the fabrication of metal-ceramic coatings to protect the surface of structures against extreme environments such as oxidation at high temperature [2], low-temperature induced corrosion from fluids [3], and aggressive erosive/corrosive environments [4]. Due to a considerably lower operating temperature in CS when compared to conventional thermal spray deposition routes, undesirable effects such as phase transformation, thermal residual stresses, melting, and oxidation are avoided [5]. In addition to providing functional surface properties, CS is increasingly evolving as an additive manufacturing (AM) technology for the rapid fabrication of complex and large-volume parts as an effective and economical solution [6]. In contrast to well-established thermal AM methods, including selective laser melting [7], direct selective laser sintering [8], and electron beam melting [9], CS additive manufacturing operates below the melting temperature of materials, resulting in 3D parts with a higher purity and fewer microstructural defects [10]. In addition, CS for additive manufacturing outperforms the powder bed fusion and the stereolithography methods in terms of the rate of

deposition and scalability, which enables the time- and cost-efficient production of larger structures [11].

Metal-ceramic composites – as a group of metal matrix composites (MMCs) – have gained increasing popularity due to their exceptional ability to enhance toughness and ductility within the metallic matrix, while also providing high stiffness and strength from the ceramic reinforcements [12], and this synergy idealizes them to be used in various industrial sectors [13, 14] – for example, the fan exit guide vanes in Pratt & Whitney 4000 series gas turbine engines, used on Boeing 777 commercial airliners, are made from particulate reinforced aluminum (Al) matrix composites. Among different metal-based coatings, Al-based metal matrix composites (Al-MMCs) have been widely used to enhance surface performance [15–18] due to their superior mechanical properties such as high stiffness and strength [19], low coefficient of thermal expansion [20], improved wear [21] and corrosion resistance [22], and better creep-fatigue performance [23]. To fabricate Al-MMCs, a wide range of reinforcing ceramic particles (e.g., SiC [24], Al₂O₃ [15], TiC [25], TiB₂ [26] and B₄C [27]) have been added to an Al matrix in the literature. Specifically, the current research focuses on CS additively manufactured (CSAM) Al-Al₂O₃ composites due to their applications as protective coatings against wear, erosion, corrosion, and high-temperature degradation in aerospace and other industrial sectors [28, 29]. The novelty and innovation of this Ph.D. research stem from the provision of a multi-scale computational framework to fill a gap in our knowledge of deformation and failure mechanisms of the material through microstructure-based modeling; the outcomes are leveraged to bridge the gap between the microstructure and macro-scale behavior of CSAM Al-MMC coatings/-materials that eventually allow designing better-performing materials with tailored microstructures.

To move towards understanding the behavior of metal-ceramic composites, both experimental mechanics [30–33] and computational mechanics [34–37] approaches have been employed in the literature. Experimental-wise, the mechanical behavior of

CSAM MMC coatings has been addressed in previous studies in terms of dry sliding wear [38], indentation [28], flexural properties [39], and erosion [29]. From a computational perspective, regardless of the manufacturing route, the majority of previous studies on Al-MMCs have focused on uniaxial tensile loading where the microstructures have been modeled via two-dimensional (2D) [40, 41] and three-dimensional (3D) [42, 43] representative volume elements (RVEs). These studies have provided new insights into the role of the material microstructure (e.g., porosity [44], shape [45], size [46], and distribution of the reinforcing ceramic particles [47]) on the macro scale behavior of the materials (e.g., stress versus strain histories and failure responses). The multi-axial time-evolving in-service loading conditions of metal-ceramic materials/coatings, however, necessitate developing stress state dependent [48] and strain rate dependent [49] models, which is indeed confirmed by our experimental observations of the material behavior in terms of the asymmetric response under uniaxial tension and compression (see Fig. 1.1(a)) and the strain rate strengthening effect under dynamic loading (see Fig. 1.1(b)). To date, the microstructure-based strain rate-dependent mechanical behavior of two-phase (e.g., Al-Al₂O₃) CSAM metal-ceramic materials subject to different stress states have not been computationally studied in the literature, which lays the foundation for the research performed in this thesis on the computational design and optimization of the material.

In this paper-based thesis, the development of microstructure-informed FE models for CSAM Al-Al₂O₃ composites provides new insights into the behavior of these CS-fabricated materials under varying strain rates and stress states. By integrating experimental data and advanced computational modeling, this research addresses a gap in the literature, particularly in understanding the complex spatiotemporal evolving failure mechanisms – such as matrix ductile failure, particle cracking, and interface debonding – that occur in metal-ceramic composites. The scientific contribution lies in the quantification of the evolution history of these mechanisms, captured by the experimentally validated micromechanical models, offering a detailed understanding

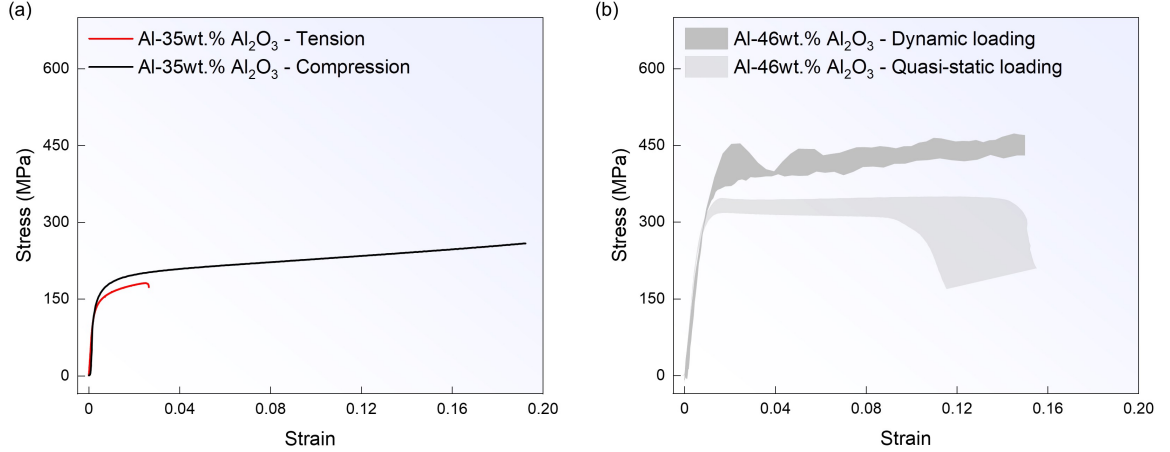


Fig. 1.1: Experimental evidence for the motivation of this thesis for developing stress state- and strain rate-dependent microstructure-based FE models for CSAM Al-Al₂O₃ composites: (a) The experimentally captured stress-strain response of CSAM Al-35 wt.% Al₂O₃ composites under quasi-static uniaxial tension [50] and compression [30]. (b) The experimentally captured stress-strain responses of CSAM Al-46 wt.% Al₂O₃ composites under quasi-static and dynamic loading [51].

of how microstructural features such as particle content, particle clustering and size affect the material mechanical behavior. This research lays the groundwork for future machine learning (ML)-based models, aimed at optimizing metal-ceramic composite materials for high-performance applications (e.g., armored vehicles [52] and aircraft brakes [53]), where CS additive manufacturing enables the required complexity in the design of structures with optimized performance. More details are provided in the following chapters, each describing a published paper that elaborates on different aspects of the research.

More specifically, this Ph.D. research builds on the previous studies of 3D modeling of tensile behavior [24, 25, 27, 42, 54–56] and 2D modeling of the compressive response [57, 58] of particulate-reinforced metal matrix composites to provide a better understanding of the deformation and competition of failure mechanisms of CSAM metal-ceramic composites through stress-state- and strain rate-dependent finite element (FE) models at a micro length scale. In addition, the experimentally validated microstructure-based FE framework will be leveraged to generate datasets for the

training and validation of computationally efficient ML-based models [36, 59, 60] to correlate the microstructure of the CSAM material to its macroscale mechanical behavior across a wide space of design (i.e., considering different microstructures and loading conditions represented by stress state and strain rate).

1.2 Thesis Objectives

The objective of this thesis is to develop microstructure-informed FE predictive models that enable us to understand key failure mechanisms and their competition/interaction (i.e., matrix ductile failure [61], ceramic particle/matrix debonding [62], and particle cracking [56]) in CSAM metal-ceramic composites under different stress states and strain rates – Al-Al₂O₃ composites in this study – for which in-situ experimental measurements are not easily accessible. Additionally, as dataset generators, the established microstructure-based FE models will be applicable to developing fast-predictive ML-based surrogate models that pave the way for spatially tailoring matrix and particle characteristics leading to the development of high-performing coatings and CSAM bulk materials. These micromechanical FE models are informed by experimental data in terms of the microstructural features (e.g., porosity, particle weight fraction, and particle size distribution) and stress-strain responses [30, 50]. To account for the strain rate dependency, the split-Hopkinson pressure bar (SHPB) [63] test is employed to probe compressive behavior at dynamic loading rates. User-developed material models (i.e., an extended Gurson-Tvergaard-Needleman (GTN) model [64] for the ductile failure of the metallic matrix, and a viscosity-regularized plasticity model for brittle materials [65] for Al₂O₃ reinforcing particles) are employed by VU-MAT subroutines in the microstructure-informed RVEs where material features and physical behaviors observed via Scanning Electron Microscopy (SEM) micrographs are incorporated explicitly into the model (e.g., porosity, and particle size distribution).

To accomplish the thesis objective, the following goals will be pursued:

1. Leveraging existing group and literature data acquired using experimental mechanics approaches to probe the material microstructure (e.g., porosity [44] and morphology of constituents [66]) and the material response under different loading rates and stress states which are induced in the material under real-world applications (e.g., wear [31] and erosion [67]). The microstructure characterization is conducted by advanced diagnostics such as SEM, and this will inform the generation of RVEs based on the particle content, particle size distribution, particle clustering, and porosity in the matrix. These experimental outcomes are used to inform and validate the micromechanical FE models of the CSAM composite material.
2. Generating microstructure-based 3D models based on the microstructural features obtained from SEM micrographs (i.e., shape, size, distribution of the reinforcing particles, and porosity) using Digimat software [42]. State-of-the-art user-developed material models are incorporated in Abaqus/Explicit FE software by VUMAT subroutines to bolster the accuracy of both qualitative and quantitative predictions. For example, the stress-state-dependent ductile failure model by Zhou et al. [64] for the Al matrix, the phenomenological viscosity-regularised Johnson-Holmquist-II (JH2-V) [68] model to incorporate stress state- and strain rate-dependent ceramic particle damage accumulation, and the cohesive zone model (CZM) [69] approach for particle/matrix interfaces. The models are verified by our experimental outcomes for different loading paths under various loading rates (e.g., the work by Jibrán et al. [50] and Shao et al. [30]) in terms of quantitative (i.e., based on stress versus strain responses) and qualitative comparisons (i.e., based on the manifestation and propagation of failure mechanisms through post-mortem fractography).
3. Quantifying the growth history of failure mechanisms, including matrix/particle debonding, particle cracking, and matrix failure by the experimentally

validated micromechanical model. Such a quantification framework is implemented by Python scripts that calculate the fraction of fully damaged regions through the course of loading, unraveling the competition and interaction of failure mechanisms across different stress states and strain rates.

4. Exploring the effects of microstructural features on the macro scale behavior of the material towards establishing microstructure-performance relationships (e.g., the effect of ceramic phase content, clustering of particles, and particle size on the stress-strain response). This parametric study uncovers key insights into structure-property-performance relationships of CSAM metal-ceramic composites, including the shifts in the growth history of failure mechanisms that are systematically tracked by the quantification approach.

1.3 Research Contributions

1. This thesis will make contributions in addressing gaps in our knowledge on the evolution and competition of micro-scale deformation and failure mechanisms of CSAM metal-ceramic composite coatings/materials which govern the macroscale mechanical performance of the material systems in a range of applications (e.g., armored vehicles [52], aircraft brakes [53], and wear-resistant coatings in oil & gas [70]).
2. For the first time, this Ph.D. research informs on the quantitative initiation and growth history of microscale failure mechanisms of CSAM metal-ceramic composites through a computational FE framework across stress states and strain rates, which is not readily accessible through in-situ experimental mechanics approaches [71, 72].
3. The outcomes of this research reveal the effect of microstructural characteristics (e.g., particle weight fraction, particle size, and particle clustering) on the

macroscale response of the CSAM metal-ceramic materials represented by the stress-strain responses and growth history of failure mechanisms at a microscale, which have implications for the design of the material with application-specific tailored properties.

4. This thesis will lay the foundation for the development of experimentally verified micromechanical FE models as dataset generators that feed the ML-assisted computational frameworks [73] for the efficient design and optimization of spatially tailored microstructures (e.g., porosity and composition) and architectures [74] that will culminate in increased performance and functionality of the CSAM composite materials.

1.4 Thesis Structure

This thesis is structured based on research published as journal articles presented as individual chapters in the following order:

- Chapter 1: “Introduction”. Discusses the background and motivation for developing microstructure-based FE models for CSAM metal-ceramic composites and the major contributions to the field delivered by the thesis.
- Chapter 2: “3D microstructure-based finite element simulation of cold-sprayed Al-Al₂O₃ composite coatings under quasi-static compression and indentation loading”. Published in the *Journal of Thermal Spray Technology*, as **Saman Sayahlatifi**, Chenwei Shao, André McDonald, and James David Hogan, 2021 [62]. This study presents the development and validation of 3D finite element (FE) models to investigate the behavior of CS Al-Al₂O₃ composite coatings under quasi-static compression and indentation loading. Using Digimat software, 3D representative volume elements (RVEs) were generated based on microstructural characteristics and then imported into Abaqus/Explicit for simulation.

The models incorporated advanced physics-based approaches to capture particle cracking, interface debonding, and matrix ductile failure. Validation against experimental data for Al-34 wt.% Al₂O₃ and Al-46 wt.% Al₂O₃ coatings demonstrated the model's accuracy in predicting stress-strain responses and failure mechanisms. This work advances computational methodologies for CS MMC coatings and provides a foundation for future material design and optimization studies.

- Chapter 3: “[Micromechanical damage analysis of Al-Al₂O₃ composites via cold-spray additive manufacturing](#)”. Published in the *International Journal of Mechanical Sciences*, as **Saman Sayahlatifi**, Zahra Zaiemyekeh, Chenwei Shao, André McDonald, and James David Hogan, 2023 [75]. This study presents a detailed micromechanical analysis of stress-state-dependent failure behavior of CSAM Al-Al₂O₃ composites. RVEs of the material are generated based on experimentally informed particle size distributions and porosity measurements, with constitutive models for the metal matrix and ceramic particles implemented via VUMAT subroutines in Abaqus/Explicit. For the first time, The FE model quantifies failure mechanisms, including matrix ductile failure, particle cracking, and matrix/particle debonding, validated by experimental data under quasi-static uniaxial compression. The study explores the effects of particle content and size on material behavior under various stress states, revealing an order of failure mechanism activation and the influence of stress state on material ductility. This work offers insights into designing better-performing CSAM Al-Al₂O₃ composites and developing micromechanism-based constitutive models for CSAM metal-ceramic materials.
- Chapter 4: “[Strain rate-dependent behavior of cold-sprayed additively manufactured Al-Al₂O₃ composites: Micromechanical modeling and experimentation](#)”. Published in *Composites Part B: Engineering*, as **Saman Sayahlatifi**,

Zahra Zaiemyekheh, Chenwei Shao, André McDonald, and James David Hogan, 2024 [51]. This study explores the strain rate-dependent behavior of CSAM Al-Al₂O₃ composites. Utilizing a combination of experimental techniques and 3D micromechanical finite element (FE) modeling, this research investigates the failure mechanisms of the material under quasi-static and dynamic compression. Upon validation with experimental data, the FE model provides insights into microscale failure progression and the effects of elevated temperatures on the material performance across strain rates. This study is the first to correlate microscale failure mechanisms with the mechanical behavior of CSAM MMCs, offering valuable implications for designing CSAM metal-ceramic structural materials.

- Chapter 5: “Conclusions & Future Work”. Summarizes the key scientific outcomes of this research and outlines directions for future work. This chapter also highlights the list of all academic publications resulting from this thesis.

Chapter 2

3D microstructure-based finite element simulation of cold-sprayed Al-Al₂O₃ composite coatings under quasi-static compression and indentation loading

Published as **Saman Sayahlatifi**, Chenwei Shao, André McDonald, and James David Hogan, “3D microstructure-based finite element simulation of cold-sprayed Al-Al₂O₃ composite coatings under quasi-static compression and indentation loading,” *Journal of Thermal Spray Technology*, vol. 31, p. 102–118, 2022.

2.1 Abstract

This study developed microstructure-based finite element (FE) models to investigate the behavior of cold-sprayed aluminum–alumina (Al-Al₂O₃) metal matrix composite (MMC) coatings subject to indentation and quasi-static compression loading. Based on microstructural features (i.e., particle weight fraction, particle size, and porosity) of the MMC coatings, 3D representative volume elements (RVEs) were generated by using Digimat software and then imported into Abaqus/Explicit. State-of-the-art physics-based modeling approaches were incorporated into the model to account for particle cracking, interface debonding, and ductile failure of the matrix. This allowed

for analysis and informing on the deformation and failure responses. The model was validated with experimental results for cold-sprayed Al-34 wt.% Al_2O_3 and Al-46 wt.% Al_2O_3 metal matrix composite coatings under quasi-static compression by comparing the stress versus strain histories and observed failure mechanisms (e.g., matrix ductile failure). The results showed that the computational framework is able to capture the response of this cold-sprayed material system under compression and indentation, both qualitatively and quantitatively. The outcomes of this work have implications for extending the model to materials design and for applications involving different types of loading in real-world applications (e.g., erosion and fatigue).

2.2 Introduction

Aluminum (Al)-based metal matrix composites (Al-MMCs) have been widely used to enhance surface performance [15–18] due to their superior mechanical properties such as high stiffness and strength [19], low coefficient of thermal expansion [20], improved wear [21] and corrosion resistance [22], and better creep-fatigue performance [23]. To fabricate Al-MMCs, a wide range of reinforcing ceramic particles (e.g., SiC [24], Al_2O_3 [15], TiC [76], TiB_2 [26] and B_4C [27]) have been added to an Al matrix in the literature. Among these reinforcing particles, Al_2O_3 has been frequently used due to improved corrosion resistance and chemical stability [54]. Recently, the Al- Al_2O_3 composites fabricated by the cold spray additive manufacturing process have been used as protective coatings against wear, erosion, corrosion, and high temperature degradation in aerospace and other industrial sectors [28, 29]. Among many deposition routes for producing coatings made of pure Al, cold spray stands out due to minimal heat loading of the substrate during the deposition process [4]. In addition, this additive manufacturing method provides the possibility of producing multi-phase coatings via mixing feedstock powders by which the hard phases such as SiC and Al_2O_3 can be incorporated effectively in the Al-MMCs coatings [5]. These hard particles play a critical role in lowering the wear rate of the ceramic–metal coatings [77].

In research studies on experimental mechanics of ceramic-metal composite coatings, the behavior of cold-sprayed MMC coatings has been extensively addressed in terms of dry sliding wear [38], indentation [28], flexural properties [39], and erosion [29]. However, there are a limited number of articles that investigate the response of MMC coatings through computational approaches, which is addressed in the current study. For example, Bolelli et al. [78] generated 2D RVEs based on the SEM images of WC-CoCr and WC-FeCrAl coatings to simulate ball-on-disk test and compression. The matrix and hard particles were modeled as elastic-plastic and pure elastic materials, respectively. The numerical results of Bolelli et al. [78] were compared with experiments based on the morphology of the worn surfaces and Young's modulus. In a separate study by Balokhonov et al., [37], 2D models at micro-, meso-, and macro-scales have been implemented by using the finite difference method for MMC coatings under tension and compression. It was found that curvilinear interfaces lead to stress concentration giving rise to the formation of shear bands in the Al matrix locally as well as cracking in the ceramic particles.

From a computational perspective, the majority of previous studies on Al-MMCs have focused on axial tensile loading, by which the microstructure has been modeled via 2D [41] and 3D [43] RVEs. In a large number of studies, the occurrence of the three competitive damage mechanisms in particulate-reinforced Al matrix composites (PRAMCs) subject to tension, such as matrix ductile failure, matrix/particle debonding, and particle cracking, has been mainly explored by using phenomenological ductile failure criteria [43], cohesive zone models [79], and a conventional brittle cracking model [27] (i.e., elastic cracking behavior which employs the Rankine criterion for failure initiation [80]), respectively. For example, Zhang et al. [43] investigated the behavior of a 7vol.% SiC_p/Al composite made by a stir casting technique and incorporated the three damage mechanisms in a real microstructure-based 3D RVE. The numerical results revealed that particle fracture and interfacial debonding emerged as the initial failure mechanisms in the composite under tensile loading.

In contrast to the numerous numerical studies that explore the tensile behavior of Al-MMCs, limited efforts have been made to address the indentation and compressive behavior computationally, particularly with an emphasis on damage mechanisms. For example, Park et al. [81] investigated Al-SiC MMCs under quasi-static compression up to 1% strain using a statistical synthetic RVE made by the DREAM.3D software – no damage mechanisms were incorporated into the model. The indentation behavior of MMCs has been frequently explored via 2D models [80]. More recently, Shedbale et al. [82] employed homogeneous and heterogeneous 3D FE models to study the ball indentation response of particulate-reinforced MMCs. The results showed that the heterogeneous model tends to overestimate the hardness compared to the experiments due to the local concentration of particles under the indenter.

Motivated by previous numerical studies, which primarily focus on the tensile response of MMCs, this work aims to investigate the compressive and indentation behavior of Al-Al₂O₃ coatings by using 3D RVEs produced by Digimat software based on microstructural characteristics obtained using scanning electron microscope images. To account for the damage mechanisms, the Gurson–Tvergaard–Needleman (GTN) model [83] was applied to the Al matrix, and the matrix/particle debonding was modeled by the CZM method [84]. For the ceramic particle phase, the Johnson–Holmquist II (JH2) model [85] was used to incorporate particle cracking into the FE model. The model was validated with the experimental data for Al-34 wt.% Al₂O₃ and Al-46 wt.% Al₂O₃ coatings in terms of stress-strain histories, failure mechanisms, and Vickers hardness. The results show that the model has the potential to be employed for future parametric studies for material design and optimization, which tailors the concentration of reinforcing particles to balance strength and density for weight-sensitive applications.

2.3 Experimental Procedures

2.3.1 Material and Specimen Preparation

In this study, pure Al and Al-Al₂O₃ composite coatings were fabricated using a low-pressure cold spray system (SST series P, CenterLine Ltd., Windsor, ON, Canada), as shown schematically in Fig. 2.1(a), which was connected to a volumetric powder feeder (5MPE, Oerlikon Metco, West-bury, NY, USA). Based on previous studies [16, 30, 86], the air temperature and pressure were set to 375 °C and 620 kPa, respectively. The nozzle was manipulated by a robot (Motoman HP-20, Yaskawa Electric Corp., Waukegan, IL, USA). The cold spray nozzle traversed across the Al substrate at a speed of 15 mm/s to transfer the feedstock powder to the substrate, and the deposition process produced five layers of the coating. The feedstock powder blend was developed through a three-step process: gas atomization, sieving, and mixing (see Fig. 2.1(a)). Aluminum (99.0%) powder (CenterLine Ltd., Windsor, ON, Canada) and α - Al₂O₃ with a purity of 99.5% (Amdry 6060, Oerlikon Metco Inc., Westbury, NY, USA) were used in this study. The Al and Al₂O₃ powders were sieved to obtain a size distribution of 40–60 μ m and 30–45 μ m, respectively. The Al and Al₂O₃ powders were admixed to produce powder blends containing 0, 60, and 90 wt.% Al₂O₃. This process was conducted using a cylinder with a 20 mm diameter whose angular velocity and operating time was set to 20 RPM and 30 minutes, respectively. As shown by Shao et al. [30], when deposited into coatings, the mixed powder blend with 60 wt.% Al₂O₃ produced coatings that were Al-34 wt.% Al₂O₃ and the mixed powder blend with 90 wt.% Al₂O₃ produced coatings that were Al-46 wt.% Al₂O₃.

2.3.2 Mechanical testing and characterization

As shown in Fig. 2.1(b), the cold-sprayed coating deposits were cut into cuboidal specimens with dimensions of 2.3 mm in length, 2.7 mm in width, and 3.5 mm in height using wire electrical discharge machining. The samples were used for quasi-

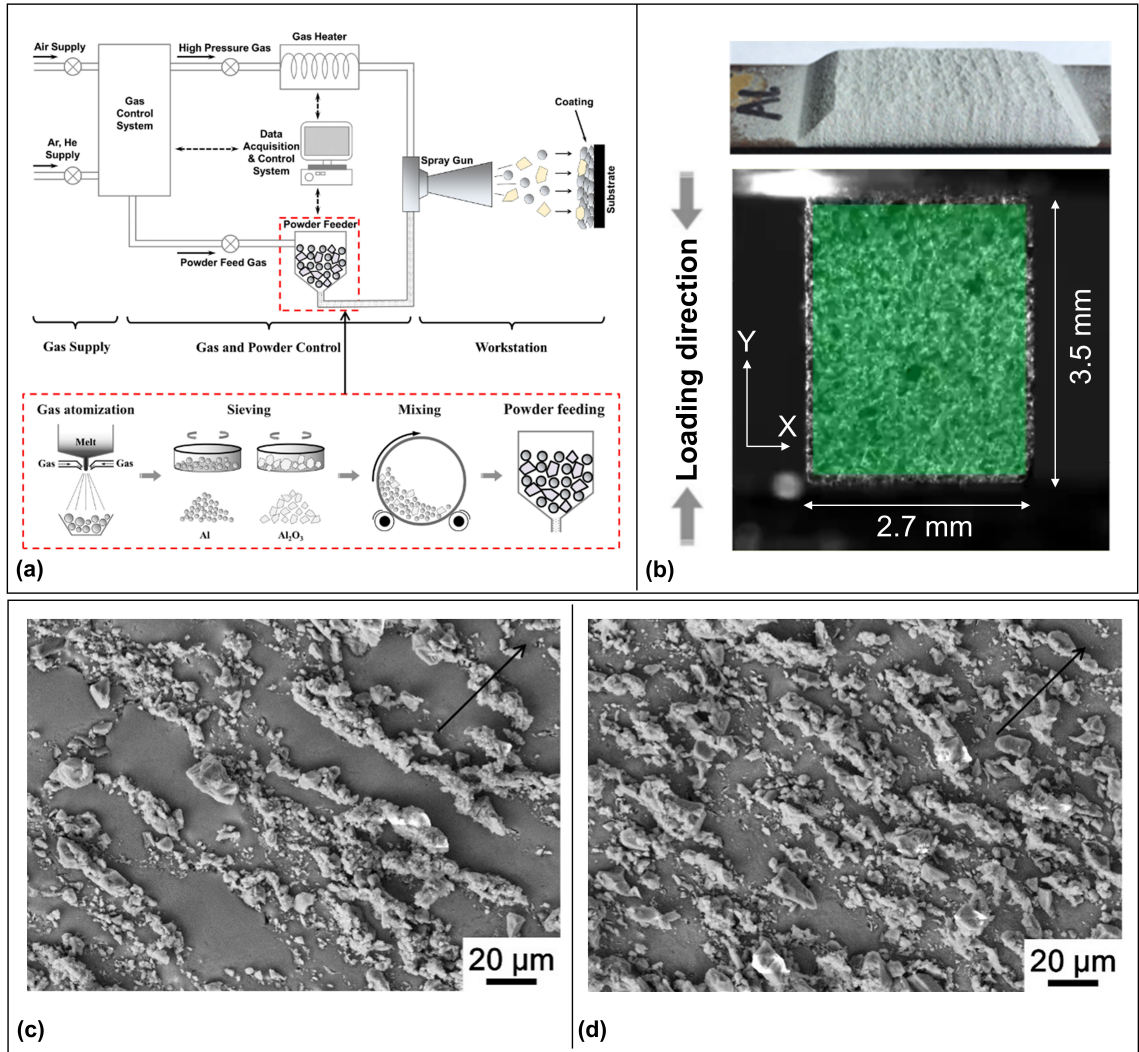


Fig. 2.1: Preparation, test, and characterization of Al-Al₂O₃ composite coatings: (a) A schematic illustration of the cold spray setup used for the fabrication of pure Al and MMC coating samples: The processing strategy for making the mixed powder includes gas atomization, sieving, and mixing using a rotated cylinder; (b) Typical compressive cuboidal specimen with dimensions 2.3 mm × 2.7 mm × 3.5 mm cut from the composite depositions via wire electrical discharge machining, which was loaded in the direction of the 3.5 mm dimension. The green contour shows the region of interest defined on the specimen surface in VIC-2D software for monitoring the strain fields. The top image shows an example of Al-Al₂O₃ coating deposited on an Al substrate from which the cuboidal specimens were cut; (c) SEM characterization of the microstructure of Al-34 wt.% Al₂O₃ composite coating showing the distribution and morphology of the reinforcing ceramic particles in the Al matrix; (d) SEM micrograph of Al-46 wt.% Al₂O₃ composite coating. Note that the black arrows on the SEM micrographs show the deposition direction. The darker regions correspond to the Al phase and the lighter regions correspond to the alumina phase.

static compression testing, where the loading was applied in the direction of the 3.5 mm dimension. The experiments were conducted using the displacement control technique up to a maximum displacement of 1 mm at a constant rate of 10^{-3} s^{-1} using an Instron 3365 testing machine (Instron, Norwood, Massachusetts, USA). To visualize the features of the macroscopic deformation of the specimen surface, the machine was equipped with an AOS PROMON U750 high-speed camera with a full resolution of 1280×1024 and a VIC 900170WOF LED laser light guide for illumination. This assembly was coupled with digital image correlation (DIC) capabilities using VIC-2D (v6 2018) software [87] (Correlated Solutions Irmo, SC, USA) to monitor the strain fields, which is detailed in Shao et al. [30]. The specimen was aligned between the loading platens made from M2-graded high-speed steel with a diameter of 1 inch (see Fig. 2.1(b)), and extreme pressure grease was applied on the interfaces to eliminate the effect of friction and allow free lateral expansion. The compression tests were carried out as per ASTM Standard C1424-15 [88] at room temperature and repeated 4 times for each coating with different reinforcing particle content. To inform the microstructure-based models as related to the reinforcing particle content, porosity, particle shape, size, and distribution, microstructural characterization was done using a field-emission SEM coupled with energy-dispersive X-ray spectroscopy (EDS) operated at 20 kV (Zeiss Sigma, Oberkochen, Baden-Württemberg, Germany), as shown in Fig. 2.1(c) for the Al-46 wt.% Al_2O_3 composite. The porosity of the samples was estimated using ImagePro software coupled with the SEM images, and it was found to be $2.84 \pm 0.31 \text{ vol}\%$ in pure Al, $0.23 \pm 0.04 \text{ vol}\%$ in Al-34 wt.% Al_2O_3 , and $0.17 \pm 0.03 \text{ vol}\%$ in Al-46 wt.% Al_2O_3 . In addition, the EDS analysis revealed that the feedstock powders with 60 and 90 wt.% Al_2O_3 led to depositions with $34 \pm 2.56 \text{ wt}\%$ and $46 \pm 2.04 \text{ wt}\%$ of ceramic particles, respectively.

2.4 Numerical Methodology

A 3D FE model based on coating microstructural features is presented to explore the behavior of Al-Al₂O₃ MMC coatings under quasi-static compressive loading. The 3D representative volume elements (RVEs) were generated by the Digimat Software for Al-34 wt.% Al₂O₃ and Al-46 wt.% Al₂O₃ MMCs. The RVEs were imported into the ABAQUS/Explicit solver (release 6.14). For the micro-indentation test, the homogenization approach [82] was applied and experimental compression data was used to extract the effective mechanical properties for each MMC coating sample.

2.4.1 Geometry and model description

RVEs with different sizes have been considered in previous studies [27, 42]. For example, Ma et al. [42] found no significant difference in the tensile stress-strain responses by varying the RVE size from 20 μm to 50 μm . In this study, an RVE length of 100 μm was chosen based on the microstructural features (e.g., average reinforcing particle size of 15 μm). The SEM images (see Fig. 2.1(c) and (d)) were first used to extract the distribution of particle size in the composites (e.g., the size of the alumina particles range from 1 to 30 μm in the Al-46 wt. % Al₂O₃ composites (see Fig. 2.1(c)). Next, the measured range of distribution was incorporated into the RVE using a uniform distribution in the Digimat software, which accounts for the variation and uncertainty in the particle size distribution that is likely to be observed through the SEM images from different locations of the sample. Additionally, the reinforcing ceramic particles represent an irregular shape in the SEM micrographs. Here, an icosahedron geometry was used to account for the shape of the particles, which has also been used to represent the irregular-shaped particles in previous studies involving MMC coatings [42, 89, 90]. The time step was set at 2 μs , which was found to meet the quasi-static loading condition [91]. As shown in Fig. 2.2(a), the top and bottom boundary faces have been fully restricted to the reference points

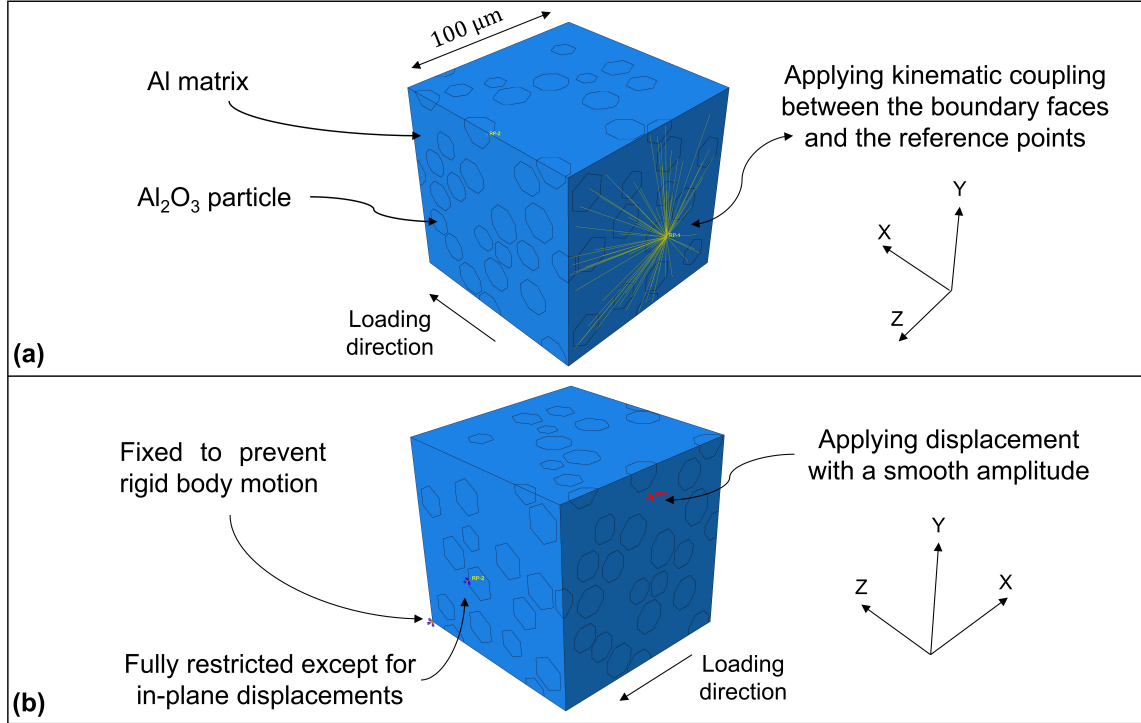


Fig. 2.2: (a) Application of kinematic coupling between the boundary faces and the reference points (RP) in yellow color to apply compressive load and boundary conditions: All degrees of freedom were coupled to each other; (b) The boundary conditions applied on the RVE: The displacement control technique was applied to the RP in red color using a smooth amplitude to meet the quasi-static condition.

(RPs) by the kinematic coupling constraints to facilitate application of load/boundary conditions and obtain the stress-strain response of the RVE. A corner of the RVE was fully restricted to prevent the material from rigid boundary motion. The degrees of freedom of the bottom boundary face were fixed within all degrees of freedom, except for the in-plane displacements (i.e., Y- and Z-directions in Fig. 2.2(b)). The same boundary conditions for application of compressive loading were also used in other studies [44, 92]. All of the constituents were discretized by 3D linear tetrahedral C3D4 elements. Following a mesh quality assessment to decrease the likelihood of element distortion at high strains, an average element size of 1.5 μm was used. On this basis, the RVE for Al-34wt.% Al₂O₃ and Al-46wt.% Al₂O₃ MMCs were meshed by 741,222 and 1,275,358 elements, respectively. Micro-indentation Vickers testing of the composite coatings was simulated via the homogenization approach [82]. The

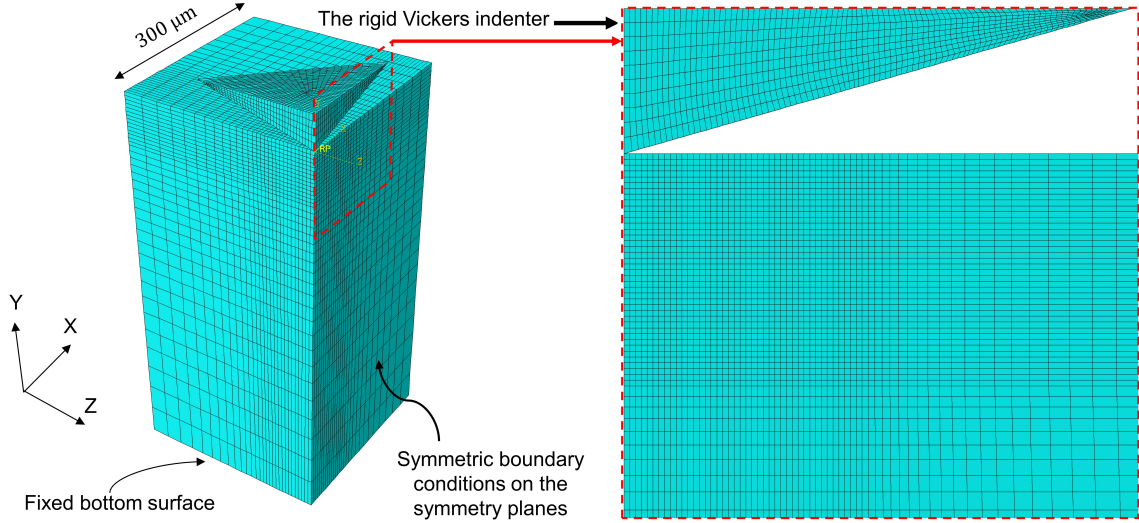


Fig. 2.3: Finite element model of the micro-indentation Vickers test. The block and the indenter were discretized by 30,276 first order 8-node 3D elements with reduced integration (C3D8R) and 2104 quadrilateral 4-node 3D rigid elements (R3D4), respectively.

effective mechanical properties, including the Young’s modulus and flow stress, were extracted from the experimental compressive stress-strain histories for each particle concentration in the coatings and was an input into the approach. Figure 3 shows the FE model of the Vickers test. Due to symmetry, only one quarter of the homogenized block with symmetric constraints was modelled. The size of the block was determined as per the work of Shedbale et al. [82] to achieve convergence in the indentation response.

As shown by Shedbale et al. [82], the Vickers indenter was considered as a discrete rigid body and fully confined, except for the vertical direction Y (see Fig. 2.3). The bottom surface of the block was fixed, and the lateral surfaces were free to deform. A frictionless contact was defined between the indenter and the top surface of the block, which was implemented by the standard surface-to-surface contact algorithm [82]. By using an average element size of 5 μm , the block and the indenter were meshed by using 30,276 first order 8-node 3D elements with reduced integration (C3D8R) and 2104 quadrilateral 4-node 3D rigid elements (R3D4), respectively.

2.5 Material models

In this study, the micromechanical-based Gurson–Tvergaard–Needleman (GTN) model [93] was applied to capture the matrix failure. Given experimental evidence of particle cracking and interfacial debonding under compression, the Johnson-Holmquist II (JH2) model [85] for the failure of ceramic particles and the cohesive zone model (CZM) approach [69] for the matrix/particle debonding failure were incorporated into the model.

2.5.1 The GTN model for matrix failure

Ductile failure of metals occurs as a result of a three-stage mechanism of nucleation, growth, and coalescence of voids. Voids are nucleated from an inclusion or as a consequence of either cracking or decohesion of second phase particles and then grow due to the localization of plastic strain under a high stress triaxiality state [94]. To analyze this phenomenon theoretically, the porous metal plasticity model proposed by Tvergaard and Needleman (i.e., the GTN model) [93], as a modified version of the Gurson model [95], has been widely used [63, 96, 97]. The yield function of the GTN model is expressed as follows:

$$\emptyset(\sigma, f) = \left(\frac{\sigma_q}{\sigma_y} \right)^2 + 2q_1 f^* \cosh \left(\frac{3q_2 p}{2\sigma_y} \right) - \left(1 + q_3 f^{*2} \right) = 0, \quad (2.1)$$

where \emptyset denotes the non-dilatational strain energy and q_1 , q_2 , and q_3 are the constants proposed by Tvergaard [98] to account for the effects induced by void interaction due to multiple-void arrays and to provide better consistency with experimental data. Here, σ_q and σ_y represent von Mises stress and the flow stress of the undamaged material, respectively. To model the rapid deterioration of the stress carrying capacity caused by void coalescence, the parameter f^* , known as the effective porosity was first introduced by Tvergaard and Needleman [83]. The function is specified as:

$$f^* = \begin{cases} f, & \text{if } f \leq f_c \\ f_c + \frac{f_u^* - f_c}{f_F - f_c} (f - f_c), & \text{if } f_c \leq f \leq f_F \\ f_u^*, & \text{if } f \geq f_F \end{cases} \quad (2.2)$$

where f_c is the critical void volume fraction (VVF) at the onset of coalescence, $f_u^* = \frac{1}{q_1}$ corresponds to zero stress carrying capacity, and f_F denotes the VVF when the material has completely failed, which governs the element deletion process. The increase in the VVF is defined as the summation of the increment owing to void nucleation and the growth of the existing voids as:

$$df = df_{nucleation} + df_{growth}. \quad (2.3)$$

Assuming a plastically incompressible behavior for the material, the void growth rate (i.e., df_{growth}) can be expressed as a function of the plastic volume change as:

$$df_{growth} = (1 - f) d\bar{\epsilon}_{ii}^p \quad (2.4)$$

where $d\bar{\epsilon}_{ii}^p$ denotes the trace of the plastic strain rate tensor. The nucleation of voids is considered to be exclusively dependent on the plastic strain and it is assumed that occurrence of void nucleation occurred only under hydrostatic tension [99, 100]. On this basis, the function of void nucleation is written as:

$$df_{nucleation} = A_n d\bar{\epsilon}_m^p, \text{ where} \quad (2.5)$$

$$A_n = \begin{cases} \frac{f_N}{S_N \sqrt{2\pi}} e^{-0.5 \left(\frac{\bar{\epsilon}^p - \epsilon_N}{S_N} \right)^2}, & \text{if } p \geq 0 \\ 0, & \text{if } p < 0 \end{cases} \quad (2.6)$$

where p represents the hydrostatic stress (pressure), f_N is the void volume fraction of the nucleated void, ϵ_N is the mean equivalent plastic strain for void nucleation, and S_N is the standard deviation of the distribution. Here, the rate of equivalent plastic strain, $d\bar{\epsilon}^p$, is obtained by enforcing equality between the matrix plastic dissipation and the rate of macroscopic plastic work as follows:

$$d\bar{\epsilon}^p = \frac{\sigma : d\epsilon^p}{(1 - f) \sigma_y}. \quad (2.7)$$

Table 2.1 summarizes the constants of the GTN model used in this study for the Al matrix. The proposed values by Tvergaard [83] were utilized for the q_1 , q_2 , and q_3 constants. From SEM characterization, the initial porosity, f_0 , was assumed to be an average quantity of 0.0017 and 0.0023 for Al-34 wt.% Al₂O₃ and Al-46 wt.% Al₂O₃ composites, respectively. The parameters ϵ_N , s_N , and f_N were obtained from previous studies for pure Al [101, 102].

2.5.2 The JH2 model for particle cracking

For damage modeling of ceramics, the phenomenological Johnson-Holmquist models have been commonly used [57, 89, 103, 104] to describe their behavior, including accounting for pressure-dependent strength, strain-rate dependency, and bulking effects [85]. The strength and damage are expressed as analytical functions of pressure and other parameters as [85]:

$$\sigma^* = \sigma_i^* - D \left(\sigma_i^* - \sigma_f^* \right), \quad (2.8)$$

$$\sigma_i^* = A (P^* + T^*)^N (1 + C \ln \dot{\epsilon}^*), \quad (2.9)$$

$$\sigma_f^* = A (P^*)^M (1 + C \ln \dot{\epsilon}^*) \leq SFMAX, \quad (2.10)$$

where σ^* and σ_i^* represent the normalized intact equivalent stress, σ_f^* denotes the normalized fracture stress, and D is the damage variable, varying from 0 to 1. Here, $\sigma^* = \frac{\sigma}{\sigma_{HEL}}$, $P^* = \frac{P}{P_{HEL}}$, $T^* = \frac{T}{P_{HEL}}$, and $\dot{\epsilon}^* = \frac{\dot{\epsilon}}{\dot{\epsilon}_0}$, where σ is the equivalent stress, σ_{HEL} is the equivalent stress at the Hugoniot elastic limit (HEL), P is the actual pressure, P_{HEL} is the pressure at the HEL, T is the maximum tensile hydrostatic

Table 2.1: GTN model constants used in this study. Here, the value of f_0 corresponds to the composites with 34wt.% of reinforcing particles. For Al-46 wt.% Al₂O₃ composites, the initial porosity was determined to be 0.0023 on average, while all other constants remain the same as the 34 wt.% case.

q_1 [83]	q_2 [83]	q_3 [83]	f_0 [30]	f_c [102]	f_F [102]	ϵ_N [101]	S_N [101]	f_N [102]
1.5	1	2.25	0.0017	0.1	0.45	0.3	0.1	0.25

pressure tolerated by the material, $\dot{\epsilon}$ is the strain rate, and $\dot{\epsilon}_0$ is the reference strain rate (commonly taken as 1 [57, 103, 105]). A, B, C, M , and N are material constants which need to be calibrated for each material. The maximum value of σ_f^* is defined by $SFMAX$ (i.e., the maximum limitation of the normalized fractured strength). Once the yield function satisfies Eq. (2.11), the damage begins to accumulate based on the incremental equivalent plastic strain defined as:

$$\emptyset(\sigma, f) = \sigma_q - \sigma_{HEL}\sigma^*, \quad (2.11)$$

$$D = \sum \frac{\Delta\epsilon_{eff}^p}{\epsilon_f^p}, \text{ and} \quad (2.12)$$

$$\epsilon_f^p = D_1 (P^* + T^*)^{D_2}, \quad (2.13)$$

where σ_q, D_1 , and D_2 are deemed as material constants. To calculate pressure, P , a polynomial equation of state (EOS) is employed, which is defined as:

$$P = \begin{cases} K_1\eta + K_2\eta^2 + K_3\eta^3 + \Delta P, & \text{if } \eta > 0 \\ K_1\eta, & \text{if } \eta \leq 0 \end{cases} \quad (2.14)$$

$$\Delta P_{t+\Delta t} = -K_1\eta_{t+\Delta t} + \sqrt{(K_1\eta_{t+\Delta t} + \Delta P_t)^2 + 2\beta K_1\Delta U}, \quad (2.15)$$

$$\Delta U = U_t - U_{t+\Delta t}, \text{ and} \quad (2.16)$$

$$U = \frac{\sigma_y^2}{6G}, \quad (2.17)$$

where K_1 denotes the bulk modulus, K_2 and K_3 are material constants, η is the specific volume, U represents the internal energy which is related to the equivalent plastic flow stress σ_y by a quadratic expression, β is the fraction of the elastic energy loss converted to potential hydrostatic energy, and the shear modulus is shown by G . The 21 constants of the JH2 model for Al_2O_3 were obtained from previous studies [57, 105], and are summarized in Table 2.2.

2.5.3 The cohesive zone model for the interfacial debonding

The cohesive zone model (CZM) formulation was first proposed by Barrenblatt [84] and Dugdale [106] and is now widely used as an effective approach for modeling the fracture process in materials such as polymers, metals, ceramics, concretes and laminated composites [107]. In the CZM used in this study, it is assumed that matrix/-particle interface debonding occurs when the quadratic interaction function involving the nominal stress ratios attains unity as follows [69]:

Table 2.2: The JH2 constants used for Al₂O₃ reinforcing particles [57, 105]

Parameter	Value	Unit
A	0.93	-
B	0.31	-
N	0.6	-
M	0.6	-
C	0	-
K_1	193	GPa
K_2	0	GPa
K_3	0	GPa
d_1	0.005	-
d_2	1	-
ρ	3890	kg/m ³
G	155	GPa
T	0.6	GPa
HEL	10.5	GPa
P_{HEL}	4.5	GPa
$\sigma_{i,max}$	12.2	GPa
$\sigma_{f,max}$	1.3	GPa
$\epsilon_{f,min}$	0	-
$\epsilon_{f,max}$	0.2	-
β	1	-

$$\left(\frac{T_n}{T_n^0}\right)^2 + \left(\frac{T_s}{T_s^0}\right)^2 + \left(\frac{T_t}{T_t^0}\right)^2 = 1 \quad (2.18)$$

where, T_n , T_s , and T_t represent the tractions acting on the interface at a load increment in normal and in two in-plane shear directions, respectively. Likewise, T_n^0 , T_s^0 , and T_t^0 denotes the tractions at the onset of damage initiation in the normal and two in-plane shear directions. Note that the normal traction is tensile, and purely compressive stress does not lead to decohesion. The components of the traction-separation law are written as:

$$T_n = \begin{cases} (1 - D) T_n^*, & \text{if } T_n^* \geq 0 \\ T_n^*, & \text{if } T_n^* < 0 \end{cases} \quad (2.19)$$

$$T_s = (1 - D) T_s^*, \text{ and} \quad (2.20)$$

$$T_t = (1 - D) T_t^*, \quad (2.21)$$

where T_n^* , T_s^* , and T_t^* are the stress components calculated by the elastic traction-separation behavior for the current strain prior to the damage initiation. D , specifically denotes the damage variable which begins to gradually increase from 0 to 1 with further loading once the debonding initiation criterion expressed by Eq. (2.18) is met. The damage variable is defined as [69]:

$$D = \begin{cases} 0, & \text{if } \delta_m^{max} \leq \delta_m^0 \\ \frac{\delta_m^f (\delta_m^{max} - \delta_m^0)}{\delta_m^{max} (\delta_m^f - \delta_m^0)}, & \text{if } \delta_m^0 < \delta_m^{max} < \delta_f^{max}, \text{ and} \\ 1, & \text{if } \delta_m^{max} > \delta_f^{max} \end{cases} \quad (2.22)$$

where, δ_m^0 and δ_m^f represent the effective separations at damage initiation and complete failure, respectively. The maximum value of the effective displacement during the loading process at each increment is denoted by δ_m^{max} . The effective separation at each load increment δ_m is calculated as [69]:

$$\delta_m = \sqrt{\delta_n^2 + \delta_s^2 + \delta_t^2}, \quad (2.23)$$

where, δ_n , δ_s , δ_t are the nominal separations in the normal and two in-plane shear directions, respectively. To obtain the effective separation at complete decohesion, one can use the fracture energy G_c , which is given as:

$$\delta_m^f = \frac{2G_c}{T_n^*}, \quad (2.24)$$

The CZM constants [103] used in this study are presented in Table 2.3. For Al-MMC composites, the CZM constants have been reported in different ranges in previous studies [27, 41, 108–110]. For example, the reported values for the interface strength varies from a quantity on the order of MPa [109] to GPa [110]. The values in Table 2.3 were selected to establish the best match between the experimental and numerical outcomes in this research study.

2.6 Results

2.6.1 Quasi-static compression

The numerically predicted results for Al-34 wt.% Al₂O₃, and Al-46 wt.% Al₂O₃ coatings under quasi-static compression are compared with those of the experiments in terms of the stress versus strain histories and observed failure mechanisms. This can provide insights for establishing an accurate computational framework to further explore the behavior of the material that can eventually give rise to a tool for material design and optimization. Shown in Fig. 2.4 is the predicted stress-strain responses in comparison to those measured by experiments. The pure Al and MMC samples were all experimentally tested in different directions, namely the nozzle traverse (travel) direction, the second in-plane direction perpendicular to the nozzle travel direction, and the deposition direction represented by X, Y, and Z, respectively, in Fig. 2.4.

For the pure Al matrix, the results based on the data for the Z-direction was compared to the experiment, as shown in the red solid curve in Fig. 2.4. The predicted curve for the pure Al matrix aligns with the experimentally measured one,

Table 2.3: Summary of the matrix/particle interface properties.

Parameter	K_{nn}, K_{ss}, K_{tt}	T_n^0, T_s^0, T_t^0 [109]	δ_m^f [109]
Value	2E7 MPa.mm ⁻¹	705 MPa	0.00035 mm

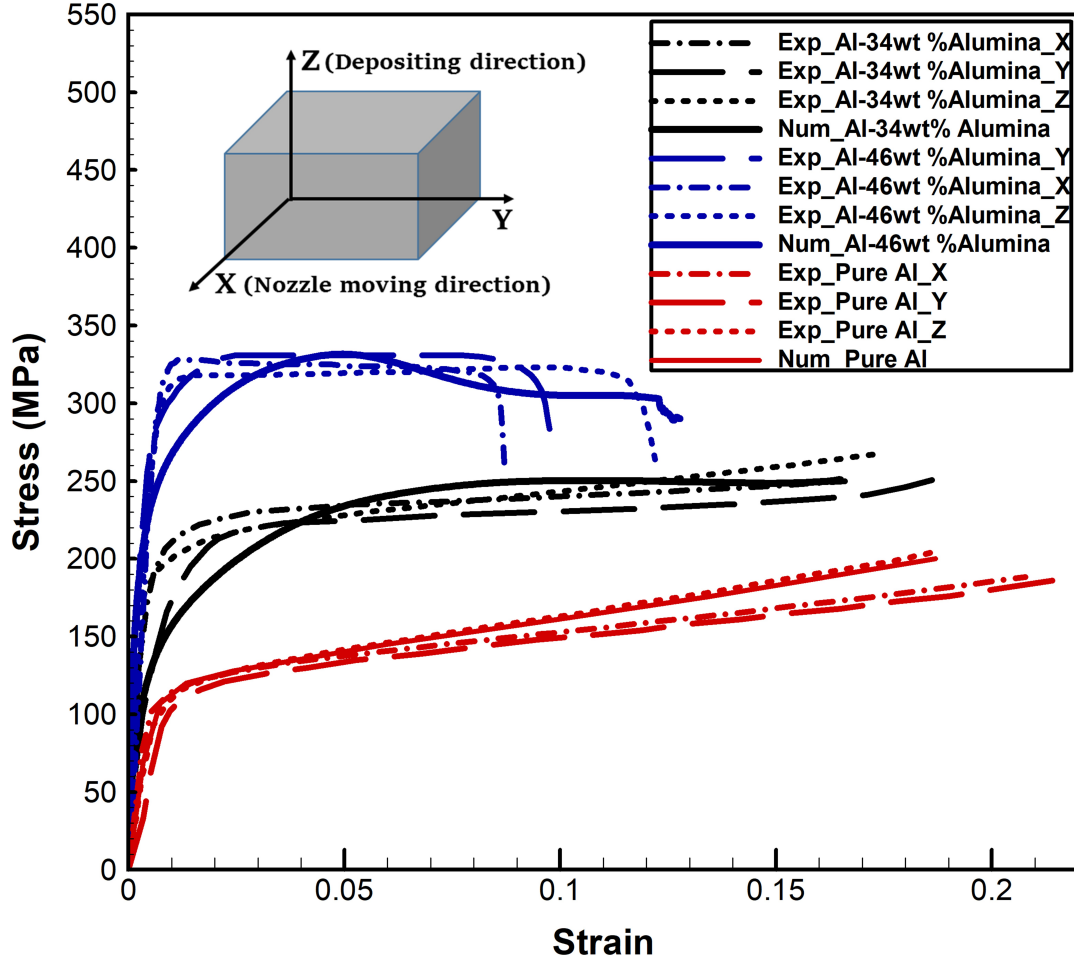


Fig. 2.4: Numerical (Num) and experimental (Exp) stress-strain responses under quasi-static compression for different weight percentage of alumina in the Al matrix. The cuboidal samples were all tested in three different directions denoted by X, Y, and Z corresponding to the nozzle moving direction, the second in-plane direction perpendicular to the nozzle moving direction, and the deposition direction, respectively. The dashed curves correspond to the experimental responses for each coating and the solid curves represent the associated numerically predicted behavior.

which shows the accuracy of the approach for modeling the pure Al coating. Regarding the predicted responses for the MMCs, the model can reasonably capture the stiffness (i.e., the Young's modulus) and the maximum load bearing capacity of the composite coatings with different reinforcing particle concentrations. In addition, the experimental trend towards decreasing ductility with increase in reinforcing particle content from 34 wt.% to 46 wt.% is reasonably reflected in the numerically predicted

curves. Namely, plastic deformation in the Al-34 wt.% Al₂O₃ composite coating begins to take place in the model at a strain of 0.6%, which leads to a yield stress of 141 MPa. The experimental yield strain ranges from 0.53% to 0.65% and yield stress ranges from 135 MPa to 178 MPa based on the different coordinate directions that were explored. The model tends to slightly underestimate the yield stress of the MMC with 34wt% of the reinforcing inclusions. The model's underestimation of the yield stress is likely due to cold working, which introduces a hardening and strengthening effect in the matrix during the cold spray process. This hardening effect is a result of the high-velocity hard ceramic particles impacting on the Al grains [5, 111], which is not yet considered in the model. In addition to cold working, there are also other mechanisms that are likely to cause the deviations observed between the predicted and experimental stress versus strain histories as it relates to strain hardening behavior and elongation at failure. Among these mechanisms, grain size effects [112, 113] (e.g., Hall-Petch relationship [114]), which require implementation of strain gradient plasticity models [115] in the model of this study, may also play a role.

Fig. 2.5 illustrates the contour of the plastic deformation [58], interfacial failure [79], and particle cracking [41] at two different axial strains during the loading process for the Al-34 wt.% Al₂O₃ composite. With further application of load, the plastic strain begins to accumulate in the ligament (i.e., the interstitial regions) between the particles that are closely aligned together (see Fig. 2.5 (a)), which has been reported in previous studies of 2D RVEs [58]. The localization of plastic strain leads to the growth of the void volume fraction in the matrix resulting in a gradual decrease in the matrix flow stress (see the solid black curve in Fig. 2.4). In addition, as the strain exceeds 4%, matrix/particle debonding and a particle cracking failure mechanism manifest and develop with the increase in applied load within the RVE (see Fig. 2.5 (b) and (c)), particularly at the sharp corners and concaves of the particles [58]. This behavior can be attributed to the mismatch between the mechanical constants and the stress concentration at the curvilinear interfaces [37]. Consequently, the flow stress

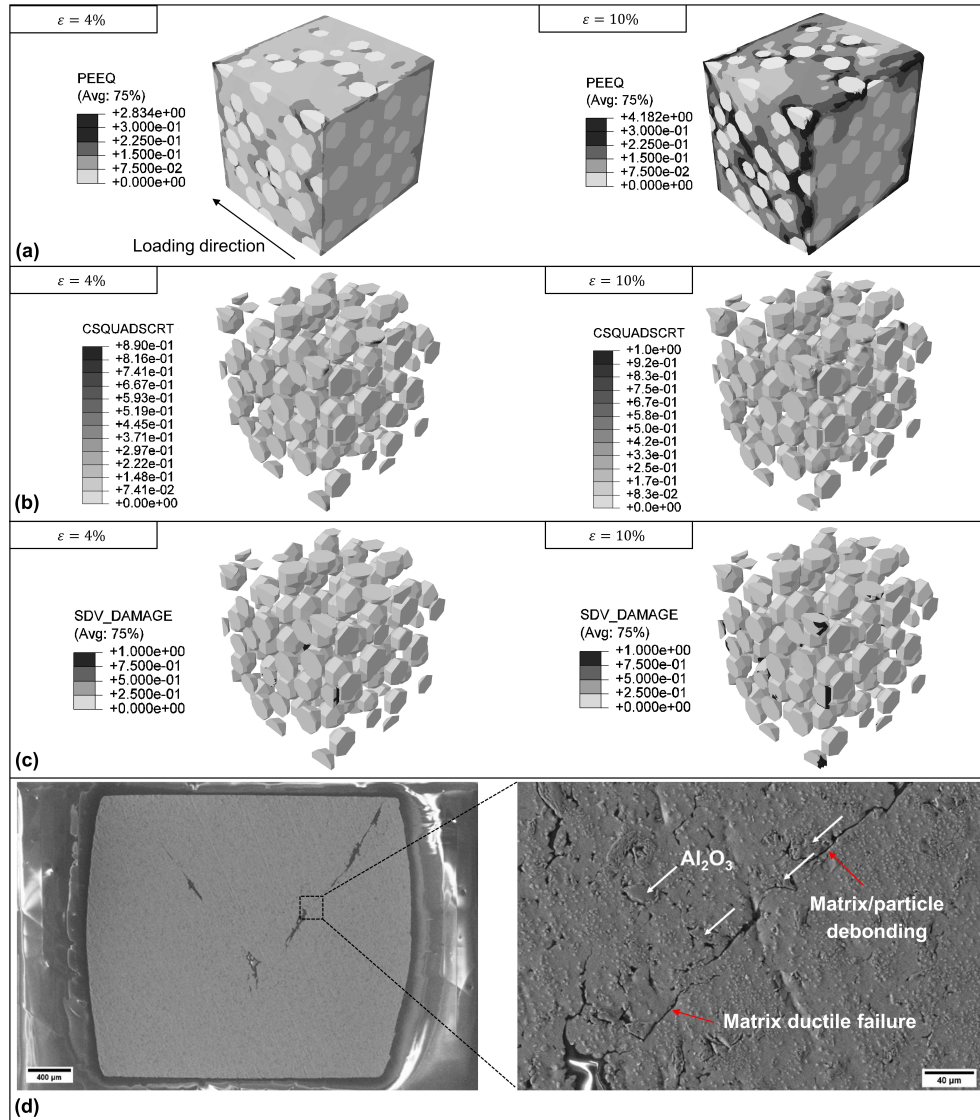


Fig. 2.5: The numerically predicted manifestation and evolution of the damage mechanisms in Al-34 wt.% Al₂O₃ MMC at an axial strain of 4% and 10%: (a) The equivalent plastic strain (PEEQ), which reveals the evolution of plastic deformation in the thin ligaments between the ceramic particles; (b) The data shows the scatter of matrix/particle debonding failure criterion demonstrating the initiation of interfacial failure at the sharp corners of inclusions; (c) The distribution of the JH2 damage parameter shows the accumulation of damage and element removal in the concaves of particles either at the boundary surfaces or considerably close to each other; (d) SEM micrograph of the Al-34 wt.% Al₂O₃ MMC subject to quasi-static compression showing the localized occurrence of damage mechanisms (e.g., matrix ductile failure, and matrix/particle decohesion) at a micro length scale, which does not lead to the coalescence of micro cracks and global failure of the composite at the macro scale.

remains almost constant from 5% strain to a strain of 15%, and then rises slightly with further increase in load up to the end of the loading cycle. This behavior is also reflected in the experimental curves, as matrix failure happens locally and does not lead to fracture of the sample (Fig. 2.4 - the dashed curves for the 34 wt.% Al₂O₃ MMCs). From simulation, it can be implied that the spatial distribution of the particles that is affected by the number of particles and the mean free path parameter (i.e., inter-particle spacing of the reinforcing phase) [116] – which is determined by the weight percentage of the inclusions – does not lead to fracture of the Al-34 wt.% Al₂O₃ MMC sample. This is attributable to the number of thin ligaments, which is not critical enough to develop a 45° shear band [54, 58], fracturing the specimen. This numerical implication (i.e., the micro cracks in the matrix do not evolve to fracture the sample) is also corroborated by the experimental observation of the deformed sample at the end of the loading and the corresponding SEM micrograph shown in Fig. 2.5 (d). As shown, damage mechanisms such as ductile matrix failure and interfacial decohesion emerge locally, leading to the formation of dispersed micro cracks that do not coalesce to cause failure in the sample at macro length scales. For the Al-46 wt.% Al₂O₃ composite, the predicted yield strain and yield strength are 0.7% and 253 MPa, respectively, while the measured yield strain varies between 0.79% and 0.83% and yield strength varies between 298 MPa and 317 MPa for the different coordinate directions. The larger discrepancy in the predicted yield stress of the Al-46 wt.% Al₂O₃ MMC compared to that of the Al-34 wt.% Al₂O₃ MMC can be another indication of the importance of including the cold spray-induced hardening effect [4, 5] in the model in order to produce more accurate numerical results, especially for the MMCs with a high percentage of particle reinforcement. Additionally, the earlier onset of the debonding failure mechanism in the model compared to the experiments can also play a role in the loss of stiffness prior to achieving peak load. Fig. 2.6 and Fig. 2.7 draw a comparison between the numerically predicted and experimentally observed failure mechanisms in the Al-46 wt.% Al₂O₃ composite. As shown, the FE

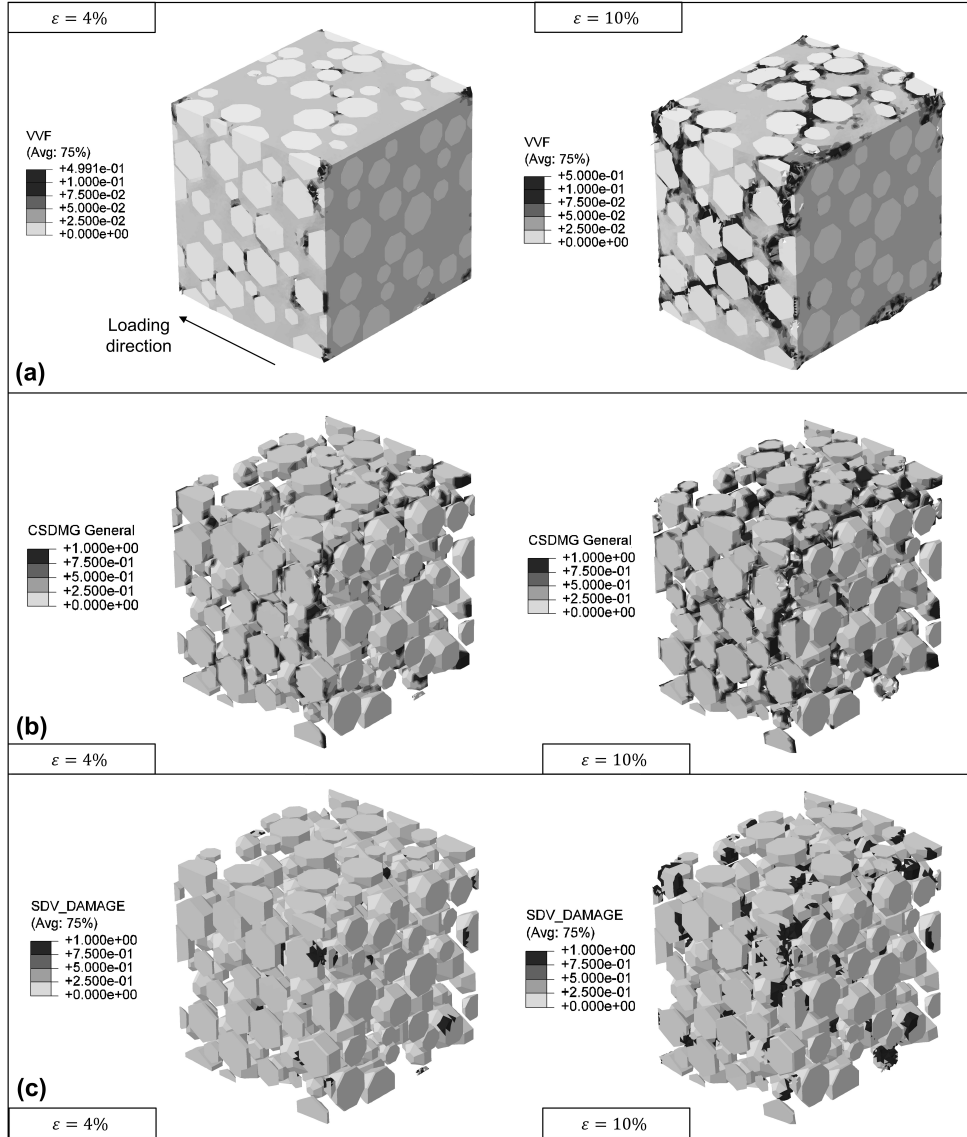


Fig. 2.6: The numerical qualitative results for the Al-46 wt.% Al_2O_3 MMC shown at an axial strain of 4% and 10%: (a) The contour shows the distribution of void volume fraction in the Al matrix, which accumulates in the thin ligaments between the alumina particles forming $\sim 45^\circ$ shear cracks as the strain reaches 10%; (b) The spatial distribution of matrix/particle decohesion damage variable (CSDMG) which illustrates more severely debonding failure compared to the Al-34 wt.% Al_2O_3 MMC (see Fig. 5(b)). This results in loss of stiffness and load sustaining capacity as shown in Fig. 4 (see the solid blue curve); (c) The data illustrates the evolution of particle cracking initiating from the sharp corners within the RVE as the axial strain increases from 4% to 10%.

model can capture the occurrence of the three competitive damage mechanisms (i.e., matrix ductile failure, matrix/particle debonding, and particle cracking) of ceramic-

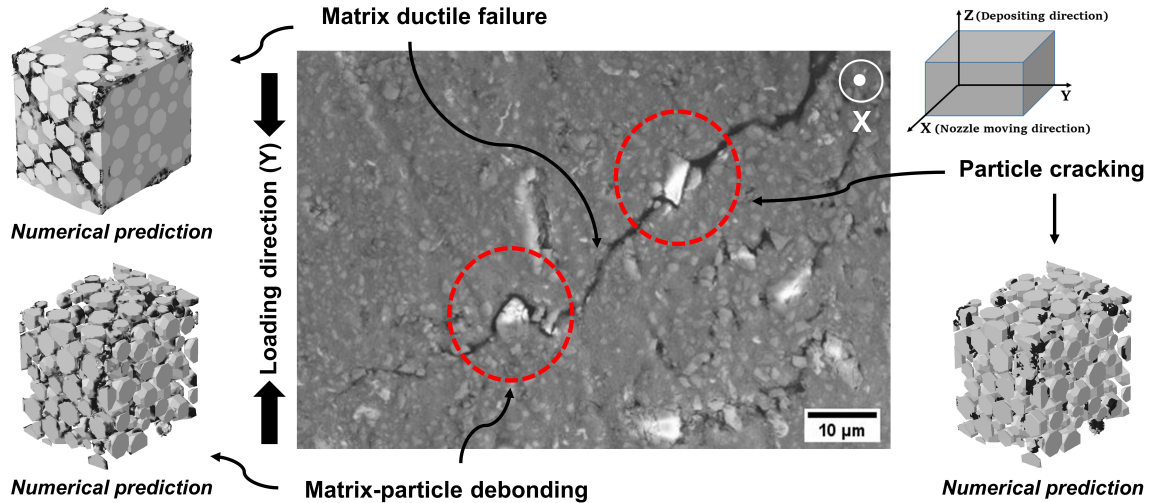


Fig. 2.7: SEM micrograph of the Al-46 wt.% Al_2O_3 MMC subject to quasi-static compression showing the simultaneous occurrence of failure mechanisms, namely matrix ductile failure, matrix/particle interfacial failure, and particle cracking. The 3D numerical predictions of the failure mechanisms (see Fig. 2.6 for more details) have been correspondingly shown, which confirm the qualitative validity of the model. The damaged areas are shown in black. Note that this micrograph represents the cuboidal sample loaded in Y direction and has been observed through X (i.e., the nozzle moving direction) direction.

metal coatings under quasi-static compressive loading. In comparison to the MMC coating with 34 wt.% alumina reinforcement, the plastic strain is severely localized in the thin ligaments between the particles (Fig. 2.6 (a)) in the model. The model predicts the formation of 45° shear cracks passing through the Al matrix between the particles as observed in SEM images, as shown in Fig. 2.7. Once the strain exceeds 4%, particle cracking and matrix/particle debonding are initiated at the sharp corners of the particles (Fig. 2.6 (b) and (c)) – which have been experimentally observed, as shown in Fig. 2.7 – and then propagate within the RVE. These failure mechanisms are accompanied by matrix failure due to void growth in the thin ligaments (Fig. 2.6 (a)). Once the strain exceeds 5%, the stress bearing capacity starts to decrease slightly and then remains constant up to a strain of 12% (Fig. 2.4 – the solid blue curve). This is a consequence of the development of the damage modes in the interfaces and particles. The elements of the Al matrix in which the porosity has exceeded the critical

value are removed from the mesh, leading to an abrupt decrease in load sustaining capacity (Fig. 2.4 – the solid blue curve at a strain of $\sim 12\%$). This behavior is in agreement with the experimental trend that the material’s load-sustaining ability decreases after a given strain is reached (Fig. 2.4 – the dashed blue curves). Overall, the reasonable agreement between the numerical and experimental findings in terms of stress-strain behaviors and failure mechanisms reveal the applicability of the current modelling approach to conduct parametric studies that inform tailoring particle and concentration size and properties in order to control competition between failure mechanisms towards improving, for example, strength-density trade-offs.

2.7 Vickers micro-indentation

The numerical outcomes of the homogenization approach were validated by Vickers hardness experiments. In the experiments, Vickers micro-indentation was applied to the samples with a load of up to 10 N as per ASTM Standard E384 [117]. Fig. 2.8(a) shows the plastically deformed area after complete unloading for the homogenized model of each MMC composite. From the figure, the diagonal length of the indented area decreased as the particle concentration increased, which results in a higher hardness. In other words, at a critical load, the composite material with a higher particle content is less deformed due to the enhanced stiffness and flow stress induced by the hard alumina particles.

Fig. 2.8(b) illustrates the residual von Mises stress distribution for a load of 10 N after unloading in the homogenized model of Al-34 wt.% Al₂O₃ MMC. The distribution pattern for different particle concentrations is the same and the magnitude of the residual stress rises with an increase in the percentage of alumina particles. From Fig. 8(b), the residual stress follows a continuous distribution as the model does not explicitly account for the microstructure, while the observations reported after using 2D heterogeneous models [80, 118] showed that the residual stress is localized between the particles. This implies that 3D microstructure-based models are needed to study

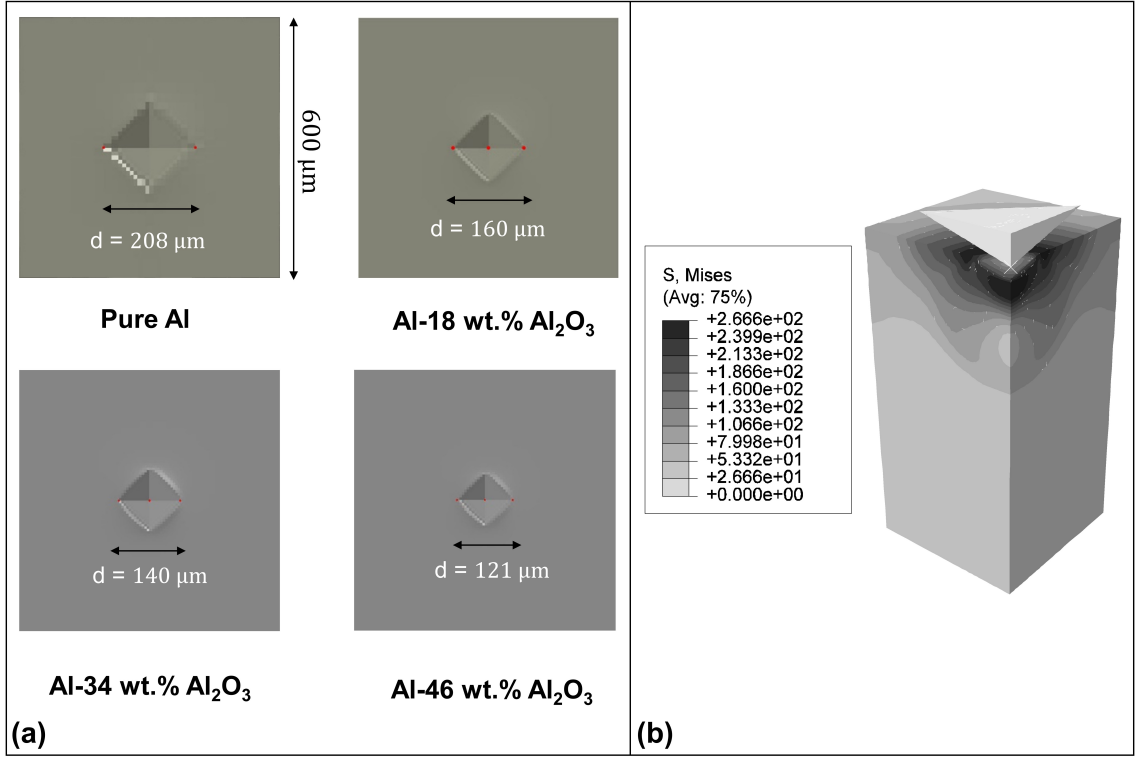


Fig. 2.8: (a) Numerical prediction of the indented area for the MMC composites based on the homogenization approach. The numerically measured diagonal length, d , of the indented profile is substituted into the Eq. (2.25) to calculate the Vickers hardness; (b) The distribution of the residual von Mises stress in the homogenized block of Al-34 wt.% Al_2O_3 composite after unloading.

how the residual stress is developed in the material more realistically. The Vickers hardness of the numerical data was computed using [119]:

$$HV \approx 0.1891 \frac{F}{d^2} [\text{Kgf} \cdot \text{mm}^{-2}], \quad (2.25)$$

where F represents the applied load and d is the diagonal length of the indented area. Shown in Fig. 2.9 are the numerically predicted Vickers hardness results in comparison with the experimental ones measured in three different directions, namely the nozzle travel direction, the deposition direction, and the third perpendicular direction represented by X , Z , and Y , respectively, in the figure. As shown, the homogenized model predicts the hardness of MMCs with an error of $10 \pm 3\%$ compared to the measured values. The heterogeneous modeling approach was reported to overestimate the

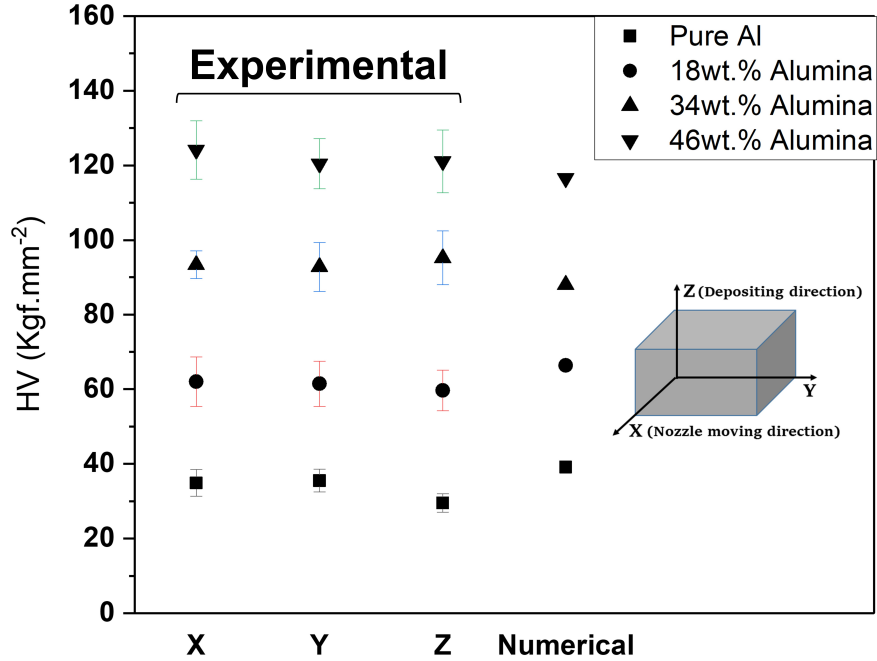


Fig. 2.9: Comparison of experimental and numerical Vickers hardness of the MMC coatings. The X, Y, Z on the horizontal axis represent the direction over which the Vickers indentation was carried out on the samples which correspond to the nozzle travel direction, the deposition direction, and the third perpendicular direction, respectively. Unlike the experimental results, there is no variation in the predicted hardness values due to the homogenization approach.

hardness of MMCs in previous studies [80, 82, 118, 120] due to particle consolidation [121], which required calibration of a significant number of parameters to reach acceptable agreement with the experiments, when compared to the homogenization approach. However, a 3D microstructure-based model allows flexibility to investigate the effect of the size, randomness, and morphology of the particles on the indentation behavior and hardness of cold-sprayed MMC coatings.

2.8 Discussion

This study is the first of its kind to develop 3D finite element models to explore the compressive behavior and hardness of Al-Al₂O₃ composite coatings fabricated by low-pressure cold spray. The presented microstructure-based models for the MMC coatings were built on previous studies of 3D modelling of tensile behavior [24, 27, 42,

54–56, 76, 122] and 2D modelling of the compressive response [57, 58] of particulate-reinforced metal matrix composites. Our model culminated in an acceptable consistency between the numerical and experimental findings, both quantitatively (i.e., based on yield strain, yield strength, and stiffness) and qualitatively (i.e., based on initiation and propagation of damage mechanisms as well as the trends of stress versus strain histories), which lays the foundation to fill the gap in our computational knowledge of ceramic-metal composite coatings. The extended 3D models of Al-Al₂O₃ MMC coatings were generated by Digimat software, where microstructural characteristics obtained by SEM micrographs and EDS analysis [30] were incorporated into the model, including the distribution of size, shape, and weight fraction (i.e., ~ 34wt. % and ~ 46wt. %) of reinforcing ceramic particles. Once the RVEs were generated, the models were validated using the experimental outcomes in terms of quantitative (i.e., stress versus strain histories) and qualitative (i.e., failure mechanisms) comparisons. This method of validation has also been used in previous studies [40, 44, 92, 123]. The experimental measurements linked with the DIC technique showed that the compressive strength of the material was between 135 MPa and 178 MPa for the composite with 34wt. % of alumina and between 298 MPa and 317 MPa for the composite with 46wt. % of alumina. These are among the highest values reported in the literature [124–126] due to the fabrication strategy in this research that employs both matrix strengthening and dispersion strengthening mechanisms [30]. In addition, the measured stiffness of our coatings varied from 28 GPa to 62 GPa for the Al-34 wt. % Al₂O₃ composites and from 48 GPa to 63 GPa for the Al-46 wt.% Al₂O₃ composites. The developed model predicted the strength of the material with an error based on the average experimental quantities of 9.6% and 17.6% for the 34wt. % alumina and the 46wt. % alumina samples, respectively. As well, the numerical prediction of the stiffness yielded a value of 38 GPa and 53 GPa for the 34wt. % alumina and the 46wt. % alumina MMCs, respectively, resulting in an error of 15.5 % and 4.5% with respect to the average measured values. With the maximum error

of 17.6%, the model is reasonably in quantitative agreement with the experimental outcomes. Qualitatively, for the first time to the best of our knowledge, the manifestation and evolution of experimentally observed failure mechanisms in ceramic-metal coatings under compression (i.e., matrix ductile failure, matrix/particle debonding, and particle cracking) were all numerically captured through a 3D micromechanical finite element framework. This improves upon previous studies using 2D models [37, 57, 58] or single-particle 3D models [76]. Additionally, the necessity of developing 3D models in this study was illustrated by Bohm et al. [127] and Soppa et al. [128] to adequately capture the plastic strain distribution in two-phase materials.

Finally, the deviations between the simulation and experimental results can stem from the differences between the assumed and real boundary conditions [129], the complexities of the real microstructures such as reinforcing particle clustering [123] that are not yet incorporated into the generated RVEs, the fracture of reinforcing particles during the cold spray deposition process [5] leading to damage accumulation, and the increase in porosity due to interface decohesion and particle cracking [130], which are not considered in the GTN model implemented in the present study. In addition, the work hardening effect [131] induced in the Al matrix by the high-velocity impact of hard ceramic particles gives rise to significant increase in dislocation density [132], which results in higher strength and hardness in the experimental samples when compared to the model material systems. To account for these crystallographic orientation effects [133] in the model, electron back scattering diffraction (EBSD)-based RVEs [134, 135] can be employed in the future as a promising future direction to numerically explore the micromechanical behavior of MMC coatings. Altogether, the presented model established a reasonable match between the predicted and measured outcomes which allows for further exploration of the microstructure-property relationships of the material (i.e., the effect of matrix porosity [33] as well as particle size [16, 46], shape [45], and distribution [47] of particles on the macro-scale behavior). This paves the way to create a 3D computational tool for the design and optimization

of ceramic-metal cold-sprayed composite coatings via tailoring the microstructure.

2.9 Conclusion

This study explored the behavior of Al-Al₂O₃ composite coatings under quasi-static compression and indentation loading via FE analysis, both quantitatively (i.e., stress versus strain response) and qualitatively (i.e., the manifestation of damage mechanisms, including matrix ductile failure, interfacial debonding, and particle cracking). For the FE models, 3D RVEs were generated by Digimat software based on the microstructural features of the MMC coating samples with different particle concentrations, and the homogenization approach was employed for modeling the Vickers micro-indentation test. To account for the matrix ductile failure and the matrix/particle decohesion, the GTN model and the CZM approach were employed, respectively. The ceramic particles were modeled using the phenomenological JH2 model to incorporate particle damage accumulation. The FE model was validated by stress-strain histories, Vickers hardness, and damage mechanisms obtained experimentally, and a reasonable agreement was observed between the results. Altogether, the outcomes of this study confirm the applicability of the model to be used as a computational tool for spatially tailoring matrix and particle properties and geometries to develop high-performing graded coating structures.

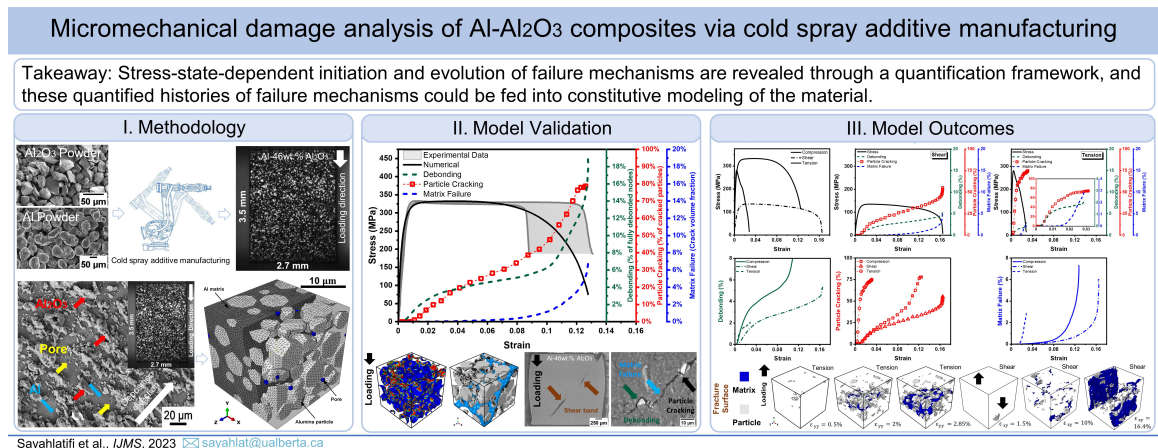
2.10 Acknowledgment

The authors gratefully acknowledge funding support from Imperial Oil (Esso), the Natural Science and Engineering Research Council Canada, the Canada Foundation for Innovation, and the Province of Alberta Ministry of Jobs, Economy, and Innovation.

Chapter 3

Micromechanical damage analysis of Al-Al₂O₃ composites via cold-spray additive manufacturing

Published as Saman Sayahlatifi, Zahra Zaiemyekheh, Chenwei Shao, André McDonald, and James David Hogan, “Micromechanical damage analysis of Al-Al₂O₃ composites via cold-spray additive manufacturing”. Published in the *International Journal of Mechanical Sciences*, vol. 259, p. 108 573, 2023.



3.1 Abstract

3D micro-scale finite element (FE) models were developed to analyze the stress-state-dependent initiation and growth of failure of cold-sprayed additively manufactured

(CSAM) Al-Al₂O₃ composites. Informed by experimental particle size distributions and porosity measurements, representative volume elements (RVEs) were generated by Digimat. Stress-state-dependent constitutive models for the Al matrix and Al₂O₃ ceramic particles were implemented by VUMAT subroutines in Abaqus/Explicit FE solver. For the first time in the literature on metal-ceramic composites, the microscale failure mechanisms involving matrix ductile failure, particle cracking, and matrix/-particle debonding were all quantified based on the crack volume fraction, the fraction of cracked particles, and the fraction of fully debonded interfacial nodes, respectively. The FE model was quantitatively and qualitatively validated by the experimental data for Al-46 wt.% Al₂O₃ under quasi-static uniaxial compression. The validated model was used to investigate the effect of the particle content and size on the material behavior subjected to different stress states. The results revealed that the failure mechanisms are activated in a specified order across different stress states: I. matrix/-particle debonding, II. particle cracking, and III. matrix ductile failure. The material ductility observed under compression/shear vanishes under tension due to the earlier activation of debonding and the faster growth (~ 10 times) of the particle cracking mechanism. Additionally, it was shown that the particle size minimally affects the material strength and flow stress under shear which is likely related to the low load transfer effect through the interfaces. The novelty of this work stems from the provision of a better understanding of the stress-state-dependent evolution of failure mechanisms through a systematic quantification framework whose outcomes have implications for the design of better-performing Al-Al₂O₃ composites via control of the evolution of failure mechanisms and developing micromechanism-based constitutive models for CSAM metal-ceramic materials.

3.2 Introduction

Al-Al₂O₃ composites have been commonly used in different industrial sectors (e.g., automotive and aerospace [136]) owing to their enhanced weight-specific stiffness/strength

[19], hardness [28], wear resistance [137], and thermal properties [138]. However, conventional manufacturing methods such as powder metallurgy [126] and casting [139] induce microstructural defects, including high void volume fraction and agglomeration of particles that restrict the performance of Al-Al₂O₃ composites. More recently, cold spray deposition is gaining popularity as an additive manufacturing technology [4] that can overcome some barriers of traditional approaches by preventing phase transformation, thermal residual stresses, melting, and oxidation [5]. Over the last decade, different CSAM Al-based composites, including Al-Al₂O₃ [140], Al-SiC [141], Al-TiB₂ [142], and Al-B₄C [143], highlight the potentials and advantages of cold spray in the concept of additive manufacturing. In their studies, Shao et al. [30, 144] fabricated a CSAM Al-46 wt.% Al₂O₃ composite that possesses the highest strength when compared to the traditionally made counterparts. To date, few studies in CSAM, and metal-based composites [72, 145], in general, have sought to explore the evolution and competition of failure mechanisms towards more optimized materials design, which is the focus of this paper.

In numerous experimental studies in the literature on ceramic particle-reinforced Al-based composites (e.g., Al-Al₂O₃ [140], Al-SiCp [146], and Al6061-B₄Cp [147] composites), the failure mechanisms were qualitatively investigated through SEM fractography only after testing, particularly under uniaxial tension. Wang et al. [148] studied the behavior of nacre-like 2024Al-B₄Cp composites produced by the freeze casting and pressure infiltration under quasi-static and dynamic compression, and the failure mechanisms were quantified based on the number fraction. It was shown that the particle cracking and matrix deformation possesses the highest (68%) and lowest (10%) quantity, respectively, for the composite with 50 vol.% of particles under a quasi-static loading rate. Lee et al. [145] investigated the effect of particle size on the compressive response of 7075-T6 Al-SiCp composites fabricated by the liquid pressing process. Through the quantification of failure mechanisms based on number fraction, it was revealed that a bimodal particle size distribution homogenizes the

propensity of failure mechanisms and this improves the strength-ductility trade-off of the material. Very recently, Yang et al. [72] studied the evolution of particle cracking and matrix failure mechanisms of Al-SiC_p composites synthesized by powder metallurgy processes under *in-situ* tensile testing. The particle cracking and matrix failure mechanisms were quantified based on the fraction number of cracked particles and the surface density of slip bands, respectively, while the interfacial failure was not considered. By tracking the evolution of mechanisms during loading, Yang et al. [72] showed how the interaction of the matrix and reinforcing particle properties affect the composite material performance.

In spite of experimental efforts to analyze the evolution of failure mechanisms of metal-ceramic composites primarily manufactured by conventional approaches, computational mechanistic approaches are not typically leveraged in the literature to quantitatively capture the history of initiation/competition of the mechanisms. In numerical studies on metal-ceramic composites, 2D [41] and 3D [62] RVEs with simplified [55] and realistic [27] representations of particle morphology were modeled, with most works being under a tensile-dominated stress state [122, 149–151], despite these materials being widely used as coatings [16, 54] in compression-dominated applications (e.g., wear in oil and gas [70], abrasion in landing gear [152]). Ma et al. [42] modeled 3D microstructure-based RVEs of Al356-Al₃Ti composites subjected to uniaxial tension with the assumption of perfect matrix/particle bonding. It was shown that the fracture strain decreases with the increase in the volume fraction of clustered particles. Among limited numerical studies focusing on other stress states (e.g., the work by Amirian et al. [92] and Jiang et al. [153] on the compressive response of ($\gamma + \alpha_2$)-TiAl/Al₂O₃ cermets and ZTAp/40cr composites, respectively), Balokhonov et al. [154] studied the fracture behavior of Al6061T6-ZrC composites under both tension and compression. In their study, a single ZrC particle was modeled as an embedded inclusion in a polycrystalline Al matrix with perfect interfacial bonding. It was shown that the tensile strength of the composite is lower than its compressive

strength due to the earlier activation of crack growth in the particle under tension. To the best of our knowledge, no computational FE model has yet been developed to quantitatively analyze the evolution and competition of multiple failure mechanisms under different stress states of metal-ceramic composites, specifically novel CSAM composites. The development of such a model is important as it systematically unravels the evolution of failure mechanisms that govern material behavior. In addition, these models enable us to design and optimize the material performance by controlling the initiation/competition of failure mechanisms via microstructural tailoring.

In this study, we build on the previous computational efforts on micromechanical modeling of the failure of metal-ceramic composites [27, 41–43, 61, 76, 122, 154] to fill the gap in stress-state-dependent quantitative damage growth analysis in CSAM metal-based materials. Microstructure-informed RVEs of CSAM Al-46 wt.% Al₂O₃ composites were developed by using Digimat software, and an experimental log-normal particle size distribution was considered. To model the failure of the Al matrix, the model by Zhou et al. [64] was implemented by a VUMAT subroutine in Abaqus/Explicit FE solver that allows ductile failure to be accounted for under different stress states. The matrix failure mechanism was quantified based on the matrix crack volume fraction [155]. The Al₂O₃ ceramic particles were modeled by a viscosity-regularized Johnson-Holmquist II model (i.e., the JH2-V model [65]) that was implemented by another VUMAT subroutine. The JH2-V model mitigates the mesh dependency of results and allows us to better account for the asymmetry of damage growth in ceramics under tension and compression [156], and particle cracking mechanism was quantified based on the number fraction of cracked particles [72]. The matrix/particle interfaces were modeled by a surface-based bi-linear cohesive zone model (CZM) [69], and this mechanism was quantified based on the number fraction of fully debonded nodes at the interfaces [157]. The simulations in this study are conducted for a quasi-static loading rate of 10^{-3} s^{-1} . After the quantitative (i.e., stress-strain and lateral strain-axial strain curves) and qualitative (i.e., the emergence

of the failure mechanisms in the SEM images) validation with experimental data, the verified model was leveraged for the analysis of strengthening mechanisms of the CSAM composite material via load partitioning between the constituents [158], the effect of particle weight fraction, stress-state-dependent failure of the material, and the effect of particle size under different stress states with consideration for the evolution of identified failure mechanisms. In the future, this work has implications for developing a micromechanism-based constitutive model [159] for CSAM metal-ceramic materials based on the provided history of failure mechanisms.

3.3 Methodology

In this section, the experimental methodologies for the fabrication and characterization of the CSAM Al-46 wt.% Al₂O₃ composites are first briefly discussed in Section 3.3.1. For more details on the experimental approaches, the reader is referred to the work by Shao et al. [30, 144]. Secondly in Section 3.3.2, the generation of RVEs of the material by Digimat software and informed by the microstructural features in terms of particle content, particle size distribution, and porosity is outlined, and the numerical setups are detailed (i.e., boundary conditions, loading, and model discretization). Lastly in Section 3.3.3, the theoretical framework for constitutive modeling of the Al matrix, Al₂O₃ ceramic particles, and matrix/particle interfaces by the Zhou model [64], the JH2-V model [65], and the bi-linear cohesive zone modeling, respectively, is presented.

3.3.1 Material fabrication and characterization

Al-46 wt.% Al₂O₃ composites were additively manufactured using a low-pressure cold spray robotized system (SST series P, CenterLine Ltd., Windsor, ON, Canada) equipped with a volumetric powder feeder (5MPE, Oerlikon Metco, Westbury, NY, USA). The as-received Al and Al₂O₃ powders were sieved to acquire a size variation of 40 to 60 μm and 30 to 45 μm , respectively, as shown in Fig. 3.1(a). A powder mixture

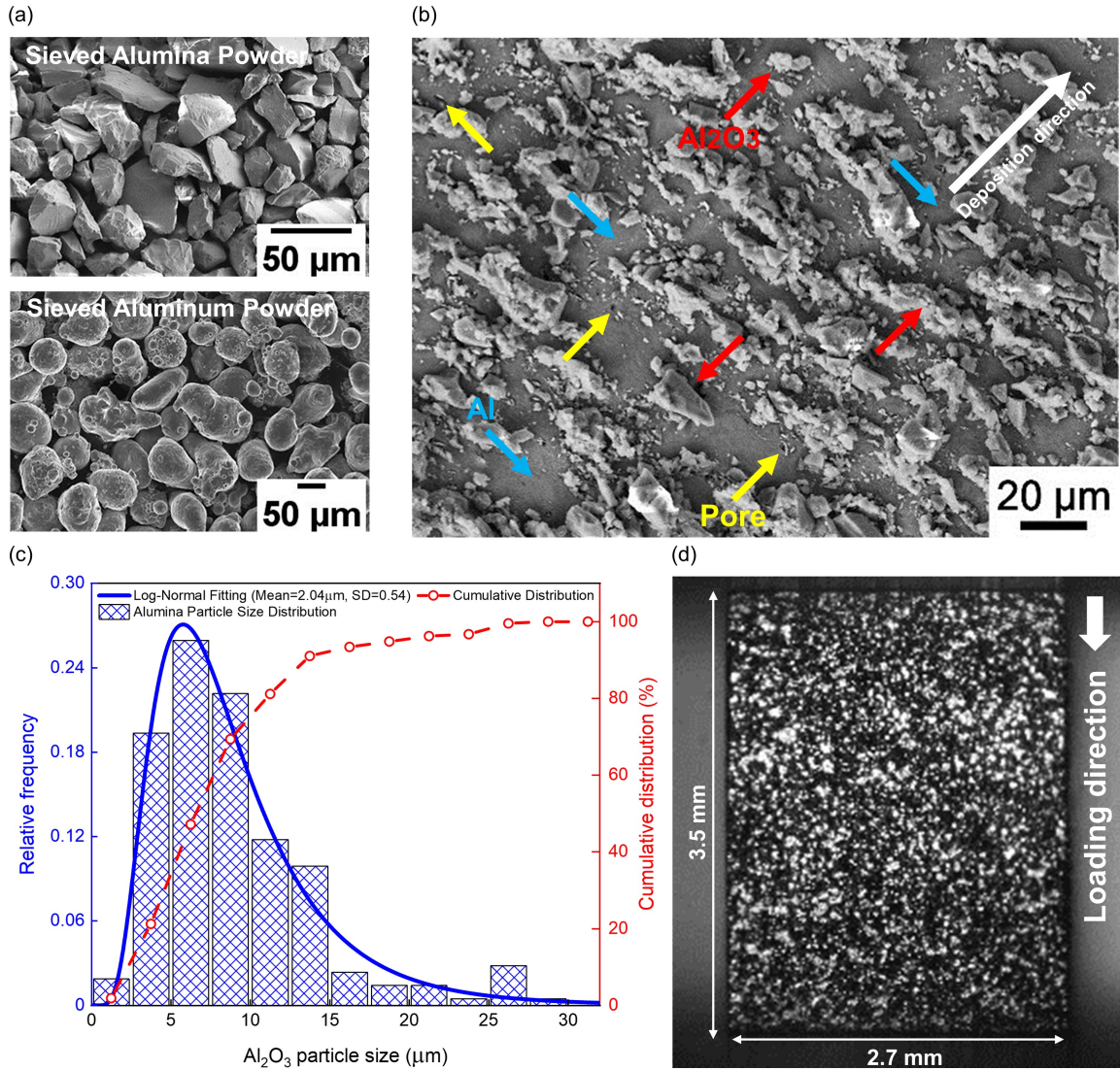


Fig. 3.1: Schematic of the experimental methodology for fabricating and testing of CSAM Al-46 wt.% Al₂O₃ composites: (a) Aluminum and Al₂O₃ powders after sieving with a size distribution of 40 to 60 μm and 30 to 45 μm, respectively. (b) An SEM image of the CSAM Al-46 wt.% Al₂O₃ composite microstructure. (c) Al₂O₃ particle size distribution obtained by ImageJ software based on SEM images of the composite. The particle size distribution follows a log-normal curve with mean and standard deviation values of 2.04 μm and 0.54, respectively, that was used to generate the microstructure-informed RVEs by Digimat software. (d) The cuboidal specimen with dimensions of 2.3 mm × 2.7 mm × 3.5 mm cut by electrical discharge machining from the CSAM bulk Al-46 wt.% Al₂O₃ composite. The specimen was loaded under quasi-static uniaxial compression at a rate of 10⁻³ s⁻¹. Note that the speckle pattern on the sample surface was applied to capture the strain fields with DIC analysis.

with 90wt.% of Al_2O_3 was prepared from the sieved powders that led to a deposited composite reinforced with 46 ± 2.04 wt.% of ceramic particles. The powder blend was deposited on a 6061 Al substrate with a thickness of 5 mm, and this process was guided by the robotized (Motoman HP-20, Yaskawa Electric Corp., Waukegan, IL, USA) nozzle with a traverse speed of 15 mm s^{-1} to manufacture the bulk Al- Al_2O_3 composite layer-by-layer. Complete details of the manufacturing procedures are found in [30, 144]. As shown in Fig. 3.1(b), the material microstructure was characterized by using a field-emission SEM coupled with energy-dispersive x-ray spectroscopy (EDS) operated at 20 kV (Zeiss Sigma, Oberkochen, Baden-Württemberg, Germany). Using ImagePro software and the SEM images, the porosity of the composite was calculated to be 0.17 ± 0.03 vol.% [30]. To inform the microstructure-based model, the SEM images were analyzed by ImageJ software, and a log-normal distribution of the particle sizes with a mean value of $2.04 \text{ }\mu\text{m}$ and a standard deviation of 0.54 was obtained, as shown in Fig. 3.1(c). The cumulative distribution on the histogram in Fig. 3.1(c) shows that $\sim 85\%$ of Al_2O_3 particles are smaller than $12.5 \text{ }\mu\text{m}$, which is ~ 3 to 4 times lower than that of the sieved Al_2O_3 in the feedstock powder; this is attributable to the fragmentation of hard Al_2O_3 particles during the cold spray process [160]. Fig. 3.1(d) shows the cuboidal test specimen with dimensions of $2.3 \text{ mm} \times 2.7 \text{ mm} \times 3.5 \text{ mm}$ that was cut from the CSAM bulk Al-46 wt.% Al_2O_3 composite. By using an Instron 3365 testing machine (Instron, Norwood, Massachusetts, USA), the specimens were loaded under uniaxial compression along the length of 3.5 mm (see Fig. 3.1(d)) at a rate of 10^{-3} s^{-1} and at room temperature. The digital image correlation (DIC) technique was used to capture the strain fields developed in the specimen. The DIC data was analyzed by VIC-2D (v6 2018) software to obtain the surface average strain histories for plotting stress-strain and lateral strain-axial strain curves. The DIC methodology is detailed in Shao et al. [30, 144]. The specimens were centrally placed between M2-graded high-speed steel platens with a 1-inch diameter. The interfaces were lubricated by extreme pressure grease to minimize the effect of friction, thereby

allowing free lateral expansion.

3.3.2 Micromechanical model and numerical procedures

Informed by the SEM image-driven measurements, the microstructure-based model for the CSAM Al-46 wt.% Al₂O₃ composite was produced by Digimat software. In the current cold-sprayed materials, the Al matrix has a complex polycrystalline microstructure with a bi-modal grain size distribution, where zones of ultra-fine grains are irregularly embedded inside coarser grains [144], which may not be successfully reproducible with the current algorithms [161, 162] for the generation of polycrystalline RVEs. Additionally, the large number of Al₂O₃ particles present in the microstructure of the Al-46 wt.% Al₂O₃ composite interfere with the signal acquisition of electron backscatter diffraction (EBSD) data on the orientation of Al matrix grains which are the inputs into crystal plasticity models [163, 164]. Inspired by the previous studies on particulate reinforced metal matrix composites [42, 43, 122, 149, 165], the Al matrix in this study was simplified as a homogeneous continuum constitutively modeled by a stress-state-dependent ductile failure model [64] that will be detailed in Section 3.3.3. As shown in Fig. 3.1(b), the Al₂O₃ particles in the CSAM Al-46 wt.% Al₂O₃ composite microstructure represent complex irregularities including clusters of irregularly shaped/oriented particles, particle contiguity, and particle fragments. Alongside the high computational cost of the inclusion of such features in the model, these morphological characteristics of particles may not be fully reconstructible by the available mathematical algorithms [166, 167], to the best of the authors' knowledge. As shown in Fig. 3.2(a), the irregular morphology of ceramic particles was reproduced by a 20-faced polyhedron geometry as a simplification that is also employed in the literature [42, 89, 90] on metal-ceramic composites. The Al₂O₃ particles with a 3D random orientation were generated based on the experimental log-normal size distribution in Fig. 3.1(c), and were randomly distributed in the domain of the cubic RVE with a length size of 25 μm (see Fig. 3.2(a)). The selection of the RVE

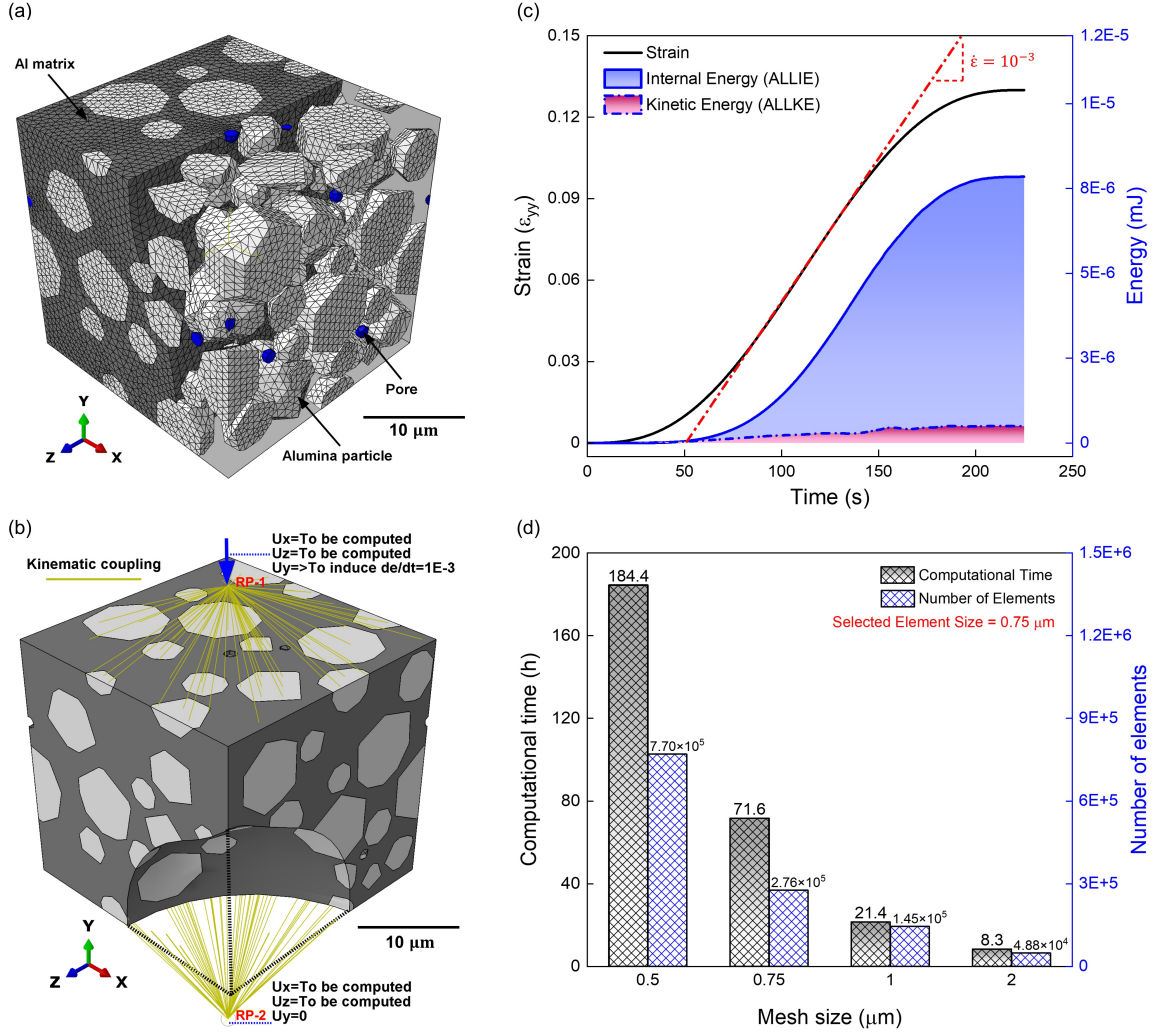


Fig. 3.2: The model description and numerical methodology: (a) The microstructure-informed RVE generated by Digimat for the CSAM Al-46 wt.% Al₂O₃ composite. Randomly oriented icosahedron-shaped (i.e., 20-faced polyhedron) Al₂O₃ particles were randomly distributed in the Al matrix with the size distribution represented in Fig. 3.1(c). Initial pores with an icosahedron morphology and with a volume fraction of 0.17% and a size of 1.5 μm were randomly dispersed in the matrix. (b) The mixed static-kinematic boundary condition [43] for applying the load on the RVE through displacement control with a smooth step amplitude. (c) The history of nominal axial strain applied to the model by displacement control and the balance of the internal (ALLIE) and the kinetic (ALLKE) energies which confirms the quasi-static condition (i.e., ALLKE/ALLIE ≤ 10%) [91]. (d) A summary of the mesh convergence study, including the element size, the number of elements, and the corresponding computational runtime. The element size of 0.75 μm was selected for further studies and this was chosen to balance the runtime and accuracy (see Fig. 3.3(b)).

length size is discussed in Section 3.4.1. To successfully reconstruct an RVE with the targeted high particle weight fraction of 46%, the particles were allowed to cross the boundaries, and their size was restricted to a maximum size of 12.5 μm , given that $\sim 85\%$ of particles is measured to be less than 12.5 μm , as shown in Fig. 3.1(c). As represented in blue in Fig. 3.2(a), randomly oriented polyhedron-shaped pores with a volume fraction of 0.17% and a size of 1.5 μm were randomly incorporated into the Al matrix. With the length of 25 μm , the synthesized RVE of the Al-46 wt.% Al_2O_3 composite comprised of 135 particles and 41 pores (see Fig. 3.2(a)). To prevent inducing Abaqus/Explicit FE solver-related negative effects on the predicted results and decrease the computational time [71], the conventional periodic boundary condition (PBC) [168] was not applied in this study. As shown in Fig. 3.2(b), a mixed static-kinematic boundary condition [43] was used to apply the load on the RVE. To do so, the top and bottom boundary surfaces were kinematically coupled with the corresponding reference points (i.e., RP-1 and RP-2 in red, respectively) in all degrees of freedom (DOFs). The RP-2 was only restricted in the Y direction, while a displacement in the Y direction as the loading axis was applied to RP-1 via a smooth step amplitude to suppress the kinetic energy. For both the RPs, the in-plane DOFs (i.e., X and Z directions) were unrestricted to be computed by the FE solver based on equilibrium conditions and the material response. The lateral surfaces were allowed to deform freely. As shown in Fig. 3.2(c), a time step of 225 s was considered for the simulations that allowed inducing a nominal axial strain (ϵ_{yy}) history in the composite with a rate of 10^{-3} s^{-1} in alignment with that of the experiments. In addition, the balance of the internal energy (ALLIE) and the kinetic energy (ALLKE) of the system was monitored to ensure the validity of the quasi-static condition. As seen, the ALLKE remains less than $\sim 10\%$ of the ALLIE throughout the loading history, which confirms the quasi-static condition [91]. Given the small stable time increment in the explicit solver (Δt_{stable} is $\mathcal{O}(10^{-12} \text{ s})$ in our study), a fixed mass scaling parameter of 1.44×10^{16} was applied to the whole RVE at the beginning of

the simulation to lower the computational time. The Al matrix and Al₂O₃ particles were discretized with 10-node modified quadratic tetrahedron (C3D10M) elements with a tetrahedron geometry. Fig. 3.2(d) shows a summary of the mesh convergence study in terms of the computational runtime and the number of elements associated with the selected mesh sizes. An element size of 0.75 μm was chosen for the simulations and this balances the runtime and accuracy (see Section 3.4.1 for more details). Accordingly, the micromechanical model of the CSAM Al-46 wt.% Al₂O₃ composite was made up of 276,272 C3D10M elements, 438,513 nodes, and 1,105,088 integration points. The models were run by using high-performance parallel computing on the Graham cluster of Compute Canada by using 5 nodes (i.e., 160 cores).

3.3.3 Material constitutive models

Stress-state-dependent ductile failure model

In metal-ceramic composites, the presence of randomly distributed hard particles with irregular geometries induces multiple time-evolving stress states in the metallic matrix. To account for this phenomenon, the model by Zhou et al. [64] (Zhou model, hereafter) was implemented by a VUMAT subroutine in this study; the Zhou model modifies the widely used GTN model [93] to capture the ductile failure under compression/shear dominated stress states through the incorporation of the stress triaxiality and the Lode angle parameters [48]. The ductile failure is triggered when the yield surface of the Zhou model exceeds zero as:

$$\Phi(\sigma, f^*, D_s) = \left(\frac{\sigma_q}{\sigma_y}\right)^2 + 2q_1 f^* \cosh\left(\frac{3q_2 p}{2\sigma_y}\right) - (1 + D^2 - 2D_s) = 0, \quad (3.1)$$

where σ_y is the flow stress of the material, p and σ_q are the hydrostatic and deviatoric stress components, respectively; $D = q_1 f^* + D_s$ represents the effective damage which combines the tension-induced void growth (f^*) proposed by Tvergaard and Needleman [93] and the contribution of void distortion/sheeting damage mechanism [169] (D_s) when shear deformation dominates; q_1 and q_2 are material constants proposed

by Tvergaard [170] to better account for void coalescence phenomenon. Known as effective porosity, f^* controls ductile failure under tension and is defined as:

$$f^* = \begin{cases} f & \text{if } f \leq f_c \\ f_c + \frac{f_u^* - f_c}{f_F - f_c} (f - f_c) & \text{if } f_c \leq f \leq f_F, \\ f_u^* & \text{if } f \geq f_F \end{cases}, \quad (3.2)$$

where f_c is the critical porosity to trigger void coalescence; $f_u^* = \frac{1}{q_1}$ corresponds to zero stress carrying capacity; and f_F denotes the porosity at complete failure. The porosity (f) increases due to the nucleation of new voids (\dot{f}_n) and the growth of existing voids (\dot{f}_g). The void nucleation is assumed to follow a normal distribution function [99] based on the equivalent plastic strain $\bar{\epsilon}_M^p$ exclusively under tensile hydrostatic pressure. Assuming the material is plastically incompressible, the void growth rate is linked with the plastic volume increment. Accordingly, the functions are written as follows:

$$\dot{f} = \dot{f}_n + \dot{f}_g, \quad (3.3)$$

$$\dot{f}_n = A_n \dot{\bar{\epsilon}}_M^p, \quad (3.4)$$

$$A_n = \begin{cases} \frac{f_N}{s_N \sqrt{2\pi}} e^{-0.5 \left(\frac{\bar{\epsilon}_M^p - \epsilon_N}{s_N} \right)^2} & \text{if } p \geq 0, \text{ and} \\ 0 & \text{if } p < 0 \end{cases} \quad (3.5)$$

$$\dot{f}_g = (1 - f) \dot{\epsilon}_{kk}^p, \quad (3.6)$$

where $\dot{\bar{\epsilon}}_M^p$ is the equivalent plastic strain rate; ϵ_N and s_N is the mean equivalent plastic strain for void nucleation, and the standard deviation of the normal distribution, respectively; $\dot{\epsilon}_{kk}^p$ denotes the trace of the plastic strain rate tensor. In the Zhou model, the shear damage parameter (see D_s in Eq. (3.1)) is assumed to grow as a function of the equivalent plastic strain and the stress state as:

$$\dot{D}_s = \psi(\theta, T^*) \frac{n D_s^{\frac{n-1}{n}}}{\epsilon_f^p} \dot{\bar{\epsilon}}_M^p, \quad (3.7)$$

$$\psi(\theta, T^*) = \begin{cases} g(\theta) & \text{if } T^* \geq 0, \\ g(\theta)(1 - k) + k & \text{if } T^* < 0 \end{cases}, \quad (3.8)$$

where θ and T^* represent the Lode angle and stress triaxiality, respectively; $\psi(\theta, T^*)$ is the weight factor function to account for ductile failure under compression/shear dominated stress states; k regulates the contribution of the weight factor to damage growth under compression; $g(\theta)$ denotes the Lode angle function proposed by Xue [171], which is defined based on the third invariant of the deviatoric stress tensor (J_3) as:

$$g(\theta) = 1 - \frac{6|\theta|}{\pi}, \quad (3.9)$$

$$\theta = \frac{1}{3} \cos^{-1} \left(\frac{27J_3}{2\sigma_q^3} \right) - \frac{\pi}{6}. \quad (3.10)$$

By considering an associative flow rule, the equivalent plastic strain and internal parameters, including f^* and D_s , are obtained at each increment of loading by solving the following partial differential equations [169] in the VUMAT subroutine through an iterative numerical Newton-Raphson scheme [172] as:

$$f_1 = \dot{\epsilon}_v^p \left(3q_1 q_2 f^* \sinh \left(\frac{3q_2 p}{2\sigma_y} \right) \frac{1}{\sigma_y} \right) - \dot{\epsilon}_d^p \left(\frac{2q}{\sigma_y^2} \right) = 0, \quad (3.11)$$

$$f_2 = \Phi(p, q, \bar{\epsilon}_M^p, f^*, D_s) = 0, \quad (3.12)$$

where $\dot{\epsilon}_v^p$ and $\dot{\epsilon}_d^p$ is the volumetric and deviatoric component of the equivalent plastic strain rate, respectively. More details on the implementation of the Zhou model are found in the work by Zhao et al. [173]. To determine the flow stress (σ_y) of the material, an isotropic hardening form with a power law definition was employed:

$$\sigma_y(\bar{\epsilon}_M^p) = \sigma_y \left(1 + \frac{E}{\sigma_y} \bar{\epsilon}_M^p \right)^n, \quad (3.13)$$

where E is the Young's modulus, and n is a material constant to be calibrated. Table 3.1 summarizes the Zhou model constants used for the Al matrix in this study. The values are taken from the literature or calibrated within their physical bounds based on a trial-and-error process to obtain the best match with the experimental stress-strain curves (see Section 3.4.2). Note that the initial porosity parameter (f_0)

was set to be zero as the initial pores were explicitly incorporated in the RVE (see Fig. 3.2(a)). In this study, the elements of the Al matrix were deleted when the effective damage parameter (i.e., $D = q_1 f^* + D_s$, see Eq. (3.1)) reached a threshold of nearly one (i.e., 0.99 in our implementation to avoid element distortion) [64] at the integration points of the element. The deleted elements are eliminated from the calculation process for updating the stress components and internal variables, while their mass remained in effect in the domain of the model. This deletion process of fully damaged elements in the Abaqus/Explicit FE solver allows an implicit reproduction of cracking in the material.

The JH2-V model for particle cracking

The phenomenological viscosity-regularized plasticity JH2-V model [65] was implemented by a VUMAT subroutine in Abaqus/Explicit to account for the particle cracking mechanism. In the JH2-V model, the yield surface is dependent on the equivalent plastic strain rate, and this allows for mitigation of the mesh dependency and mesh-related localization of strain present in the JH2 model [68]. Additionally, the JH2-V model introduces a new tri-linear formulation of fracture strain (see Eq. (3.20)) to better control the damage growth rate under tension and compression independently [174]. The normalized strength (σ^*) of ceramic materials is defined as a function of pressure, accumulated damage, and equivalent plastic strain rate as:

$$\sigma^* = \sigma_i^* - D \left(\sigma_i^* - \sigma_f^* \right), \quad (3.14)$$

$$\sigma_i^* = A \left(p^* + T^* (\dot{\epsilon}_p) \right)^N, \text{ and} \quad (3.15)$$

$$\sigma_f^* = B (p^*)^M, \quad (3.16)$$

where σ_i^* and σ_f^* is the normalized intact and fractured strength, respectively; D represents the accumulation of damage; $\sigma^* = \frac{\sigma}{\sigma_{HEL}}$ and σ_{HEL} is the equivalent stress at the Hugoniot elastic limit; $p^* = \frac{p}{p_{HEL}}$ and $T^* = \frac{T}{p_{HEL}}$ is the normalized pressure and tensile hydrostatic strength, respectively, and p_{HEL} denotes the pressure at the

HEL. In Eq. (4.15), the hydrostatic tensile strength of the material is regulated as a function of the equivalent plastic strain rate $\dot{\epsilon}_p$ that introduces rate dependency into the yield surface of the JH2-V model (see Eq. (3.18)). The empirical constants include A , B , M , and N which are required to be tuned for the material. In the JH2-V model, T is linked to $\dot{\epsilon}_p$ as:

Table 3.1: The parameters of the material constitutive models used in this study. Note that the values without a reference were tuned to achieve the best match with the experimental data in this study.

Al matrix (Zhou model) [64]	Value	Al ₂ O ₃ particle (JH2-V model) [65]	Value
E (GPa)	40	ρ (kg m ⁻³)	3890
ν	0.33	G (GPa)	155
σ_y (GPa)	0.236	A	0.93 [65]
n (Eq. (3.13))	0.025	B	0.31 [65]
q_1	1.5 [170]	N	0.6 [65]
q_2	1 [170]	M	0.6 [65]
q_3	2.25 [170]	K_1 (GPa)	226
f_0	0	K_2	0 [65]
f_c	0.04	K_3	0 [65]
f_F	0.15 [102]	T_0 (GPa)	0.2 [65]
ϵ_N	0.3 [90]	HEL (GPa)	6.25 [65]
s_N	0.1 [90]	p_{HEL} (GPa)	7.5 [65]
f_N	0.02 [102]	β	1 [65]
n (Eq. (3.7))	10	η (GPa s)	28×10^{-6} [65]
k	0.5 [64]	$\dot{\epsilon}_p^T$ (s ⁻¹)	10000 [156]
ϵ_s^f	1	$\bar{\epsilon}_p^{min}$	0.00015 [65]
-	-	$\bar{\epsilon}_p^{max}$	0.496 [65]
-	-	p_t (GPa)	-0.17 [65]
-	-	p_c (GPa)	3.02 [65]

$$T(\dot{\bar{\epsilon}}_p) = \begin{cases} T_0 + \eta \dot{\bar{\epsilon}}_p & \text{if } \dot{\bar{\epsilon}}_p < \dot{\bar{\epsilon}}_p^T, \\ (T_0 + \eta \dot{\bar{\epsilon}}_p) \left(1 + \frac{\eta \dot{\bar{\epsilon}}_p^T}{(T_0 + \eta \dot{\bar{\epsilon}}_p)} \left(\ln \left(\frac{\dot{\bar{\epsilon}}_p}{\dot{\bar{\epsilon}}_p^T} \right) \right) \right) & \text{if } \dot{\bar{\epsilon}}_p \geq \dot{\bar{\epsilon}}_p^T \end{cases} \quad (3.17)$$

where T_0 denotes the reference tensile strength; the regularization parameters η and $\dot{\bar{\epsilon}}_p^T$ represents the viscosity and the transitional equivalent plastic strain rate, respectively. The latter automatically adjusts the size of the failure zone at higher strain rates. When the yield surface of the JH2-V model (see Eq. (3.18)) is met, D gradually increases from 0 to 1 as a function of the equivalent plastic strain ($\bar{\epsilon}_p$) as:

$$\Phi(\sigma, D, \dot{\bar{\epsilon}}_p) = \sigma_q - \sigma_{HEL} \sigma^*, \quad (3.18)$$

$$\dot{D} = \frac{\dot{\bar{\epsilon}}_p}{\bar{\epsilon}_p^f(p)}, \quad \text{and} \quad (3.19)$$

$$\bar{\epsilon}_p^f(p) = \begin{cases} \bar{\epsilon}_p^{min} & \text{if } p(\sigma) < p_t \\ \frac{p(\sigma) - p_t}{p_c - p_t} (\bar{\epsilon}_p^{max} - \bar{\epsilon}_p^{min}) + \bar{\epsilon}_p^{min}, & p_t < p(\sigma) < p_c, \\ \bar{\epsilon}_p^{max} & p(\sigma) > p_c \end{cases} \quad (3.20)$$

where σ_q is the von Mises stress, and $\bar{\epsilon}_p^f$ is the equivalent plastic strain at failure. Here, $\bar{\epsilon}_p^{min}$, $\bar{\epsilon}_p^{max}$, p_t , and p_c are the material constants describing the transitional behavior of ceramics from a brittle to a ductile material with the increase in tri-axial pressure [175], which is obtained by experimental testing, including spall [176] and plate impact [177] experiments. By using a polynomial equation, the hydrostatic pressure p is defined as a function of volumetric strain (μ) as:

$$p = \begin{cases} K_1 \mu + K_2 \mu^2 + K_3 \mu^3 + \Delta p, & \text{if } \mu > 0, \\ K_1 \mu & \text{if } \mu \leq 0 \end{cases} \quad (3.21)$$

$$\Delta p_{t+\Delta t} = -K_1 \mu_{t+\Delta t} + \sqrt{(K_1 \mu_{t+\Delta t} + \Delta P_t)^2 + 2\beta K_1 \Delta U}, \quad (3.22)$$

$$\Delta U = U_t - U_{t+\Delta t}, \quad \text{and} \quad (3.23)$$

$$U = \frac{\sigma_y^2}{6G}, \quad (3.24)$$

where K_1 is the bulk modulus; K_2 and K_3 are the material constants; the internal energy is denoted by U ; σ_y is the flow stress; and G represents the shear modulus. In

Eq. (4.21), Δp is the pressure increment induced by the bulking effect when damage is bigger than zero, which is calculated as per the conversion of elastic energy to potential hydrostatic energy (see Eq. (4.22)), and β determines the fraction of conversion. The JH2-V model constants used for the Al_2O_3 particles are summarized in Table 3.1. An equivalent plastic strain ($\bar{\epsilon}_p$) larger than 0.2 at the element integration points [62, 100, 156] was considered as the criterion for the deletion of fully damaged elements (i.e., an element with $D = 1$ at the integration points).

Cohesive zone modeling (CZM) for matrix and particle interfaces

To model the failure of interfaces in metal-ceramics composites, the bi-linear CZM has been commonly used in the literature [178, 179]. In this study, a quadratic stress-based function was employed as the interfacial failure criterion:

$$\left(\frac{\langle t_n \rangle}{t_n^0}\right)^2 + \left(\frac{t_s}{t_s^0}\right)^2 + \left(\frac{t_t}{t_t^0}\right)^2 = 1, \quad (3.25)$$

where t_n , t_s , and t_t represent the normal and in-plane component of traction on the interfaces, respectively; t_n^0 , t_s^0 , and t_t^0 is the corresponding interfacial strength. When the failure criterion (see Eq. (4.25)) is triggered at an interfacial node, the traction components start deteriorating linearly as a function of a scalar damage parameter (D):

$$t_i = (1 - D)t_i^*, \quad i \in [n, s, t], \quad (3.26)$$

$$D = \begin{cases} 0 & \text{if } \delta_m^{max} \leq \delta_m^0 \\ \frac{\delta_m^f(\delta_m^{max} - \delta_m^0)}{\delta_m^{max}(\delta_m^f - \delta_m^0)} & \text{if } \delta_m^0 < \delta_m^{max} < \delta_m^f, \text{ and} \\ 1 & \text{if } \delta_m^{max} \geq \delta_m^f \end{cases} \quad (3.27)$$

$$\delta_m^{max} = \sqrt{\langle \delta_n^2 \rangle + \delta_s^2 + \delta_t^2}, \quad (3.28)$$

where the undamaged traction components are denoted by t_i^* , and these are calculated based on the elastic traction-separation law; δ_m^0 and δ_m^f is the effective separation at the onset of debonding and complete failure, respectively; δ_m^{max} is the effective

separation at the nodal points that is calculated based on the Euclidean norm of the relative separation components (see Eq. (3.28)). The CZM constants used for the Al and Al₂O₃ interfaces in this study are listed in Table 3.2.

3.4 Results and discussion

The variation in the model prediction of the stress-strain response of the material based on the RVE length size, mesh size, the randomness of RVE generation, and loading direction is first investigated in Section 3.4.1, whose outcomes are used to set the numerical parameters for the validation and application of the model. Next in Section 3.4.2, the model is validated by the experimental data on the CSAM Al-46 wt.% Al₂O₃ composite in terms of the stress-strain curves and the failure mechanisms observed in the SEM images after testing under quasi-static uniaxial compression. Here, the initiation and evolution of microscale failure mechanisms, namely matrix failure, particle cracking, and matrix/particle debonding, are quantitatively determined. The validated model is next employed to provide insights into the contribution of strengthening mechanisms and strain hardening rate behavior through load partitioning analysis presented in Section 3.4.3. The model was employed to study the effect of particle weight fraction in Section 3.4.4, where a new correlation is introduced between the failure mechanisms across different Al₂O₃ particle content, and the material properties (i.e., Young’s modulus and yield strength) are analytically defined as functions of particle weight fraction. In Section 3.4.5, the stress-state-dependent initiation and evolution of failure mechanisms are quantitatively analyzed for the first time in the literature, to the best of our knowledge. Lastly, in Section 3.4.6, the

Table 3.2: The parameters used for the CZM of matrix/particle interfaces. Note that the parameter δ_m^f was tuned to achieve the best match with the experimental stress-strain responses in this study.

Parameter	K_{nn}, K_{ss}, K_{tt} [62]	t_n^0, t_s^0, t_t^0 [109]	δ_m^f
Value	2E4 GPa mm ⁻¹	0.705 GPa	75 × 10 ⁻⁶ mm

effect of Al_2O_3 particle size on the stress-strain response and the history of failure mechanisms is studied under different stress states.

3.4.1 The effect of geometric parameters

First, the effect of the geometric parameters, including the RVE length size, element size, randomness of RVE generation, and loading direction on the predicted stress-strain curve of Al-46 wt.% Al_2O_3 composite under quasi-static uniaxial compression was studied. Fig. 3.3(a) shows the predicted stress-strain curves by an RVE size of 15 μm , 25 μm , and 35 μm . As seen, the 15 μm long RVE shows a slightly smaller yield stress and a different strain hardening behavior when compared to the larger RVEs. This may be attributable to the number of particles (i.e., the mean free path parameter [116]) and how it affects the failure evolution. The predicted response remains almost unchanged when the length size exceeds 25 μm , hence an RVE with a length size of 25 μm was selected for further simulations in this study, which is considerably less computationally expensive (i.e., ~ 2 times) than the 35 μm long RVE. The same range of the ratio of RVE length to average particle size (6.5 μm in our work) is also used in previous studies [27, 43]. Fig. 3.3(b) shows the stress-strain curves captured by different mesh sizes ranging from 0.5 μm to 2 μm . Accordingly, an element size of 0.75 μm was selected to balance the accuracy and runtime (see Fig. 3.2(d) for the runtime and the number of elements associated with each mesh size). As shown in Fig. 3.3(c), three different RVEs, namely RVE A, RVE B, and RVE C were randomly generated to study the effect of the model variability. Note that the RVEs only differ in terms of the spatial distribution of Al_2O_3 particles and pores that are randomly positioned based on the random sequential adsorption (RSA) [166] algorithm. As seen, the elastic modulus and predicted yielding point remain the same, but the strain hardening behavior slightly varies. The most noticeable difference is observed in the softening regime and elongation at failure when the type of the RVE changes; the more the strain hardening rate the less the elongation at failure. This

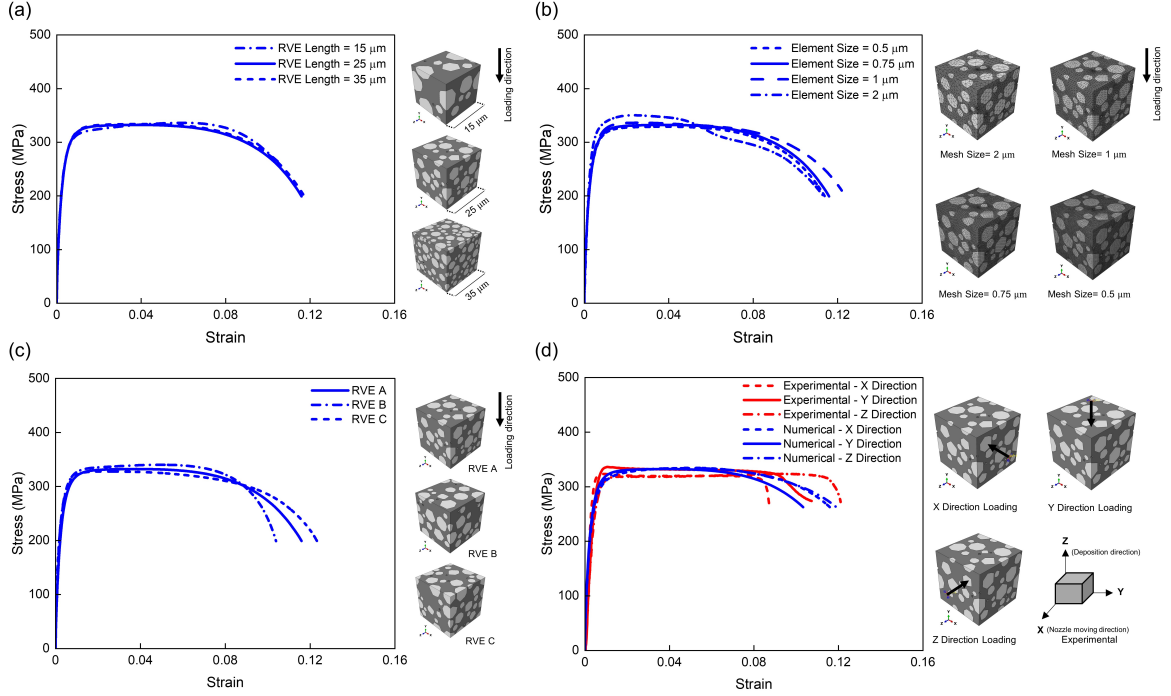


Fig. 3.3: The effect of the model and numerical variables on the predicted stress-strain response of CSAM Al-46 wt.% Al₂O₃ composite under quasi-static uniaxial compression: (a) The effect of the RVE length size on the predicted response. An RVE size of 25 μm was selected for further studies. (b) The figure shows the mesh sensitivity analysis. As seen, the predicted curves converge for an element size less than 0.75 μm. The corresponding runtimes are represented in Fig. 3.2(d). (c) The effect of RVE randomness on the predicted stress-strain curve. Note that the spatial distribution of particles and voids only differs between the RVEs. (d) The predicted response for different loading directions compared to the experimental data.

implies that the spatial distribution of hard particles affects the matrix ductile failure evolution (i.e., the coalescence of microcracks), and this results in a variation in the softening rate of the composite and therefore the elongation at failure. Here, the RVE A was selected for the rest of the study due to better agreement with the experimental data (see Fig. 3.4(a)). As shown in Fig. 3.3(d), the RVE A with a mesh size of 0.75 μm was loaded in different directions. Numerically, the elongation at failure varies when the RVE is loaded along different directions, which is likely to be caused by the anisotropy in the load transfer effect due to the different effective aspect ratio of Al₂O₃ particles along each direction [180], and this observation is also confirmed by the experimentally measured responses in Fig. 3.3(d). The mechanical anisotropy is

more pronounced in the experimental stress-strain curves when compared to those of the model, which may be attributed to the existence of splats and the bi-modal grain size distribution of the Al matrix, and these microstructural features deform differently with respect to the deposition direction [144] which are not incorporated in the continuum-based model in this study.

3.4.2 Model validation and quantification of failure mechanisms

The microstructure-based FE model was validated by the quantitative and qualitative experimental data for the CSAM Al-46 wt.% Al₂O₃ composite under uniaxial quasi-static compression. Fig. 3.4(a) compares the numerical stress-strain curve with those of the experiments presented as a range of data in gray. As seen, the model reasonably reproduces the elastic response, strain hardening behavior, and elongation at failure of the material. The model predicts a more gradual softening regime compared to the experiments, and this is attributable to the rate of the damage growth in the Al matrix as a ductile material in the model, and the boundary conditions that may not fully represent those of the experiments at a macro scale [42, 43]. Through Python scripting in Abaqus software, the numerical stress and strain components were calculated by the homogenization approach [181] throughout the loading history as:

$$\bar{\sigma}_{ij} = \frac{\sum_{k=1}^{N_{ip}} \sigma_{ij,k} V_k}{\sum_{k=1}^{N_{ip}} V_k}, \quad (3.29)$$

$$\bar{\epsilon}_{ij} = \frac{\sum_{k=1}^{N_{ip}} \epsilon_{ij,k} V_k}{\sum_{k=1}^{N_{ip}} V_k}, \quad (3.30)$$

where $\bar{\sigma}_{ij}$ and $\bar{\epsilon}_{ij}$ are the homogenized stress and strain components, respectively, plotted in Fig. 3.4(a); $\bar{\sigma}_{ij,k}$ and $\bar{\epsilon}_{ij,k}$ is the stress and strain component at the integration point, respectively; N_{ip} is the total number of integration points; and V_k is the volume of element at the integration point. To further assess the validity of the model, the lateral strain ($\bar{\epsilon}_{xx}$) versus axial strain ($\bar{\epsilon}_{yy}$) was plotted in comparison to those from experiments obtained from the DIC analysis, as shown in Fig. 3.4(b), which implies

that the development of deformation in the model aligns with the experiments. Next, by developing Python scripts, the validated model was used to quantify the evolution of failure mechanisms as:

$$DE = \frac{\sum_{k=1}^{N_d} N_k}{\sum_{k=1}^{N_t} N_k}, \quad (3.31)$$

$$PC = \frac{\sum_{k=1}^{P_c} P_k}{\sum_{k=1}^{P_t} P_k}, \text{ and} \quad (3.32)$$

$$MF = \frac{\sum_{k=1}^{ME_d} V_k}{\sum_{k=1}^{ME_t} V_k}, \quad (3.33)$$

where DE is the fraction number of fully debonded nodes at the interfaces; PC is the fraction number of cracked particles; MF is the matrix crack volume fraction; N_d and N_t are the number of fully debonded nodes and the total number of interfacial nodes, respectively; P_c and P_t is the number of cracked particles and the total number of particles, respectively; ME_d and ME_t is the number of deleted elements of the matrix and the total number of the matrix elements, respectively. As shown in Fig. 3.4(a), the debonding failure mechanism is activated at a strain of $\sim 0.35\%$ as the first mechanism closely prior to the yielding point of the composite, and this implies that the strength of interfaces plays an important role in the material strength. At a strain of $\sim 1\%$, the particle cracking mechanism is initiated, and the growth of particle cracking stabilizes the rate of debonding up to a strain of 10% as the load transfer effect vanishes with the increase in the number of cracked particles. The stress-bearing capacity follows nearly a plateau up to a strain of $\sim 7\%$ due to the simultaneous increase in interfacial failure, particle cracking, and plastic strain development in the Al matrix (see Fig. 3.4(c)). At a strain of $\sim 4\%$, the matrix failure mechanism is triggered and exponentially grows (see Fig. 3.4(a) and the last row of Fig. 3.4(c)), where $\sim 20\%$ of particles are cracked and $\sim 4\%$ of interfaces are failed. At a strain of $\sim 10\%$, the matrix volume crack exceeds $\sim 1\%$, and consequently, the other two mechanisms gain an ascending rate again similar to that of the matrix failure that accelerates the softening regime. At the elongation at failure, the matrix

volume crack is $\sim 8\%$, $\sim 80\%$ of particles are cracked, and the debonding mechanism reaches $\sim 19\%$; these quantities are consistent with those of the previous studies at the fracture strain of the materials (e.g., the crack volume fraction measured by transmission X-ray microscopy for Mg-SiC composite [155], experimentally measured fraction number of cracked particles for 2024Al-B₄C composite [148], and the computationally calculated interfacial failure for Cu-TiB₂ composite [151]). Fig. 3.4(c) shows the predicted qualitative history of failure mechanisms at the lettered strain levels in Fig. 3.4(a) that are reflected in the SEM images of the material after testing, as shown in Fig. 3.4(d). Additionally, Supplementary Video S1 shows the correlated qualitative and quantitative evolution of failure mechanisms in the material under uniaxial compression. As seen, the matrix/particle interfaces begin to fail at the sharpest corners with a high stress concentration, and the interfacial failure propagates along the neighboring faces mainly parallel to the compressive loading direction where tension is more likely to be produced at the matrix/particle boundaries. The damage first accumulates at the sharp concaves of the particles where the load transfer effect is at a maximum level. Then it mainly propagates parallel to the loading direction under the dominant role of the tensile stress state (i.e., negative pressure (see Eqs. (3.19) and (3.20))). The time-resolved images show that the plastic deformation initiates in the thin ligaments of the Al matrix that are trapped between the hard particles with the highest intensity at the interfaces due to the mismatch in the elastic constants. With the increase in load, the dispersed localized plastic areas coalesce into plastic bands that form an angle of $\sim 45^\circ$ with the loading axis (see the third row in Fig. 3.4(c) at a strain of 9% and 12.8%), and these plastic bands are the sites where the matrix crack is developed. In the last row of Fig. 3.4(c), the evolution of the fractured areas of the RVE is visualized in 3D by reactivating the deleted elements of the matrix and the particles in blue and gray, respectively. The figures reveal that the matrix cracking initiates in the vicinity of the cracked particles due to the unloading of the fractured particle. Subsequently, the matrix crack propagates in

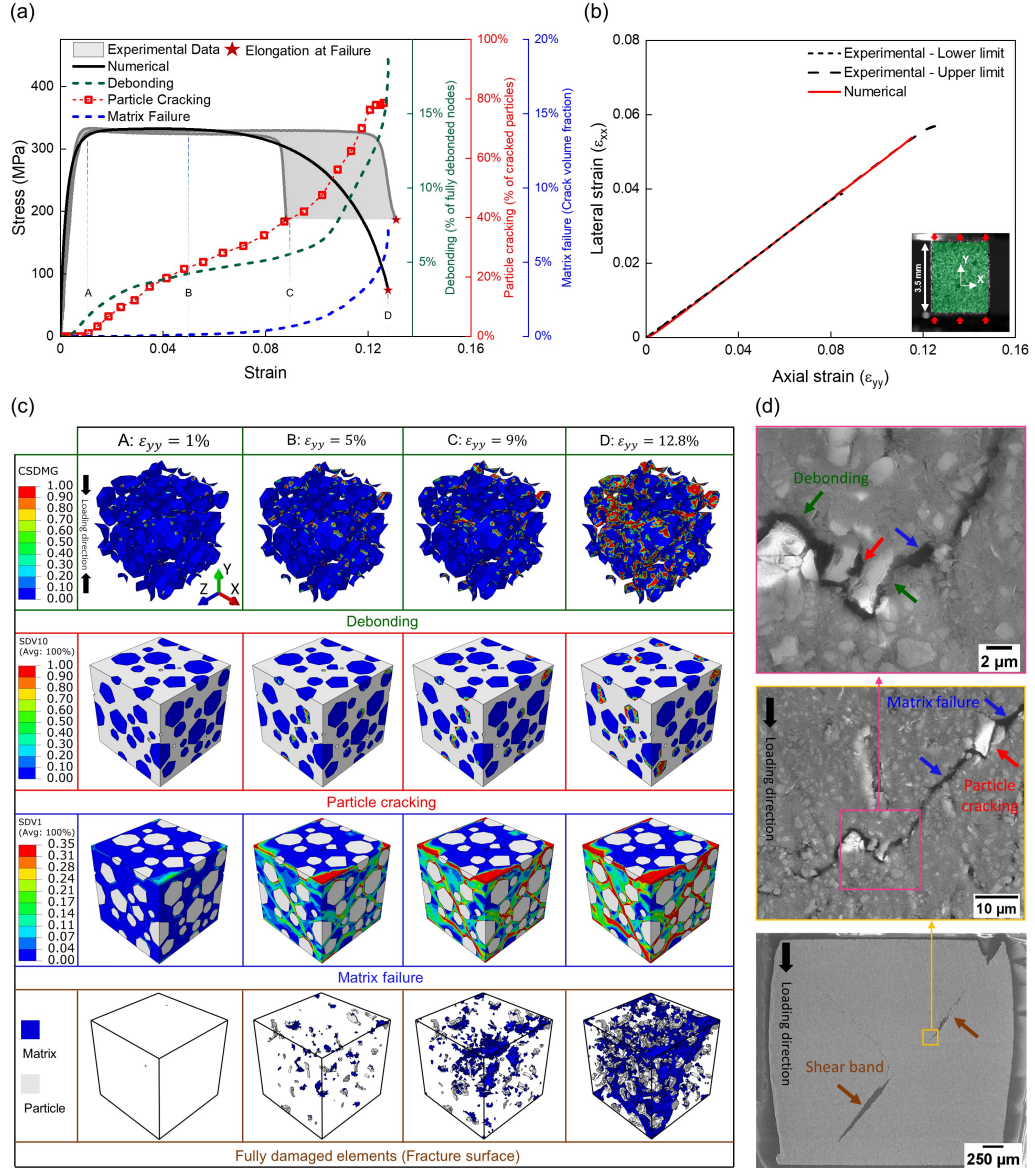


Fig. 3.4: The quantitative and qualitative validation of the micromechanical model with quasi-static uniaxial compression experimental data for CSAM Al-46 wt.% Al₂O₃ composite: (a) The numerically predicted stress-strain curve compared to the experimental data represented by the gray area. The dashed curves show the quantified history of failure mechanisms based on Eqs. (3.31), (3.33) and (4.32). (b) The numerical lateral strain-axial strain curve compared to those of the experiments. (c) The qualitative history of failure mechanisms and the morphology of fractured areas in 3D at specified strains with the lettered point on Fig. 3.4(a). In the legends, SDV10 and SDV1 represent the accumulated damage in the particle and the equivalent plastic strain in the matrix, respectively. (d) The experimentally observed failure mechanisms across the length scales that are reflected in the numerical predictions (see Fig. 3.4(c)).

the central areas of the RVE towards the boundaries with an angle of $\sim 45^\circ$ following the coalescence of $\sim 45^\circ$ -angled plastic bands. This pattern of failure is also reflected in the cross-scale experimental images in Fig. 3.4(d).

3.4.3 Load partitioning analysis

The load partitioning analysis was conducted based on the validated model of the CSAM Al-46 wt.% Al₂O₃ composite to provide insights into the strengthening mechanisms of the material. Fig. 3.5(a) shows the numerically obtained homogenized stress-strain responses of the composite, the Al matrix, and the Al₂O₃ particles. The experimental data for CSAM pure Al [30] is also plotted as broken (dashed) red lines. Accordingly, the shaded area in red reflects the strengthening effect introduced in the Al matrix of the composite when compared to the pure Al, and the shaded area in black shows the particle strengthening effect. Given the cold spray manufacturing process, the strengthening effect induced in the matrix is attributable to the work hardening mechanism due to the increase in the density of dislocations (i.e., $\Delta\sigma_{Wh} = \alpha M G b \sqrt{\rho}$ [182] where α is the strength coefficient of the dislocation network, M is the Taylor factor, G is the shear modulus, and b is the Burgers vector of Al) and the grain refinement mechanism (i.e., the Hall-Petch (H-P) relationship that reads $\Delta\sigma_{H-P} = Q (d_c^{-0.5} - d_m^{-0.5})$ [183], where Q is a material constant to account for the strengthening effect of grain boundaries, d_c and d_m is the average grain size of the composite and pure Al, respectively) that are induced in the material as a result of high-velocity hard ceramic particles impacting on the Al grains [28, 144]. Here, the Orowan strengthening mechanism was neglected as the average particle size is not less a 1 μm [42]. The strengthening effect from the particles (see the gray area in Fig. 3.5(a)) is also known as the load transfer effect (i.e., $\Delta\sigma_{LT} = 0.5V_p\sigma_m$ [184], where V_p is the particle volume fraction and σ_m is the matrix yield stress), by which the load applied on the composite is transferred from the ductile Al matrix to the hard Al₂O₃ particles through the interfaces. The present load partitioning

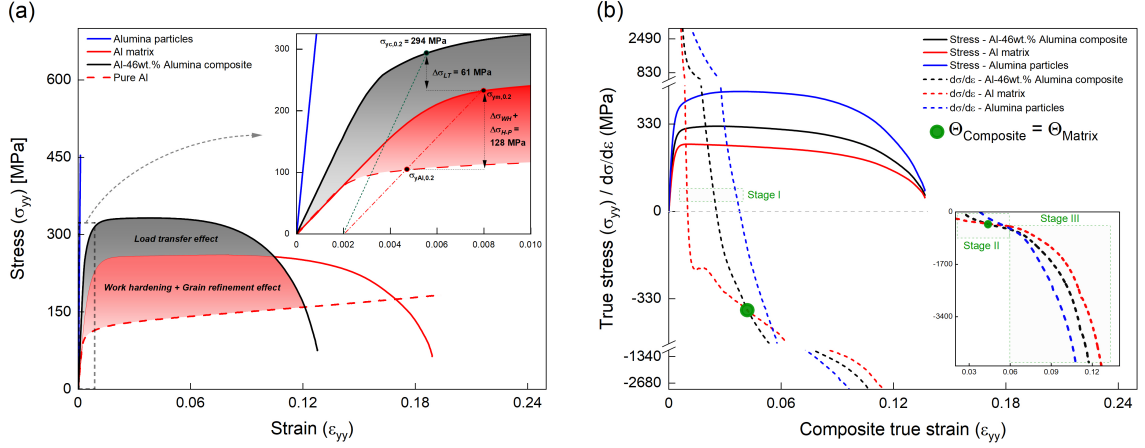


Fig. 3.5: The micromechanical analysis of the strengthening mechanisms of the Al-46 wt.% Al₂O₃ composite under quasi-static uniaxial compression: (a) The load partitioning analysis used to unravel the contribution of strengthening mechanisms. (b) The true stress versus composite true strain curves of the composite and its constituents to analyze the strain hardening rate behavior of the material.

analysis may reveal the contribution of each mechanism as shown in the inset in Fig. 3.5(a): The yield stress of the CSAM composite reinforced with 46 wt.% Al₂O₃ particles is higher than that of the CSAM pure Al by $\sim 180\%$ where the contribution of $(\Delta\sigma_{Wh} + \Delta\sigma_{H-P})$ and $\Delta\sigma_{LT}$ is $\sim 68\%$ and $\sim 32\%$, respectively. For our case, the analytical $\Delta\sigma_{LT}$ [184] leads to a value of 46.6 MPa which is in acceptable agreement with the value of 61 MPa by our micromechanical simulation, which confirms the load partitioning analysis in this study. Fig. 3.5(b) shows the numerically captured true stress ($\bar{\sigma}_{yy}$) history of the composite, the Al matrix, and Al₂O₃ particles versus the true strain ($\bar{\epsilon}_{yy}$) of the composite. To better analyze the post-yielding behavior of the material, the corresponding strain hardening rates (i.e., $\Theta = \frac{d\sigma}{d\epsilon}$) are plotted in dashed curves. As seen, the strain hardening behavior is divided into three regimes, namely stage I, stage II, and stage III. In stage I, the Θ is positive with a descending trend for the composite and its constituents, during which the Al₂O₃ particles possess the highest Θ , and this positively affects the Θ of the composite when compared to the Al matrix. In stage II starting from a strain of $\sim 2.5\%$ to $\sim 6\%$, the Θ of the composite becomes negative indicating the continuous decrease in the load-bearing

capacity. At this stage, the Θ slightly decreases compared to the other stages, and the Θ of ceramic particles keeps positively affecting the Θ of the composite. In stage III starting at a strain of $\sim 6\%$, the Θ of the composite and the constituents follow a sharp decreasing trend up to the elongation at failure, and the Θ of Al_2O_3 particles keeps the lowest throughout this stage which negatively affects the ductility of the composite. The present strain hardening rate analysis reveals that the junction of the composite Θ and the matrix Θ (i.e., $\Theta_{\text{composite}} = \Theta_{\text{matrix}}$ at a strain of $\sim 4\%$) correlates to the initiation of matrix failure, where the particle cracking mechanism exceeds the threshold of 20% (see Fig. 3.4(a) at a strain of 4%). Overall, this analysis shows that the stress-bearing behavior of reinforcing particles plays an important role in the ductility of the composite. While the high strain hardening rate of the hard particles increases the ultimate stress of the composite, it leads to a decrease in the elongation at failure/ductility due to the brittle fracture.

3.4.4 The effect of particle content

The validated model was used to study the effect of Al_2O_3 content on the behavior of the CSAM Al- Al_2O_3 composites under quasi-static uniaxial compression to provide analytical expressions for the mechanical properties and the correlation between the failure mechanisms, and these relationships are applicable for developing micromechanism-based constitutive models. The particle wt.% was changed between 6 wt.% and 46 wt.% with an interval of 10 wt.%. Due to the cold spray process and the hammering effect of the particles, the porosity decreases with the increase in particle content [30]. For the micromechanical model of the composites with different particle wt.%, the corresponding porosity was determined according to the work by Shao et al. [144]. Additionally, the yield stress of the Al matrix increases with the increase in particle content: The greater the particle content the greater work hardening and grain refinement effect are induced in the metallic matrix as discussed in Section 3.4.3. Here, to account for the cold spray-induced strengthening effects into the

matrix in the model, we adopted an inverse method to tune the matrix yield stress as a function of the Al_2O_3 content that will be discussed later in this section. Fig. 3.6(a) shows a waterfall diagram of the predicted stress-strain response and the corresponding history of failure mechanisms of the composite with different particle content. As seen, with the increase in particle wt.%, the strength of the material increases while the elongation at failure decreases, showing the existence of a strength-density trade-off. The strain hardening effect decreases more noticeably when the particle wt.% increases from 36% to 46% which is attributable to the higher growth rate of the failure mechanisms in the latter, particularly for the interfacial failure and particle cracking as shown in Fig. 3.6(b) and (c). From Fig. 3.6(a), the results reveal that the sequence of the activation of failure mechanisms remains the same across different particle wt.% $\geq 16\%$: I. Interfacial failure, II. Particle cracking, and III. Matrix failure. For the composite with 6 wt.% of Al_2O_3 , no particle cracking occurs up to the strain of 20%, while matrix failure is activated, reflecting the existence of a transition in the behavior of failure mechanisms when particle wt.% increases from 6% to 16%. As shown in Fig. 3.6(b) and (c), with the increase in particle content, the debonding and particle mechanisms initiate at a lower strain level and grow faster due to more stress concentration at the matrix/particle boundaries caused by a smaller mean free path parameter (i.e., a higher number of particles) and a more predominant load transfer effect due to a higher volume fraction of particles and a matrix with higher yield stress [72]. Accordingly, the matrix failure is also activated sooner and grows at a higher rate as the particle content increases (see Fig. 3.6(d)). As shown in Supplementary Fig. 3.13, the qualitative pattern of debonding and particle damage initiation and growth show no difference across different particle wt.%. As well, with the increase in particle content, the matrix failure tends to emerge as a primary $\sim 45^\circ$ -angled fracture surface with respect to the compressive loading direction instead of the formation of dispersed cracks. To provide insights into the relationship between the failure mechanisms of the composite with different particle content, the

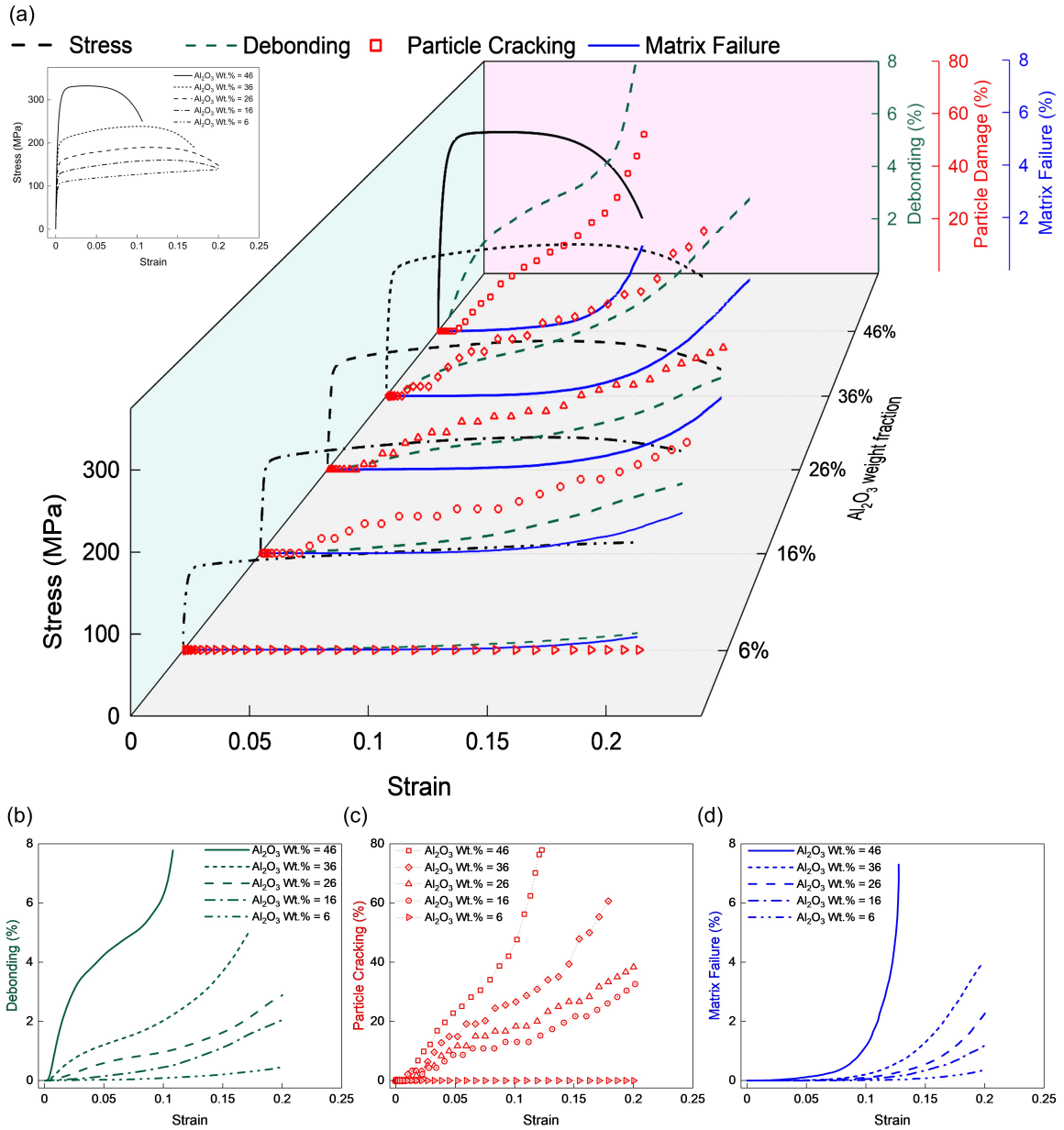


Fig. 3.6: The numerical study of the effect of particle content on the CSAM Al-Al₂O₃ composites under quasi-static uniaxial compression: (a) The waterfall diagram shows the stress-strain curves with the history of failure mechanisms for the composite with different weight fraction of Al₂O₃ particles ranging from 6% to 46% with an increment of 10%. (b-d) The evolution of failure mechanisms in the composite reinforced with different weight fractions of Al₂O₃ particles.

normalized matrix failure (MF^*) as the mechanism with the latest sequence of activation is plotted versus the normalized debonding (DE^*) and the normalized particle cracking (PC^*) for the simulated composites with different particle wt.%, as shown

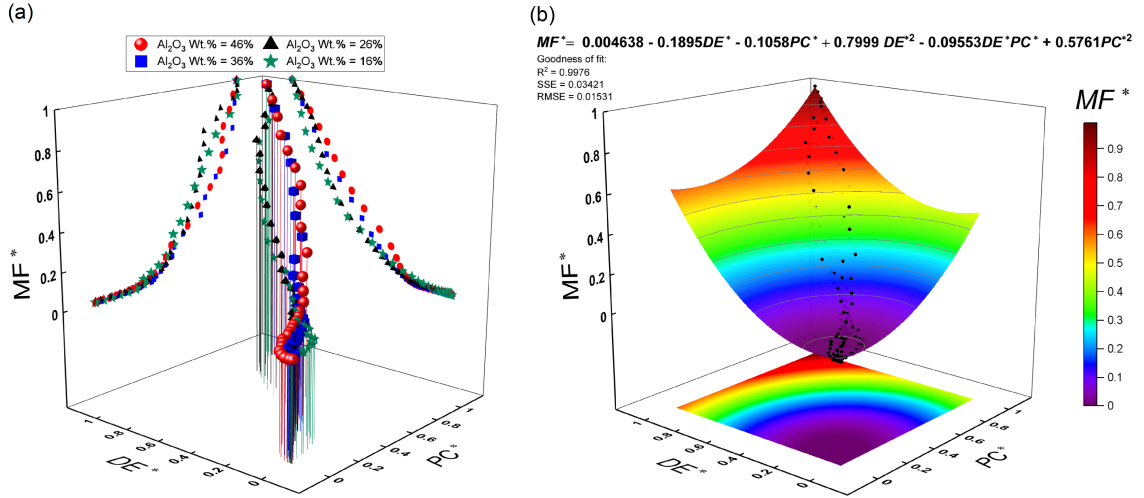


Fig. 3.7: The trajectory of the growth of normalized failure mechanisms of the composite reinforced with different weight fractions of particles. Note that the composite with 6 wt.% Al₂O₃ was excluded due to no particle cracking. The mechanisms were normalized with respect to their maximum value. (b) Surface fitting on the normalized failure mechanism data across different particle weight fractions greater than or equal to 16% through a second-order polynomial function to analytically correlate the mechanisms. Note that the output of the equation needs to be set to zero for DE^* and PC^* less than 0.2 to achieve the highest accuracy.

in Fig. 3.7(a) - the mechanisms were normalized with respect to their corresponding maximum values. As seen, the composites reinforced with different Al₂O₃ wt.% follow a relatively specified growth trajectory, particularly almost identical for 16 wt.% and 26 wt.% as a group and for 36 wt.% and 46 wt.% as another group based on the 2D projected scattered data on MF^*-DE^* and MF^*-PC^* planes. The projected data also shows that the contribution of debonding to the matrix failure increases with the increase in particle content while that of the particle cracking follows a reverse trend. In other words, a certain level of particle cracking results in higher matrix damage in the composites with a smaller particle content, and a certain level of interfacial failure results in higher matrix damage in the composites with a higher particle content. Fig. 3.7(a) reveals that the matrix failure mechanism initiates when the both DE^* and PC^* exceeds ~ 0.2 as a conservative threshold. As shown in Fig. 3.7(b), a second-order polynomial function fits reasonably well (i.e., $R^2 = 0.9976$) the data in Fig. 3.7(a)

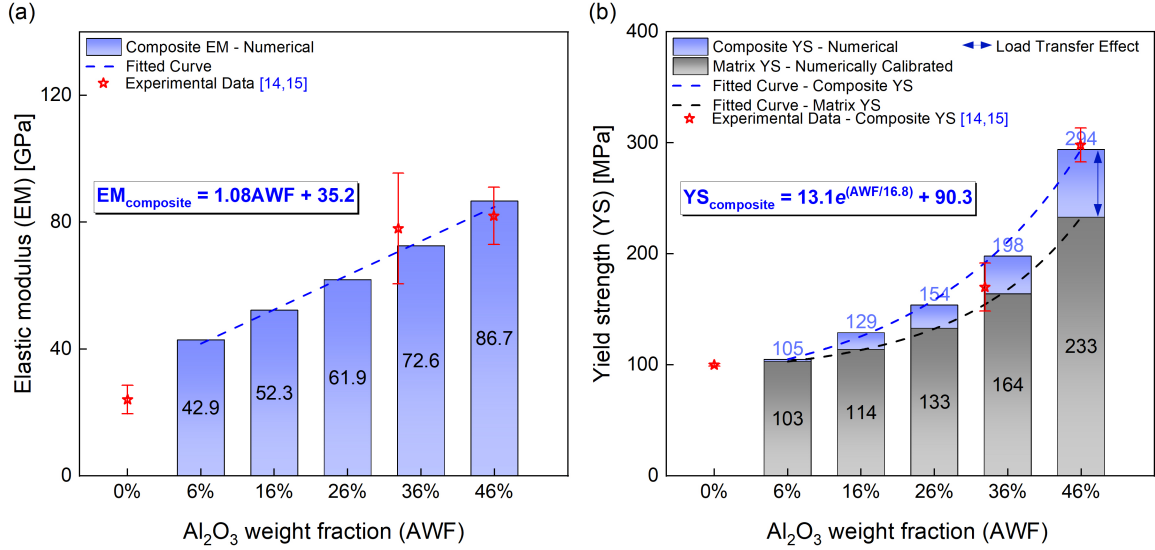


Fig. 3.8: The effect of the particle weight fraction on the mechanical properties of the CSAM Al-Al₂O₃ composite: (a) The variation of the composite Young’s modulus (YS) with the Al₂O₃ wt.% that follows a linear relationship expressed by the dashed fitted line in blue. (b) The variation of the composite yield strength (YS) represented in blue with the Al₂O₃ wt.% that follows an exponential relationship expressed by the dashed fitted curve in blue. The values used for the matrix yield strength depicted in gray were calibrated based on the experimental data [30, 144] to account for the work hardening and grain refinement effect induced in the matrix by high-velocity impacting Al₂O₃ particles during the cold spray process.

that are represented in black points in Fig. 3.7(b) as an analytical descriptor of the relationship between the mechanisms. Note that the provided expression is applicable to the CSAM Al-Al₂O₃ composites with a particle wt.% greater than or equal to 16% under quasi-static compression, and with the inputs (i.e., DE^* and PC^*) higher than 0.2 to achieve the highest accuracy. For values of the inputs, including DE^* and PC^* less than 0.2, the MF^* is set to be zero. The numerically predicted Young’s modulus and the yield strength of the CSAM Al-Al₂O₃ composites with different particle wt.% are compared with those of the available experimental data [30, 144] in Fig. 3.8(a) and (b), respectively. As seen, the numerical Young’s modulus is in agreement with the experimental data, and the model predicts that it increases almost linearly with the increase in the particle content. A linear fit was provided in Fig. 3.8(a) for the analytical description of the elastic modulus of the CSAM composite as a function of

the particle wt.%. In Fig. 3.8(b), the bars in gray represent the tuned values used for the yield strength of the Al matrix at different wt.% of particles to obtain the best match with the available experimental data on the composite yield strength depicted in red stars. This inverse method of calibrating the yield strength of the Al matrix is required to account for the increasing effect of $\Delta\sigma_{Wh}$ and $\Delta\sigma_{H-P}$ with the increase in particle content in the microstructure-based numerical simulations. The difference between the blue bars (i.e., the composite yield strength) and the gray bars could be attributed to the load transfer effect (i.e., $\Delta\sigma_{LT}$) at each particle wt.%. As seen in Fig. 3.8(b), the micromechanical model in this study fills the gap for the unavailable experimental data and this allows developing a fitted exponential function to analytically correlate the yield strength of the CSAM Al-Al₂O₃ composite to the particle content. The analytical expressions developed for the relationships between the failure mechanisms and the mechanical constants will lay the foundation for developing a micromechanism-based constitutive model for CSAM metal-ceramic composites involving the effect of ceramic particle content, and this will be addressed as a future work by the authors.

3.4.5 The effect of stress state

The validated model for the CSAM Al-46 wt.% Al₂O₃ was leveraged to study the effect of stress state on the material response. Fig. 3.9(a) shows the numerically predicted stress-state-dependent stress-strain behavior of the material. As shown, the material ductility observed under uniaxial compression almost vanishes when uniaxial tension is applied, and this result is also confirmed by previous experimental studies on CSAM metal-ceramic composites [116, 140]. As well, the model predicts a lower strength under tension when compared to compression. The predicted brittle response and a lower tensile strength will be discussed later in this section based on the history of the failure mechanisms. The homogenized shear stress-shear strain (i.e., $\bar{\sigma}_{xy} - \bar{\epsilon}_{xy}$) shown in the dash-dot curve in Fig. 3.9(a) represents a lower elastic

slope and flow stress when compared to other stress states which are attributable to the difference between the shear modulus (G) and Young's modulus (E) of the constituent materials (i.e., $G = E/2(1 + \nu)$) of the composite. Additionally, the strain hardening effect under shear appears to be less than that of the compression and this may reflect that the ceramic particles contribute less to the load-bearing capacity of the composite under shear when compared to a compression-dominated stress state. In Fig. 3.9(b) and (c), the evolution of the failure mechanisms of the composite under shear and tension are shown, respectively. The figures show that the failure mechanisms are activated in the same order regardless of the general stress state: I. Interfacial failure, II. Particle cracking, and III. Matrix failure. Under shear, the debonding and particle cracking mechanism is triggered at a shear strain of $\sim 0.35\%$ and $\sim 1\%$, respectively, and subsequently, the post-yielding regime initiates during which the Al matrix plastically deforms. The growth trend of the failure mechanisms under shear is consistent with that of the material under compression described in Section 3.4.2. From Fig. 3.9(b), the matrix failure mechanism starts to grow from zero at a shear strain of $\sim 6\%$, where $\sim 20\%$ of particles are cracked. This threshold of 20% is the same as that of the compression stress state. As shown in Fig. 3.9(c) for the tensile response of the material, the debonding and particle cracking mechanism is activated at a strain of $\sim 0.15\%$ and $\sim 0.35\%$, respectively. The failure behavior of the material is then governed by the particle cracking mechanism, and when particle cracking exceeds $\sim 10\%$ at a strain of $\sim 0.4\%$, the peak stress of 280 MPa is reached, and then the stress-bearing capacity sharply decreases due to the high growth rate of particle cracking. Next, at a strain of $\sim 1.15\%$, where $\sim 60\%$ of particles are cracked, the matrix failure is triggered and governs the failure response of the composite up to the end of loading. During this final stage, the particle cracking mechanism is relatively stabilized and such numerically predicted behavior is in agreement with the experimental study by Yang et al. [72]. Fig. 3.9(d) to (f) compares the failure mechanisms of the composite under different stress states. From Fig. 3.9(d), the

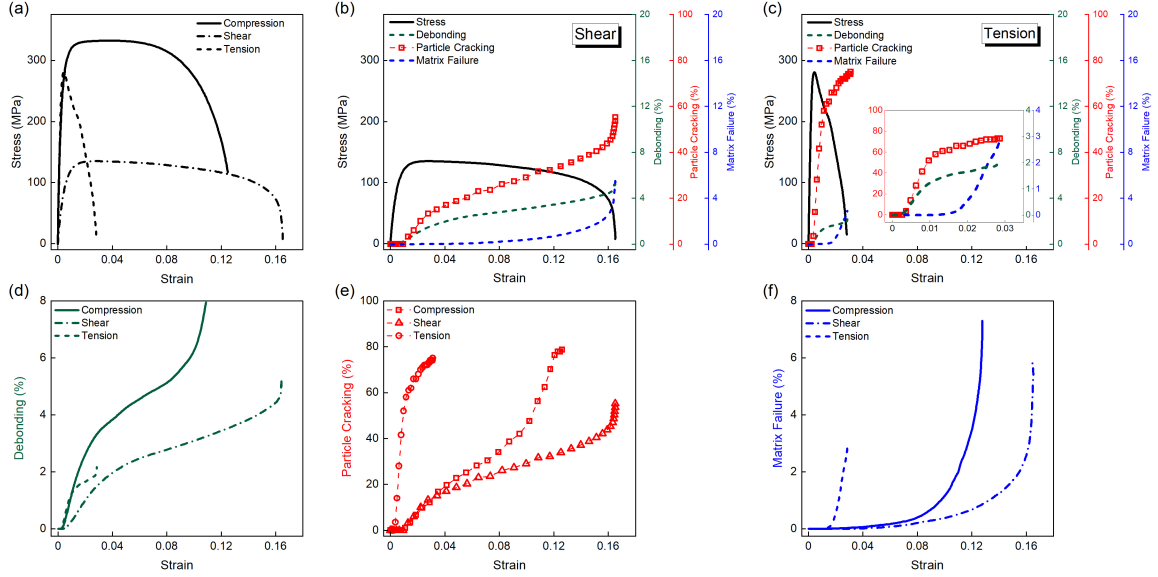


Fig. 3.9: The effect of the stress state, including uniaxial compression, uniaxial tension, and shear on the behavior of the CSAM Al-46 wt.% Al₂O₃ composite under a quasi-static loading rate: (a) The comparison of the stress-state-dependent stress-strain response of the material. (b) The history of failure mechanisms under a shear stress state. (c) The history of failure mechanisms under uniaxial tension. The inset is provided to better show the evolution of the failure mechanisms. (d-f) Comparing the evolution of failure mechanisms in the composite under different stress states.

debonding mechanism is activated at the same strain of $\sim 0.35\%$ for the shear and compression stress states, while it is triggered sooner at a strain of $\sim 0.15\%$ under tension. This is likely to be caused by a higher load transfer effect through the interfaces under tension. The initial growth rate of the debonding mechanism is nearly the same for tension and compression, while it is the slowest under shear. The figure also shows that the debonding mechanism follows the three-staged growth trend – which is governed by the particle cracking mechanism – across different stress states. From Fig. 3.9(e), the particle cracking mechanism is activated at a strain of $\sim 1\%$ for both shear- and compression-dominated stress states, while it starts to grow sooner at a strain of $\sim 0.35\%$. The earlier activation of the particle cracking mechanism along with the interfacial failure under tension leads the composite material to show a tensile strength smaller than compressive strength, as shown in Fig. 3.9(a). Upon activation, the number fraction of cracked particles increases at a remarkably higher

rate (~ 10 times) under tension than compression/shear, and this results in a brittle failure response from the material (see Fig. 3.9(a)). The higher rate of particle cracking in the composite when tension/negative pressure dominates in the ceramic particles could be attributed to the lower tensile strength of ceramic materials than compressive strength, as well as the higher rate of damage growth under tension than compression [185]. These effects are incorporated in the JH2-V model in this study. The weak splat-splat boundaries/interfaces between the Al particles [18, 186] result in the matrix behaving in a brittle manner in as-deposited CSAM metal-ceramic composites under tension. As such phenomena are not incorporated in our continuum-based model, the tensile stress-strain curve in Fig. 3.9(a) may not fully capture the brittle behavior of the material, particularly after a strain of $\sim 1.15\%$ where the matrix failure mechanism is activated. Following the approach by Ma et al. [42], tensile elongation at failure of $\sim 0.4\%$ is determined, and this is consistent with the experimental measurements on CSAM Al-Al₂O₃ composites [50]. As seen in Fig. 3.9(e), for both compression and shear stress states, the particle cracking mechanism follows the same growth pattern at low strains up to $\sim 4\%$. Subsequently, the curves diverge and the particle cracking under shear possesses the lowest quantity to the end of loading compared to other stress states; this may confirm the minimal contribution of reinforcing particles to the stress-bearing capacity of the composite when shear deformation dominates. From Fig. 3.9(d), the matrix failure mechanism is activated when the particle cracking mechanism exceeds $\sim 20\%$ for both compression and shear stress states, and $\sim 60\%$ for tension. These quantities may be used as thresholds/criteria when tailoring the microstructure to increase the ductility of the composite by delaying matrix failure. The figure also shows that the matrix failure possesses the lowest quantity under tension. Accordingly, a stress-state-dependent matrix failure analysis was conducted based on the volumetrically averaged equivalent plastic strain ($\bar{\epsilon}_M^p$), void growth (f^*), and void distortion (D_s) parameters. Note that these parameters were volumetrically averaged based on the homogenization concept [181] (see

Eqs. (3.29) and (3.30)) implemented by Python scripting. Fig. 3.10(a) reveals that the void growth mechanism (f^*) dominantly contributes to the matrix failure when the composite is under tension, while the void distortion/sheeting mechanism (D_s) governs the matrix failure when a global compressive stress state is applied on the composite. Under shear, both the void growth and void distortion mechanisms contribute to the matrix failure, while the latter takes the lead at the final stages of the softening regime. Note that the porosity shown by the dashed curves is not set to zero due to the initial porosity. Fig. 3.10(b) shows the history of the volumetrically averaged equivalent plastic strain ($\bar{\epsilon}_M^p$) in the matrix when the composite is subjected to different stress states. As seen, the volumetrically averaged $\bar{\epsilon}_M^p$ increases nearly linear up to the elongation at failure. The figure also reveals that the plastic deformation is minimally developed in the matrix when the composite is loaded under tension which is likely to be caused by the early activation of the interfacial failure mechanism as well as the dominant role of particle cracking mechanism with a high growth rate, thereby impeding the development of plastic deformation in the matrix. The experimental study by He et al. [187] also confirms the negligible plastic deformation of the matrix of CSAM metal-based composites under tensile loading. Fig. 3.11 shows the qualitative history of failure mechanisms of the composite under tension and shear. Additionally, Supplementary Video S2 and Video S3 show the correlated qualitative and quantitative evolution of failure mechanisms in the material under tension and shear, respectively. As seen, for both stress states, the matrix/particle interfaces fail at the sharpest corners. The interfacial failure primarily propagates along the adjacent faces perpendicular and parallel to the global tensile and shear loading direction, respectively. Under tension, the way that particles bear the transferred load results in developing areas with negative pressure oriented perpendicularly to the loading direction that leads to particle fracture. Similar to the uniaxial compression, the particles are mainly cracked along the loading direction under shear. Under both uniaxial tension and shear, the matrix undergoes plastic deformation in the interstitial areas

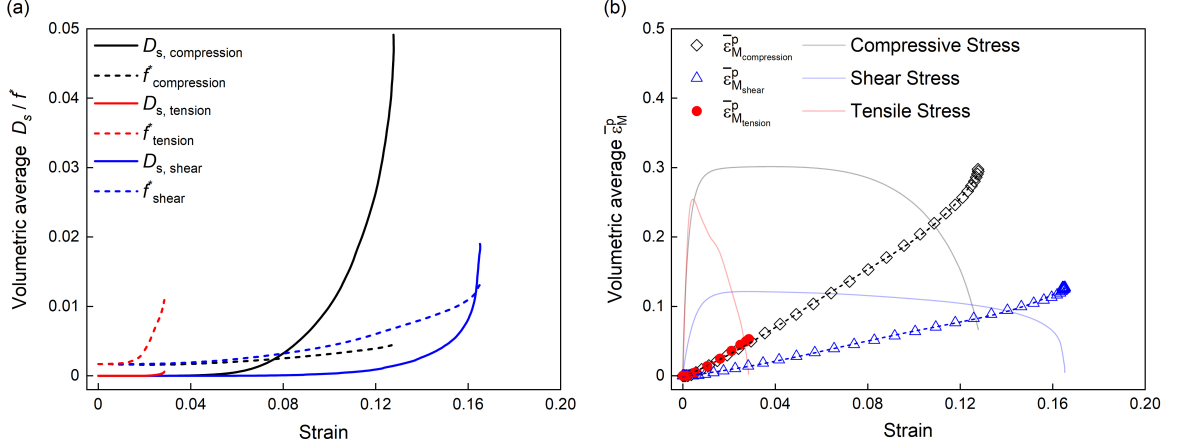


Fig. 3.10: The micromechanical analysis of the stress-state-dependent ductile failure of the Al matrix of the CSAM Al-46 wt.% Al₂O₃ composite under a quasi-static loading rate: (a) The evolution of the volumetrically averaged void growth (f^*) and void distortion (D_s) mechanisms in the Al matrix when the composite is subjected to different stress states. (b) The history of volumetrically averaged equivalent plastic strain ($\bar{\epsilon}_M^p$) accumulation in the Al matrix when the composite is subjected to different stress states. The transparent stress-strain curves of the composite are added to provide a better understanding of the development of plastic deformation in the matrix. Note that all the parameters are volumetrically averaged in the whole domain of the RVE based on the equation $Q_{ave} = \sum_{k=1}^{N_{ip}} Q_k V_k / \sum_{k=1}^{N_{ip}} V_k$, where Q is the value of the intended parameter at each integration point, V_k is the volume of the integration point, and N_{ip} is the total number of integration points in the domain of the RVE.

primarily between the cracked particles due to the regeneration of the stress state, and this shows that the spatial distribution of the fractured particles determines the morphology of the fracture surface. The last row of Fig. 3.11 represents the numerically captured fracture morphology of the material in 3D under tension and shear by visualizing the deleted elements. The matrix cracking depicted in blue first occurs in the vicinity of the cracked particles in gray for both tension and shear similar to that of the compression. The model predicts that the primary fracture surface is perpendicular to the loading direction under tension, and this is in agreement with experiments [50, 116], while it is parallel to the loading direction under shear. And, as previously discussed in Section 3.4.2, the predicted fracture surface is oriented $\sim 45^\circ$ with respect to the compression direction. It could be inferred from the model that the morphology and geometrical features of the fracture surface are determined by

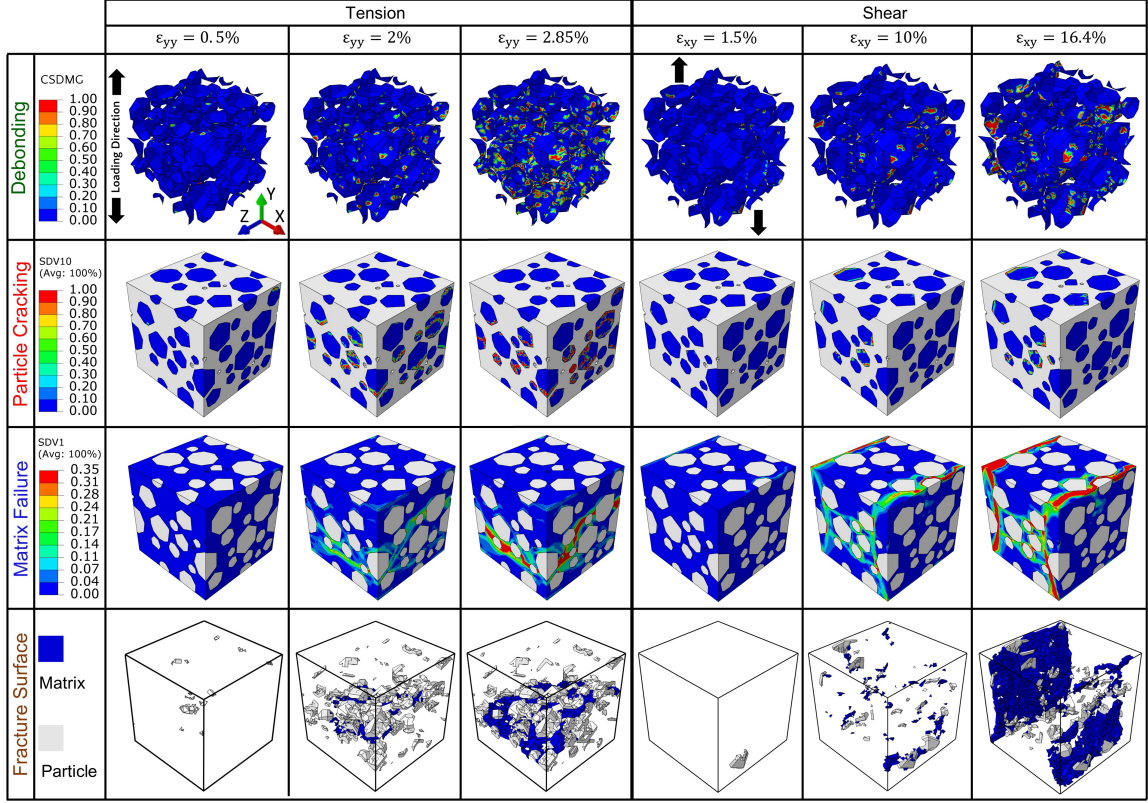


Fig. 3.11: The numerically predicted qualitative history of failure mechanisms of the Al-46 wt.% Al₂O₃ composite under tension and shear at quasi-static loading rate. In the last row, for both stress states, the fracture surface progression was visualized in 3D by the deleted elements of the composite constituents (i.e., the matrix in blue and the Al₂O₃ particles in gray). Note that SDV10 and SDV1 represent the accumulated damage in the particle and the equivalent plastic strain in the matrix, respectively.

the spatial distribution of the cracked particles and the dominant mechanisms (i.e., the void growth (f^*) and void distortion (D_s)) contributing to the matrix failure as discussed in Fig. 3.10 that are governed by the stress state applied on the composite.

3.4.6 The effect of particle size

The experimental study by Munday et al. [32] on CSAM Ni-WC composites showed that the average size of reinforcing ceramic particles in the deposited composite is ~ 6.5 times lower than that of the particles in the feedstock powder when the weight fraction of particles exceeds $\sim 35\%$, and this is a result of particle fragmentation occurring during the cold spray process. In our study, the size of the sieved Al₂O₃

particles varied from $\sim 30 \mu\text{m}$ to $\sim 45 \mu\text{m}$ that led to an average particle size of $\sim 6.5 \mu\text{m}$ (see Fig. 3.1(c)) in the deposited composite, which confirms the observation of Munday et al. [32]. Accordingly, to study the effect of the Al_2O_3 particle size on the behavior of CSAM Al- Al_2O_3 composite by using the present micromechanical model, RVEs of the Al-46 wt.% Al_2O_3 composite with the average particle size of $4.5 \mu\text{m}$ (i.e., an average sieved Al_2O_3 powder size of $\sim 30 \mu\text{m}$), and $8.5 \mu\text{m}$ (i.e., an average sieved Al_2O_3 powder size of $\sim 55 \mu\text{m}$) were produced and subjected to different stress states. Here, the length size of the RVE, the entire numerical setups (e.g., simulation time step, stable time increment, and element size), and mechanical constants of the material models (see Tables 3.1 and 3.2) were preserved among the models; the only variable was the size of the Al_2O_3 particles that was explicitly incorporated into the RVEs. The same methodology was also employed in previous studies [42, 149] to investigate the role of particle size on the response of the composite. Note that the particle size in the models follows the experimental log-normal distribution presented in Fig. 3.1(c) for the three average particle sizes (i.e., $4.5 \mu\text{m}$, $6.5 \mu\text{m}$, and $8.5 \mu\text{m}$). Fig. 3.12 shows the predicted stress-state-dependent stress-strain curves and the corresponding evolution of failure mechanisms of the composite with different average particle sizes. As shown in Fig. 3.12(a-c), the flow stress of the material under compression and the strength under tension slightly increases with the decrease in particle size while the elongation at failure decreases, and no difference is observed in the material strength and flow stress when the shear stress state dominates. These numerical outcomes are explained in the following by the quantified failure mechanisms presented in Fig. 3.12(d-l). As the particle size decreases in the deposited composite, the interfacial failure increases (see Fig. 3.12(d-f)) while less particle cracking occurs (see Fig. 3.12(g-i)), and this interaction of debonding/-particle cracking mechanisms is consistent among different stress states. The higher number of particles in the composite with a smaller average particle size may homogenize the load transferred to the particles and therefore dampens the particle cracking

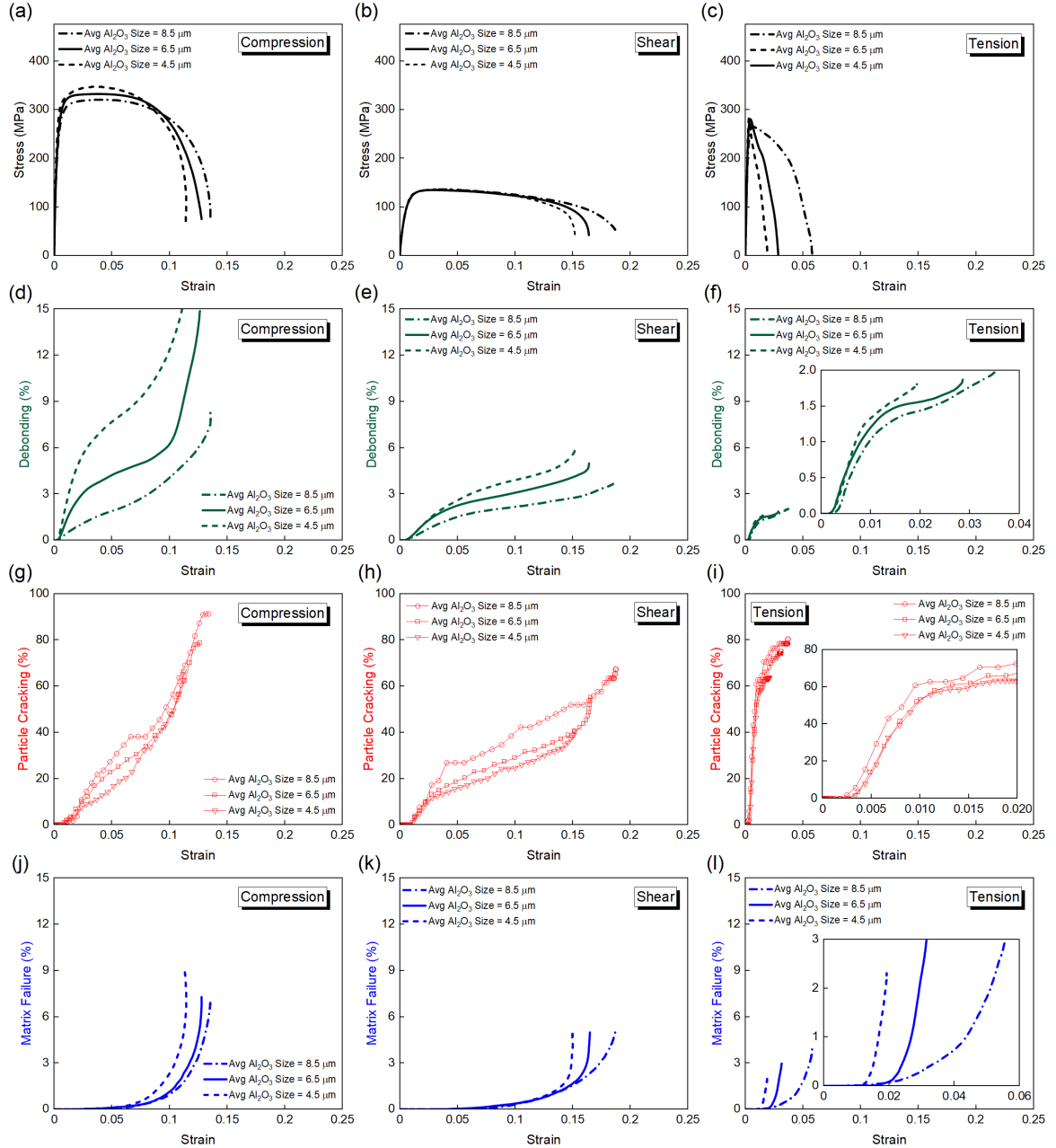


Fig. 3.12: The numerically predicted stress-state-dependent effect of average Al_2O_3 particle size on the behavior of the CSAM Al-46 wt.% Al_2O_3 composite under a quasi-static loading condition: (a-c) The stress-strain responses. (d-f) The quantified history of matrix/particle debonding mechanism. (g-i) The quantified history of particle cracking mechanism. (j-l) The quantified history of matrix ductile failure.

mechanism. Accordingly, stress states with a higher magnitude in quantity are more likely to develop at the interfaces that cause more matrix/particle debonding when the particle size decreases. From Fig. 3.12(g-i), for compression and tension, at the

early stages of activation, the particle cracking mechanism holds smaller quantities and rises with a slower rate in the composite with a smaller average particle size (i.e., a higher particle strengthening effect), and this explains the higher flow stress of the composite under compression and the slightly higher tensile strength of the composite reinforced with smaller Al_2O_3 particles. Under shear (see Fig. 3.12(h)), the particle cracking history follows the same trajectory at the initial stages upon activation in the material with different particle sizes, resulting in no difference in the shear strength (see Fig. 3.12(b)). Additionally, the post-yielding stress-bearing behavior of the material shows no significant difference under shear when the average particle size varies. These observations confirm the stress-state-dependent failure analysis in Section 3.4.5 that the reinforcing ceramic particles contribute minimally to the composite response when a shear-dominated stress state is induced which is likely to be caused by the low load transfer mechanism through the interfaces (see the lower magnitude of debonding under shear in Fig. 3.12(e) when compared to that of compression in Fig. 3.12(d)). As shown in Fig. 3.12(j-l), under different stress states, the matrix failure initiates sooner and grows with a higher rate when the particle size decreases, and this leads to a smaller elongation at failure as seen in stress-strain curves in Fig. 3.12(a-c). The earlier activation and the faster growth of matrix failure in the composite with smaller particle size are attributable to a more dominant interfacial failure (i.e., vanishing load transfer to the particles) and the presence of more localized plastically deformed bands due to the higher number of particles that accelerates the coalescence of micro cracks and formation of the matrix fracture surface (see Supplementary Fig. 3.14).

3.5 Conclusions

In this study, we developed 3D microstructure-informed FE models for the analysis of damage initiation and propagation in CSAM Al- Al_2O_3 composites under quasi-static loading. The Al matrix and reinforcing Al_2O_3 ceramic particles were consti-

tutively modeled by stress-state-dependent material models via the VUMAT subroutines in Abaqus/Explicit. The micro-scale failure mechanisms, including matrix/particle debonding, particle cracking, and matrix ductile failure, were quantified to track the evolution and interaction of the failure mechanisms. The model was validated by using experimental data obtained from CSAM Al-46 wt.% Al₂O₃ composite, both quantitatively (i.e., stress-strain curves) and qualitatively (i.e., failure mechanisms observed in SEM images after testing).

Upon validation, a strain hardening rate (Θ) analysis was conducted and it showed the existence of a critical strain at which $\Theta_{\text{composite}} = \Theta_{\text{matrix}}$, which correlates to the activation of the matrix ductile failure mechanism of the composite under compression. The current quantification framework revealed the sequence of activation of the failure mechanisms of the CSAM Al-46 wt.% Al₂O₃ composite is consistent across different stress states: I. Matrix/particle debonding, II. Particle cracking, and III. Matrix ductile failure. It was also found that the composite material ductility revealed under compression/shear vanishes when tension dominates due to the earlier activation of debonding and a remarkably faster growth rate (10 times) of the particle cracking mechanism that impedes plastic deformation in the matrix. The model was employed to study the effect of particle weight fraction on the compressive behavior of the material. It showed that with the increase in particle content, the debonding and particle cracking mechanisms are initiated earlier and grow faster. This is likely caused by a higher stress concentration at the matrix/particle interfaces due to a smaller mean free path parameter and a more predominant load transfer effect attributable to the higher volume fraction of particles and a matrix with higher yield stress. Accordingly, the matrix failure is also activated sooner and grows at a higher rate as the particle content increases and this leads to a lower elongation at failure. The effect of particle size was studied across different stress states, and it was found that with the decrease in particle size, the compressive flow stress and tensile strength of the composite increases while yielding and flow stress under shear show

no significant difference. This may reflect the minimal contribution of particles to the stress-bearing capacity of the composite when shear dominates. Additionally, as the particle size decreases, fewer particles are cracked while interfacial failure becomes more dominant, and matrix failure is activated earlier and grows faster. The latter is attributable to more debonded interfaces (i.e., less load transferring to the particles) and the facilitated coalescence of localized plastic bands as a result of a higher number of particles, and this causes a lower elongation at failure with the decrease in particle size.

Altogether, the outcomes of this study provide a better understanding of the initiation and competition of the failure mechanisms of CSAM Al-Al₂O₃ composites under different stress states through a systematic quantification framework, which have implications for developing a micromechanism-based constitutive model for the material.

3.6 Acknowledgment

The authors gratefully acknowledge funding support from the Alberta Innovates Graduate Student Scholarship, Imperial Oil (Esso), the Natural Science and Engineering Research Council Canada (NSERC), the Alberta Graduate Excellence Scholarship (AGES), the RR Gilpin Memorial Scholarship, the Canada Foundation for Innovation, the Province of Alberta Ministry of Technology and Innovation.

3.7 Supplementary materials

This section provides the Supplementary Fig. [3.13](#) and Fig. [3.14](#). The links to the [Supplementary Videos](#) are provided in the text.

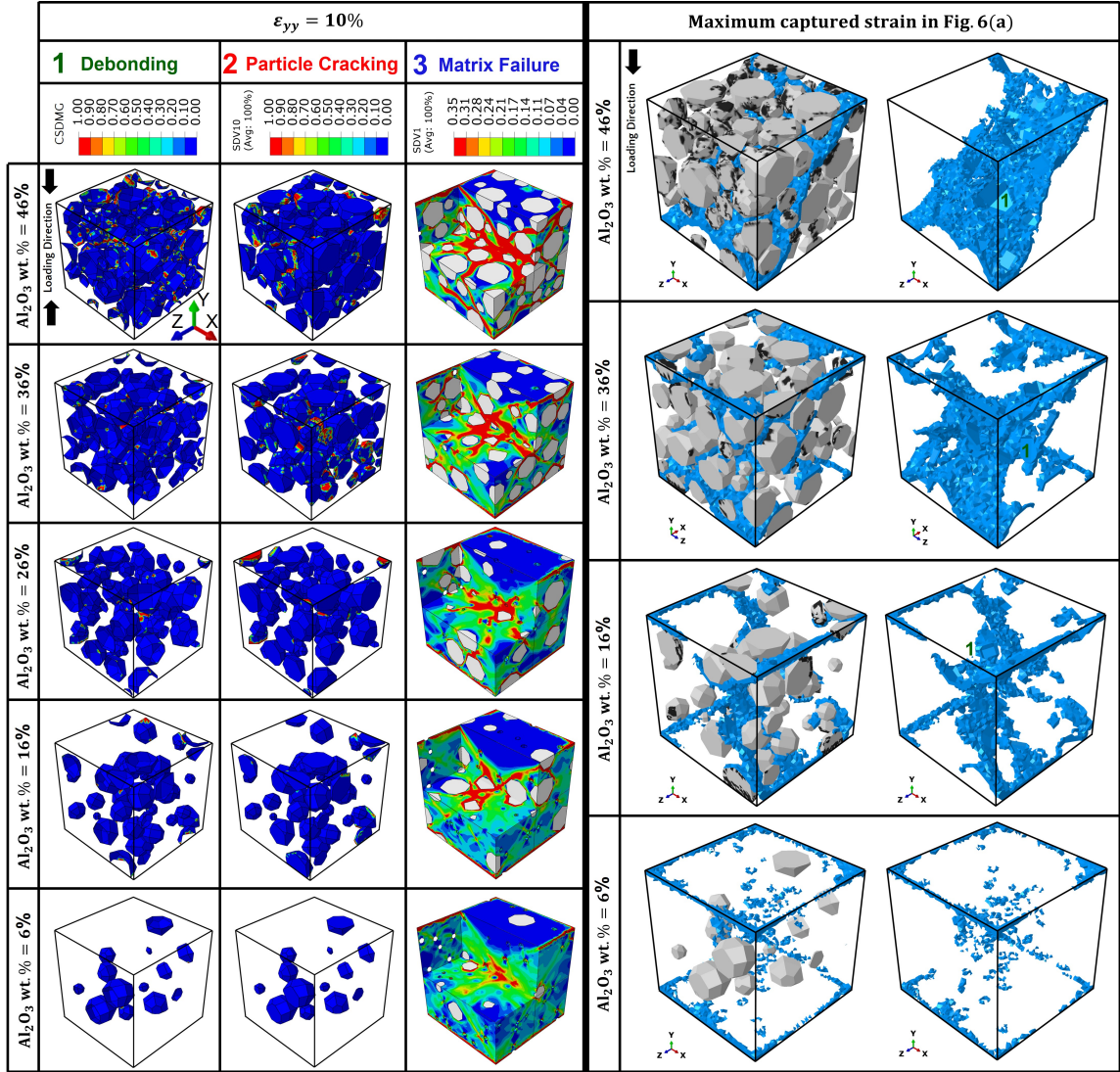


Fig. S 3.13: The predicted qualitative history of failure mechanisms in CSAM Al-Al₂O₃ composites with different weight fraction of Al₂O₃ particles under quasi-static uniaxial compression. The contours are provided at a global uniaxial strain of 10% (see Fig. 3.6(a)). The view-cut representations of the RVEs in the column of “Matrix Failure” show that the higher number of particles in the composite with 46 wt.% of particles leads to an earlier coalescence of plastic bands and the formation of fracture surface shown in blue on the right-hand side images, thereby a smaller elongation at failure when compared to the composites with a lower particle content (see Fig. 3.6(a)). The images numerically captured at the maximum strain show the 3D morphology of fractured areas of the composites via reactivating the deleted elements, where matrix fracture is shown by blue and fractured areas of particles are shown in black. As seen, the fracture surface of the composite under compression makes an angle of $\sim 45^\circ$ with respect to the loading direction. The debonded areas (flat surfaces) are numbered by 1 in green on the matrix fracture surface.

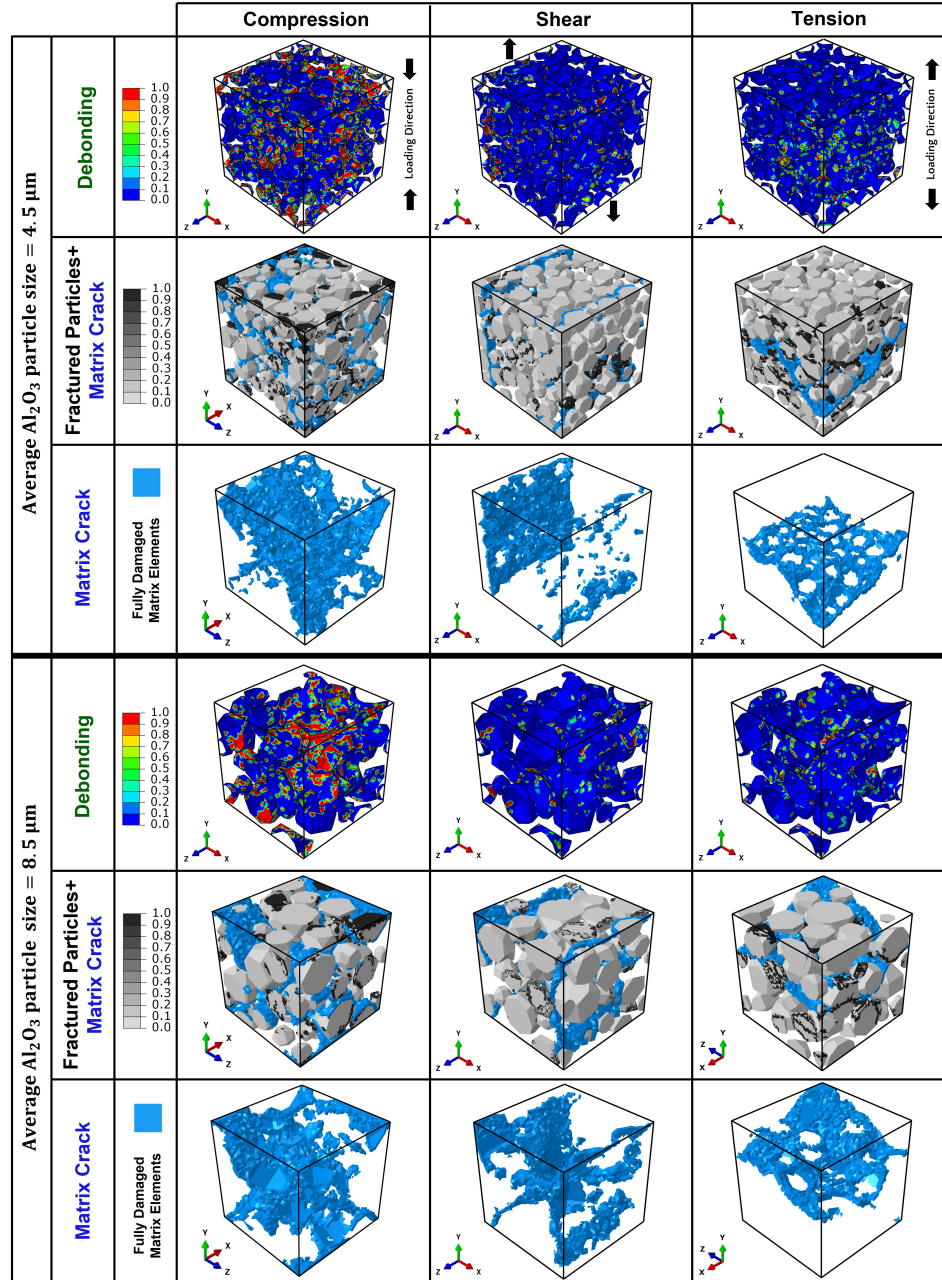
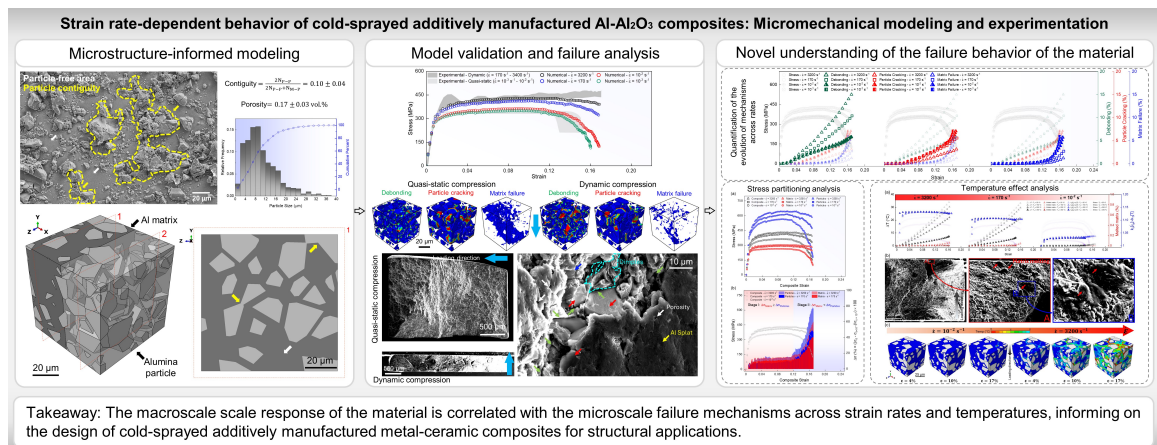


Fig. S 3.14: The visualization of failure mechanisms in CSAM Al-46 wt.% Al_2O_3 composites with different average Al_2O_3 particle sizes under different stress states. For different stress states, the pattern of initiation and propagation of debonding and particle cracking mechanisms show no difference when particle size changes. The fractured areas of the matrix and particles are shown in blue and black, respectively. Under tension, the fracture surface forms perpendicular to the loading direction, while it is parallel to the loading direction when shear dominates. Under compression, the fracture surface makes an angle of $\sim 45^\circ$ with respect to the loading direction. The hollow sections on the matrix fracture surface in blue represent the position of fractured particles located on the fracture surface. Additionally, the flat faces on the matrix fracture surface represent the debonded interface.

Chapter 4

Strain rate-dependent behavior of cold-sprayed additively manufactured Al-Al₂O₃ composites: Micromechanical modeling and experimentation

published as Saman Sayahlatifi, Zahra Zaiemyekheh, Chenwei Shao, André McDonald, and James David Hogan, “Strain rate-dependent behavior of cold-sprayed additively manufactured Al-Al₂O₃ composites: Micromechanical modeling and experimentation”. Published in *Composites Part B: Engineering*, vol. 280, p. 111 479, 2024.



4.1 Abstract

Metal matrix composites (MMCs) fabricated by cold spray additive manufacturing (CSAM) are increasingly gaining attention as structural materials due to their rapid production and scalability. Herein, the failure behavior of CSAM Al-Al₂O₃ composites under quasi-static and dynamic compression was studied by an experimentally informed/validated 3D microstructure-based finite element (FE) model. The debonding mechanism was found to grow at a higher rate consequently dampening the particle cracking mechanism when the strain rate rises to dynamic regimes. The stress-bearing capacity of the particles plays a key role in enhancing the flow stress and elongation at failure of the CSAM composite under high strain rates due to the lower propensity of particle cracking. Eventually, the model was exercised to study the microscale failure progression in the material under elevated temperatures. For the first time in the literature, this study informs on the correlation between the microscale failure mechanisms and the mechanical performance of CSAM MMCs at the macro scale across strain rates and temperatures whose outcomes are applicable to the design of next-generation materials with a tailored performance.

4.2 Introduction

Aluminum matrix composites (AMCs) reinforced by ceramic particles have shown great potential as structural materials in aerospace [188], automotive [189], marine [190], and defense [191] applications due to their superior weight-specific mechanical properties (e.g., exhibiting high wear resistance [192], hardness [30], and fracture toughness [193]). Cold spray additive manufacturing (CSAM) of AMCs is increasing in popularity as it holds promise for the cost-effective, scalable [194], and rapid production of the materials [195] while eliminating solidification-associated undesirable effects (e.g., high porosity, phase transformation, thermal residual tensile stresses, and grain growth/coarsening) [4, 196, 197] by laser-based AM methods [198] or con-

ventional liquid-state fabrication processes [139]. Among many types of functional ceramic particles (e.g., SiC [199], B₄C [200], and TiB₂ [201]), we focus on CSAM AMCs reinforced by micron-sized Al₂O₃ particles as a low-cost and commonly-used structural composite material in various industrial sectors (e.g., landing gears in aerospace and engine blocks in automotive [202, 203]). The expansion in the application of CSAM AMCs as structural materials (e.g., armored vehicles [52] and ballistic application [204]) requires multiscale exploration of the mechanisms that govern the failure behavior of the material under different ranges of strain rates and temperatures which is rarely addressed in the literature on CSAM composites [75], and this is the focus of the present paper.

The strain rate-dependent behavior of conventionally made AMCs reinforced by ceramic particles (e.g., 6061-T6 Al/Al₂O₃ [205], 2024Al-B₄C_p [148], and Al-SiC [206]) under uniaxial tension [207] and compression [208] stress states is experimentally investigated in the literature, where the role of particle size [27], particle volume fraction [209], and initial temperature [210, 211] is accounted for. For example, the study by Marchi et al. [19] on Al-Al₂O₃ composites by gas-pressure infiltration showed that smaller particle size leads to higher flow stress in the composite and lower strain rate sensitivity, while a higher particle content increases both flow stress and strain rate sensitivity. Sun et al. [212] studied the strain rate-dependent behavior of Al-SiC_p composites by vacuum pressure infiltration under elevated temperatures, and it was found that the dynamic compressive behavior of the material tends to converge to that of the Al matrix with the increase in temperature and this leads to a decrease in strengthening effect of the particles. In addition to the role of microstructural features, the competition and contribution of microscale failure mechanisms to the strain rate-dependent behavior of conventionally made AMCs are explored through experimental mechanics in previous studies [38, 204, 213, 214]. In the work by Lee et al. [38] on A356 Al-SiC by liquid pressing process, for example, the failure mechanisms observed in scanning electron microscopy (SEM) images after uniaxial compression

testing were quantified and it showed that the interplay between the mechanisms depends on the interaction of the matrix and particle properties. In contrast to these extensive experimental studies, very limited 3D microstructure-based computational efforts [44] have been made to address the strain rate- and temperature-dependent failure behavior of AMCs, specifically the ones fabricated by more novel approaches such as CSAM, which is the focus of the current work.

Unlike the extensive efforts on the structural failure behavior of conventionally made AMCs [19, 148, 199, 206, 208, 215–217], the performance of CSAM AMCs is widely explored in terms of functional performance (i.e., thermal [39] and electrical [5] characteristics), micro-hardness [28], wear [38] and corrosion [54] resistance concerning their broad range of applications as coating materials. In addition, the quasi-static tensile strength of the CSAM AMCs (e.g., Al-Al₂O₃ [50], Al-SiC [218]) is experimentally investigated in the literature, showing the brittle behavior of the as-sprayed materials due to weak splat/splat and particle/particle interfacial properties [142]. To promote the application of AMCs by CSAM as load-bearing structural materials [219], the failure behavior of the material needs to be explored across strain rates and temperatures through experimentally validated microstructure-informed models that unravel the spatial-temporal evolution of failure mechanisms. To the best of our knowledge, no experimentally verified physics-based computational effort has yet been developed to inform on the contribution and interaction of failure mechanisms of CSAM AMCs – Al-Al₂O₃ in this study – subjected to quasi-static and dynamic loading rates across different temperatures. The novelty and importance of such micromechanical models stem from providing a better understanding of the material failure behavior that informs the design of better-performing CSAM AMCs as emerging structural AM materials with tailored mechanical properties and microstructures.

In the present work, to fill the gap in the understanding of strain rate-dependent progression of failure in CSAM AMCs, experimentally-validated 3D microstructure-based FE models are developed that build on the previous micromechanical FE efforts

on metal matrix composites (MMCs) [42, 61, 62]. To inform and validate the micromechanical model, A1-Al₂O₃ composites were additively manufactured by low-pressure cold spray technology (Section 4.3). 3D RVEs of the CSAM A1-Al₂O₃ composites were generated by Digimat software and informed by the SEM images of the materials in terms of the particle size distribution and weight fraction, particle clustering represented by the contiguity concept [220], irregularity of the particle morphology, and porosity (Section 4.4.1). The Al matrix and brittle Al₂O₃ particles were constitutively modeled by strain rate-dependent material models implemented by the VUMAT subroutines in Abaqus/Explicit FE solver where thermal softening and melting effects were incorporated into the matrix constitutive model (Section 4.4.2). The micromechanical FE model was then validated with the experimental data for quasi-static and dynamic loading rates (i.e., from 10⁻³ s⁻¹ to 3200 s⁻¹) based on the stress-strain curves and failure mechanisms/features observed in post-mortem SEM images (Section 4.5.1 and Section 4.5.2). Once validated, the history of failure mechanisms, including matrix/particle debonding, particle cracking, and matrix failure were quantified by Python scripting to unveil the growth and interaction of mechanisms across strain rates (Section 4.5.3). Next, the model was leveraged to uncover the contribution of matrix and particles to the strain rate-dependent behavior of the CSAM composite by a stress partitioning analysis (Section 4.5.4). Additionally, the effect of particle clustering on the material stress-bearing behavior and evolution of failure mechanisms was addressed (Section 4.5.5). The model was eventually extended to explore the strain rate-dependent failure behavior of the CSAM material under elevated temperatures (i.e., from 25 °C to 350 °C) (Section 4.5.6). Overall, the outcomes of this study provide novel insights into the relationship between the macro-scale mechanical response and the microscale failure mechanisms of CSAM A1-Al₂O₃ composites across strain rates and temperatures applicable to the design of CSAM AMCs with enhanced performance as future AM structural materials.

4.3 Experimental methods

Using a low-pressure (90 psig) cold spray setup (SST series P, CenterLine Ltd., Windsor, ON, Canada), Al-Al₂O₃ composites were additively manufactured in this present study with the air temperature set to be 375 °C. The cold spray setup was equipped with a robotized (Motoman HP-20, Yaskawa Electric Corp., Waukegan, IL, USA) 120 mm long nozzle with an exit diameter of 6.4 mm. The as-received pure Al (99.0%) (CenterLine, Ltd., Windsor, ON, Canada) and pure α -Al₂O₃ (99.5%) (Oerlikon Metco Inc., Westbury, NY, USA) powder was sieved by using 40 μ m and 60 μ m sieves [30]. The size of the sieved powders was measured by an image-based automated particle size analyzer (Morphologi G3, Malvern Panalytical Ltd, Malvern, Worcestershire, UK), showing a size distribution of $\sim 53.3 \pm 4.9 \mu\text{m}$ and $\sim 38.7 \pm 3.9 \mu\text{m}$ for the Al and Al₂O₃ powder, respectively. The particle size distribution of the sieved powders is shown in Supplementary Fig. 4.12. Using Argon as the carrier gas with a pressure of 60 psig, a mixture of the sieved powders comprised of 90 wt.% Al₂O₃ was cold sprayed with a nozzle traverse speed of 15 mm s⁻¹ and a standoff distance of 10 mm on a 5 mm thick pre-roughened 6061 Al substrate, resulting in a bulk deposit with dimensions of 50 mm \times 20 mm \times 4 mm. More details on the CSAM process are found in [30, 144]. Cuboidal specimens with dimensions of 2.3 mm \times 2.7 mm \times 3.5 mm were cut from the as-sprayed bulk deposits by wire electrical discharge machining, and these were used for experimental investigations into the strain rate-dependent failure behavior of the material in this paper. The specimens were subjected to uniaxial compression along the 3.5 mm long dimension under quasi-static loading rates (i.e., 10⁻³ s⁻¹ to 10⁻² s⁻¹) using a standard MTS series 810 servo-hydraulic machine, and dynamic loading rates (i.e., 170 s⁻¹ to 3200 s⁻¹) by using a split-Hopkinson Pressure Bar (SHPB) setup at room temperature. Extreme pressure grease was applied on the interface between the platens/bars and specimen to reduce friction and allow free lateral expansion. Complete details on the testing setups are found in the work

by Li et al. [221]. The MTS and SHPB apparatus was equipped with a high-speed AOS PROMON U750 camera and an ultra-high-speed Shimadzu HPV-X2 camera, respectively, to capture the deformation/failure history and full-field strain fields by the digital image correlation (DIC) technique. The DIC analysis was conducted by using VIC-2D (v6 2018) software to visualize the contour of strain fields and calculate averaged strain histories for plotting stress-strain responses. The microstructure of as-sprayed CSAM Al-Al₂O₃ composites was characterized via a field-emission SEM coupled with energy-dispersive x-ray spectroscopy (EDS) operated at 20 kV (Zeiss Sigma, Oberkochen, Baden-Württemberg, Germany). The EDS analysis revealed the presence of reinforcing Al₂O₃ particles with a 46 ± 2.04 wt.% in the CSAM Al-Al₂O₃ deposits, and the porosity was measured to be 0.17 ± 0.03 vol.% by using ImagePro software and the SEM images.

4.4 Micromechanical modeling

4.4.1 RVE reconstruction and numerical setups

By using Digimat software, RVEs of the CSAM Al-46 wt.% Al₂O₃ composites were generated accounting for the particle content, particle size distribution, particle clustering, and irregular geometries observed in the SEM images. As shown in Fig. 4.1(a) inside the yellow dashed arrows, clusters of Al₂O₃ particles are formed within the microstructure of the composite due to the cold spray process [222]. Here, the contiguity concept (i.e., the percentage of particle-particle boundaries) [220] was used to measure the clustering of particles to be incorporated into the RVEs. Accordingly, as formulated in Fig. 4.1(b), the linear intercept method [220] was conducted by using ImageJ software and SEM/EDS images that led to a contiguity parameter of 0.10 ± 0.04 . The size distribution of particles was also analyzed by the ImageJ software to follow a log-normal distribution with 90% of particles smaller than 18 μm (i.e., $D_{90} = 18 \mu\text{m}$), as shown in Fig. 4.1(b). Next, the geometry of particles was gen-

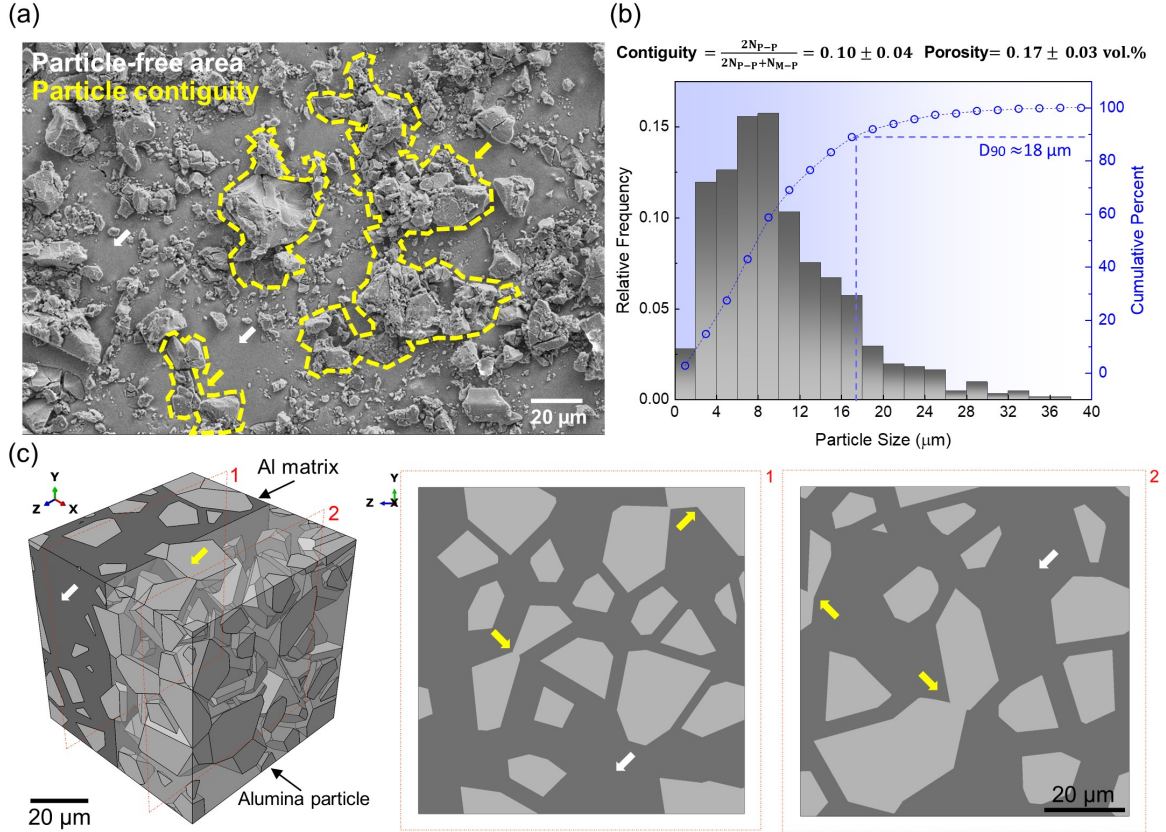


Fig. 4.1: Microstructure-informed RVE generation of the CSAM Al-Al₂O₃ composites: (a) SEM image of the CSAM Al-46 wt.% Al₂O₃ composite before testing. (b) Characterization of the composite microstructure in terms of particle size distribution, particle contiguity, and porosity. (c) A random RVE realization with a length size of 80 microns of the CSAM Al-46 wt.% Al₂O₃ composite for micromechanical FE simulations. Note that the white and yellow arrow refers to the particle-free areas and particle contiguity (clustering) in the material microstructure and the reconstructed RVE.

erated by leveraging the Voronoi tessellation algorithm [161] for cemented carbides in Digimat software, where the particle wt.% (i.e., 46 wt.%), the histogram of particle size distribution up to D₉₀ (see Fig. 4.1(b)), and the measured contiguity parameter were the inputs. Fig. 4.1(c) shows the reconstructed RVE with 225 randomly distributed and 3D oriented grain-shaped (i.e., low polyhedron morphology) particles that acceptably represent the irregularly shaped Al₂O₃ particles in the SEM images (see Fig. 4.1(a)) particles that reasonably reproduces the experimentally-observed microstructural features, including particle clustering and the existence of particle-free

areas (see Fig. 4.1(a)); these particle-free areas are mainly attributed to severely deformed Al particles (i.e., splats) upon the ballistic impingement on the as-deposited layer [143]. Informed by the literature [42, 75], a length size of 80 μm was selected for the RVEs which is more than 8 times higher than the average measured particle size. To reduce the computational cost, the measured initial average porosity of 0.17 vol.% was incorporated into the micromechanism-based constitutive model of the Al matrix [64] rather than an explicit geometrical representation in the RVE. To produce the RVE in Abaqus/CAE with a high-quality mesh and mitigate the run-time, a Python script was first developed to modify the small edges (i.e., less than 1 μm in this study) of the as-imported polyhedron-shaped particles generated by Digimat, and then the matrix was produced by Boolean operation. Based on previous studies [27], the strength and interfacial properties of reinforcing particles proportionate to the inverse square root of their equivalent diameter (i.e., $\sigma \propto \frac{1}{\sqrt{d}}$). A Python script was developed by which the equivalent diameter of each particle (225 particles in total) was calculated based on the volume and then the corresponding hydrostatic tensile strength and interfacial strengths were assigned based on the equivalent diameter histogram and size-dependent property curves (i.e., the blue and red symbolic data points for tensile strength and interfacial strengths, respectively), as shown in Fig. 4.2(a). The RVE was loaded under uniaxial compression by a mixed static-kinematic boundary condition (see Fig. 4.2(b)). As seen, the Y-direction degree of freedom (DOF) of the top and bottom surfaces of the RVE was coupled with that of the corresponding reference points (i.e., red-colored RP-1 and RP-2, respectively) by defining equations, while the Y-direction DOF of RP-2 was restricted, and the lateral surfaces were left unconstrained. To avoid rigid body motions, DOFs of the two corners of the bottom surface, namely P1 and P2 were restricted as shown in Fig. 4.2(b). To induce a constant strain rate throughout loading, a displacement history along the negative Y direction was applied to the RP-1 (see the red arrow on RP-1 in Fig. 4.2(b)) via a tabular amplitude which was defined as $U_{Y, RP-1}(t) = L_0 \dot{\epsilon} t / (1 + \dot{\epsilon} t)$, where L_0 ,

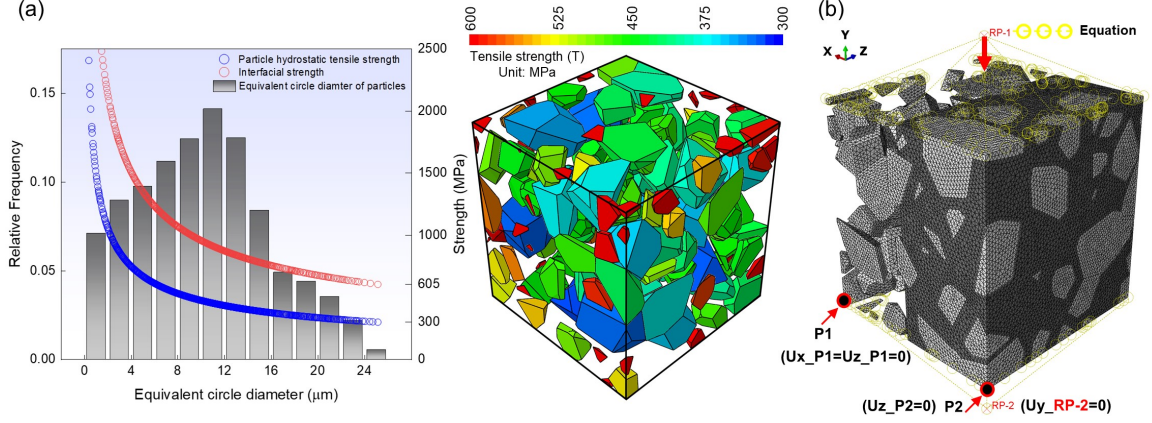


Fig. 4.2: The micromechanical FE model setups: (a) Particle-size-dependent distribution of mechanical properties assigned to the hydrostatic tensile strength of the Al_2O_3 particles and the matrix/particle interfacial strength. (b) Mixed-kinematic boundary condition applied on the meshed RVE model of the CSAM Al-46 wt.% Al_2O_3 composite in Abaqus/Explicit. Here, the Al matrix in gray is half-cut to better show the spatial distribution of particles inside.

$\dot{\epsilon}$, and t represents the initial length of the RVE, the experimentally measured strain rate, and time, respectively. Here, to alleviate the computational cost, the RVE was compressed up to a nominal axial strain of 20% and this led to a simulation step time of 250 s, 25 s, 1.47×10^{-3} s, and 7.81×10^{-5} s for the experimental strain rates of 10^{-3} s^{-1} , 10^{-2} s^{-1} , 170 s^{-1} , and 3200 s^{-1} , respectively. The original stable time of the micromechanical model was found to be in the order of 10^{-12} s, which was mass-scaled to be in the order of 10^{-6} s for all the strain rates to avoid artificial effects concerning the strain rate-dependent constitutive models. The history of the internal energy (ALLIE) and the kinetic energy (ALLKE) of the model is shown in Supplementary Fig. 4.13(a) to demonstrate that the condition required for quasi-static loading rates is met (i.e., $\text{ALLKE}/\text{ALLIE} \leq 10\%$ [91]). Both the Al matrix and particles were discretized with 10-node modified quadratic tetrahedron (C3D10M) elements. Following a mesh convergence study (see Supplementary Fig. 4.13(b)), an element size of $2 \mu\text{m}$ was selected that compromised between the runtime and accuracy in terms of stress-strain curves (see Supplementary Fig. 4.13(c)). The reliability of the model was ensured in terms of the effect of randomness in RVE generation on the predicted

stress-strain responses, as shown in Supplementary Fig. 4.14. The micromechanical models were run via parallel computing on the Digital Research Alliance of Canada supercomputers with an average runtime of ~ 60 hours and ~ 35 hours for quasi-static (i.e., $\dot{\epsilon} = 10^{-2} \text{ s}^{-1}$) and dynamic (i.e., $\dot{\epsilon} = 3200 \text{ s}^{-1}$) loading conditions, respectively, by using 80 cores (Intel Gold 6148 Skylake @ 2.4 GHz).

4.4.2 Constitutive modeling of materials/interfaces

The Al matrix of the CSAM Al-Al₂O₃ composites presents a highly distorted and complex polycrystalline structure in which zones of ultra-fine grains are embedded inside micron-sized grains [144, 223]. In addition, the current CSAM Al-46 wt.% Al₂O₃ composites include a considerable number of coarse Al₂O₃ particles and large clusters which interfere with the signal acquisition of electron backscatter diffraction (EBSD) data required for capturing the Euler angles of grains as inputs for crystal plasticity models [224]. Accordingly, the Al matrix of the current CSAM Al-46 wt.% Al₂O₃ composites was modeled as a continuum (see Fig. 4.2(b)) with a stress state-dependent ductile failure model (i.e., the Zhou et al. model [64]) in which strain rate and thermal softening effects were incorporated in the current paper. In the Zhou model [64], the ductile failure under tension-dominated stress states is accounted for by void initiation and growth mechanism, and failure progression under compression- and shear-dominated stress states is incorporated by void distortion and shear damage growth. The state of stress is defined at the integration points of elements by the stress triaxiality and Lode angle parameters. The enhanced Zhou model and the constants used in the current study are described in detail in the Supplementary materials (see Section 4.8.1). Note that the inter-splat failure mechanism in the Al matrix is not explicitly incorporated into the model as the microstructure of the Al matrix of the CSAM Al-46 wt.% Al₂O₃ composite is simplified as a homogeneous continuum. However, the inter-splat failure mechanism primarily occurs under tension-dominated stress states due to the weak mechanical interlocking between the Al particles rather

than metallurgical bonding [142, 225]. Upon the emergence of inter-splat failure, the porosity in the Al matrix increases, and such effect is implicitly accounted for in the Zhou model by the void initiation and growth mechanism under tension-dominated stress states (see f^* in Section 4.8.1). The Al_2O_3 particles were constitutively modeled by a viscosity-regularized plasticity model for brittle materials (i.e., the JH2-V model [65]) that accounts for the strain rate-dependent spallation of ceramics and the asymmetry in damage behavior under tension and compression [156]. Surface-based cohesive zone modeling (CZM) approach with a bi-linear traction-separation law was used to model the matrix/particle interfaces, and the particle/particle interfaces were defined by a hard kinematic contact with a coefficient of friction set to be 0.01 due to the weak bonding of clustered hard ceramic particles [141] by the CSAM process which induces ceramic particle rebound or fragmentation upon high-velocity particle/particle impact rather than mechanical interlocking [143, 226]. The CZM constants used for the particle/matrix interfaces are given in Table 4.3 in the Supplementary materials. The interfacial strengths are exclusively assigned to each particle/matrix interface based on the equivalent circle diameter of the particle as discussed in Section 4.4.1 and Fig. 4.2(a). Note that the minimum value of 605 MPa in Fig. 4.2(a) for the interfacial strengths was tuned to obtain the best match with the experimental stress-strain curves following a trial-and-error process. This value is in agreement with the range of previously reported interfacial strength of AMCs in the literature [43]. In this study, the Zhou et al. model [64] and the JH2-V model [65] were implemented by VUMAT subroutines in the Abaqus/Explicit FE solver. The complete details of the constitutive models and the CZM approach with the corresponding material constants used in this study are provided in the Supplementary materials.

4.5 Results and discussion

4.5.1 Micromechanical model validation

Fig. 4.3(a) compares the predicted stress-strain responses (i.e., the circular symbolic data points) with those of the experiments (i.e., the shaded gray areas accounting for all the conducted tests) for the CSAM Al-46 wt.% Al₂O₃ composites under quasi-static and dynamic loading rates. Note that the numerical stress-strain data points are calculated by the homogenization approach [181] over the whole domain of the RVE. As shown, for all the strain rates, the numerical response acceptably agrees with that of the experiments in terms of elastic response, yielding point, and strain hardening behavior. The experimental stress-strain response under the strain rate of 3200 s⁻¹ (i.e., the upper bound of the shaded area for dynamic loading) exhibits oscillations likely to be caused by stress wave reflections that dominate the equilibrium condition at the earlier stages of loading. Such an effect is not reflected by the model due to proper tuning of the numerical solution time increment that guarantees the presence of equilibrium from the beginning. The model also reasonably replicates the softening behavior of the material under quasi-static strain rates (see the green and red curves upon strain of $\sim 12\%$ in Fig. 4.3(a)). Under dynamic loading, however, the micromechanical model predictions more noticeably deviate from the experimental responses when a strain of $\sim 12\%$ is exceeded. When the material is dynamically compressed, the cracked areas due to the formation of microcracks (see Fig. 4.3(b), the third row, and the shear cracks by dashed yellow lines) of the specimen may come in contact as a result of the short duration of the loading process (i.e., $\sim 100 \mu\text{s}$) and this results in an increasing stress-bearing capacity. In addition, as evidenced by the time-resolved images of dynamic loading in Fig. 4.3(b), the specimen undergoes a barreling effect under dynamic loading which amplifies the strain hardening behavior under dynamic compression [13]. These are the macro scale phenomena that are not present in the microscale model, leading to the difference between the micromechan-

ically predicted and macro scale experimental softening regime of behavior on the stress-strain responses in Fig. 4.3(a) under dynamic loading. In addition, compared to the experimental stress-strain curves, the earlier initiation of the softening regime following a gradual trend in the numerical stress-strain curves is also attributable to the boundary conditions of the micromechanical model that may not fully represent those of the experiments at the macroscale. Similar differences between the macroscale experimental stress-strain curves and those of a micromechanical model are also reported in the published literature on particle reinforced MMCs [42, 61]. In Fig. 4.3(b), the macro-scale deformation history and evolving axial strain contours (ϵ_{yy}) captured by the DIC analysis are correlated with those at the microscale by the current model under quasi-static and dynamic loading. The DIC analysis shows that the strain field localizes in a $\sim 45^\circ$ slip band initiating from the corners with respect to the loading direction under quasi-static strain rates which leads to the shear failure (shown by dashed yellow lines in Fig. 4.3(a)) of the CSAM composite specimen at an elongation between 13% and 15%. On the contrary, under dynamic loading, the material accommodates deformation more diffusely (see the DIC strain contours at the strain of 12% for strain rates of 10^{-2} s^{-1} and 3200 s^{-1} in Fig. 4.3(b)) that delays the initiation of failure and also allows the propagation of multiple shear cracks when compared to the quasi-static condition. As the micromechanical model shows in Fig. 4.3(b), the heterogeneity of the microstructure induces a complex strain field in the Al matrix that involves both tension-dominated (i.e., areas in purple) and compression-dominated (i.e., areas in red) regions. As the strain exceeds 6%, the clustered particles are found to be debonded (yellow arrows) which results in porosity (i.e., yellow circles), and this facilitates the initiation/coalescence of shear failure (yellow dashed line) in the matrix as the composite is strained to 12%. Here, particle cracking (black arrow) is observed under the quasi-static strain rate in contrast to the strain rate of 3200 s^{-1} . With the increase in strain from 12% to 17%, under quasi-static loading, the primary shear crack highlighted by the yellow dashed line

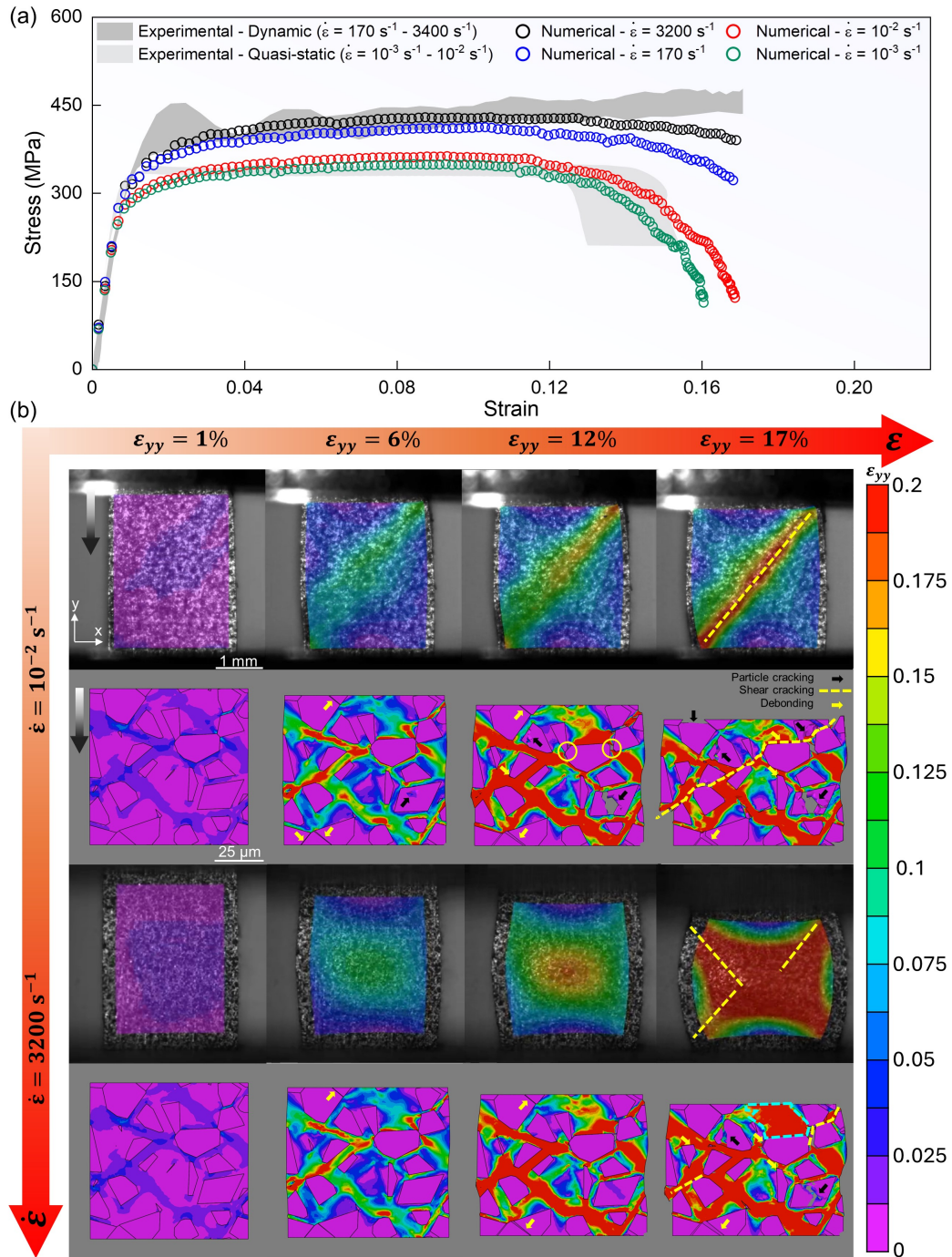


Fig. 4.3: Validation of the micromechanical model:(a) Quantitative validation of the model in comparison with the experimental stress-strain responses of CSAM Al-46 wt.% Al₂O₃ composites across quasi-static and dynamic loading rates. (b) Macro scale deformation pattern/failure and axial strain evolution ϵ_{yy} in the composite under quasi-static and dynamic loading conditions in correlation with those of the model at the microscale. Note that the numerical strain colormap is set to be the same as that of the DIC analysis for the sake of comparison.

emerges primarily due to the coalescence of shear cracks in the matrix starting in the thin ligaments at the corners and matrix/particle debonding. In addition, along the shear path at the strain of 17% under quasi-static loading, some Al_2O_3 particles are observed that are damaged as a result of coming in contact due to sliding in the deformable Al matrix, thereby contributing to the formation of the $\sim 45^\circ$ micro-crack that is also reflected in the macro scale experiments. Regarding the dynamic strain fields at the strain of 17%, the micromechanical model also confirms the diffusive DIC pattern (e.g., see the teal-colored dashed area in the RVE model) and less localization of failure under dynamic loading. The effect of strain rate on the stress-bearing behavior of the CSAM composite will be further discussed in terms of the quantitative evolution of failure mechanisms and a stress-partitioning analysis in Section 4.5.3 and Section 4.5.4.

4.5.2 Post-mortem SEM fractography

Fig. 4.4(a) shows the fracture surface of the CSAM Al-46 wt.% Al_2O_3 composite under quasi-static loading (i.e., strain rate of 10^{-2} s^{-1}) that is $\sim 45^\circ$ -angled from the axial compression direction. As shown in the red and blue boxes A and B, respectively, the fracture surface demonstrates two distinctive features distinguishable by the surface roughness. Based on the magnified views of the rough region in the red box shown in Fig. 4.4(b), matrix failure is predominantly caused by splat/splat debonding (i.e., the flat darker areas annotated by the yellow arrow that include porosity) due to weak mechanical interlocking in the as-sprayed deposit [225]. As shown by the micromechanical model in Fig. 4.3(b), the microstructural heterogeneity of the CSAM composite induces tension-dominated stress states in the Al matrix which triggers the splat/splat debonding mechanism as a brittle mode of failure. Shallow dimple-like features (i.e., the dashed teal-colored arrow) and particle sliding traces (blue arrows) are scarcely observed on the rough portion of the fracture surface and the scarcity of these ductile failure-associated characteristics confirms the low plastic deformation of

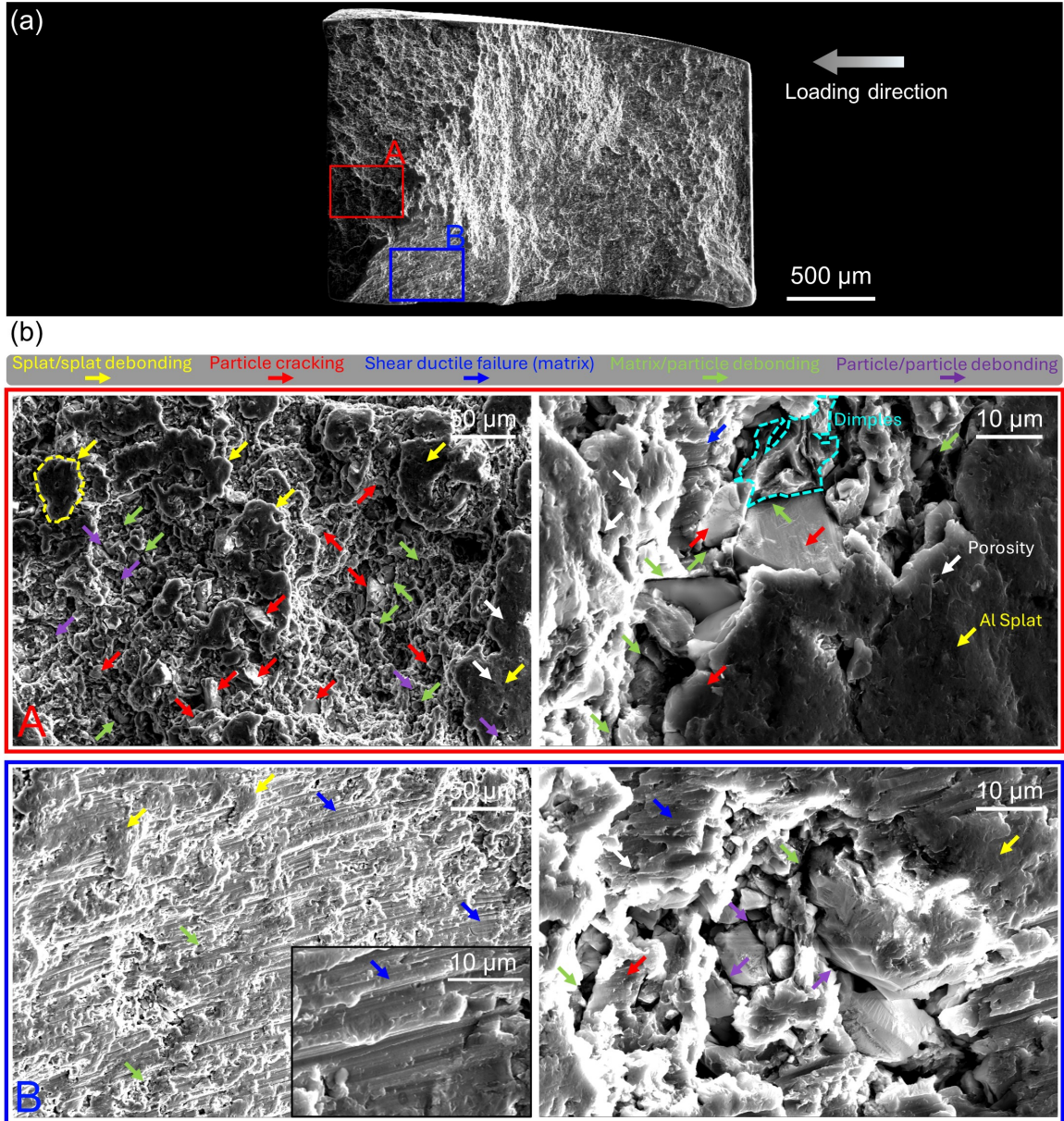


Fig. 4.4: Fractures surface morphology of the CSAM Al-46 wt.% Al_2O_3 composite under quasi-static uniaxial compression: (a) SEM image of the full-scale fracture surface of the specimen, (b) Magnified views of the features observable on the full-scale fracture surface shown in boxes A and B.

the Al matrix in these areas. Particle cracking manifested by cleavage facets and river patterns (red arrows) is frequently observed in the rough area which is attributable to the dominant brittle failure of the matrix (i.e., inter-splat failure) [227, 228] that leads to more load to be sustained by the Al_2O_3 particles. In addition, interfacial failure

at the matrix/particle (green arrow) and particle/particle (purple arrow) interfaces are commonly detectable on the rough fracture surface likely caused by the weak interfacial properties as a result of mechanical interlocking rather than metallurgical bonding [142]. Unlike that of the rough areas, as shown in Fig. 4.4(b) in the blue box, the Al matrix primarily fails due to shear distortion caused by particle sliding (i.e., grooves annotated by blue arrows in the inset) in the smoother areas of the fracture surface. Accordingly, less particle cracking is observed in such areas when compared to the rough areas since the load is mainly accommodated by the plastic deformation and shear failure of the matrix accompanied by interfacial failure. Fig. 4.5(a) shows that the CSAM composite is compressed to $\sim 750 \mu\text{m}$ from the initial length of $3.5 \mu\text{m}$ under dynamic loading without being shattered which demonstrates a great potential for applications requiring energy absorbing capabilities (e.g., impact events [52, 204]). Unlike quasi-static conditions, multiple microcracks, including $\sim 45^\circ$ -tilted shear cracks and nearly axial cracks are propagated in the material as strain localization is impeded under dynamic compression and induces more deformability in the Al matrix by adiabatic heating [229]. According to ultra-high-speed imaging (see Fig. 4.3), the axial cracks are thought to be initiated and grow after the propagation of shear cracks by which the structural integrity of the specimen deteriorates. High-magnification SEM images of the fracture surfaces on the shear (i.e., the area in the red box named A) and axial (i.e., the area in the blue box named B) crack paths are shown in Fig. 4.5(b). As seen, a combination of splat/splat debonding (i.e., brittle failure mode) and shear failure promoted by particle sliding contributes to the matrix failure on the shear crack path. Additionally, interfacial failure mainly manifested by particle pull-out is observed to be a predominant contributor to the initiation and growth of shear failure under dynamic compression, and this could be attributed to the reverberation of stress waves under high-strain rate loading that induces tension at the matrix/particle interfaces [230]. Accordingly, the failure of interfaces degrades the load transfer mechanism [184] and decreases particle cracking probability when

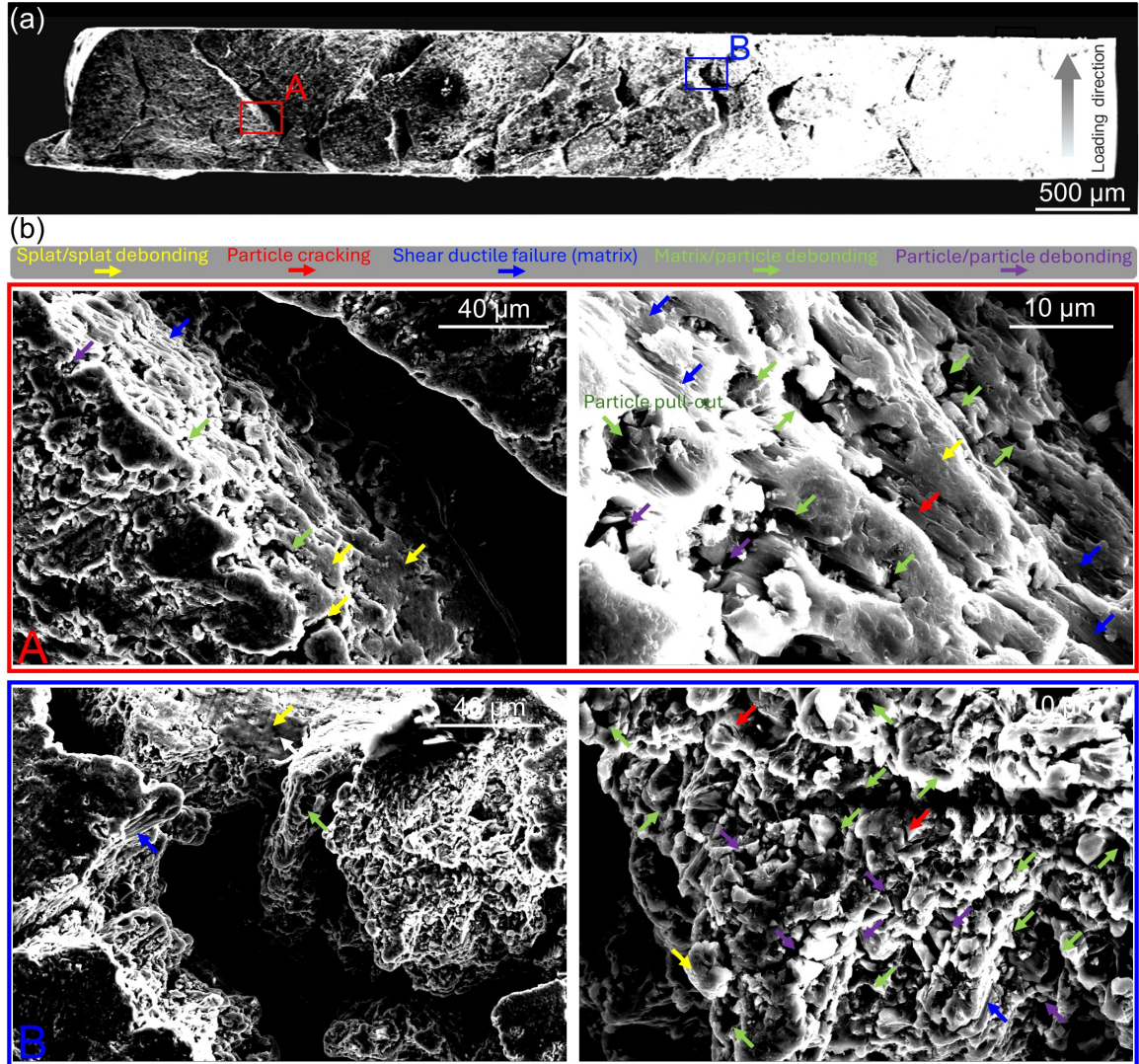


Fig. 4.5: Fractures surface morphology of the CSAM Al-46 wt.% Al₂O₃ composite under dynamic uniaxial compression: (a) Low-magnification SEM image of the deformed specimen after testing, (b) Magnified views of the shear and axial cracks on side surface of the specimen shown in boxes A and B, respectively.

compared to quasi-static loading, as observed in Fig. 4.5(b). Interfacial failure in terms of particle/particle and matrix/particle debonding appears to be more prominent on the axial crack surface (see the magnified views in the blue box in Fig. 4.5(b)). In addition, matrix failure mechanisms (i.e., inter-splat debonding and shear failure) are hardly seen compared to the shear crack surface. This observation may signal that the axial cracks are initiated in particle-rich regions of the CSAM composite under dynamic compression loading where interfacial failure – particularly, particle pull-out

mechanism – plays the major role. Next, the strain rate-dependent interplay between the failure mechanisms is further discussed by the micromechanical FE model.

4.5.3 Strain rate-dependent evolution of failure mechanisms

While the SEM fractography in Section 4.5.2 provides insights into the contribution of failure mechanisms, the strain rate-dependent interaction and growth of mechanisms through the course of loading remains uncovered. To do so, the validated micromechanical model is leveraged to unravel the history of failure mechanisms, as shown in Fig. 4.6(a). Note that the stress-strain curves are also plotted in transparent mode to provide a better correlation with the mechanisms. Here, via Python scripting, the mechanisms are quantified in terms of number fraction of fully debonded nodes at the interfaces (i.e., debonding mechanism) and fully damaged elements (i.e., elements with zero stress-bearing capacity due to failure) of Al_2O_3 particles (i.e., particle cracking mechanism) and Al matrix (i.e., matrix failure mechanism). The model shows that the mechanisms are triggered as per the same sequence regardless of the strain rate: I. Interfacial failure, II. Particle cracking, and III. Matrix failure. In correlation with the yielding point, the debonding mechanism is first activated at a strain of $\sim 1\%$ for different strain rates. Upon initiation, the debonding mechanism grows (nearly in a linear fashion) faster with the increase in strain rate and this agrees with the SEM fractography in Section 4.5.2. At an axial strain of $\sim 5\%$, the particle cracking mechanism is activated and rises at the fastest for quasi-static rates. As opposed to the debonding mechanism, particle damage decreases in magnitude with strain rate, and this may be attributable to higher interfacial failure that weakens the transferable load (i.e., $\Delta\sigma = 0.5V_p\sigma_m$ [184], where V_p and σ_m denotes the particle volume fraction and matrix flow stress, respectively) from the Al matrix to the particles. Eventually, as the the axial strain exceeds $\sim 6\%$, matrix failure is initiated but it grows marginally up to the onset of softening regime at $\sim 12\%$. Next, the matrix failure mechanism follows an exponential growth trajectory with the highest

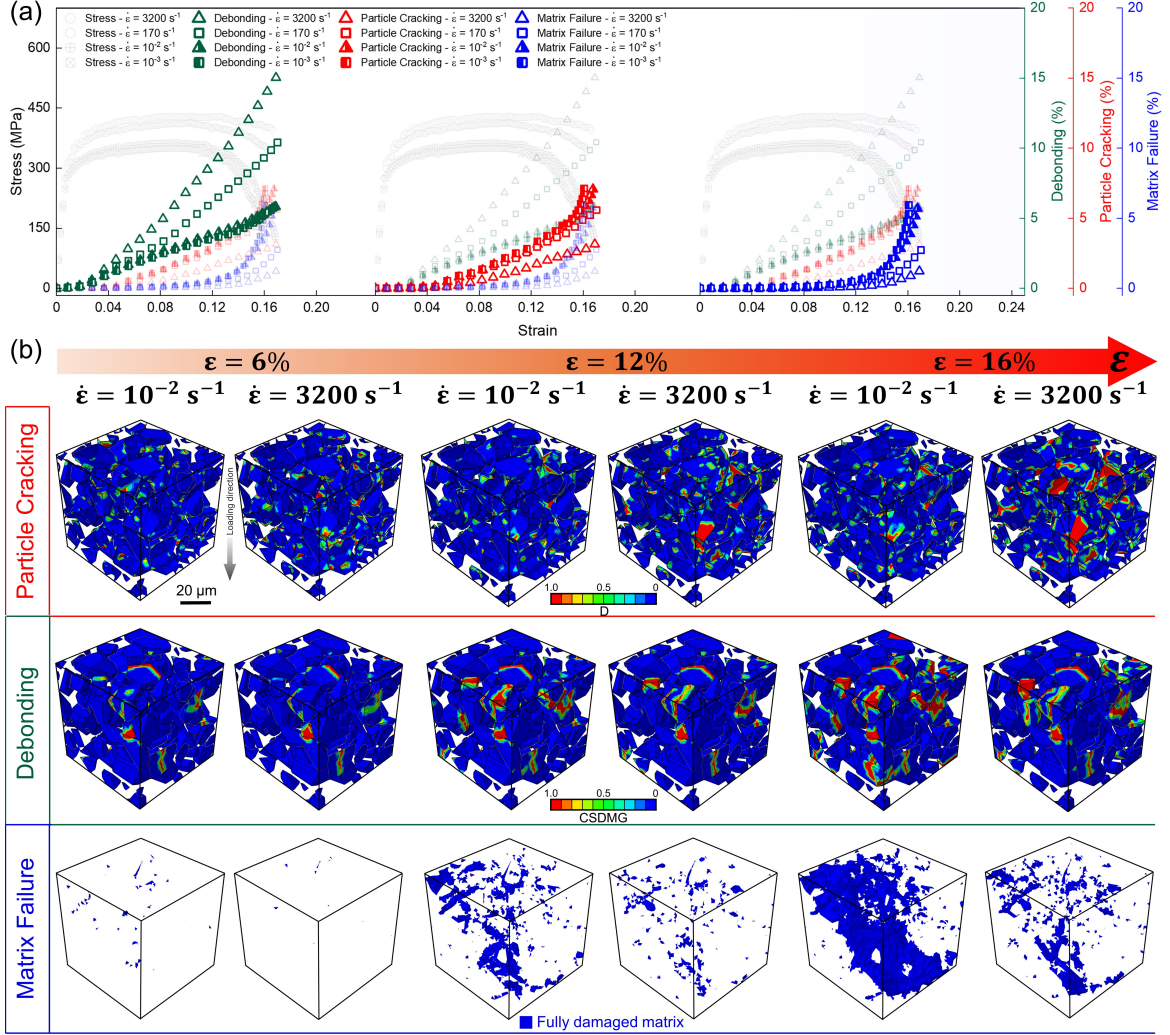


Fig. 4.6: Evolution of the failure mechanisms predicted by the micromechanical model: (a) Quantified history of the initiation and growth of failure mechanisms of the CSAM Al-46 wt.% Al_2O_3 composite across quasi-static and dynamic loading rates. (b) Strain rate-dependent time-resolved images of the qualitative evolution of the failure mechanisms.

rate for quasi-static loading which is promoted by the higher percentage of damage in the particles when compared to dynamic strain rates. The particle cracking mechanism gains an ascending growth rate in the softening regime, which is consistent with the previously reported experimental studies on AMCs [230]. This coalescence of matrix failure with the highest growth rate accelerates the softening rate of the composite which leads to a noticeably smaller elongation at failure under quasi-static strain rates. Fig. 4.6(b) shows the predicted qualitative evolution of failure mecha-

nisms presented for both quasi-static and dynamic loading conditions. As seen, the debonding mechanism is primarily triggered and propagates at the sharp concaves – which is induced by the stress concentration at these areas – of coarse-sized particles, and the particles involved in a cluster due to weaker interfacial properties (see Fig. 4.2(a)) and non-bonded particle/particle contacts, respectively. Particle cracking mechanism is frequently observed in the clustered particles due to particle-to-particle load transfer that is higher in magnitude compared to matrix-to-particle load transfer. Pattern-wise, consistent with the cleavage facets/river-like pattern on the fracture surface morphology, the damage in the particles is predicted to mainly grow parallel to the axial global compression direction (see Fig. 4.6(b)) likely caused by the formation of tension-dominated stress states, and also particle crushing at the junctions within the clusters, and this is further discussed in Section 4.5.5. The last row of Fig. 4.6(b) shows the strain rate-dependent evolution of the fractured area of the Al matrix rendered by reactivation of the fully damaged elements in blue. The matrix failure first nucleates in the form of voids in the vicinity of damaged particles and thin ligaments trapped between the particles (see Fig. 4.6(b) at the strain of 6%). As the strain reaches 12%, the nucleated voids coalesce into micro cracks under the rate of 10^{-2} s^{-1} while they rather grow in a scattered pattern under the rate of 3200 s^{-1} likely due to the strain rate hardening effect in the matrix and less damage in the particles. With the increase in strain to 16%, the micro-cracks grow and merge into a $\sim 45^\circ$ fracture plane under quasi-static loading that replicates that of the experiments in Fig. 4.4. Contrarily, under dynamic loading, at the same strain of 16%, a few $\sim 45^\circ$ micro-cracks appear at different locations with no coalescence due to the mitigated localization of the strain field in the matrix, and this agrees with the dynamic experimental data in Fig. 4.3 and Fig. 4.5. Note that this study does not draw a direct comparison between the numerically predicted history of failure mechanisms and those observed in the post-mortem SEM images due to the following reasons: I. The SEM images are only available after the loading process and this does not

allow to provide an experimental history of the growth of microscale mechanisms to be compared with those of the micromechanical model. II. Computationally, the failure mechanisms are quantified based on the number fraction of debonded interfacial nodes and fully damaged elements; such quantification framework may not be fully reconstructible by SEM images of the fracture surfaces to draw a consistent direct comparison between the micromechanical model and the experiments. Regardless of the direct comparison, the numerically predicted histories of failure mechanisms (Fig. 4.6) are in reasonable agreement with the trends of the manifestations of the mechanisms in the fractography analysis across strain rates. Accordingly, as previously discussed in this section, with the increase in strain rate from quasi-static to dynamic regimes, the model predicts the increase in particle debonding, the decrease in particle cracking, and the decrease in matrix failure, and such a shift in failure mechanisms is consistent with the observations from the post-mortem SEM images shown in Fig. 4.4 and Fig. 4.5.

4.5.4 Stress-bearing partitioning analysis

By using the micromechanical model, a stress-bearing partitioning analysis is conducted to uncover the contribution of the Al matrix and Al₂O₃ particles to the strain rate-dependent behavior of the CSAM Al-46 wt.% Al₂O₃ composite. Fig. 4.7(a) shows the homogenized axial stress (σ_{yy} , see Fig. 4.3b) borne by the Al matrix, Al₂O₃ particles, and the composite versus the homogenized axial strain (ϵ_{yy} , see Fig. 4.3b) of the composite under quasi-static and dynamic strain rates. Bulk Al and its alloys are found to show strain rate independency [231] or low strain rate sensitivity [191] under strain rates varying from 10^{-3} s^{-1} to 10^3 s^{-1} . As shown in Fig. 4.7(a), the Al matrix in the composite, however, demonstrates strain rate sensitivity, and this is attributable to the constraining effect by the particles [232] and the heterogeneity of the microstructure that induces high local strain rates (i.e., $\geq 10^4 \text{ s}^{-1}$) in the matrix in the vicinity of particles. With the increase in strain rate, the stress-bearing capacity of

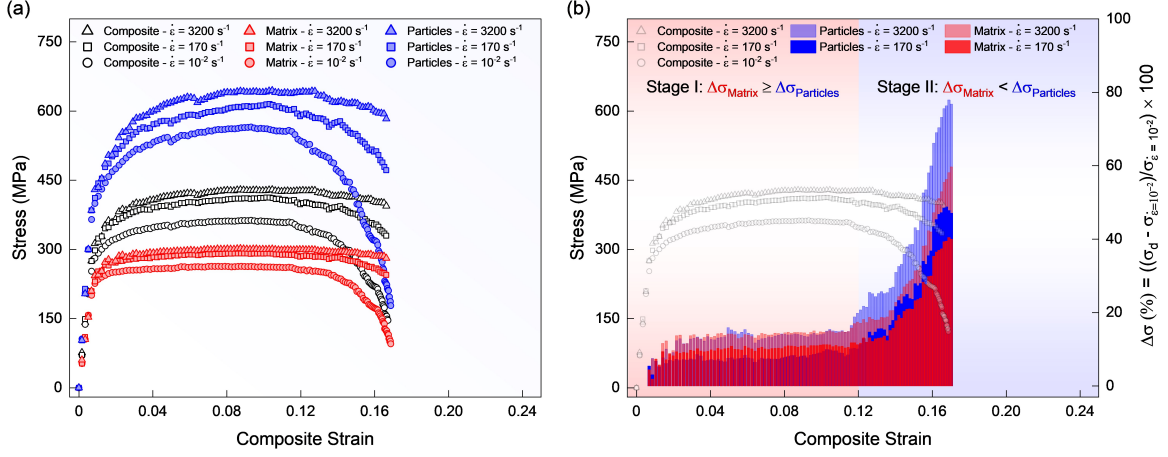


Fig. 4.7: Stress-bearing partitioning analysis via the micromechanical model:(a) Stress-bearing capacity partitioning of the CSAM Al-46 wt.% Al₂O₃ composite across quasi-static and dynamic loading rates. (b) The percentage of increase ($\Delta\sigma$ (%)) in the stress-bearing capacity of Al matrix and Al₂O₃ particles of the composite under dynamic strain rates with respect to the quasi-static strain rate of 10^{-2} s^{-1} . Note that σ_d and $\sigma_{\dot{\epsilon}=10^{-2}}$ denotes the matrix/particle stress under dynamic rates and the reference quasi-static rate, respectively.

the particles noticeably increases compared to that of the Al matrix (see Fig. 4.7(a)), and this reflects that the strain rate-dependent flow stress of the composite primarily originates from the ceramic particles. This may be attributable to the increase in the spall strength of ceramic particles under high strain rate loading [65] – and such effect is incorporated into the JH2-V constitutive model [65] – that promotes less particle cracking with the increase in strain rate (see Fig. 4.6(a)), and the Al matrix with higher flow stress and less localization of deformation that transfers more load to the skeleton of the particles. The partitioning analysis also shows that the onset of the softening regime and the softening rate of the CSAM composite are remarkably dependent on the reinforcing particles across strain rates. Under quasi-static rates, the stress-bearing capacity of particles follows a sharp decreasing trend due to the higher level of damage (see Fig. 4.4(b) and Fig. 4.6(a)) which accelerates the matrix failure, and this combination causes the fastest softening rate in the composite compared to the dynamic rates. Fig. 4.7(b) shows the percentage of increase in the stress-bearing capacity (i.e., $\Delta\sigma$) of the Al matrix and Al₂O₃ particles with respect

to a reference strain rate of 10^{-2} s^{-1} (i.e., $\Delta\sigma = \frac{\sigma_d - \sigma_s}{\sigma_s} \times 100$, where σ_d and σ_s represents the matrix/particle stress under dynamic rates and the reference quasi-static rate, respectively). As seen, this analysis reveals a two-staged behavior in terms of the relationship between $\Delta\sigma_{matrix}$ and $\Delta\sigma_{particles}$ when the strain rate increases from quasi-static to dynamic. In stage I up to a strain of $\sim 12\%$, $\Delta\sigma_{matrix} \geq \Delta\sigma_{particles}$ and this relationship tends to equality as the strain rate increases from 170 s^{-1} to 3200 s^{-1} . Next, in close correspondence with the onset of softening, stage II is initiated where $\Delta\sigma_{particle} > \Delta\sigma_{particles}$; this equality is triggered earlier and amplified with the increase in strain rate. The presence of these stages implies that as the strain rate increases from quasi-static conditions to dynamic regimes the stress-bearing capacity of particles becomes more important than that of the matrix and this plays a key role in increasing the strain rate-induced ductility of the CSAM composite that is observable by the experiments as well (see Fig. 4.3(a)).

4.5.5 The role of particle clustering

In this section, the effect of particle clustering on the failure behavior of the CSAM composites is explored by partitioning the stress-bearing capacity and history of failure mechanisms under quasi-static (10^{-2} s^{-1}) and dynamic (3200 s^{-1}) strain rates. As shown in Fig. 4.8, for both quasi-static and dynamic loading, with the increase in clustering from 0 to 20%, the ultimate compressive strength of the composite increases while the strain hardening regime and elongation at failure are degraded. The stress-bearing capacity of the particles remarkably increases with the increase in clustering while that of the matrix is weakened. The former may be attributable to the direct load transfer between clustered particles acting as a continuous phase and the latter is likely to be caused by the weakened particle-induced plastic deformation in the Al matrix (i.e., thin ligaments of Al matrix trapped between fine-distributed particles). Accordingly, the enhanced stress-bearing capacity of particles is the mechanism leading to the increase in the ultimate compressive strength of the CSAM composite

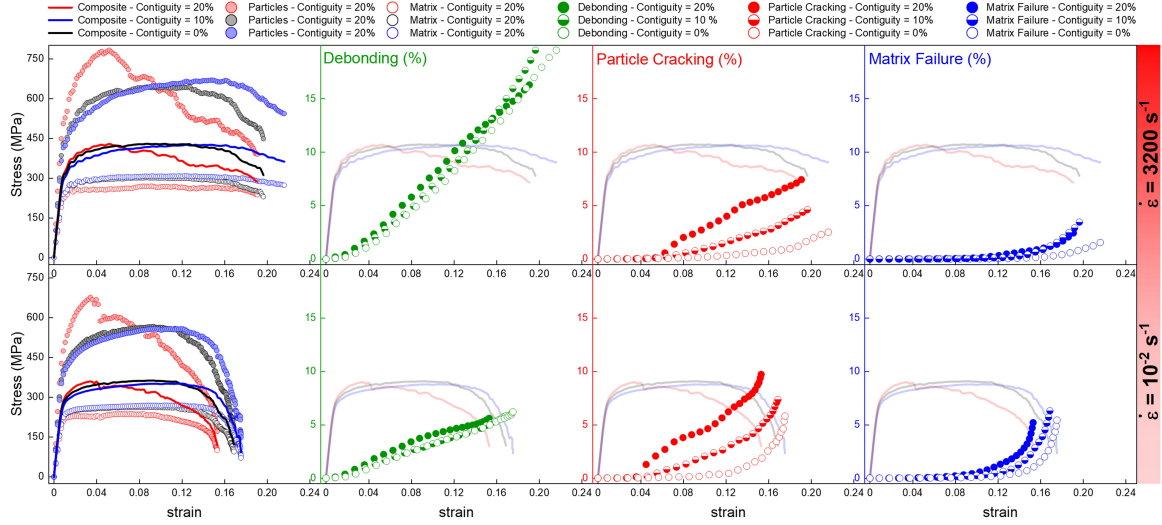


Fig. 4.8: The role of particle clustering in the mechanical behavior of the CSAM Al-46 wt.% Al₂O₃ composite under quasi-static and dynamic compression analyzed by stress-bearing capacity partitioning and the quantified history of the evolution of the failure mechanisms.

involving clustered particles. The quantified history of failure mechanisms shows that particle cracking is initiated earlier and grows faster with the increase in clustering due to a higher stress level which leads to a sharper decrease in the stress-bearing capacity of particles and this negatively affects the strain hardening behavior of the composite. Matrix/particle interfacial failure emerges as the first mechanism regardless of the level of particle clustering, but it increases with the increase in clustering magnitude. This is likely due to a smaller number of shared interfaces transferring the load from the matrix to particles, resulting in a higher level of interfacial stresses that increases the propensity of debonding when particles are not homogeneously distributed. The matrix failure growth is more noticeably affected by particle clustering under quasi-static loading owing to strain localization and the absence of strain rate hardening effects that are amplified by severe cracking in clustered particles. Fig. 4.9(a) shows the effect of particle clustering on the evolution of the spatiotemporal distribution of the equivalent stress and deformation pattern of the CSAM composite. As seen at an axial strain of 1% for the composite with 20% particle clustering under the quasi-static strain rate, the clustered particles form a continuous phase that transfers the

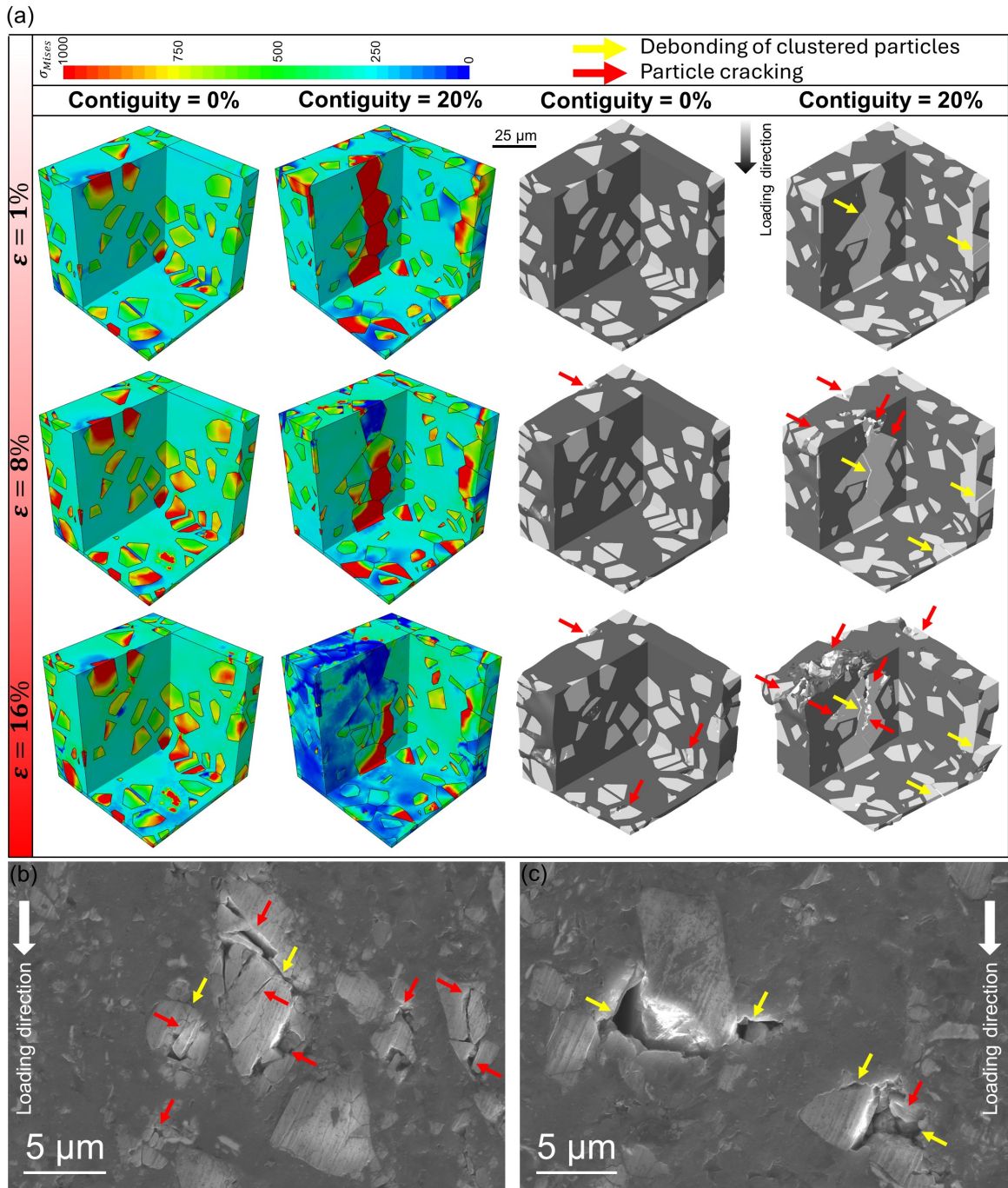


Fig. 4.9: (a) The effect of particle clustering on the stress distribution and particle cracking mechanism in the CSAM Al-46 wt.% Al₂O₃ composite. (b) and (c) SEM images of the material after testing that confirm the numerical predictions of the features of cracking and debonding of clustered particles.

load internally by particle/particle contact which results in local regions with high stress-bearing capacity. However, the non-homogeneous spatial distribution of parti-

cles leads to a more noticeable emergence of low-stress regions in the matrix of the composite with particle clustering at earlier stages of loading (i.e., blueish areas at the strain of 1% and 8% in Fig. 4.9(a)). Regarding the deformation history, at a strain of 1% close to the yielding point of the composite, debonding (see the yellow arrows) is observed within the clustered particles. When the strain exceeds 8% towards 16%, particle damage (see the red arrows) in the form of crushing and axial cracking (i.e., parallel to the loading direction) in the clustered particles is more frequently detected when compared to the composite with homogeneous particle scattering. As shown in Fig. 4.9(b) and (c), the post-mortem SEM images of the CSAM Al-46 wt.% Al₂O₃ composite represent the debonding of particles in the clusters (see purple arrows in Fig. 4.4(b)) and the damage in the clustered particles with crushing and axial cracking patterns and these are the phenomena that the current micromechanical model also reproduces.

4.5.6 The failure behavior of the material under elevated temperatures

In this section, the developed micromechanical model was further exercised to explore the effect of initial temperature on the failure behavior of the CSAM Al-46 wt.% Al₂O₃ composite across different strain rates. The importance of such exploration stems from providing insights into the role of working temperature (e.g., aircraft brakes [53]) in the failure growth in the material for elevated temperature applications [233] which is not addressed at the microscale in the literature on CSAM metal-ceramic composites. It is well-established in the literature [234, 235] that the elastic modulus and yield strength of Al alloys decrease under high temperatures – specifically beyond 200 °C – which is attributable to grain coarsening/recrystallization [236], the increase in the mobility of dislocations [237] and grain boundary sliding, weakening the material resistance to deformation and the flow stress. Supplementary Fig. 4.15 shows temperature-dependent yield strength and Young’s modulus of different Al alloys in

previous studies. As seen in Supplementary Fig. 4.15(a), the higher the yield strength of the Al alloy at room temperature (RT), the sharper the decreasing trend of the yield strength with elevating the initial temperature. Accordingly, as the RT yield strength of the pure Al in the current CSAM composite is close to that of the Al6061-T6, the temperature-dependent yield stress of the pure Al (see red star data points in Supplementary Fig. 4.15(a)) was replicated from that of the Al6061-T6 by Roy et al. [235] based on the ratio of reduction in the yield strength with the increase in temperature. Similarly, as shown in Supplementary Fig. 4.15(b), temperature-dependent Young's modulus of the pure Al in the CSAM composite was reconstructed based on the work by Rojas et al. [238]. As seen, the elastic modulus of the as-sprayed CSAM Al is calibrated to be considerably lower than that of the bulk Al, which is attributable to premature inter-splat cracking due to weak mechanical interlocking as the bonding mechanism [239]. Note that the temperature-dependent yield strength and elastic constant shown in Supplementary Fig. 4.15 were used as the inputs to the FE model for the Al matrix. In addition, the specific heat capacity of the Al matrix as a function of temperature [234] was incorporated into the constitutive model (see Eq. (4.16) in the Supplementary material). The reinforcing Al₂O₃ ceramic particles were constitutively modeled independent of temperature due to their thermally stable mechanical properties up to 500 °C [240]. Fig. 4.10 shows the stress-strain response and the history of failure mechanisms of the CSAM Al-46 wt.% Al₂O₃ composite under elevated temperatures up to 350 °C (i.e., ~ half the melting point of the Al matrix of 660 °C [86]) across quasi-static and dynamic strain rates. As seen, with the increase in temperature, both the debonding and particle cracking mechanisms decrease in magnitude under both the quasi-static and dynamic strain rates, as the matrix becomes softer and possesses a lower yield strength at higher temperatures, and these result in a lower level of load being transferred through the interfaces to the particles, thereby decreasing the propensity of the interfacial failure and particle cracking. This prediction of the current micromechanical model is consistent with

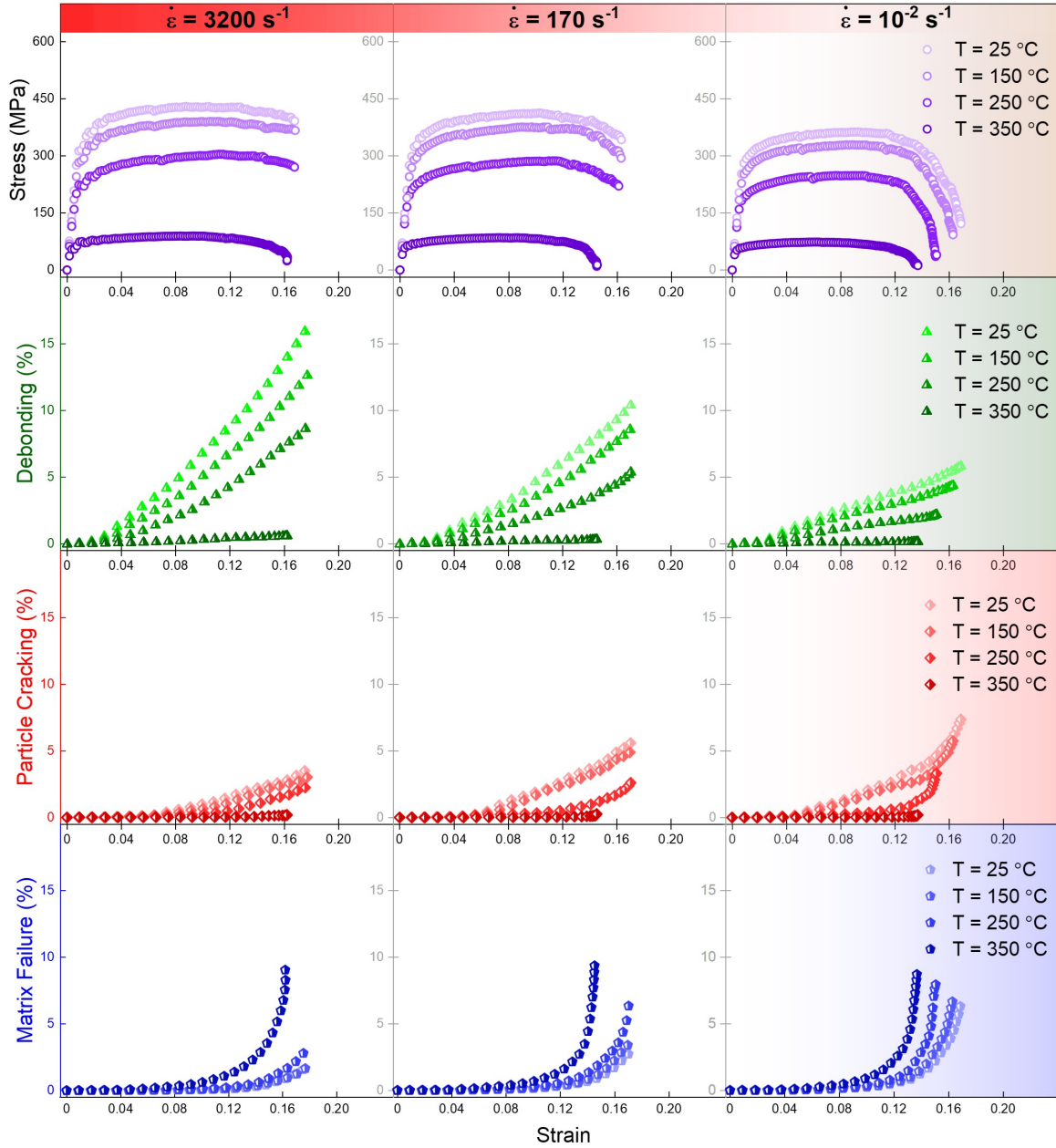


Fig. 4.10: The effect of initial working temperature on the strain rate-dependent stress-strain response of the CSAM Al-46 wt.% Al₂O₃ and the evolution of failure mechanisms predicted by the micromechanical model.

that of previous experimental studies on MMCs [211, 241]. The quantified histories of failure mechanisms show that matrix failure becomes the predominant mechanism with the rise in initial working temperature; regardless of strain rates, debonding and particle cracking mechanisms are suppressed at the temperature of 350 °C, and matrix

failure governs the failure of the CSAM composite. From the stress-strain responses, the strain hardening behavior of the composite appears to be unaltered up to 250 °C across strain rates, but it slightly decreases with the increase in temperature to 350 °C which is likely caused by the marked decrease in the yield strength/elastic modulus of the Al matrix (see Supplementary Fig. 4.15(a)) that consequently weakens the contribution of the alumina particles to the stress-bearing capacity of the composite in the post-yielding regime. In previous experimental studies on the conventionally made MMCs, the elongation at failure of the material is frequently shown to increase with the increase in temperature when the composite is under uniaxial tension [211, 242] and uniaxial compression [231, 241] due to the improved deformability of the metallic matrix and less probability of particle cracking and debonding mechanisms. However, in some experimental studies on the hot compressive deformation behavior of AMCs [13, 243], no increase in the elongation of failure with the temperature rise is reported. Here, the micromechanical model predicts that the elongation at failure of the CSAM composite under uniaxial compression decreases at the microscale with the increase in temperature, and this is attributable to the localization of deformation in the thermally softened matrix accompanied by a weakened contribution of particles evidenced by the lower level of the particle cracking mechanism that triggers the matrix failure sooner and with a higher growth rate (see Fig. 4.10, the last row), leading to a lower elongation at failure of the composite. Under elevated temperatures, the dislocation recovery and grain recrystallization mechanisms [243] play a role in increasing the ductility of the metallic matrix by facilitating the migration of dislocations and nucleation of strain-free grains, respectively, and these mechanisms are not incorporated in the current model which may result in an underestimation of the failure strain of the composite under high working temperatures. Fig. 4.11(a) shows the volumetrically averaged temperature rise (ΔT) history in the CSAM composite across strain rates and initial working temperatures. Under dynamic strain rates, the ΔT profile starts to almost linearly grow from zero at the early stages ($\sim 2\%$)

of the strain hardening regime due to the adiabatic heating condition by which the plastic dissipation energy is converted to heat (see Eq. (4.15) in the Supplementary materials). This predicted nearly linear growth of the ΔT in the material under dynamic loading agrees with experimental measurements in the literature [244, 245]. The micromechanical model shows that with the increase in working temperature, the adiabatic thermal softening effect is alleviated (i.e., a lower ΔT) which is attributable to a lower flow stress and a higher specific heat capacity under elevated temperatures. The adiabatic temperature rise of the CSAM Al-46 wt.% Al₂O₃ composite under the strain rate of 3200 s⁻¹ is predicted to be ~ 20 °C at a strain of 10% at RT which is in agreement with that of previous studies – e.g., the ΔT of ~ 18.6 °C in Al/40%SiC composite at a strain of 10% under a strain rate of 2000 s⁻¹ at RT [212] – confirming the quantitative validation of the micromechanical model. Under quasi-static loading, regardless of the initial working temperature, the ΔT in the composite remains zero up to the onset of softening after which it increases slightly by ~ 2 °C at the maximum due to the isothermal condition which is implicitly incorporated into the constitutive model (see Section 4.8.1 in the Supplementary material). As shown in Fig. 4.11(a), a negligible fraction of the Al matrix – i.e., $\sim 0.1\%$ of the whole volume of the matrix – is predicted to be melted (i.e., $T \geq 660$ °C) under dynamic loading. According to the fractography analysis on the CSAM composite under the strain rate of 3200 s⁻¹, as shown in Fig. 4.11(b), evidence of adiabatic heating-induced Al matrix melting is rarely found close to the loading platen possibly driven by the excessive stress concentration effect, and this may confirm the corresponding numerical prediction on the melting of the Al matrix. Based on the micromechanical model qualitative outcomes shown in Fig. 4.11(c), the melting of the Al matrix under high strain rates is remarkably facilitated by the particle network that promotes the localization of temperature field at the matrix/particle interfaces and the trapped thin ligaments leading to adiabatic heating-induced melting of Al. Additionally, such phenomena also produce local high-temperature areas in the Al

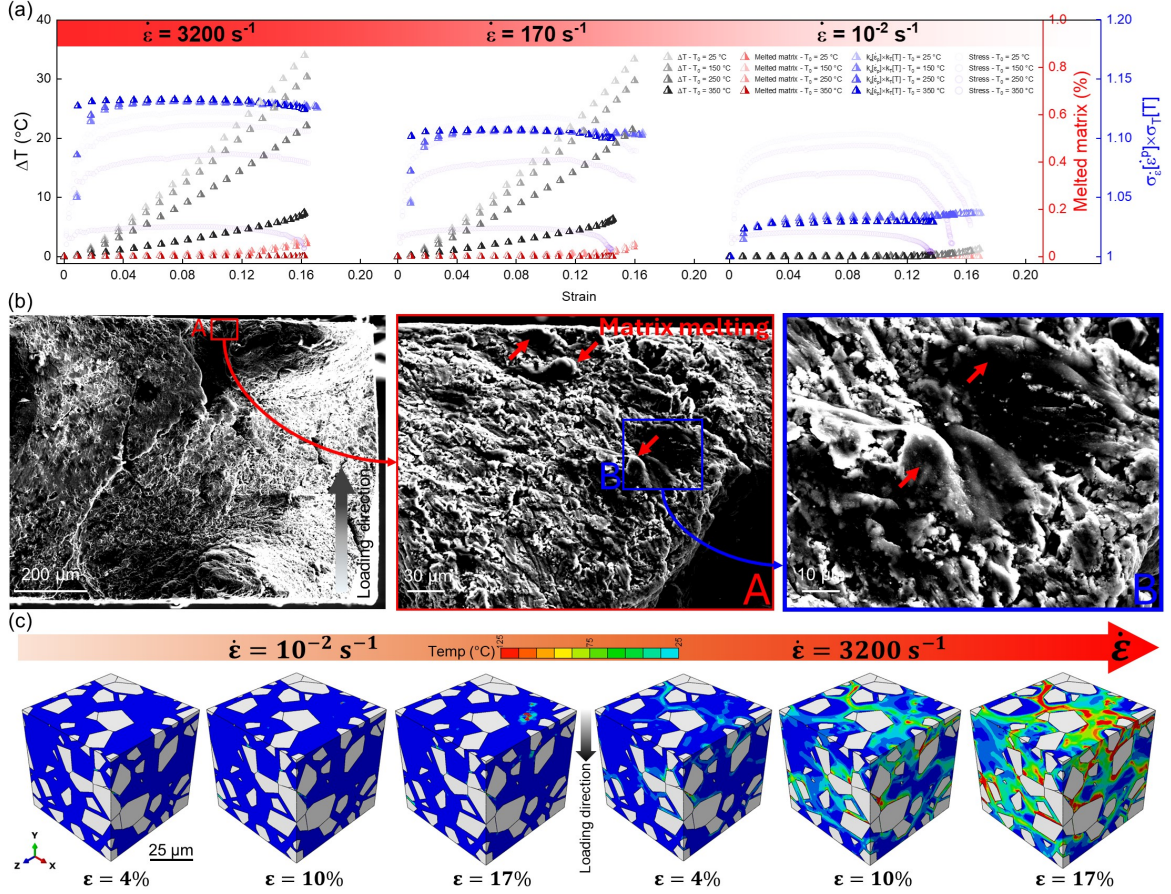


Fig. 4.11: (a) Volumetrically-averaged homogenized temperature increase (ΔT) profile of the CSAM composite, the volume fraction of the melted Al matrix, and the multiplicative contribution of the strain rate hardening and thermal softening mechanisms ($\sigma_{\dot{\epsilon}}[\dot{\epsilon}_M^p]\sigma_T[T]$) of the Al matrix of the composite across temperatures and strain rates predicted by the micromechanical model. (b) SEM images of the tested CSAM Al-46 wt.% Al_2O_3 composite under the strain rate of 3200 s^{-1} at RT, showing evidence of partial matrix melting near the loading surfaces. (c) Qualitative evolution of temperature field in the Al matrix of the CSAM composite under quasi-static and dynamic loading at RT predicted by the micromechanical model.

matrix of the composite under quasi-static loading (see Fig. 4.11(c)) in which melting is not promoted as shown in Fig. 4.11(a). To inform on the competition between the strain rate hardening and thermal softening mechanisms in the matrix denoted by $\sigma_{\dot{\epsilon}}[\dot{\epsilon}_M^p]$ and $\sigma_T[T]$ in Section 4.8.1 in the Supplementary material, respectively, the history of the multiplication of $\sigma_{\dot{\epsilon}}[\dot{\epsilon}_M^p]\sigma_T[T]$ is quantified as a volumetric average in Fig. 4.11(a). Regardless of the working temperature and strain rate, the quantity of $\sigma_{\dot{\epsilon}}[\dot{\epsilon}_M^p]\sigma_T[T]$ holds greater than one, implying the prevalence of the strain rate hard-

ening mechanism over the thermal softening mechanism in the CSAM Al-46 wt.% Al₂O₃; this agrees with the experimental dynamic stress-strain curves in Fig. 4.3(a) reflecting a positive strain hardening rate.

4.6 Conclusions

We investigated the strain rate-dependent failure behavior of CSAM Al-46 wt.% Al₂O₃ by a 3D micromechanical FE model, accounting for experimentally captured particle size distribution and particle clustering. Strain rate-dependent constitutive models were implemented by VUMAT subroutines for the Al matrix and Al₂O₃ particles in Abaqus/Explicit FE solver. The fractography analysis showed that the Al matrix failed due to the splat/splat debonding and shear failure induced by particle sliding. Under dynamic compression loading, particle pull-outs are frequently observed as the indicator of matrix/particle debonding on the fracture surface while particle cracking is rarely detected when compared to quasi-static loading, and this may be attributable to the reverberation of stress wave under high strain rates that induces a tensile-dominated stress state at the interfaces. The micromechanical model showed that the sequence of activation of mechanisms is independent of strain rate; I. Interfacial failure, II. Particle cracking, and III. Matrix failure. Additionally, consistent with the fractography analysis, particle debonding was found to grow at a higher rate under dynamic loading, dampening the particle cracking mechanism as a result of the deterioration of the load transfer mechanism. According to the stress partitioning analysis, the stress-bearing capacity of the reinforcing particles predominantly contributes to the enhanced flow stress and elongation at failure of the CSAM composite under high strain rates due to the lower propensity of particle cracking. The clustering of particles increases the compressive strength of the material but negatively affects the strain hardening behavior and elongation at failure. The former is ascribed to the particle/particle load transfer and the latter is caused by the amplified particle cracking mechanism leading to matrix failure with a higher growth rate. Under

elevated temperatures, the model showed that the debonding and particle cracking mechanisms vanish due to the softened matrix that ineffectively transfers the load to the skeleton of particles, and matrix failure plays the dominant role across the strain rates. It was also found that the strain rate hardening mechanism prevails over the thermal softening mechanism in the CSAM composite, regardless of the initial temperature and strain rate. Altogether, this study provides novel insights into the correlation between the microscale failure behavior and the macro-scale mechanical behavior of the material across strain rates and working temperatures that pave the way for the design of better-performing CSAM metal-ceramic composites as future structural materials.

4.7 Acknowledgment

The authors gratefully acknowledge funding support from the Alberta Innovates Graduate Student Scholarship, Imperial Oil (Esso), the Natural Science and Engineering Research Council Canada (NSERC), the Alberta Graduate Excellence Scholarship (AGES), the Sadler Graduate Scholarship in Mechanical Engineering, the RR Gilpin Memorial Scholarship, the Canada Foundation for Innovation, the Province of Alberta Ministry of Technology and Innovation.

4.8 Supplementary materials

This section provides the Supplementary Text and the Supplementary Figures of this published chapter, including the constitutive models and Fig. 4.12, Fig. 4.13, Fig. 4.14, and Fig. 4.15.

4.8.1 Constitutive models

Strain rate-dependent failure model for Al matrix

In particulate-reinforced metal matrix composites, the spatial random distribution of hard particles with irregular morphology induces multiple time-evolving stress states

in the metallic matrix. To incorporate such phenomena in the micromechanical model in this article, the ductile failure constitutive model by Zhou et al. [64] was implemented by a VUMAT subroutine in Abaqus/Explicit FE solver in this study. In the Zhou et al. model, the widely used GTN model [93] is modified by the stress triaxiality and the Lode angle parameters [48] to capture ductile failure under both compression- and tension-dominated stress states. The ductile failure is initiated when the Zhou et al. model [64] yield criterion is triggered:

$$\Phi(\sigma, f^*, D_s) = \left(\frac{\sigma_q}{\sigma_y}\right)^2 + 2q_1 f^* \cosh\left(\frac{3q_2 p}{2\sigma_y}\right) - (1 + D^2 - 2D_s) > 0, \quad (4.1)$$

where σ_y , p and σ_q denotes the flow stress of the material, hydrostatic pressure, and deviatoric stress component, respectively. The effective damage is represented by $D = q_1 f^* + D_s$ as a combination of void growth under tension (f^*) proposed by Tvergaard and Needleman [93] and void distortion under shear (D_s) [169]. Proposed by Tvergaard [170], q_1 and q_2 are empirical material constants for the better reproduction of the void coalescence mechanism. The effective porosity f^* governs ductile failure under tension as:

$$f^* = \begin{cases} f & \text{if } f \leq f_c \\ f_c + \frac{f_u - f_c}{f_F - f_c} (f - f_c) & \text{if } f_c < f < f_F \\ f_u & \text{if } f_F \leq f \end{cases}, \quad (4.2)$$

where f_c , $f_u = \frac{1}{q_1}$, and f_F represents the critical porosity for the activation of void coalescence, porosity corresponding to zero stress-bearing capacity, and the porosity at complete failure. f is the total porosity as the accumulation of nucleated voids (\dot{f}_n) and the growth of existing voids (\dot{f}_g). Here, a normal distribution function [99] with the equivalent plastic strain $\bar{\epsilon}_M^p$ as the input is considered for the void nucleation under tensile hydrostatic pressure. The rate of the void growth is correlated with the increment in plastic volume with the assumption that the material is plastically incompressible. Correspondingly, the functions are:

$$\dot{f} = \dot{f}_n + \dot{f}_g, \quad (4.3)$$

$$\dot{f}_n = A_n \dot{\epsilon}_M^p, \quad (4.4)$$

$$A_n = \begin{cases} \frac{f_N}{s_N \sqrt{2\pi}} e^{-0.5 \left(\frac{\epsilon_M^p - \epsilon_N}{s_N} \right)^2} & \text{if } p \geq 0, \text{ and} \\ 0 & \text{if } p < 0 \end{cases} \quad (4.5)$$

$$\dot{f}_g = (1 - f) \dot{\epsilon}_{kk}^p, \quad (4.6)$$

where $\dot{\epsilon}_M^p$, ϵ_N , s_N , and $\dot{\epsilon}_{kk}^p$ denotes the equivalent plastic strain rate, the mean equivalent plastic strain for void nucleation, the standard deviation of the normal distribution, and the trace of the plastic strain rate tensor, respectively. The shear damage parameter D_s in the Zhou et al. model (see Eq. (4.1)) is defined as a function of equivalent plastic strain and the stress state as:

$$\dot{D}_s = \psi(\theta, T^*) \frac{n D_s^{n-1}}{\epsilon_s^f} \dot{\epsilon}_M^p, \quad (4.7)$$

$$\psi(\theta, T^*) = \begin{cases} g(\theta) & \text{if } T^* \geq 0, \\ g(\theta)(1 - k) + k & \text{if } T^* < 0 \end{cases}, \quad (4.8)$$

where θ , T^* , and $\psi(\theta, T^*)$ is the Lode angle, stress triaxiality, and the weight factor function to account for ductile failure under compression and shear dominated stress states, respectively. Here, the contribution of the weight factor to damage growth under compression is regulated by k . Proposed by Xue [171], $g(\theta)$ is the Lode angle function based on the third invariant of the deviatoric stress tensor (J_3) as:

$$g(\theta) = 1 - \frac{6|\theta|}{\pi}, \quad (4.9)$$

$$\theta = \frac{1}{3} \cos^{-1} \left(\frac{27 J_3}{2 \sigma_q^3} \right) - \frac{\pi}{6}. \quad (4.10)$$

In this study, the original model by Zhou et al. [64] is enhanced via a multiplicative flow stress function [246] where the strain rate strengthening and thermal softening mechanisms are incorporated as:

$$\sigma_y[\dot{\epsilon}_M^p, \dot{\epsilon}_M^p, T] = \sigma_\epsilon[\dot{\epsilon}_M^p] \sigma_\epsilon[\dot{\epsilon}_M^p] \sigma_T[T], \quad (4.11)$$

$$\sigma_\epsilon[\dot{\epsilon}_M^p] = A \left(1 + \frac{E}{A} \dot{\epsilon}_M^p \right)^n, \quad (4.12)$$

$$\sigma_\epsilon[\dot{\epsilon}_M^p] = 1 + C \ln \left(\frac{\dot{\epsilon}_M^p}{\dot{\epsilon}_0} \right), \quad (4.13)$$

$$\sigma_T[T] = 1 - \left(\frac{T - T_r}{T_m - T_r} \right)^m, \quad (4.14)$$

where A and E is the yield strength, Young's modulus of the material; n , C , and m are empirical constants of the material to be calibrated by experimental data; $\dot{\epsilon}_0$ is the reference strain rate; T , T_r , and T_m denotes the temperature, initial working temperature, and the melting temperature of the material, respectively. The evolution of temperature is linked with the dissipation of plastic work in the material as [247]:

$$\dot{T} = \omega[\dot{\epsilon}_M^p] \frac{\chi}{\rho C_p(T)} \boldsymbol{\sigma} : \dot{\boldsymbol{\epsilon}}_M^p, \quad (4.15)$$

$$C_p(T) = 0.8736 + 3e^{-4}T + 4e^{-7}T^2 + 3e^{-10}T^3 \quad (20^\circ C \leq T \leq 350^\circ C), \quad (4.16)$$

where χ , ρ , and C_p denotes the Taylor–Quinney coefficient, mass density, and the specific heat of the material as a function of temperature [234], respectively. To incorporate the transition from the isothermal to adiabatic condition into the pure mechanical simulations in the current work, ω is defined as a function of the equivalent plastic strain rate as [247]:

$$\omega[\dot{\epsilon}_M^p] = \begin{cases} 0 & \text{if } \dot{\epsilon}_M^p < \dot{\epsilon}_0 \\ \frac{(\dot{\epsilon}_M^p - \dot{\epsilon}_0)^2 (3\dot{\epsilon}_a - 2\dot{\epsilon}_M^p - \dot{\epsilon}_0)}{(\dot{\epsilon}_a - \dot{\epsilon}_0)^3} & \text{if } \dot{\epsilon}_0 \leq \dot{\epsilon}_M^p \leq \dot{\epsilon}_a, \\ 1 & \text{if } \dot{\epsilon}_a < \dot{\epsilon}_M^p \end{cases}, \quad (4.17)$$

where $\dot{\epsilon}_0$ and $\dot{\epsilon}_a$ represents the upper and lower strain rate limit of the isothermal and adiabatic condition, respectively. Following an associative flow rule, the equivalent plastic strain and internal parameters, including f^* , D_s , and T are obtained at each increment of loading by solving the following partial differential equations [169] in the VUMAT subroutine through an iterative numerical Newton-Raphson scheme [172] as:

$$f_1 = \dot{\epsilon}_v^p \left(3q_1q_2f^* \sinh \left(\frac{3q_2p}{2\sigma_y} \right) \frac{1}{\sigma_y} \right) - \dot{\epsilon}_d^p \left(\frac{2q}{\sigma_y^2} \right) = 0, \quad (4.18)$$

$$f_2 = \Phi(p, q, \bar{\epsilon}_M^p, f^*, D_s, T) = 0, \quad (4.19)$$

where $\dot{\epsilon}_v^p$ and $\dot{\epsilon}_d^p$ is the volumetric and deviatoric component of the equivalent plastic strain rate, respectively. In the work by Zhao et al. [173], more details are found on the

Table 4.1: The constants of the enhanced Zhou et al. model [64] in the current work used in modeling of strain rate-dependent behavior of CSAM Al-Al₂O₃ composites.

Parameter	Value	Unit
E	See Supplementary Fig. 4.15(b)	GPa
ν	0.33	-
A	See Supplementary Fig. 4.15(a)	GPa
n (Eq. (4.12))	0.025	-
q_1	1.5 [170]	-
q_2	1 [170]	-
q_3	2.25 [170]	-
f_0	0.0017 (measured by SEM images)	-
f_c	0.04	-
f_F	0.15	-
ϵ_N	0.3 [90]	-
s_N	0.1 [90]	-
f_N	0.02 [102]	-
n (Eq. (4.7))	10	-
k	0.5 [64]	-
C (Eq. (4.13))	0.006	-
$\dot{\epsilon}_0$	10^{-3}	s ⁻¹
m	1.8	-
T_m	660 [86]	°C
χ	0.9 [212]	-
ρ	2700	kg m ⁻³

implementation of the model. The constants of the Zhou et al. model used for the Al matrix in the current work are listed in Table 4.1, which are either taken from previous studies or tuned within their physical bounds through an iterative process to achieve the best match with the experimentally captured stress-strain responses under both quasi-static and dynamic loading conditions (see Fig. 3(a) in the manuscript). Here, the measured initial porosity in the Al matrix by the SEM analysis is incorporated into the micromechanical model through the f_0 parameter. The elements of the Al matrix were deleted from the calculation process (i.e., updating the stress components and internal variables) when the effective damage parameter (i.e., $D = q_1 f^* + D_s$, see Eq. (4.1)) reached a threshold of nearly one (i.e., 0.99 in our implementation to avoid element distortion) [64] at the integration points of the element. This deletion process of fully damaged elements in the Abaqus/Explicit FE solver allows an implicit reproduction of cracking in the material (see Fig. 6(b) in the manuscript).

The JH2-V model for strain rate-dependent failure of Al_2O_3 ceramic particles

To account for the particle cracking mechanism, the phenomenological viscosity-regularized plasticity JH2-V model [65] was implemented by a VUMAT subroutine in Abaqus/Explicit FE solver. In the JH2-V model, the equivalent plastic strain rate is incorporated into the yield surface by a viscosity parameter, and this leads to mesh regularization. In addition, the original formulation of failure strain proposed by Johnson and Holmquist [85] is revised in the JH2-V model to better account for the asymmetry in damage growth in the material under tension and compression [174]. In the JH2-V model, the normalized strength (σ^*) of ceramic materials is defined as a function of pressure, accumulated damage, and equivalent plastic strain rate as:

$$\sigma^* = \sigma_i^* - D \left(\sigma_i^* - \sigma_f^* \right), \quad (4.20)$$

$$\sigma_i^* = A \left(p^* + T^* (\dot{\epsilon}_p) \right)^N, \text{ and} \quad (4.21)$$

$$\sigma_f^* = B (p^*)^M, \quad (4.22)$$

where the normalized intact and fractured strength is denoted by σ_i^* and σ_f^* , respectively. The accumulated damage in the material is represented by D . $\sigma^* = \frac{\sigma}{\sigma_{HEL}}$, $p^* = \frac{p}{p_{HEL}}$, and $T^* = \frac{T}{p_{HEL}}$ is the normalized equivalent stress, the normalized pressure, and the normalized tensile hydrostatic strength, respectively; σ_{HEL} and p_{HEL} is the equivalent stress and pressure at the Hugoniot elastic limit (HEL), respectively. A , B , M , and N are empirical constants that are required to be tuned for the material. In the JH2-V model, the spall strength (i.e., $T(\dot{\bar{\epsilon}}_p)$) of ceramic materials is linked with the equivalent plastic strain rate according to experimental observations [65] as:

$$T(\dot{\bar{\epsilon}}_p) = \begin{cases} T_0 + \eta \dot{\bar{\epsilon}}_p & \text{if } \dot{\bar{\epsilon}}_p < \dot{\bar{\epsilon}}_p^T, \\ (T_0 + \eta \dot{\bar{\epsilon}}_p) \left(1 + \frac{\eta \dot{\bar{\epsilon}}_p^T}{(T_0 + \eta \dot{\bar{\epsilon}}_p)} \left(\ln \left(\frac{\dot{\bar{\epsilon}}_p}{\dot{\bar{\epsilon}}_p^T} \right) \right) \right) & \text{if } \dot{\bar{\epsilon}}_p \geq \dot{\bar{\epsilon}}_p^T \end{cases} \quad (4.23)$$

where T_0 , η , $\dot{\bar{\epsilon}}_p^T$ denotes the reference tensile strength, the viscosity parameter, and the transitional equivalent plastic strain rate, respectively. $\dot{\bar{\epsilon}}_p^T$ is employed to automatically adjust the size of the failure zone at higher strain rates. When the yield surface of the JH2-V model (see Eq. (4.24)) is met, D begins to grow from 0 to 1 as a function of the equivalent plastic strain ($\bar{\epsilon}_p$) as:

$$\Phi(\sigma, D, \dot{\bar{\epsilon}}_p) = \sigma_q - \sigma_{HEL} \sigma^*, \quad (4.24)$$

$$\dot{D} = \frac{\dot{\bar{\epsilon}}_p}{\bar{\epsilon}_p^f(p)}, \text{ and} \quad (4.25)$$

$$\bar{\epsilon}_p^f(p) = \begin{cases} \bar{\epsilon}_p^{min} & \text{if } p(\sigma) < p_t \\ \frac{p(\sigma) - p_t}{p_c - p_t} (\bar{\epsilon}_p^{max} - \bar{\epsilon}_p^{min}) + \bar{\epsilon}_p^{min}, & p_t \leq p(\sigma) \leq p_c, \\ \bar{\epsilon}_p^{max} & p(\sigma) > p_c \end{cases} \quad (4.26)$$

where σ_q and $\bar{\epsilon}_p^f$ is the von Mises stress and the equivalent plastic strain at failure (i.e., failure strain), respectively. $\bar{\epsilon}_p^{min}$, $\bar{\epsilon}_p^{max}$, p_t , and p_c denotes the empirical constants describing the transitional behavior of ceramic materials from a brittle to a ductile mode with the increase in tri-axial pressure [175]. These constants are achieved by experimentation, including spall [176] and plate impact [177] testing. In the current work, the hydrostatic pressure (p) is defined as a function of volumetric strain (μ) by a polynomial equation of state as:

$$p = \begin{cases} K_1\mu + K_2\mu^2 + K_3\mu^3 + \Delta p, & \text{if } \mu > 0, \\ K_1\mu & \text{if } \mu \leq 0 \end{cases}, \quad (4.27)$$

$$\Delta p_{t+\Delta t} = -K_1\mu_{t+\Delta t} + \sqrt{(K_1\mu_{t+\Delta t} + \Delta P_t)^2 + 2\beta K_1\Delta U}, \quad (4.28)$$

$$\Delta U = U_t - U_{t+\Delta t}, \text{ and} \quad (4.29)$$

$$U = \frac{\sigma_y^2}{6G}, \quad (4.30)$$

where K_1 is the bulk modulus; K_2 and K_3 are the material constants. U is the internal energy; σ_y is the flow stress; and G is the shear modulus. In Eq. (4.28), the pressure increment (Δp) is induced by the bulking effect when damage (D) is bigger than zero, which is calculated based on the conversion of elastic energy to potential hydrostatic energy (see Eq. (4.30)), where the fraction of conversion is determined by β . Table 4.2 lists the JH2-V model constants used for the Al_2O_3 particles in this study. As the criterion for the deletion of fully damaged elements (i.e., an element with $D = 1$ at the integration points), an equivalent plastic strain ($\bar{\epsilon}_p$) larger than 0.2 at the element integration points was considered [62, 100, 156].

Size-dependent matrix/particle interfaces: CZM approach

The bi-linear CZM approach [178, 179] was used to model the interfaces between the Al matrix and Al_2O_3 particles. In this study, the surface-based CZM was employed to mitigate the high computational cost of the micromechanical model instead of the element-based CZM method. The interfacial failure is initiated when a quadratic function of tractions is met:

$$\left(\frac{\langle t_n \rangle}{t_n^0}\right)^2 + \left(\frac{t_s}{t_s^0}\right)^2 + \left(\frac{t_t}{t_t^0}\right)^2 = 1, \quad (4.31)$$

where t_n , t_s , and t_t represent the normal and in-plane traction components acting on the interfaces, respectively. t_n^0 , t_s^0 , and t_t^0 is the corresponding interfacial strength. When the failure criterion (see Eq. (4.31)) is triggered at an interfacial node, the traction components begin to linearly degrade as a function of a scalar damage parameter (D):

Table 4.2: The JH2-V model constants used for Al₂O₃ reinforcing particles accounting for the size of the particles in modeling of strain rate-dependent behavior of CSAM Al-Al₂O₃ composites.

Parameter	Value	Unit
A	0.93 [65]	-
B	0.31 [65]	-
N	0.6 [65]	-
M	0.6 [65]	-
K_1	226	GPa
K_2	0 [65]	GPa
K_3	0 [65]	GPa
T_0	See Fig. 4.2(a)	GPa
HEL	6.25 [65]	GPa
P_{HEL}	7.5 [65]	GPa
ρ	3890	kg m ⁻³
G	155	GPa
HEL	10.5 [65]	GPa
P_{HEL}	4.5 [65]	GPa
η	28×10^{-6} [65]	GPa s
$\dot{\bar{\epsilon}}_p^T$	10000 [156]	s ⁻¹
$\bar{\epsilon}_p^{min}$	0.00015 [65]	-
$\bar{\epsilon}_p^{max}$	0.496 [65]	-
p_t	-0.17 [65]	GPa
p_c	3.02 [65]	GPa
β	1	-

$$t_i = (1 - D) t_i^*, \quad i \in [n, s, t], \quad (4.32)$$

$$D = \begin{cases} 0 & \text{if } \delta_m^{max} \leq \delta_m^0 \\ \frac{\delta_m^f (\delta_m^{max} - \delta_m^0)}{\delta_m^{max} (\delta_m^f - \delta_m^0)} & \text{if } \delta_m^0 < \delta_m^{max} < \delta_f^{max}, \text{ and} \\ 1 & \text{if } \delta_m^{max} \geq \delta_f^{max} \end{cases} \quad (4.33)$$

$$\delta_m^{max} = \sqrt{\langle \delta_n^2 \rangle + \delta_s^2 + \delta_t^2}, \quad (4.34)$$

Table 4.3: The particle size-dependent interfacial properties in modeling of strain rate-dependent behavior of CSAM Al-Al₂O₃ composites.

Parameter	K_{nn}, K_{ss}, K_{tt} [75]	t_n^0, t_s^0, t_t^0	δ_m^f [75]
Value	2E4 GPa.mm ⁻¹	See Fig. 4.2(a)	75×10^{-6} mm

where t_i^* denotes the undamaged traction components that are calculated based on the elastic traction-separation law. δ_m^0 and δ_m^f represent the effective separation at the onset of debonding and complete failure, respectively. Denoted by δ_m^{max} , the effective separation at the nodal points is computed based on the Euclidean norm of the relative separation components (see Eq. (4.34)). Table 4.3 summarizes the CZM constants used for the Al/Al₂O₃ interfaces in the current work.

4.8.2 Supplementary figures

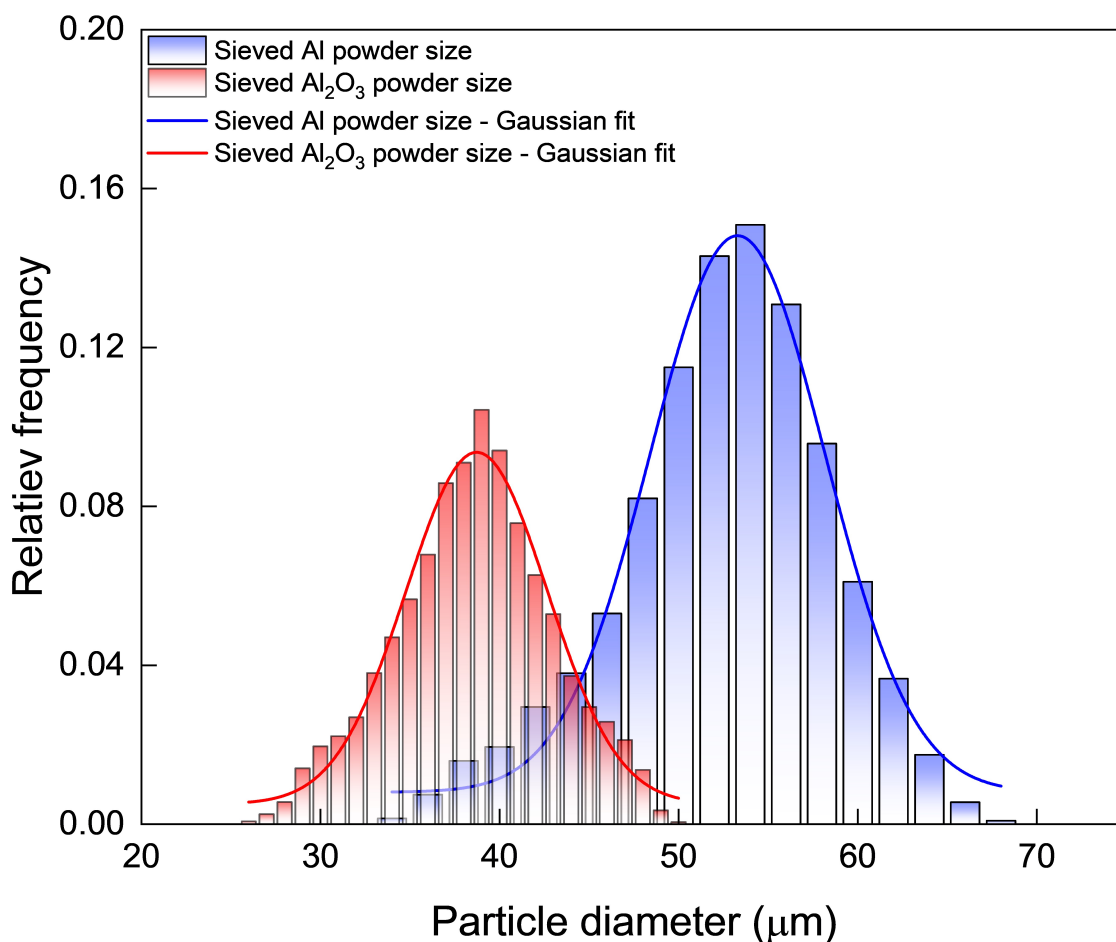


Fig. S 4.12: Particle size distribution of the sieved pure Al (99.0%) and pure α -Al₂O₃ (99.5%) powder used for the fabrication of CSAM Al-46 wt.% Al₂O₃ composites in this study measured by an image-based automated particle size analyzer, resulting in a size of $\sim 53.3 \pm 4.9 \mu\text{m}$ and $\sim 38.7 \pm 3.9 \mu\text{m}$ for the sieved Al and Al₂O₃ powder, respectively. Note that both particle size distributions are fitted by a Gaussian function in the figure.

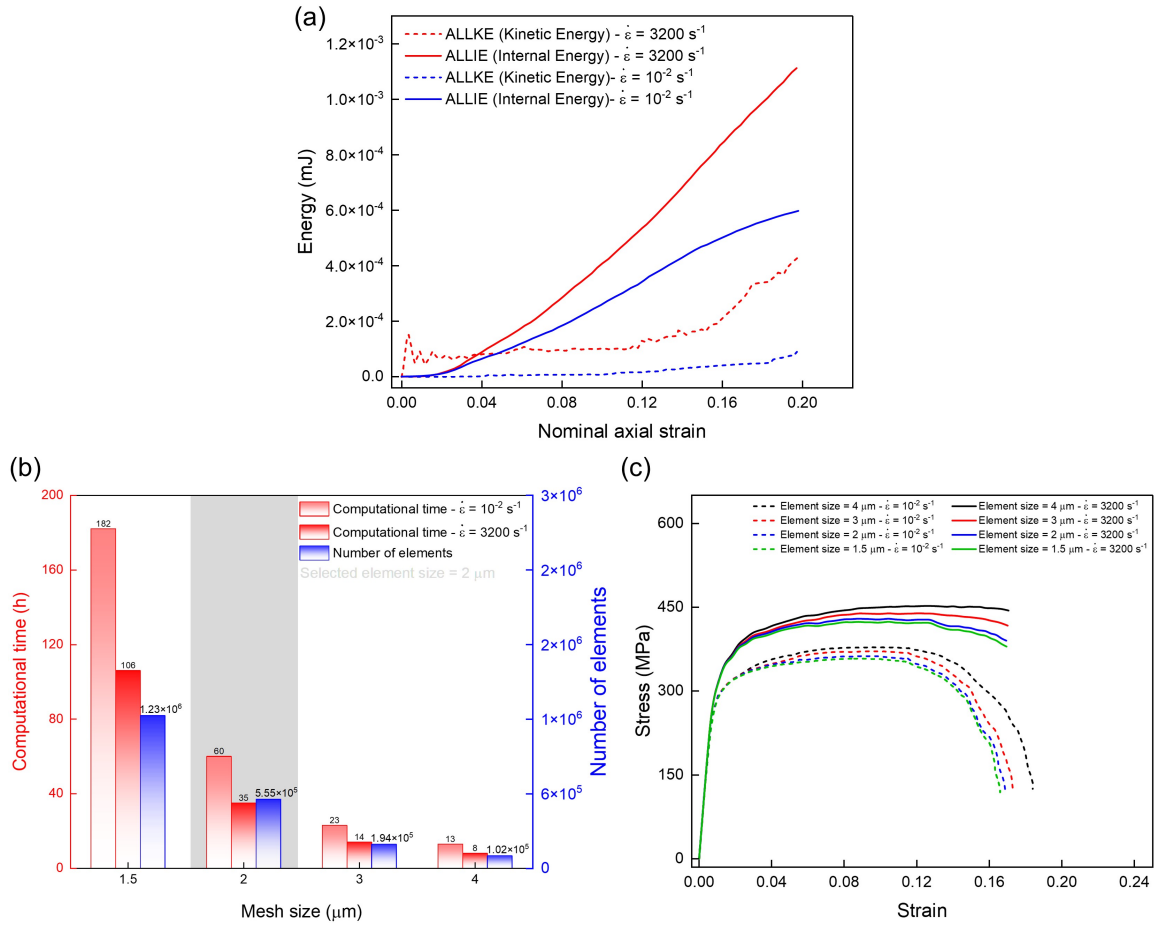


Fig. S 4.13: (a) The balance of the internal (ALLIE) and the kinetic (ALLKE) energies of the RVE model under quasi-static (i.e., $\dot{\epsilon} = 10^{-2} \text{ s}^{-1}$) and dynamic (i.e., $\dot{\epsilon} = 3200 \text{ s}^{-1}$) strain rates. Under quasi-static loading, the figure shows that the ratio of ALLKE/ALLIE holds less than 10% through the course of loading which confirms the quasi-static condition [91]. (b) A summary of the mesh convergence study that involves the element size, the number of elements, and the corresponding computational runtime under quasi-static and dynamic loading. (c) The strain rate-dependent stress-strain responses of the CSAM Al-46 wt.% Al_2O_3 composite captured with different element sizes shown in Fig. 4.13(b). With regard to the convergence pattern of stress-strain responses and the corresponding computational times represented in Fig. 4.13(b), an element size of $2 \mu\text{m}$ was selected for further studies in the current work.

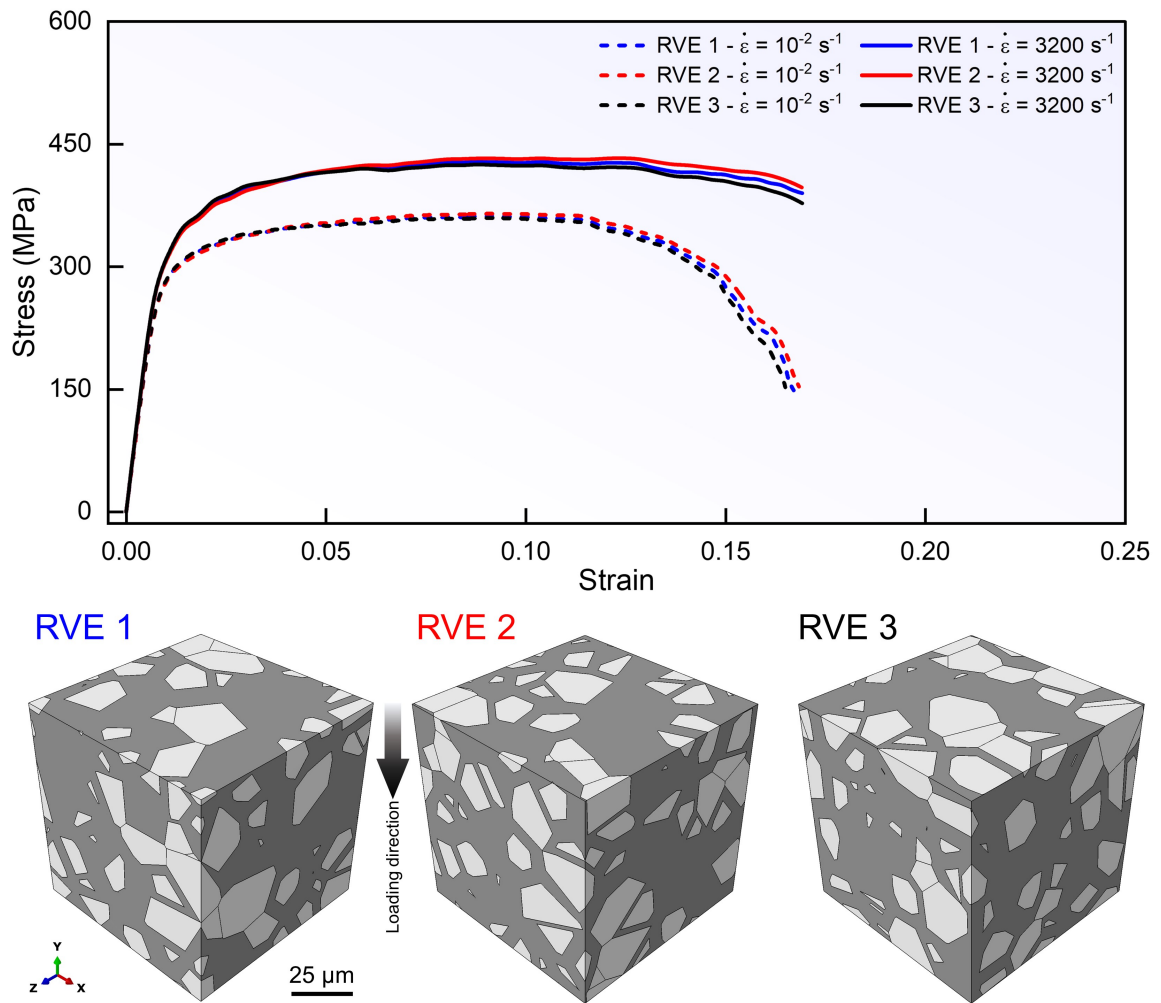


Fig. S 4.14: The effect of RVE randomness on the predicted stress-strain response of the CSAM Al-46 wt.% Al_2O_3 composite under quasi-static and dynamic compression. As seen, the predicted stress-strain curves by different realizations, namely RVE 1, RVE 2, and RVE 3 slightly varies across strain rates which confirms the reliability of the developed micromechanical model of the material. Note that the results obtained by RVE 1 are only reported in the paper for brevity.

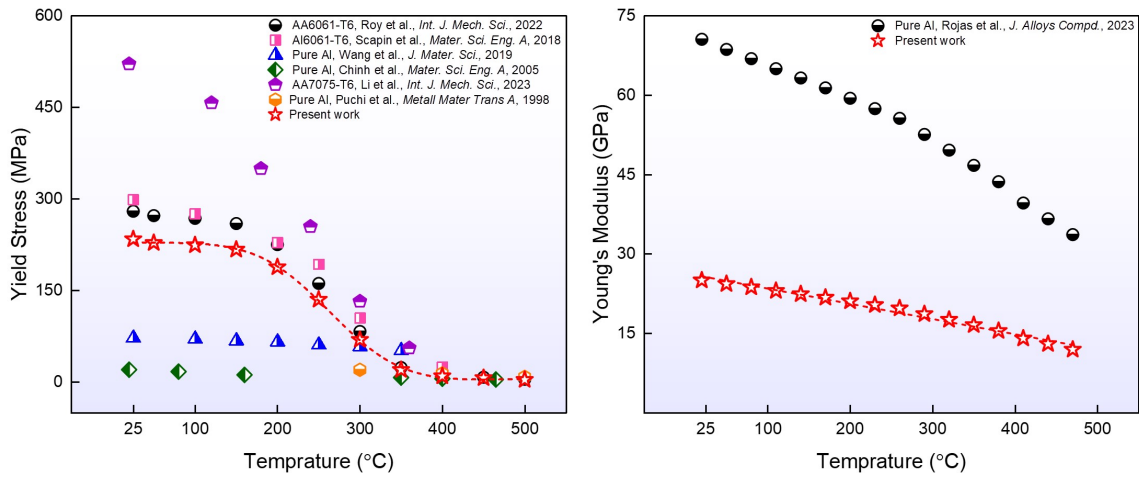


Fig. S 4.15: (a) The temperature-dependent yield strength profile of the Al matrix used as the input to the micromechanical model in this study that is reconstructed based on the corresponding data on Al alloys in the literature. (b) The temperature-dependent Young's modulus of the Al matrix used in the current study as a function of initial temperature, which is reproduced based on data for pure Al in the literature.

Chapter 5

Conclusions & Future Work

5.1 Conclusions

This thesis focused on the development of microstructure-based FE models to provide a foundational understanding of failure progression in CSAM metal-ceramic composites – Al-Al₂O₃ in this research – under different stress states and strain rates. RVEs of the material were generated informed by the SEM characterization in terms of the ceramic particle content, particle size distribution, particle clustering, and porosity in the matrix. Abaqus/Explicit FE solver was employed to conduct the simulations, where the RVE geometries were imported. To capture the stress state- and strain rate-dependent behavior of the materials, state-of-the-art constitutive models were implemented by VUMAT subroutines, including the model by Zhou et al. [64] for the Al matrix, and the JH2-V model [68] for brittle Al₂O₃ ceramic particles. The bi-linear CZM approach [69] was employed to account for the failure of Al and Al₂O₃ interfaces. The micromechanical model was verified with the available experimental data based on the stress-strain responses and post-mortem SEM images under quasi-static and dynamic loading. This thesis is the first of its kind that leveraged an experimentally validated micromechanical FE model to quantitatively unravel the growth history of microscale failure mechanisms of CSAM metal-ceramic composites. Upon validation, the model was further exercised to provide insights into the correlations between the microstructure and macroscale mechanical response of the material

(i.e., stress-strain response) across stress states and strain rates. This thesis achieves its objective of providing a better understanding of the initiation and propagation of key failure mechanisms (i.e., interfacial failure, particle cracking, and matrix failure) of CSAM metal-ceramic composites under different stress states and strain rates in the form of three peer-reviewed papers (Chapter 2, Chapter 3, and Chapter 4). The key outcomes from this thesis are summarized below for further emphasis:

- The strain hardening rate (Θ) analysis by the micromechanical model revealed the existence of a critical strain corresponding to $\Theta_{composite} = \Theta_{matrix}$, which correlates to the activation of the matrix failure mechanism of the CSAM composite under uniaxial compression.
- The quantification framework revealed the sequence of activation of the failure mechanisms of the CSAM Al-46 wt% Al₂O₃ composite – as the material with the highest performance in terms of stiffness and strength – is consistent across different stress states and strain rates: I. Matrix/particle debonding, II. Particle cracking, and III. Matrix ductile failure.
- The ductility of the CSAM composites revealed under compression/shear vanishes when tension dominates due to the earlier activation of debonding and a remarkably faster growth rate (~ 10 times) of the particle cracking mechanism that impedes plastic deformation in the Al matrix.
- The model unravels that with the increase in particle content, the debonding and particle cracking mechanisms are initiated earlier and grow faster. This is likely caused by a higher stress concentration at matrix/particle interfaces due to a smaller mean free path parameter and a more predominant load transfer effect attributable to the higher content of particles and a matrix with higher yield stress induced by the work hardening effect during the cold spray process. Accordingly, the matrix failure is also activated sooner and grows at a higher

rate as the particle content increases and this leads to a lower elongation at failure.

- The model was used to study the effect of particle size on the stress state-dependent behavior of the CSAM Al-46 wt% Al₂O₃ composite: With the decrease in particle size, the compressive flow stress and tensile strength of the composite increased while yielding and flow stress under shear showed no significant difference. This may reflect the minimal contribution of the ceramic particles to the stress-bearing capacity of the composite when shear dominates.
- The model uncovered that the particle debonding mechanism is amplified under dynamic compression loading, which consequently dampens the particle cracking mechanism due to the loss of the load transfer mechanism by the failed interfaces. This computational outcome is consistent with the fractography analysis where particle pull-outs were frequently observed as the indicator of matrix/-particle debonding on the fracture surface under dynamic loading, while particle cracking was rarely detected when compared to quasi-static loading, and this may be attributable to the reverberation of stress waves under high strain rates that induces a tensile-dominated stress state at the interfaces.
- The stress partitioning analysis by the model showed that the stress-bearing capacity of the reinforcing ceramic particles predominantly contributes to the enhanced flow stress and elongation at failure of the CSAM composite under high strain rates which is attributable to the lower propensity of particle cracking under dynamic loading.
- The clustering of particles increases the compressive strength of the material but negatively affects the strain hardening behavior and elongation at failure. The clustering-induced improvement in compressive strength is attributed to the particle/particle load transfer and the decrease in ductility is caused by the

amplified particle cracking mechanism leading to matrix failure with a higher growth rate as per the quantification of the growth history of failure mechanisms by the model.

- The model was further extended to inform on the role of temperature in the material behavior. Under elevated temperatures, the model showed that the debonding and particle cracking mechanisms vanish due to the softened matrix that transfers a lower level of load to the particles, and matrix failure plays the dominant role across the strain rates. Additionally, the strain rate hardening mechanism was found to prevail over the thermal softening mechanism in the CSAM Al-46 wt% Al₂O₃ composite, regardless of the initial temperature and strain rate. This computational outcome agrees with the stress-strain responses experimentally captured under high strain rates that reflect a positive strain hardening rate in addition to the rarely observable sites of melted matrix on the SEM images of fracture surfaces.

5.2 Future work

While this study has provided novel insights into the stress state- and strain rate-dependent failure behavior of the CSAM metal-ceramic composites via microstructure-based FE modeling, there remain several research thrusts to be built on the current work, which will eventually expand the practical applications of better-performing CSAM metal-ceramic composites as coatings and structural materials. Accordingly, emerging from this thesis, the following research directions are recommended:

- Generating 3D EBSD-based RVEs of the material to incorporate the polycrystalline structure of the Al matrix. This requires the implementation of crystal plasticity models [248] that are informed by the grain crystallographic orientations captured by the EBSD analysis. Such models with a more explicit representation of the microstructure will allow us to better understand the role

of the CS manufacturing-induced highly distorted and complex polycrystalline microstructure of the matrix on the stress state-dependent and failure behavior of the CSAM metal-ceramic composite materials.

- Developing 2D micromechanical models from the current 3D FE modeling framework to be employed as dataset generators involving a variety of stress states and strain rates. Here, reducing the order of the current model to 2D is a necessary step to be taken with regard to the high computational cost of the 3D micromechanical model. The generated datasets will feed into the training and validation process of neural networks (e.g., conventional neural network [249] and graph neural network [250]) to be leveraged as surrogate models for establishing microstructure-property-performance relationships. The importance of such ML-based surrogate models stems from serving as a non-destructive testing tool for the real-time prediction of the material mechanical performance (i.e., stress-strain response [251]) as a function of microstructural characterization outcomes in terms of the SEM images (i.e., particle size distribution, particle content, porosity in the matrix, etc).
- Accelerating the concurrent multiscale simulation (namely the direct FE² modeling) [252] of the material as a scale-bridging computational approach for the design and optimization of CSAM metal-ceramic composites for structural applications while simultaneously accounting for their microstructural features. To do so, the present micromechanical FE framework could be leveraged to produce data for training a deep neural network [253] that communicates with the structural scale FE model at the integration points of the elements, which significantly reduces the computational cost of conventional FE² simulations.

5.3 Academic contributions

As of the date of publication of this thesis, the efforts towards the achievement of the objectives of this thesis have resulted in the following academic contributions in the form of journal publications and conference presentations.

Journal publications:

1. Zahra Zaiemyekheh, **Saman Sayahlatifi**, Dan L. Romanyk, and James David Hogan, “[Understanding the effect of microstructure on the failure behavior of additively manufactured Al₂O₃ ceramics: 3D micromechanical modeling](#),” *Materials & Design*, vol. 244, p. 113 167, 2024.
2. **Saman Sayahlatifi**, Zahra Zaiemyekheh, Chenwei Shao, André McDonald, and James David Hogan, “[Strain rate-dependent behavior of cold-sprayed additively manufactured Al-Al₂O₃ composites: Micromechanical modeling and experimentation](#),” *Composites Part B: Engineering*, vol. 280, p. 111 479, 2024.
3. **Saman Sayahlatifi**, Zahra Zaiemyekheh, Chenwei Shao, André McDonald, and James David Hogan, “[Micromechanical damage analysis of Al-Al₂O₃ composites via cold-spray additive manufacturing](#),” *International Journal of Mechanical Sciences*, vol. 259, p. 108 573, 2023.
4. Zahra Zaiemyekheh, Haoyang Li, **Saman Sayahlatifi**, Min Ji, Jie Zheng, Dan L. Romanyk, and James David Hogan, “[Computational finite element modeling of stress-state- and strain-rate-dependent failure behavior of ceramics with experimental validation](#),” *Ceramic International*, vol. 49, no. 9, p. 13878–13895, 2023.
5. James David Hogan, Haoyang Li, **Saman Sayahlatifi**, Sara Sheikhi, Zahra Zaiemyekheh, and Jie Zheng, “[Dynamic behavior of ceramics, ceramic composites, and structures: Experimental and computational mechanics to inform advanced manufacturing](#),” *The iMechanica Journal Club*, 2023.

6. **Saman Sayahlatifi**, Chenwei Shao, André McDonald, and James David Hogan, “3D microstructure-based finite element simulation of cold-sprayed Al-Al₂O₃ composite coatings under quasi-static compression and indentation loading,” *Journal of Thermal Spray Technology*, vol. 31, p. 102–118, 2022.

Conference presentations:

1. **Saman Sayahlatifi**, Zahra Zaiemyekheh, André McDonald, and James David Hogan, “Microstructure-informed data-driven modeling of mechanical behavior of cold-sprayed additively manufactured metal-ceramic composites,” WCCM 2024. Vancouver, British Columbia.
2. **Saman Sayahlatifi**, Zahra Zaiemyekheh, André McDonald, and James David Hogan, “Data-driven modeling of the correlation between the microstructure and macroscale mechanical behavior of cold-sprayed additively manufactured ceramic-metal composites,” CSME 2024. Toronto, Ontario.
3. **Saman Sayahlatifi**, Zahra Zaiemyekheh, Chenwei Shao, André McDonald, and James David Hogan, “A coupled machine learning and micromechanical model of the mechanical behavior of cold-sprayed additively manufactured Al-Al₂O₃ composites,” ITSC 2024. Milan, Italy.
4. **Saman Sayahlatifi**, Chenwei Shao, André McDonald, and James David Hogan, “Strain-rate-dependent mechanical behavior of cold-sprayed additively manufactured Al-Al₂O₃ composites: Micromechanical modeling,” FEGRS 2023. Edmonton, Alberta.
5. **Saman Sayahlatifi**, Zahra Zaiemyekheh, Chenwei Shao, André McDonald, and James David Hogan, “3D microstructure-informed modeling of cold-sprayed additively manufactured Al-Al₂O₃ composites: computational damage analysis,” CSME 2023. Sherbrooke, Quebec.

6. **Saman Sayahlatifi**, Chenwei Shao, André McDonald, and James David Hogan, “Finite element micromechanical modeling of strain-rate-dependent behavior of Al-Al₂O₃ composite coatings via cold spray additive manufacturing,” ITSC 2023. Quebec City, Quebec.
7. **Saman Sayahlatifi**, Zahra Zaiemyekheh, Chenwei Shao, Wania Jibrán, André McDonald, James David Hogan, “On the development of stress state and rate-dependent micromechanical FE models for cold-sprayed ceramic-metal composite coatings,” CSME 2022. Edmonton, Alberta.
8. **Saman Sayahlatifi**, Chenwei Shao, André McDonald, and James David Hogan, “3D microstructure-based FE simulation of cold-sprayed Al-Al₂O₃ composite coatings under indentation and quasi-static compression,” ITSC 2021. Quebec City, Quebec.

Bibliography

- [1] C. U. Hardwicke and Y.-C. Lau, “Advances in thermal spray coatings for gas turbines and energy generation: A review,” *Journal of Thermal Spray Technology*, vol. 22, no. 5, pp. 564–576, 2013.
- [2] S. Yin *et al.*, “Cold spray additive manufacturing and repair: Fundamentals and applications,” *Additive Manufacturing*, vol. 21, pp. 628–650, 2018, ISSN: 2214-8604.
- [3] A. Fardan, C. C. Berndt, and R. Ahmed, “Numerical modelling of particle impact and residual stresses in cold sprayed coatings: A review,” *Surface and Coatings Technology*, vol. 409, p. 126 835, 2021.
- [4] H. Assadi, H. Kreye, F. Gärtner, and T. Klassen, “Cold spraying – a materials perspective,” *Acta Materialia*, vol. 116, pp. 382–407, 2016, ISSN: 1359-6454.
- [5] L. He and M. Hassani, “A review of the mechanical and tribological behavior of cold spray metal matrix composites,” *Journal of Thermal Spray Technology*, vol. 29, no. 7, pp. 1565–1608, 2020.
- [6] H. Wu *et al.*, “3D volume construction methodology for cold spray additive manufacturing,” *Additive Manufacturing*, vol. 92, p. 104 407, 2024.
- [7] S. Kolomy, M. Jopek, J. Sedlak, M. Benc, and J. Zouhar, “Study of dynamic behaviour via Taylor anvil test and structure observation of M300 maraging steel fabricated by the selective laser melting method,” *Journal of Manufacturing Processes*, vol. 125, pp. 283–294, 2024.
- [8] F. Lupi, A. Pacini, and M. Lanzetta, “Laser powder bed additive manufacturing: A review on the four drivers for an online control,” *Journal of Manufacturing Processes*, vol. 103, pp. 413–429, 2023.
- [9] Y. Li *et al.*, “Microstructure, mechanical properties and strengthening mechanisms of IN738LC alloy produced by Electron Beam Selective Melting,” *Additive Manufacturing*, vol. 47, p. 102 371, 2021.
- [10] M. Armstrong, H. Mehrabi, and N. Naveed, “An overview of modern metal additive manufacturing technology,” *Journal of Manufacturing Processes*, vol. 84, pp. 1001–1029, 2022.

- [11] R. Krishna, M. Manjaiah, and C. Mohan, “Chapter 3 - developments in additive manufacturing,” in *Additive Manufacturing*, ser. Woodhead Publishing Reviews: Mechanical Engineering Series, M. Manjaiah, K. Raghavendra, N. Balashanmugam, and J. P. Davim, Eds., Woodhead Publishing, 2021, pp. 37–62.
- [12] L.-Y. Chen, P. Qin, L. Zhang, and L.-C. Zhang, “An overview of additively manufactured metal matrix composites: Preparation, performance, and challenge,” *International Journal of Extreme Manufacturing*, 2024.
- [13] Z. Wang *et al.*, “Hot deformation behavior and microstructure evolution of flaky Ti₃AlC₂ particles reinforced pure Al composite,” *Journal of Alloys and Compounds*, vol. 927, p. 167 118, 2022.
- [14] S. Tang, R. Ummethala, C. Suryanarayana, J. Eckert, K. G. Prashanth, and Z. Wang, “Additive manufacturing of aluminum-based metal matrix composites—a review,” *Advanced engineering materials*, vol. 23, no. 7, p. 2 100 053, 2021.
- [15] K. J. Hodder, H Izadi, A. G. McDonald, and A. P. Gerlich, “Fabrication of aluminum–alumina metal matrix composites via cold gas dynamic spraying at low pressure followed by friction stir processing,” *Materials Science and Engineering: A*, vol. 556, pp. 114–121, 2012.
- [16] K. J. Hodder, J. A. Nychka, and A. G. McDonald, “Comparison of 10 μ m and 20 nm Al-Al₂O₃ Metal Matrix Composite Coatings Fabricated by Low-Pressure Cold Gas Dynamic Spraying,” *Journal of Thermal Spray Technology*, vol. 23, no. 5, pp. 839–848, 2014.
- [17] Q. Wang *et al.*, “The influence of cold and detonation thermal spraying processes on the microstructure and properties of Al-based composite coatings on Mg alloy,” *Surface and Coatings Technology*, vol. 352, pp. 627–633, 2018.
- [18] Y. Tao, T. Xiong, C. Sun, H. Jin, H. Du, and T. Li, “Effect of α -Al₂O₃ on the properties of cold sprayed Al/ α -Al₂O₃ composite coatings on AZ91D magnesium alloy,” *Applied Surface Science*, vol. 256, no. 1, pp. 261–266, 2009.
- [19] C San Marchi, F. Cao, M Kouzeli, and A Mortensen, “Quasistatic and dynamic compression of aluminum-oxide particle reinforced pure aluminum,” *Materials Science and Engineering: A*, vol. 337, no. 1, pp. 202–211, 2002.
- [20] Yashpal, Sumankant, C. S. Jawalkar, A. S. Verma, and N. M. Suri, “Fabrication of Aluminium Metal Matrix Composites with Particulate Reinforcement: A Review,” *Materials Today: Proceedings*, vol. 4, no. 2, Part A, pp. 2927–2936, 2017.
- [21] J. M. Shockley, S Descartes, P Vo, E Irissou, and R. R. Chromik, “The influence of Al₂O₃ particle morphology on the coating formation and dry sliding wear behavior of cold sprayed Al–Al₂O₃ composites,” *Surface and Coatings Technology*, vol. 270, pp. 324–333, 2015.

- [22] O. Meydanoglu, B. Jodoin, and E. S. Kayali, "Microstructure, mechanical properties and corrosion performance of 7075 Al matrix ceramic particle reinforced composite coatings produced by the cold gas dynamic spraying process," *Surface and Coatings Technology*, vol. 235, pp. 108–116, 2013.
- [23] D. Giugliano, D. Barbera, H. Chen, N.-K. Cho, and Y. Liu, "Creep-fatigue and cyclically enhanced creep mechanisms in aluminium based metal matrix composites," *European Journal of Mechanics - A/Solids*, vol. 74, pp. 66–80, 2019.
- [24] Q. Shen, Z. Yuan, H. Liu, X. Zhang, Q. Fu, and Q. Wang, "The damage mechanism of 17vol.%SiCp/Al composite under uniaxial tensile stress," *Materials Science and Engineering: A*, vol. 782, p. 139 274, 2020.
- [25] R. R. Balokhonov *et al.*, "Formation of Bulk Tensile Regions in Metal Matrix Composites and Coatings under Uniaxial and Multiaxial Compression," *Physical Mesomechanics*, vol. 23, no. 2, pp. 135–146, 2020.
- [26] Y. Ma, Z. Chen, M. Wang, D. Chen, N. Ma, and H. Wang, "High cycle fatigue behavior of the in-situ TiB₂/7050 composite," *Materials Science and Engineering: A*, vol. 640, pp. 350–356, 2015.
- [27] P. Peng *et al.*, "Deformation behavior and damage in B₄Cp/6061Al composites: An actual 3D microstructure-based modeling," *Materials Science and Engineering: A*, vol. 781, p. 139 169, 2020.
- [28] R. Fernandez and B. Jodoin, "Cold Spray Aluminum–Alumina Cermet Coatings: Effect of Alumina Content," *Journal of Thermal Spray Technology*, vol. 27, no. 4, pp. 603–623, 2018.
- [29] T. Peat, A. Galloway, A. Toumpis, P. McNutt, and N. Iqbal, "The erosion performance of cold spray deposited metal matrix composite coatings with subsequent friction stir processing," *Applied Surface Science*, vol. 396, pp. 1635–1648, 2017.
- [30] C. Shao, C. Lo, K. Bhagavathula, A. McDonald, and J. Hogan, "High strength particulate aluminum matrix composite design: Synergistic strengthening strategy," *Composites Communications*, vol. 25, p. 100 697, 2021.
- [31] S. A. Alidokht, P. Manimunda, P. Vo, S. Yue, and R. R. Chromik, "Cold spray deposition of a Ni-WC composite coating and its dry sliding wear behavior," *Surface and Coatings Technology*, vol. 308, pp. 424–434, 2016.
- [32] G. Munday, J. Hogan, and A. McDonald, "On the microstructure-dependency of mechanical properties and failure of low-pressure cold-sprayed tungsten carbide-nickel metal matrix composite coatings," *Surface and Coatings Technology*, vol. 396, p. 125 947, 2020.
- [33] W. Jibrán, J. Hogan, and A. McDonald, "Towards optimization of thickness, hardness, and porosity of low-pressure cold sprayed WC-Ni coatings," *The International Journal of Advanced Manufacturing Technology*, 2021.

- [34] K Holmberg *et al.*, “Computational modelling based wear resistance analysis of thick composite coatings,” *Tribology International*, vol. 72, pp. 13–30, 2014.
- [35] K. Holmberg, A. Laukkanen, E. Turunen, and T. Laitinen, “Wear resistance optimisation of composite coatings by computational microstructural modelling,” *Surface and Coatings Technology*, vol. 247, pp. 1–13, 2014.
- [36] M. Parsazadeh, G. Fisher, A. McDonald, and J. Hogan, “Computational investigation of the effect of microstructure on the scratch resistance of tungsten-carbide nickel composite coatings,” *Wear*, vol. 478-479, p. 203 888, 2021, ISSN: 0043-1648.
- [37] R. R. Balokhonov, V. A. Romanova, S Schmauder, and E. S. Emelianova, “A numerical study of plastic strain localization and fracture across multiple spatial scales in materials with metal-matrix composite coatings,” *Theoretical and Applied Fracture Mechanics*, vol. 101, pp. 342–355, 2019.
- [38] Y. T. R. Lee, H. Ashrafizadeh, G. Fisher, and A. McDonald, “Effect of type of reinforcing particles on the deposition efficiency and wear resistance of low-pressure cold-sprayed metal matrix composite coatings,” *Surface and Coatings Technology*, vol. 324, pp. 190–200, 2017.
- [39] L Gyansah *et al.*, “Cold spraying SiC/Al metal matrix composites: effects of SiC contents and heat treatment on microstructure, thermophysical and flexural properties,” *Materials Research Express*, vol. 5, no. 2, p. 26 523, 2018.
- [40] S. I. Gad, M. A. Attia, M. A. Hassan, and A. G. El-Shafei, “Predictive Computational Model for Damage Behavior of Metal-Matrix Composites Emphasizing the Effect of Particle Size and Volume Fraction,” *Materials*, vol. 14, no. 9, 2021.
- [41] S. I. Gad, M. A. Attia, M. A. Hassan, and A. G. El-Shafei, “A random microstructure-based model to study the effect of the shape of reinforcement particles on the damage of elastoplastic particulate metal matrix composites,” *Ceramics International*, vol. 47, no. 3, pp. 3444–3461, 2021, ISSN: 0272-8842.
- [42] S. Ma, X. Zhuang, and X. Wang, “3D micromechanical simulation of the mechanical behavior of an in-situ Al₃Ti/A356 composite,” *Composites Part B: Engineering*, vol. 176, p. 107 115, 2019.
- [43] J. Zhang *et al.*, “3D Microstructure-based finite element modeling of deformation and fracture of SiCp/Al composites,” *Composites Science and Technology*, vol. 123, pp. 1–9, 2016.
- [44] B Amirian, H. Y. Li, and J. D. Hogan, “The mechanical response of a α_2 (Ti₃Al) + γ (TiAl)-submicron grained Al₂O₃ cermet under dynamic compression: Modeling and experiment,” *Acta Materialia*, vol. 181, pp. 291–308, 2019.
- [45] A. Rasool and H. J. Böhm, “Effects of particle shape on the macroscopic and microscopic linear behaviors of particle reinforced composites,” *International Journal of Engineering Science*, vol. 58, pp. 21–34, 2012.

- [46] J. Liu, X. Huang, K. Zhao, Z. Zhu, X. Zhu, and L. An, “Effect of reinforcement particle size on quasistatic and dynamic mechanical properties of Al-Al₂O₃ composites,” *Journal of Alloys and Compounds*, vol. 797, pp. 1367–1371, 2019.
- [47] Q. Liu *et al.*, “The influence of particles size and its distribution on the degree of stress concentration in particulate reinforced metal matrix composites,” *Materials Science and Engineering: A*, vol. 731, pp. 351–359, 2018.
- [48] W. Jiang, Y. Li, and J. Su, “Modified GTN model for a broad range of stress states and application to ductile fracture,” *European Journal of Mechanics - A/Solids*, vol. 57, pp. 132–148, 2016.
- [49] L. E. B. Dæhli, D. Morin, T. Børvik, A. Benallal, and O. S. Hopperstad, “A Numerical Study on Ductile Failure of Porous Ductile Solids With Rate-Dependent Matrix Behavior,” *Journal of Applied Mechanics*, vol. 87, no. 3, Dec. 2019, 031014, ISSN: 0021-8936.
- [50] W. Jibrán, P. Wanjara, J. Gholipour Baradari, M. Ophelia Jarligo, and A. McDonald, “Localised surface modification of high-strength aluminium–alumina metal matrix composite coatings using cold spraying and friction stir processing,” *Advances in Applied Ceramics*, vol. 122, no. 3-4, pp. 181–196, 2023.
- [51] S. Sayahlatifi, Z. Zaiemyekheh, C. Shao, A. McDonald, and J. D. Hogan, “Strain rate-dependent behavior of cold-sprayed additively manufactured Al–Al₂O₃ composites: Micromechanical modeling and experimentation,” *Composites Part B: Engineering*, vol. 280, p. 111 479, 2024, ISSN: 1359-8368.
- [52] H. Karakoç, Ş. Karabulut, and R. Çıtak, “Study on mechanical and ballistic performances of boron carbide reinforced Al 6061 aluminum alloy produced by powder metallurgy,” *Composites Part B: Engineering*, vol. 148, pp. 68–80, 2018.
- [53] M. Granata, G. Gautier di Confienigo, and F. Bellucci, “High-pressure cold spray coatings for aircraft brakes application,” *Metals*, vol. 12, no. 10, p. 1558, 2022.
- [54] Z. Zhang, F. Liu, E.-H. Han, L. Xu, and P. C. Uzoma, “Effects of Al₂O₃ on the microstructures and corrosion behavior of low-pressure cold gas sprayed Al 2024-Al₂O₃ composite coatings on AA 2024-T3 substrate,” *Surface and Coatings Technology*, vol. 370, pp. 53–68, 2019.
- [55] L. Weng, T. Fan, M. Wen, and Y. Shen, “Three-dimensional multi-particle FE model and effects of interface damage, particle size and morphology on tensile behavior of particle reinforced composites,” *Composite Structures*, vol. 209, pp. 590–605, 2019.
- [56] X. Gao, X. Zhang, A. Li, and L. Geng, “Plastic deformation and fracture behaviors in particle-reinforced aluminum composites: A numerical approach using an enhanced finite element model,” *Journal of Composite Materials*, pp. 1977–1985, 2019.

- [57] J.-T. Zhang, L.-S. Liu, P.-C. Zhai, Z.-Y. Fu, and Q.-J. Zhang, “The prediction of the dynamic responses of ceramic particle reinforced MMCs by using multi-particle computational micro-mechanical method,” *Composites Science and Technology*, vol. 67, no. 13, pp. 2775–2785, 2007.
- [58] J.-T. Zhang, H.-J. Shi, L.-S. Liu, and P.-C. Zhai, “Numerical analysis on the effects of particle configuration on the damage and mechanical properties of particle reinforced MMCs under dynamic compression,” *Computational Materials Science*, vol. 50, no. 2, pp. 496–502, 2010.
- [59] C. Yang, Y. Kim, S. Ryu, and G. X. Gu, “Prediction of composite microstructure stress-strain curves using convolutional neural networks,” *Materials & Design*, vol. 189, p. 108509, 2020.
- [60] R. Shoghi and A. Hartmaier, “A machine learning constitutive model for plasticity and strain hardening of polycrystalline metals based on data from micromechanical simulations,” *Machine Learning: Science and Technology*, vol. 5, no. 2, p. 025008, 2024.
- [61] Q. Wu, W. Xu, and L. Zhang, “Microstructure-based modelling of fracture of particulate reinforced metal matrix composites,” *Composites Part B: Engineering*, vol. 163, pp. 384–392, 2019.
- [62] S. Sayahlatifi, C. Shao, A. McDonald, and J. Hogan, “3D microstructure-based finite element simulation of cold-sprayed Al-Al₂O₃ composite coatings under quasi-static compression and indentation loading,” *Journal of Thermal Spray Technology*, pp. 1–17, 2021.
- [63] H. Li, P. Motamedi, and J. D. Hogan, “On the rate-dependency of mechanical properties and failure mechanisms of a ($\gamma + \alpha_2$) - TiAl/Ti₃Al-Al₂O₃ cermet,” *Materials Science and Engineering: A*, vol. 791, p. 139747, 2020.
- [64] J. Zhou, X. Gao, J. C. Sobotka, B. A. Webler, and B. V. Cockeram, “On the extension of the Gurson-type porous plasticity models for prediction of ductile fracture under shear-dominated conditions,” *International Journal of Solids and Structures*, vol. 51, no. 18, pp. 3273–3291, 2014.
- [65] E. Simons, J. Weerheijm, and L. Sluys, “Simulating brittle and ductile response of alumina ceramics under dynamic loading,” *Engineering Fracture Mechanics*, vol. 216, p. 106481, 2019, ISSN: 0013-7944.
- [66] S. A. Alidokht, S. Yue, and R. R. Chromik, “Effect of WC morphology on dry sliding wear behavior of cold-sprayed Ni-WC composite coatings,” *Surface and Coatings Technology*, vol. 357, pp. 849–863, 2019.
- [67] S. Ahmad Alidokht, P. Vo, S. Yue, and R. R. Chromik, “Erosive wear behavior of Cold-Sprayed Ni-WC composite coating,” *Wear*, vol. 376-377, pp. 566–577, 2017.
- [68] E. Simons, J. Weerheijm, and L. Sluys, “A viscosity regularized plasticity model for ceramics,” *European Journal of Mechanics - A/Solids*, vol. 72, pp. 310–328, 2018, ISSN: 0997-7538.

- [69] P. Camanho and C. Dávila, “Mixed-Mode Decohesion Finite Elements for the Simulation of Delamination in Composite Materials,” 2002.
- [70] M. MacLean, Z. Farhat, G. Jarjoura, E. Fayyad, A. Abdullah, and M. Hassan, “Fabrication and investigation of the scratch and indentation behaviour of new generation Ni-P-nano-NiTi composite coating for oil and gas pipelines,” *Wear*, vol. 426-427, pp. 265–276, 2019, 22nd International Conference on Wear of Materials, ISSN: 0043-1648.
- [71] Q. Sun, S. Asqardoust, A. Sarmah, and M. K. Jain, “Elastoplastic analysis of AA7075-O aluminum sheet by hybrid micro-scale representative volume element modeling with really-distributed particles and in-situ SEM experimental testing,” *Journal of Materials Science & Technology*, vol. 123, pp. 201–221, 2022, ISSN: 1005-0302.
- [72] Z. Yang, J. Fan, Y. Liu, Z. Yang, Y. Kang, and J. Nie, “Effect of combination variation of particle and matrix on the damage evolution and mechanical properties of particle reinforced metal matrix composites,” *Materials Science and Engineering: A*, vol. 806, p. 140 804, 2021, ISSN: 0921-5093.
- [73] W. Dai, H. Wang, Q. Guan, D. Li, Y. Peng, and C. N. Tomé, “Studying the micromechanical behaviors of a polycrystalline metal by artificial neural networks,” *Acta Materialia*, vol. 214, p. 117 006, 2021, ISSN: 1359-6454.
- [74] X. Gao, X. Zhang, M. Qian, and L. Geng, “Effect of reinforcement shape on fracture behaviour of SiC/Al composites with network architecture,” *Composite Structures*, vol. 215, pp. 411–420, 2019.
- [75] S. Sayahlatifi, Z. Zaiemyekheh, C. Shao, A. McDonald, and J. D. Hogan, “Micromechanical damage analysis of Al-Al₂O₃ composites via cold-spray additive manufacturing,” *International Journal of Mechanical Sciences*, vol. 259, p. 108 573, 2023.
- [76] R. Balokhonov, V. Romanova, and A. Kulkov, “Microstructure-based analysis of deformation and fracture in metal-matrix composite materials,” *Engineering Failure Analysis*, vol. 110, p. 104 412, 2020, ISSN: 1350-6307.
- [77] J. M. Shockley, E. F. Rauch, R. R. Chromik, and S Descartes, “TEM microanalysis of interfacial structures after dry sliding of cold sprayed Al-Al₂O₃,” *Wear*, vol. 376-377, pp. 1411–1417, 2017.
- [78] G. Bolelli, A. Candeli, H. Koivuluoto, L. Lusvarghi, T. Manfredini, and P. Vuoristo, “Microstructure-based thermo-mechanical modelling of thermal spray coatings,” *Materials & Design*, vol. 73, pp. 20–34, 2015.
- [79] M. A. Eltaher and A Wagih, “Micromechanical modeling of damage in elastoplastic nanocomposites using unit cell representative volume element and cohesive zone model,” *Ceramics International*, 2020.

- [80] R. Ekici, M Kemal Apalak, M. Yildirim, and F. Nair, “Simulated and actual micro-structure models on the indentation behaviors of particle reinforced metal matrix composites,” *Materials Science and Engineering: A*, vol. 606, pp. 290–298, 2014.
- [81] H. K. Park, J. Jung, and H. S. Kim, “Three-dimensional microstructure modeling of particulate composites using statistical synthetic structure and its thermo-mechanical finite element analysis,” *Computational Materials Science*, vol. 126, pp. 265–271, 2017.
- [82] A. S. Shedbale, I. V. Singh, and B. K. Mishra, “Heterogeneous and homogenized models for predicting the indentation response of particle reinforced metal matrix composites,” *International Journal of Mechanics and Materials in Design*, vol. 13, no. 4, pp. 531–552, 2017.
- [83] V Tvergaard and A Needleman, “Analysis of the cup-cone fracture in a round tensile bar,” *Acta Metallurgica*, vol. 32, no. 1, pp. 157–169, 1984.
- [84] G. I. Barenblatt, “The Mathematical Theory of Equilibrium Cracks in Brittle Fracture,” in *Advances in Applied Mechanics*, H. L. Dryden, T. von Kármán, G Kuerti, F. H. van den Dungen, and L Howarth, Eds., vol. 7, Elsevier, 1962, pp. 55–129, ISBN: 0065-2156.
- [85] G. R. Johnson and T. J. Holmquist, “An improved computational constitutive model for brittle materials,” *AIP Conference Proceedings*, vol. 309, no. 1, pp. 981–984, 1994.
- [86] M. Dewar, A. McDonald, and A. Gerlich, “Interfacial heating during low-pressure cold-gas dynamic spraying of aluminum coatings,” *Journal of Materials Science*, vol. 47, pp. 184–198, 2012.
- [87] *VIC-2D, Correlated Solutions Inc., Irmo, South Carolina.*
- [88] *ASTM C1425-15, Standard Test Method for Monotonic Compressive Strength of Advanced Ceramics at Ambient Temperature, West Conshohocken (PA).*
- [89] M. Parsazadeh, G. Fisher, A. McDonald, and J. D. Hogan, “Computational modelling of the effect of microstructure on the abrasive wear resistance of tungsten-carbide nickel composite coatings under sub-critical cyclic impact loading,” *Ceramics International*, vol. 48, no. 10, pp. 14 338–14 348, 2022, ISSN: 0272-8842.
- [90] N. K. Sharma, R. K. Mishra, and S. Sharma, “3D micromechanical analysis of thermo-mechanical behavior of Al₂O₃/Al metal matrix composites,” *Computational Materials Science*, vol. 115, pp. 192–201, 2016, ISSN: 0927-0256.
- [91] S. Sayahlatifi, G. Rahimi, and A. Bokaei, “The quasi-static behavior of hybrid corrugated composite/balsa core sandwich structures in four-point bending: Experimental study and numerical simulation,” *Engineering Structures*, vol. 210, p. 110 361, 2020, ISSN: 0141-0296.

- [92] B. Amirian, H. Li, and J. Hogan, “An experimental and numerical study of novel nano-grained $(\gamma + \alpha_2)$ -TiAl/Al₂O₃ cermets,” *Materials Science and Engineering: A*, vol. 744, pp. 570–580, 2019, ISSN: 0921-5093.
- [93] V. Tvergaard and A. Needleman, “Analysis of the cup-cone fracture in a round tensile bar,” *Acta Metallurgica*, vol. 32, no. 1, pp. 157–169, 1984, ISSN: 0001-6160.
- [94] S. Gatea, H. Ou, B. Lu, and G. McCartney, “Modelling of ductile fracture in single point incremental forming using a modified GTN model,” *Engineering Fracture Mechanics*, vol. 186, pp. 59–79, 2017.
- [95] A. L. Gurson, “Continuum Theory of Ductile Rupture by Void Nucleation and Growth: Part I—Yield Criteria and Flow Rules for Porous Ductile Media,” *Journal of Engineering Materials and Technology*, vol. 99, no. 1, pp. 2–15, 1977.
- [96] A. Kami, B. M. Dariani, A. Sadough Vanini, D. S. Comsa, and D. Banabic, “Numerical determination of the forming limit curves of anisotropic sheet metals using GTN damage model,” *Journal of Materials Processing Technology*, vol. 216, pp. 472–483, 2015.
- [97] F. Abbassi, S. Mistou, and A. Zghal, “Failure analysis based on microvoid growth for sheet metal during uniaxial and biaxial tensile tests,” *Materials & Design*, vol. 49, pp. 638–646, 2013.
- [98] V. Tvergaard, “Influence of void nucleation on ductile shear fracture at a free surface,” *Journal of the Mechanics and Physics of Solids*, vol. 30, no. 6, pp. 399–425, 1982.
- [99] C. Chu and A Needleman, “Void nucleation effects in biaxially stretched sheets,” 1980.
- [100] *Abaqus, User’s Manual, Version 6.14, Dassault Systèmes, 2014.*
- [101] N. K. Sharma, R. K. Misra, and S. Sharma, “Modeling of thermal expansion behavior of densely packed Al/SiC composites,” *International Journal of Solids and Structures*, vol. 102-103, pp. 77–88, 2016.
- [102] N. Benseddiq and A. Imad, “A ductile fracture analysis using a local damage model,” *International Journal of Pressure Vessels and Piping*, vol. 85, no. 4, pp. 219–227, 2008, ISSN: 0308-0161.
- [103] J Venkatesan, M. A. Iqbal, and V Madhu, “Experimental and numerical study of the dynamic response of B4C ceramic under uniaxial compression,” *Thin-Walled Structures*, vol. 154, p. 106 785, 2020.
- [104] M. R. I. Islam, J. Q. Zheng, and R. C. Batra, “Ballistic performance of ceramic and ceramic-metal composite plates with JH1, JH2 and JHB material models,” *International Journal of Impact Engineering*, vol. 137, p. 103 469, 2020.
- [105] Y. Zhu, G. R. Liu, Y. Wen, C. Xu, W. Niu, and G. Wang, “Back-Spalling process of an Al₂O₃ ceramic plate subjected to an impact of steel ball,” *International Journal of Impact Engineering*, vol. 122, pp. 451–471, 2018.

- [106] D. S. Dugdale, “Yielding of steel sheets containing slits,” *Journal of the Mechanics and Physics of Solids*, vol. 8, no. 2, pp. 100–104, 1960.
- [107] D. V. Kubair, P. H. Geubelle, and Y. Y. Huang, “Analysis of a rate-dependent cohesive model for dynamic crack propagation,” *Engineering Fracture Mechanics*, vol. 70, no. 5, pp. 685–704, 2002.
- [108] G. V. Jagadeesh and S. Gangi Setti, “A review on micromechanical methods for evaluation of mechanical behavior of particulate reinforced metal matrix composites,” *Journal of Materials Science*, vol. 55, no. 23, pp. 9848–9882, 2020.
- [109] Q. Meng and Z. Wang, “Prediction of interfacial strength and failure mechanisms in particle-reinforced metal-matrix composites based on a micromechanical model,” *Engineering Fracture Mechanics*, vol. 142, pp. 170–183, 2015, ISSN: 0013-7944.
- [110] A Sazgar, M. R. Movahhedy, M Mahnama, and S Sohrabpour, “Development of a molecular dynamic based cohesive zone model for prediction of an equivalent material behavior for Al/Al₂O₃ composite,” *Materials Science and Engineering: A*, vol. 679, pp. 116–122, 2017.
- [111] X.-T. Luo, G.-J. Yang, and C.-J. Li, “Multiple strengthening mechanisms of cold-sprayed cBNp/NiCrAl composite coating,” *Surface and Coatings Technology*, vol. 205, no. 20, pp. 4808–4813, 2011.
- [112] J. Wang, C. Li, Y. Wan, C. Zhang, J. Ran, and M. W. Fu, “Size effect on the shear damage under low stress triaxiality in micro-scaled plastic deformation of metallic materials,” *Materials & Design*, vol. 196, p. 109 107, 2020.
- [113] K. Tun *et al.*, “Enhancing tensile and compressive strengths of magnesium using nanosize (Al₂O₃+Cu) hybrid reinforcements,” *Journal of Composite Materials*, vol. 46, no. 15, pp. 1879–1887, 2012.
- [114] C. Pande and K. Cooper, “Nanomechanics of hall–petch relationship in nanocrystalline materials,” *Progress in Materials Science*, vol. 54, no. 6, pp. 689–706, 2009, “THE NABARRO LEGACY – PERSPECTIVES FOR ADVANCED MATERIALS IN THE 21ST CENTURY” A collection of invited lectures at the MRS Spring Meeting 2008, ISSN: 0079-6425.
- [115] H. Lim, C. C. Battaile, J. E. Bishop, and J. W. Foulk, “Investigating mesh sensitivity and polycrystalline rves in crystal plasticity finite element simulations,” *International Journal of Plasticity*, vol. 121, pp. 101–115, 2019, ISSN: 0749-6419.
- [116] G. Munday, J. Hogan, and A. McDonald, “On the microstructure-dependency of mechanical properties and failure of low-pressure cold-sprayed tungsten carbide-nickel metal matrix composite coatings,” *Surface and Coatings Technology*, vol. 396, p. 125 947, 2020, ISSN: 0257-8972.
- [117] A. B. Hardness, “Standard test method for microindentation hardness of materials,” *ASTM Committee: West Conshohocken, PA, USA*, vol. 384, p. 399, 1999.

- [118] R. Ekici, M Kemal Apalak, M. Yıldırım, and F. Nair, “Effects of random particle dispersion and size on the indentation behavior of SiC particle reinforced metal matrix composites,” *Materials & Design*, vol. 31, no. 6, pp. 2818–2833, 2010.
- [119] E. ISO *et al.*, “Metallic materials,” in *Vickers hardness test. Part 1: test method*, 2005.
- [120] Y. L. Shen and Y. L. Guo, “Indentation modelling of heterogeneous materials,” *Modelling and Simulation in Materials Science and Engineering*, vol. 9, no. 5, pp. 391–398, 2001.
- [121] R Pereyra and Y. L. Shen, “Characterization of Indentation-induced ‘Particle Crowding’ in Metal Matrix Composites,” *International Journal of Damage Mechanics*, vol. 14, no. 3, pp. 197–213, 2005.
- [122] J. Zhang, X. Zhang, Q. Wang, B. Xiao, and Z. Ma, “Simulations of deformation and damage processes of SiCp/Al composites during tension,” *Journal of Materials Science Technology*, vol. 34, no. 4, pp. 627–634, 2018, ISSN: 1005-0302.
- [123] S. Ma, X. Zhuang, and X. Wang, “Particle distribution-dependent micromechanical simulation on mechanical properties and damage behaviors of particle reinforced metal matrix composites,” *Journal of Materials Science*, vol. 56, no. 11, pp. 6780–6798, 2021.
- [124] S. Amirkhanlou, M. R. Rezaei, B. Niroumand, and M. R. Toroghinejad, “Refinement of microstructure and improvement of mechanical properties of Al/Al₂O₃ cast composite by accumulative roll bonding process,” *Materials Science and Engineering: A*, vol. 528, no. 6, pp. 2548–2553, 2011.
- [125] D Garbiec, M Jurczyk, N Levintant-Zayonts, and T Mościcki, “Properties of Al–Al₂O₃ composites synthesized by spark plasma sintering method,” *Archives of Civil and Mechanical Engineering*, vol. 15, no. 4, pp. 933–939, 2015.
- [126] M. Rahimian, N. Parvin, and N. Ehsani, “Investigation of particle size and amount of alumina on microstructure and mechanical properties of al matrix composite made by powder metallurgy,” *Materials Science and Engineering: A*, vol. 527, no. 4, pp. 1031–1038, 2010, ISSN: 0921-5093.
- [127] H. J. Böhm and W Han, “Comparisons between three-dimensional and two-dimensional multi-particle unit cell models for particle reinforced metal matrix composites,” *Modelling and Simulation in Materials Science and Engineering*, vol. 9, no. 2, pp. 47–65, 2001.
- [128] E. Soppa, J. Nellesen, V. Romanova, G. Fischer, H.-A. Crostack, and F. Beckmann, “Impact of 3D-model thickness on FE-simulations of microstructure,” *Materials Science and Engineering: A*, vol. 527, no. 3, pp. 802–811, 2010.
- [129] H. Qing, “Automatic generation of 2D micromechanical finite element model of silicon–carbide/aluminum metal matrix composites: Effects of the boundary conditions,” *Materials & Design*, vol. 44, pp. 446–453, 2013.

- [130] K. Dorhmi, L. Morin, K. Derrien, Z. Hadjem-Hamouche, and J.-P. Chevalier, “A homogenization-based damage model for stiffness loss in ductile metal-matrix composites,” *Journal of the Mechanics and Physics of Solids*, vol. 137, p. 103 812, 2020.
- [131] A Góral, W Żórawski, and M Makrenek, “The effect of the standoff distance on the microstructure and mechanical properties of cold sprayed Cr₃C₂-25(Ni₂₀Cr) coatings,” *Surface and Coatings Technology*, vol. 361, pp. 9–18, 2019.
- [132] B. Liu, W. Huang, L. Huang, and H. Wang, “Size-dependent compression deformation behaviors of high particle content B₄C/Al composites,” *Materials Science and Engineering: A*, vol. 534, pp. 530–535, 2012.
- [133] M. Groeber, S. Ghosh, M. D. Uchic, and D. M. Dimiduk, “A framework for automated analysis and simulation of 3D polycrystalline microstructures.: Part 1: Statistical characterization,” *Acta Materialia*, vol. 56, no. 6, pp. 1257–1273, 2008.
- [134] J Genée, S Berbenni, N Gey, R. A. Lebensohn, and F Bonnet, “Particle inter-spacing effects on the mechanical behavior of a Fe–TiB₂ metal matrix composite using FFT-based mesoscopic field dislocation mechanics,” *Advanced Modeling and Simulation in Engineering Sciences*, vol. 7, no. 1, p. 6, 2020.
- [135] W Kayser, A Bezold, and C Broeckmann, “EBSD-based FEM simulation of residual stresses in a WC₆wt.-%Co hardmetal,” *International Journal of Refractory Metals and Hard Materials*, vol. 73, pp. 139–145, 2018.
- [136] X. Xie *et al.*, “Al matrix composites fabricated by solid-state cold spray deposition: A critical review,” *Journal of Materials Science & Technology*, vol. 86, pp. 20–55, 2021, ISSN: 1005-0302.
- [137] E. Irissou, J.-G. Legoux, B. Arsenault, and C. Moreau, “Investigation of Al-Al₂O₃ cold spray coating formation and properties,” *Journal of Thermal Spray Technology*, vol. 16, no. 5, pp. 661–668, 2007.
- [138] J Sobczak, N Sobczak, P Darlak, Z Slawinski, R Asthana, and P Rohatgi, “Thermal fatigue resistance of discontinuously reinforced cast aluminum-matrix composites,” *Journal of Materials Engineering and Performance*, vol. 11, no. 6, pp. 595–602, 2002.
- [139] H. Ezatpour, M. Torabi-Parisi, and S. Sajjadi, “Microstructure and mechanical properties of extruded Al/Al₂O₃ composites fabricated by stir-casting process,” *Transactions of Nonferrous Metals Society of China*, vol. 23, no. 5, pp. 1262–1268, 2013, ISSN: 1003-6326.
- [140] K. Yang, W. Li, P. Niu, X. Yang, and Y. Xu, “Cold sprayed AA2024/Al₂O₃ metal matrix composites improved by friction stir processing: Microstructure characterization, mechanical performance and strengthening mechanisms,” *Journal of Alloys and Compounds*, vol. 736, pp. 115–123, 2018, ISSN: 0925-8388.

- [141] C. Huang, A. List, L. Wiehler, M. Schulze, F. Gärtner, and T. Klassen, “Cold spray deposition of graded Al-SiC composites,” *Additive Manufacturing*, vol. 59, p. 103 116, 2022, ISSN: 2214-8604.
- [142] X. Xie *et al.*, “Cold spray additive manufacturing of metal matrix composites (MMCs) using a novel nano-TiB₂-reinforced 7075Al powder,” *Journal of Alloys and Compounds*, vol. 819, p. 152 962, 2020, ISSN: 0925-8388.
- [143] L. Zhao *et al.*, “Effect of particle size on ceramic particle content in cold sprayed Al-based metal matrix composite coating,” *Journal of Thermal Spray Technology*, pp. 1–12, 2022.
- [144] C. Shao *et al.*, “Nano-additive manufacturing of multilevel strengthened aluminum matrix composites,” *International Journal of Extreme Manufacturing*, vol. 5, no. 1, p. 015 102, 2022.
- [145] H. Lee *et al.*, “Effects of SiC particulate size on dynamic compressive properties in 7075-T6 Al-SiCp composites,” *Materials Science and Engineering: A*, vol. 738, pp. 412–419, 2018, ISSN: 0921-5093.
- [146] T. Lee *et al.*, “Overcoming brittleness of high volume fraction Al/SiCp composites by controlling interface characteristics,” *Materials Design*, vol. 222, p. 111 038, 2022, ISSN: 0264-1275.
- [147] M. Gao *et al.*, “Enhanced strength-ductility synergy in a boron carbide reinforced aluminum matrix composite at 77 k,” *Journal of Alloys and Compounds*, vol. 818, p. 153 310, 2020, ISSN: 0925-8388.
- [148] Y. Wang *et al.*, “Mechanical response and damage evolution of bio-inspired B₄C-reinforced 2024Al composites subjected to quasi-static and dynamic loadings,” *Materials Science and Engineering: A*, vol. 840, p. 142 991, 2022, ISSN: 0921-5093.
- [149] L. Nan *et al.*, “Numerical evaluation and experimental verification of mechanical properties and fracture behavior for TiB₂/Cu composites prepared by in-situ mixing casting,” *Journal of Alloys and Compounds*, vol. 895, p. 162 475, 2022, ISSN: 0925-8388.
- [150] Y. Peng *et al.*, “3D multiscale tri-level finite element analysis of aluminum matrix composites with Nano & Micro hybrid inclusions,” *Composite Structures*, vol. 305, p. 116 545, 2023, ISSN: 0263-8223.
- [151] N. Liu *et al.*, “Experimental verification and numerical analysis on plastic deformation and mechanical properties of the in-situ TiB₂ homogeneous composites and TiB₂/Cu network composites prepared by powder metallurgy,” *Journal of Alloys and Compounds*, vol. 920, p. 165 897, 2022, ISSN: 0925-8388.
- [152] P. Sirvent, M. Garrido, S. Lozano-Perez, and P. Poza, “Oscillating and unidirectional sliding wear behaviour of cold sprayed Ti-4Al-4V coating on Ti-4Al-4V substrate,” *Surface and Coatings Technology*, vol. 382, p. 125 152, 2020, ISSN: 0257-8972.

- [153] C. Jiang, D. Lu, M. Zhou, B. Kou, and W. Gong, “A numerical study of the mechanical and fracture properties of ZTA (zirconia toughened alumina)p/40Cr steel spatial spherical dot matrix composite,” *International Journal of Solids and Structures*, vol. 260-261, p. 112 047, 2023, ISSN: 0020-7683.
- [154] R. Balokhonov, V. Romanova, O. Zinovieva, and A. Zemlianov, “Microstructure-based analysis of residual stress concentration and plastic strain localization followed by fracture in metal-matrix composites,” *Engineering Fracture Mechanics*, vol. 259, p. 108 138, 2022, ISSN: 0013-7944.
- [155] X. Luo *et al.*, “Evading strength and ductility trade-off in an inverse nacre structured magnesium matrix nanocomposite,” *Acta Materialia*, vol. 228, p. 117 730, 2022, ISSN: 1359-6454.
- [156] Z. Zaiemyekheh *et al.*, “Computational finite element modeling of stress-state-and strain-rate-dependent failure behavior of ceramics with experimental validation,” *Ceramics International*, 2023, ISSN: 0272-8842.
- [157] N. Liu *et al.*, “Numerical investigations on the hybrid effect and deformation mechanism of TiB_{2p} and TiB_w reinforced Cu composites prepared by in-situ mixing casting,” *Computational Materials Science*, vol. 213, p. 111 657, 2022, ISSN: 0927-0256.
- [158] X. Zhang *et al.*, “Multiscale constitutive modeling of additively manufactured Al–Si–Mg alloys based on measured phase stresses and dislocation density,” *International Journal of Plasticity*, vol. 140, p. 102 972, 2021, ISSN: 0749-6419.
- [159] Q. Niu *et al.*, “A constitutive model of Al/50 wt%Si_p composites considering particle damage effects,” *Materials Science and Engineering: A*, vol. 836, p. 142 726, 2022, ISSN: 0921-5093.
- [160] E. Sansoucy, P. Marcoux, L. Ajdelsztajn, and B. Jodoin, “Properties of SiC-reinforced aluminum alloy coatings produced by the cold gas dynamic spraying process,” *Surface and Coatings Technology*, vol. 202, no. 16, pp. 3988–3996, 2008, ISSN: 0257-8972.
- [161] Q. Du, V. Faber, and M. Gunzburger, “Centroidal Voronoi tessellations: Applications and algorithms,” *SIAM review*, vol. 41, no. 4, pp. 637–676, 1999.
- [162] R. Quey and L. Renversade, “Optimal polyhedral description of 3D polycrystals: Method and application to statistical and synchrotron X-ray diffraction data,” *Computer Methods in Applied Mechanics and Engineering*, vol. 330, pp. 308–333, 2018, ISSN: 0045-7825.
- [163] S. Ha, J.-H. Jang, and K. Kim, “Finite element implementation of dislocation-density-based crystal plasticity model and its application to pure aluminum crystalline materials,” *International Journal of Mechanical Sciences*, vol. 120, pp. 249–262, 2017, ISSN: 0020-7403.
- [164] W. Liu, J. Huang, Y. Pang, K. Zhu, S. Li, and J. Ma, “Multi-scale modelling of evolving plastic anisotropy during Al-alloy sheet forming,” *International Journal of Mechanical Sciences*, vol. 247, p. 108 168, 2023, ISSN: 0020-7403.

- [165] X. He, S. Song, X. Luo, J. Liu, L. An, and Y. Bai, “Predicting ductility of Mg/SiCp nanocomposite under multiaxial loading conditions based on unit cell modeling,” *International Journal of Mechanical Sciences*, vol. 184, p. 105 831, 2020, ISSN: 0020-7403.
- [166] J. Feder, “Random sequential adsorption,” *Journal of Theoretical Biology*, vol. 87, no. 2, pp. 237–254, 1980, ISSN: 0022-5193.
- [167] S. Naderi and M. Zhang, “An integrated framework for modelling virtual 3D irregular particulate mesostructure,” *Powder Technology*, vol. 355, pp. 808–819, 2019, ISSN: 0032-5910.
- [168] D. Garoz, F. Gilabert, R. Sevenois, S. Spronk, and W. Van Paepegem, “Consistent application of periodic boundary conditions in implicit and explicit finite element simulations of damage in composites,” *Composites Part B: Engineering*, vol. 168, pp. 254–266, 2019, ISSN: 1359-8368.
- [169] Z. He, H. Zhu, and Y. Hu, “An improved shear modified GTN model for ductile fracture of aluminium alloys under different stress states and its parameters identification,” *International Journal of Mechanical Sciences*, vol. 192, p. 106 081, 2021, ISSN: 0020-7403.
- [170] V. Tvergaard, “On localization in ductile materials containing spherical voids,” *International Journal of fracture*, vol. 18, no. 4, pp. 237–252, 1982.
- [171] L. Xue, “Constitutive modeling of void shearing effect in ductile fracture of porous materials,” *Engineering Fracture Mechanics*, vol. 75, no. 11, pp. 3343–3366, 2008, Local Approach to Fracture (1986–2006): Selected papers from the 9th European Mechanics of Materials Conference, ISSN: 0013-7944.
- [172] N. Aravas, “On the numerical integration of a class of pressure-dependent plasticity models,” *International Journal for Numerical Methods in Engineering*, vol. 24, no. 7, pp. 1395–1416,
- [173] P. Zhao, Z. Chen, and C. Dong, “Failure analysis based on microvoids damage model for DP600 steel on in-situ tensile tests,” *Engineering Fracture Mechanics*, vol. 154, pp. 152–168, 2016, ISSN: 0013-7944.
- [174] E. Simons, J. Weerheijm, G. Toussaint, and L. Sluys, “An experimental and numerical investigation of sphere impact on alumina ceramic,” *International Journal of Impact Engineering*, vol. 145, p. 103 670, 2020, ISSN: 0734-743X.
- [175] W. Chen and G. Ravichandran, “Dynamic compressive failure of a glass ceramic under lateral confinement,” *Journal of the Mechanics and Physics of Solids*, vol. 45, no. 8, pp. 1303–1328, 1997, ISSN: 0022-5096.
- [176] J. Zinszner, B. Erzar, P. Forquin, and E. Buzaud, “Dynamic fragmentation of an alumina ceramic subjected to shockless spalling: An experimental and numerical study,” *Journal of the Mechanics and Physics of Solids*, vol. 85, pp. 112–127, 2015, ISSN: 0022-5096.
- [177] Y Partom, “Calibrating a material model for AD995 alumina from plate impact VISAR profiles,” *Le Journal de Physique IV*, vol. 4, no. C8, pp. C8–495, 1994.

- [178] Y. Peng *et al.*, “Multiscale 3D finite element analysis of aluminum matrix composites with *nano & micro* hybrid inclusions,” *Composite Structures*, vol. 288, p. 115 425, 2022, ISSN: 0263-8223.
- [179] A. Kurşun, E. Bayraktar, and H. M. Enginsoy, “Experimental and numerical study of alumina reinforced aluminum matrix composites: Processing, microstructural aspects and properties,” *Composites Part B: Engineering*, vol. 90, pp. 302–314, 2016, ISSN: 1359-8368.
- [180] J. Zhang, X. Zhang, Q. Wang, B. Xiao, and Z. Ma, “Simulation of anisotropic load transfer and stress distribution in SiCp/Al composites subjected to tensile loading,” *Mechanics of Materials*, vol. 122, pp. 96–103, 2018, ISSN: 0167-6636.
- [181] J. Zhou, A. M. Gokhale, A. Gurumurthy, and S. P. Bhat, “Realistic microstructural RVE-based simulations of stress–strain behavior of a dual-phase steel having high martensite volume fraction,” *Materials Science and Engineering: A*, vol. 630, pp. 107–115, 2015, ISSN: 0921-5093.
- [182] C. Chen *et al.*, “Ductile and high strength Cu fabricated by solid-state cold spray additive manufacturing,” *Journal of Materials Science & Technology*, vol. 134, pp. 234–243, 2023, ISSN: 1005-0302.
- [183] N. Hansen, “Hall–petch relation and boundary strengthening,” *Scripta materialia*, vol. 51, no. 8, pp. 801–806, 2004.
- [184] C.-S. Kim *et al.*, “Prediction models for the yield strength of particle-reinforced unimodal pure magnesium (Mg) metal matrix nanocomposites (MMNCs),” *Journal of Materials Science*, vol. 48, no. 12, pp. 4191–4204, 2013.
- [185] M. Ji, H. Li, J. Zheng, S. Yang, Z. Zaiemyek, and J. D. Hogan, “An experimental study on the strain-rate-dependent compressive and tensile response of an alumina ceramic,” *Ceramics International*, vol. 48, no. 19, Part A, pp. 28 121–28 134, 2022, ISSN: 0272-8842.
- [186] J. Huang *et al.*, “Pure copper components fabricated by cold spray (CS) and selective laser melting (SLM) technology,” *Surface and Coatings Technology*, vol. 395, p. 125 936, 2020, ISSN: 0257-8972.
- [187] L. He, D. C. Pagan, A. Nardi, and M. Hassani, “Synchrotron X-ray diffraction studies of the phase-specific deformation in additively manufactured Ni–CrC composites,” *Composites Part B: Engineering*, vol. 222, p. 109 086, 2021, ISSN: 1359-8368.
- [188] W. Yu *et al.*, “Texture evolution, segregation behavior, and mechanical properties of 2060 Al–Li (aluminium–lithium) composites reinforced by TiC (titanium carbide) nanoparticles,” *Composites Part B: Engineering*, vol. 255, p. 110 611, 2023.
- [189] X. Dong, H. Youssef, Y. Zhang, S. Wang, and S. Ji, “High performance Al/TiB₂ composites fabricated by nanoparticle reinforcement and cutting-edge super vacuum assisted die casting process,” *Composites Part B: Engineering*, vol. 177, p. 107 453, 2019.

- [190] R. Raelison, C. Verdy, and H. Liao, “Cold gas dynamic spray additive manufacturing today: Deposit possibilities, technological solutions and viable applications,” *Materials & Design*, vol. 133, pp. 266–287, 2017.
- [191] D. Zhu, G. Wu, G. Chen, and Q. Zhang, “Dynamic deformation behavior of a high reinforcement content TiB₂/Al composite at high strain rates,” *Materials Science and Engineering: A*, vol. 487, no. 1, pp. 536–540, 2008.
- [192] Q. Han, Y. Geng, R. Setchi, F. Lacan, D. Gu, and S. L. Evans, “Macro and nanoscale wear behaviour of Al-Al₂O₃ nanocomposites fabricated by selective laser melting,” *Composites Part B: Engineering*, vol. 127, pp. 26–35, 2017.
- [193] H. Enginsoy, E. Bayraktar, D. Katundi, F. Gatamorta, and I. Miskioglu, “Comprehensive analysis and manufacture of recycled aluminum based hybrid metal matrix composites through the combined method; sintering and sintering + forging,” *Composites Part B: Engineering*, vol. 194, p. 108 040, 2020.
- [194] X. Yang *et al.*, “Evolution of microstructure and mechanical properties of cold spray additive manufactured aluminum deposit on copper substrate,” *Materials Science and Engineering: A*, vol. 891, p. 146 024, 2024.
- [195] S. Bagherifard *et al.*, “Tailoring cold spray additive manufacturing of steel 316 L for static and cyclic load-bearing applications,” *Materials & Design*, vol. 203, p. 109 575, 2021.
- [196] W. Li, C. Cao, G. Wang, F. Wang, Y. Xu, and X. Yang, “‘Cold spray+’ as a new hybrid additive manufacturing technology: A literature review,” *Science and Technology of Welding and Joining*, vol. 24, no. 5, pp. 420–445, 2019.
- [197] W. Li, K. Yang, S. Yin, X. Yang, Y. Xu, and R. Lupoi, “Solid-state additive manufacturing and repairing by cold spraying: A review,” *Journal of Materials Science & Technology*, vol. 34, no. 3, pp. 440–457, 2018.
- [198] S. Bagherifard *et al.*, “Cold spray deposition of freestanding inconel samples and comparative analysis with selective laser melting,” *Journal of Thermal Spray Technology*, vol. 26, pp. 1517–1526, 2017.
- [199] H. He *et al.*, “Enhanced distribution and mechanical properties of high content nanoparticles reinforced metal matrix composite prepared by flake dispersion,” *Composites Part B: Engineering*, vol. 252, p. 110 514, 2023.
- [200] W. Xue *et al.*, “Research on low flow stress and quantitative DRX analysis in B₄C/Al composites with interfacial amorphous B₂O₃ layer,” *Composites Part B: Engineering*, vol. 272, p. 111 226, 2024.
- [201] Y. Li *et al.*, “Influence of surface integrity on the fatigue performance of TiB₂/Al composite treated by ultrasonic deep rolling: Experiments and simulations,” *Composites Part B: Engineering*, vol. 271, p. 111 160, 2024.
- [202] P. Garg, A. Jamwal, D. Kumar, K. K. Sadasivuni, C. M. Hussain, and P. Gupta, “Advance research progresses in aluminium matrix composites: Manufacturing applications,” *Journal of Materials Research and Technology*, vol. 8, no. 5, pp. 4924–4939, 2019.

- [203] D. Miracle, “Metal matrix composites – from science to technological significance,” *Composites Science and Technology*, vol. 65, no. 15, pp. 2526–2540, 2005, 20th Anniversary Special Issue.
- [204] M. C. Jo *et al.*, “Novel dynamic compressive and ballistic properties in 7075-T6 Al-matrix hybrid composite reinforced with SiC and B4C particulates,” *Composites Part B: Engineering*, vol. 174, p. 107041, 2019.
- [205] S. Yadav, D. Chichili, and K. Ramesh, “The mechanical response of a 6061-T6 Al/Al₂O₃ metal matrix composite at high rates of deformation,” *Acta Metallurgica et Materialia*, vol. 43, no. 12, pp. 4453–4464, 1995.
- [206] T. Ye, Y. Xu, and J. Ren, “Effects of SiC particle size on mechanical properties of sic particle reinforced aluminum metal matrix composite,” *Materials Science and Engineering: A*, vol. 753, pp. 146–155, 2019, ISSN: 0921-5093.
- [207] Y. Li, K. Ramesh, and E. Chin, “Comparison of the plastic deformation and failure of A359/SiC and 6061-T6/Al₂O₃ metal matrix composites under dynamic tension,” *Materials Science and Engineering: A*, vol. 371, no. 1, pp. 359–370, 2004.
- [208] Y. Wang *et al.*, “Dynamic compressive response and impact resistance of bioinspired nacre-like 2024Al/B4C composites,” *Materials Science and Engineering: A*, vol. 831, p. 142261, 2022.
- [209] Z. Zaiemyek, G. Liaghat, H. Ahmadi, M. Khan, and O. Razmkhah, “Effect of strain rate on deformation behavior of aluminum matrix composites with Al₂O₃ nanoparticles,” *Materials Science and Engineering: A*, vol. 753, pp. 276–284, 2019.
- [210] X. Sun *et al.*, “Significant improvement of the room and cryogenic mechanical properties of an AlN particle reinforced Al matrix composite by alloying element magnesium,” *Composites Part B: Engineering*, vol. 268, p. 111056, 2024.
- [211] M. Gao, X. Song, C. Wang, and Y. Fu, “Tensile property and fracture mechanism of a neutron absorbing B4Cp/Al composite at elevated temperatures,” *Materials Science and Engineering: A*, vol. 848, p. 143300, 2022.
- [212] W. Sun, C. Duan, and W. Yin, “Development of a dynamic constitutive model with particle damage and thermal softening for Al/SiCp composites,” *Composite Structures*, vol. 236, p. 111856, 2020.
- [213] J. Nafar Dastgerdi, B. Anbarlooie, A. Miettinen, H. Hosseini-Toudeshky, and H. Remes, “Effects of particle clustering on the plastic deformation and damage initiation of particulate reinforced composite utilizing X-ray CT data and finite element modeling,” *Composites Part B: Engineering*, vol. 153, pp. 57–69, 2018.
- [214] X. Zhang, T. Chen, S. Ma, H. Qin, and J. Ma, “Overcoming the strength-ductility trade-off of an aluminum matrix composite by novel core-shell structured reinforcing particulates,” *Composites Part B: Engineering*, vol. 206, p. 108541, 2021.

- [215] Q. Ren, Z. Yue, C. Soyarslan, Z. Tan, F. Yuan, and Z. Li, “A coupled ductile damage model for metal matrix composites: Development and application,” *Composites Part B: Engineering*, vol. 272, p. 111 229, 2024.
- [216] X. Kai *et al.*, “Effects of Zr element on the microstructure and mechanical properties of B₄C/Al composites fabricated by melt stirring method,” *Composites Part B: Engineering*, vol. 224, p. 109 156, 2021.
- [217] D. Gong, M. Zhu, Z. You, H. Han, Z. Chao, and L. Jiang, “In-situ TEM study on the effect of stacking faults on micro-plasticity and proportional limit in SiC/Al composites,” *Composites Part B: Engineering*, vol. 244, p. 110 180, 2022.
- [218] S. Kumar, S. K. Reddy, and S. Joshi, “Microstructure and performance of cold sprayed Al-SiC composite coatings with high fraction of particulates,” *Surface and Coatings Technology*, vol. 318, pp. 62–71, 2017, 7th Rencontres Internationales de la Projection Thermique.
- [219] S. Yin *et al.*, “Towards high-strength cold spray additive manufactured metals: Methods, mechanisms, and properties,” *Journal of Materials Science & Technology*, vol. 170, pp. 47–64, 2024.
- [220] K. P. Mingard and B. Roebuck, “Interlaboratory measurements of contiguity in WC – Co hardmetals,” *Metals*, vol. 9, no. 3, p. 328, 2019.
- [221] H. Li, P. Motamedi, and J. Hogan, “Characterization and mechanical testing on novel ($\gamma + \alpha_2$) – TiAl/Ti₃Al/Al₂O₃ cermet,” *Materials Science and Engineering: A*, vol. 750, pp. 152–163, 2019.
- [222] X. Xie *et al.*, “Effect of annealing treatment on microstructure and mechanical properties of cold sprayed TiB₂/AlSi10Mg composites,” *Surfaces and Interfaces*, vol. 26, p. 101 341, 2021.
- [223] R. Nikbakht, M. Saadati, H. Assadi, K. Jahani, and B. Jodoin, “Dynamic microstructure evolution in cold sprayed NiTi composite coatings,” *Surface and Coatings Technology*, vol. 421, p. 127 456, 2021.
- [224] T. Blesgen, “A variational model for dynamic recrystallization based on Cosserat plasticity,” *Composites Part B: Engineering*, vol. 115, pp. 236–243, 2017.
- [225] Y. Ren *et al.*, “Effects of different heat treatments on anisotropy of cold sprayed 7075 Al deposits,” *Materials Characterization*, vol. 199, p. 112 828, 2023.
- [226] M. Khomutov *et al.*, “Structure and properties of AA7075-SiC composite parts produced by cold spray additive manufacturing,” *The International Journal of Advanced Manufacturing Technology*, vol. 116, no. 3-4, pp. 847–861, 2021.
- [227] Z. GUO, T. MA, X. YANG, J. LI, W. LI, and A. VAIRIS, “Multi-scale analyses of phase transformation mechanisms and hardness in linear friction welded Ti17($\alpha + \beta$)/Ti17(β) dissimilar titanium alloy joint,” *Chinese Journal of Aeronautics*, vol. 37, no. 1, pp. 312–324, 2024.
- [228] X. Yang *et al.*, “A review on linear friction welding of Ni-based superalloys,” *International Journal of Minerals, Metallurgy and Materials*, 2023.

- [229] X. Wu, L. Li, W. Liu, S. Li, L. Zhang, and H. He, “Development of adiabatic shearing bands in 7003-T4 aluminum alloy under high strain rate impacting,” *Materials Science and Engineering: A*, vol. 732, pp. 91–98, 2018.
- [230] Y. Suo *et al.*, “High-temperature compressive response of SiCp/6092Al composites under a wide range of strain rates,” *Materials*, vol. 14, no. 21, p. 6244, 2021.
- [231] Q. Guo, L. Jiang, G. Chen, D. Feng, D. Sun, and G. Wu, “SEM and TEM characterization of the microstructure of post-compressed TiB₂/2024Al composite,” *Micron*, vol. 43, no. 2, pp. 380–386, 2012.
- [232] G. Bao and Z. Lin, “High strain rate deformation in particle reinforced metal matrix composites,” *Acta Materialia*, vol. 44, no. 3, pp. 1011–1019, 1996.
- [233] Z. Zhu *et al.*, “Recent progress on the additive manufacturing of aluminum alloys and aluminum matrix composites: Microstructure, properties, and applications,” *International Journal of Machine Tools and Manufacture*, vol. 190, p. 104047, 2023.
- [234] X. Wang, F. Jiang, T. Zhang, and L. Wang, “Study on dynamic mechanical properties and constitutive model of 10B/Al composite compared with its matrix of high-purity aluminum,” *Journal of Materials Science*, vol. 55, no. 2, pp. 748–761, 2020.
- [235] B. K. Roy, Y. P. Korkolis, Y. Arai, W. Araki, T. Iijima, and J. Kouyama, “Plastic deformation of AA6061-T6 at elevated temperatures: Experiments and modeling,” *International Journal of Mechanical Sciences*, vol. 216, p. 106943, 2022.
- [236] P. T. Summers *et al.*, “Overview of aluminum alloy mechanical properties during and after fires,” *Fire Science Reviews*, vol. 4, no. 1, pp. 1–36, 2015.
- [237] M. Li, Y. Wang, H. Gao, J. Wang, and B. Sun, “Thermally stable microstructure and mechanical properties of graphene reinforced aluminum matrix composites at elevated temperature,” *Journal of Materials Research and Technology*, vol. 9, no. 6, pp. 13230–13238, 2020.
- [238] J. I. Rojas, B. Venkata Siva, K. L. Sahoo, and D. Crespo, “Viscoelastic behavior of a novel aluminum metal matrix composite and comparison with pure aluminum, aluminum alloys, and a composite made of Al–Mg–Si alloy reinforced with SiC particles,” *Journal of Alloys and Compounds*, vol. 744, pp. 445–452, 2018.
- [239] G. Sundararajan, N. M. Chavan, and S. Kumar, “The elastic modulus of cold spray coatings: Influence of inter-splat boundary cracking,” *Journal of Thermal Spray Technology*, vol. 22, pp. 1348–1357, 2013.
- [240] P. Forquin, “14 - dynamic behavior of ceramic materials,” in *Dynamic Behavior of Materials*, M. Hokka, Ed., Elsevier, 2024, pp. 449–482.

- [241] Y. Wang *et al.*, “Dynamic mechanical response and damage mechanisms of nacre-inspired 2024Al/B4C composite at elevated temperature,” *Materials Science and Engineering: A*, vol. 831, p. 142 263, 2022.
- [242] C. Shin and J. Huang, “Effect of temper, specimen orientation and test temperature on the tensile and fatigue properties of SiC particles reinforced PM 6061 Al alloy,” *International Journal of Fatigue*, vol. 32, no. 10, pp. 1573–1581, 2010.
- [243] S. Chen *et al.*, “Revealing the influence of SiC particle size on the hot workability of SiCp/6013 aluminum matrix composites,” *Materials*, vol. 16, no. 18, p. 6292, 2023.
- [244] A. Eisenlohr, I. Gutierrez-Urrutia, and D. Raabe, “Adiabatic temperature increase associated with deformation twinning and dislocation plasticity,” *Acta Materialia*, vol. 60, no. 9, pp. 3994–4004, 2012.
- [245] N. Ranc, L. Taravella, V. Pina, and P. Herve, “Temperature field measurement in titanium alloy during high strain rate loading—adiabatic shear bands phenomenon,” *Mechanics of Materials*, vol. 40, no. 4, pp. 255–270, 2008.
- [246] B. Erice, C. C. Roth, and D. Mohr, “Stress-state and strain-rate dependent ductile fracture of dual and complex phase steel,” *Mechanics of Materials*, vol. 116, pp. 11–32, 2018, IUTAM Symposium on Dynamic Instabilities in Solids, ISSN: 0167-6636.
- [247] C. C. Roth and D. Mohr, “Effect of strain rate on ductile fracture initiation in advanced high strength steel sheets: Experiments and modeling,” *International Journal of Plasticity*, vol. 56, pp. 19–44, 2014.
- [248] J Genée, N Gey, F Bonnet, R. A. Lebensohn, and S Berbenni, “Experimental and numerical investigation of key microstructural features influencing the localization of plastic deformation in Fe-TiB₂ metal matrix composite,” *Journal of Materials Science*, vol. 56, no. 19, pp. 11 278–11 297, 2021.
- [249] Q. Liu and D. Wu, “Machine learning and feature representation approaches to predict stress-strain curves of additively manufactured metamaterials with varying structure and process parameters,” *Materials Design*, vol. 241, p. 112 932, 2024, ISSN: 0264-1275.
- [250] M. Maurizi, C. Gao, and F. Berto, “Predicting stress, strain and deformation fields in materials and structures with graph neural networks,” *Scientific reports*, vol. 12, no. 1, p. 21 834, 2022.
- [251] P. M. Flávio, L. C. Muniz, and T. Doca, “ANN strategies for the stress–strain analysis of metallic materials: Modeling, database, supervised learning, validation and performance analysis,” *Finite Elements in Analysis and Design*, vol. 230, p. 104 097, 2024, ISSN: 0168-874X.

- [252] B. G. Christoff, J. H. S. Almeida, M. L. Ribeiro, M. M. Maciel, R. M. Guedes, and V. Tita, “Multiscale modelling of composite laminates with voids through the direct FE² method,” *Theoretical and Applied Fracture Mechanics*, vol. 131, p. 104424, 2024, ISSN: 0167-8442.
- [253] S. Li and S. Hou, “A machine learning method of accelerating multiscale analysis for spatially varying microstructures,” *International Journal of Mechanical Sciences*, vol. 266, p. 108952, 2024, ISSN: 0020-7403.